Atomic Layer Deposition Functionalization and Modification of Three Dimensional Nanostructures for Energy Storage and Conversion

Dissertation

zur Erlangung des Doktorgrades

Dr. rer. nat.

vorgelegt der
Fakultät für Mathematik und Naturwissenschaften der
Technischen Universität Ilmenau

von
M. Sc. Yan Mi
Ilmenau

Doktorvater und 1. Gutachter: Prof. Dr. Yong Lei

2. Gutachter: Prof. Dr. ir. J.E. ten Elshof

3. Gutachter: Prof. Dr. rer. nat. habil. Andreas Schober

Tag der Einreichung: 08.12.2015

Tag der wissenschaftlichen Aussprache: 11.05.2016

urn:nbn:de:gbv:ilm1-2016000217

Acknowledgment

Foremost, I would like to sincerely thank my supervisor Prof. Dr. Yong Lei for providing me the opportunity to study and do academic research in his research group at TU-Ilmenau in Germany. I specially want to thank him for his encouragement, support and guidance during my entire work period. He has been actively supervising my research work, and has always provided fruitful advice and suggestions to inspire me to solve the problems in my work. And he has also given me the opportunities to visit and cooperate with other excellent research groups in the world. Meanwhile, I was always encouraged by him to attend more scientific conferences and give talks there, and also to participate in teachings in our group. He has not only been a scientific supervisor to me, moreover, he has encouraged me to be very active when facing challenging scientific topics. I really feel very happy with the memorable and precious experiences that I have gained in our group.

I also want to thank the colleagues in our group for their kind help, active and pleasant discussion and cooperation. It was a great pleasure to work in such an international and diverse scientific research group. My special thanks to Mr. Liaoyong Wen for his valuable academic discussion and the collaboration works in AAO template, and also works in energy devices. Many thanks to Dr. Dawei Cao, Dr. Zhijie Wang, Dr. Min Zhou, Dr. Chengliang Wang, Dr. Yang Xu, Dr. Zhibing Zhan, Dr. Huaping Zhao, Dr. Fabian Grote, Mr. Rui Xu, Ms. Liying Liang, and Mr. Ahmed Shukur Hameed Al-Haddad for their experiment and technique support. Thanks to Prof. Dr. Stefan Krischok and Dr. Marcel Himmerlich for the Pt nanotube XPS measurement. And also thanks the colleagues in ZMN for their kind help in my work. Especially I thank to Dr. Arne Albrecht, Dipl.-Ing. Tirsten Sändig, Dr. Henry Romanus and Dr. Thomas Kups for their technique support.

Moreover, I want to thank Prof. Dr. Shuhong Yu from the University of Science and Technology of China for giving me the opportunity to work in his research group. The active academic atmosphere has inspired me, and the collaboration work has resulted in excellent scientific results with the help of Mr. Ziyou Yu and Dr. Yarong Zheng in his group. I also need to thank Dr. Chong Xiao in USTC for the fruitful discussion in photoelectrochemical.

I acknowledge the “Volkswagen Stiftung”, “Bundesministerium für Bildung und Forschung” (ZIK-3DNanoDevice: 03Z1MN11) and the “European Research Council” (ThreeDsurface: 240144) for the financial support during my Ph. D.

Finally, I would like to thank my dear family members for their encouragement and support. Especially, I thank my husband Mr. Feilong Hu for his understanding, support and sacrifice during the entire process of my Ph.D.

Abstract

In order to fulfill the increasing demands for various sustainable and renewable energy sources in future, many efforts have been paid to construct high-efficient energy storage and conversion devices for the corresponding energy sources. The boom of nanomaterials provides new opportunities for the development of high efficient energy related devices. Meanwhile, the fabrication of three-dimensional architecture nanomaterials to replace their planer counterparts for devices fabrication has been regarded as one of the promising strategy to improve the efficiency of devices. In this thesis, through effectively combining three-dimensional micro/nanoarchitecture with atomic layer deposition, we carried out a series of systematic research works on controllable fabrication, assembly and functionalization of three-dimensional micro/nanoarchitecture for high-efficient energy storage and conversion devices. The main achievements are outlined as following:

1. A low-cost and controlled assembly route was employed to construct three-dimensional aluminum doped zinc oxide transparent electrode using atomic layer deposition on varies micro/nanostructures, including three-dimensional nanopore array and three-dimensional porous nanostructure and so on. The two main properties of transparent electrode, electroconductivity and transparence of the synthesized three-dimensional aluminum doped zinc were systematically investigated by the adjusting of doping and growth conditions by atomic layer deposition. The constructed three-dimensional aluminum doped zinc oxide could serve as a good transparent electrode to be used in the new generations of photovoltaic and optoelectronic devices.

2. Core/shell nanostructures with optimal structure and composition could maximize the solar light utilization. A feasible route was performed toward scalable fabrication of well-modulated core/shell nanostructures and can be easily applied to other metal/semiconductor composites for high-performance photoelectrochemical electrodes. An aluminum nanocone array as a substrate, well-defined regular array of aluminum doped zinc oxide/titanium dioxide core/shell nanocones with uniformly dispersed gold nanoparticles was successfully realized through three sequential steps of atomic layer

deposition, physical vapor deposition and annealing processes. By tuning the structural and compositional parameters, the advantages of light trapping and short carrier diffusion from the core/shell nanocone array, as well as the surface plasmon resonance and catalytic effects from the gold nanoparticles can be maximally utilized. Accordingly, a remarkable photoelectrochemical performance could be acquired.

3. A cost-effective atomic layer deposition process was introduced to realize well-defined three-dimensional platinum nanotube array based on alumina nano-porous template. Through the special introduction of a low-nitrogen-filling step and the control of atomic layer deposition conditions, continuous and smooth surface of platinum nanotube array could be obtained. And to achieve those platinum nanotube arrays, half numbers of the atomic layer deposition cycles and 10% platinum precursor pulsing time are only needed, compared to conventional atomic layer deposition process. The achieved platinum nanotube array was explored as a current collector to construct three-dimensional core/shell platinum/manganese dioxide nanotube array for supercapacitors. The constructed three-dimensional core/shell nanostructure electrode exhibited a high specific capacitance, an excellent rate capability and a negligible capacitance loss after long-term charging-discharging cycling.

4. An ultra-low loading amount of ultrasmall platinum nanoparticles on three-dimensional bacterial cellulose derived carbon nanofiber was achieved by using a convenient modified atomic layer deposition process. The ultrasmall platinum nanoparticles surface-modified three-dimensional carbon nanofiber exhibited good electrocatalytic activity and stability towards hydrogen evolution reaction. The synthesis process provides a general strategy for minimizing the demand of precious metal catalysts while maintaining their high catalytic efficiency.

The achieved results within this dissertation on three-dimensional nanostructures fabrication and functionalization, and the integration in energy storage and conversion device should provide a strong insight and guidance on the design and structure of the high efficient energy storage and conversion devices.

Zusammenfassung

Um der steigende Nachfrage nach nachhaltigen und erneuerbaren Energiequellen in der Zukunft gerecht zu werden, wurden viele Anstrengen unternommen um hoch effiziente Energiespeicher und Bauelemente zur Energieumwandlung zu entwickeln. Insbesondere bieten Nanomaterialien neue Möglichkeiten um energiebezogene Bauelemente noch effizienter zu machen. Hier verspricht man sich von der Herstellung von dreidimensionalen Nanostrukturen weitere Effizienzsteigerungen im Vergleich zu planaren Strukturen. In dieser Arbeit werden hocheffiziente Energiespeicher und -umwandler durch die effektive Kombination von dreidimensionaler Mikro- und Nanotechnologie mit Atomlagenabscheidung hergestellt und systematisch charakterisiert. Im Folgenden die wichtigsten Ergebnisse:

1. Dreidimensionale nanoporöse Aluminiumdotierte Zinkoxid Elektroden wurden kostengünstig und kontrolliert mit Hilfe von Atomlagenabscheidung hergestellt. Die wichtigsten Parameter, Transparenz und elektrische Leitfähigkeit der Elektrode, wurde systematisch charakterisiert und der Einfluss der Dopingkonzentration und der Wachstumsbedingungen wurde analysiert. Es hat sich herausgestellt, dass die dreidimensionalen nanoporöse Aluminiumdotierte Zinkoxid Elektroden sich insbesondere als gute transparente Elektroden in der Photovoltaik und in optoelektronischen Bauelementen eignen.
2. Kern/Mantelnanostrukturen mit optimierter Struktur und Zusammensetzung können die ausbaute von Sonnenlicht deutlich erhöhen. Eine vielversprechende Route mit starkem Fokus auf die skalierbare Herstellung von gut modulierten Kern/Mantel-Nanostrukturen wurde entwickelt, welche leicht an andere Metall und Halbleiter für photoelektrochemische Elektroden angepasst werden kann. Als Substrat dient ein regelmäßig angeordnetes Aluminium nano-Kegel-Array, welches mit einer Aluminium-dotiertem Zinkoxid / Titandioxid Kern/Mantel Struktur und regelmäßig verteilten Goldnanopartikeln überzogen ist. Die Herstellung wurde Hilfe von Atomlagenabscheidung, physikalischer Dampfabscheidung und einem Glühprozess realisiert. Durch gezielte Abstimmung der Struktur und Zusammensetzung konnte der

Lichteinfang verbessert und die Ladungsträgerdiffusion optimiert werden. Plasmonenresonanz und katalytische Effekte konnten durch Goldnanopartikel kontrolliert werden. Dementsprechend konnte eine bemerkenswerte photoelektrochemische Leistungsfähigkeit erzielt werden.

3. Ein kostengünstiger Prozess für die Synthese von dreidimensionalen Platin Nanoröhren-Arrays, basierend auf der Atomlagenabscheidung und nanoporösen Templaten, wurde entwickelt. Dies gelang durch die Einführung eines low-nitrogen-filling Schritts. Kontinuierliche Platin Nanoröhren mit glatter Oberfläche wurden erzielt. Dabei wurde die Anzahl der Zyklen halbiert und die Pulszeit des Platinprecursors um 10 % reduziert im Vergleich zu herkömmlichen Verfahren. Die hergestellten Platinnanoröhren-Arrays wurden als Stromkollektoren für dreidimensionale Pt/MnO_2 Kern/Mantel Strukturen in Superkondensatoren eingesetzt. Die synthetisierte Struktur zeigte eine hohe spezifische Kapazität, gute Performance unter schneller Entladung und eine gute Zyklenbeständigkeit.

4. Eine ultra-niedrige Lademenge von sehr kleinen Platin Nanopartikeln auf Kohlenstoffnanofasern, welche mittels bakterieller Zellulose hergestellt wurde, wurde mit Hilfe der Atomlagenabscheidung erzielt. Die mit Platinpartikeln oberflächenmodifizierte Kohlenstoffnanofasern zeigten gute elektrokatalytische Aktivität und Stabilität gegenüber der Wasserstoffentwicklungsreaktion. Das Syntheseverfahren stellt eine allgemeine Strategie dar, um den Einsatz von Edelmetallkatalysatoren unter Beibehaltung ihrer hohen katalytischen Effizienz zu minimieren.

Die im Rahmen dieser Arbeit erzielten Ergebnisse in Bezug auf die Herstellung von dreidimensionalen Nanostrukturen, ihre Funktionalisierung und die Implementierung in Bauelemente zur Energiespeicherung und -umwandlung, sollte eine starke Basis für zukünftige Bauelemente mit verbesserter Leistung liefern.

Table of Contents

List of Figures

1. Introduction

2. Experiments and methods

3. Atomic layer deposition fabrication of three-dimensional Al-doped ZnO for transparent electrode

4. Construction of three-dimensional core/shell AZO/TiO_2/Au nanocone array based on atomic layer deposition for enhancing photoelectrochemcial water splitting

5. Fabrication of three-dimensional Pt/MnO_2 nanotube arrays for supercapacitor

6. Surface modification of three-dimensional carbon nanofiber aerogel with ultrasmall Pt nanoparticles by ALD for electrocatalytic hydrogen evolution

Extended works

List of Tables

List of Abbreviations

Cu_2O	cuprous oxide
AAO	anodic aluminum oxide
SiC	silicon carbide
Al	aluminum
ALD	atomic layer deposition
Al_2O_3	aluminium oxide
$Al(CH_3)_3$	trimethylaluminium
CH_4	methane
DSSC	dye-sensitized solar cell
FTO	fluorine-doped tin-oxide
CdS	cadmium sulfide
TiO_2	titanium dioxide
ZnO	zinc oxide
Si	silicon
H_2	hydrogen
O_2	oxygen
$TiSi_2$	titanium disilicde
CVD	chemical vapor deposition
WO_3	tungsten oxide
ITO	indium tin oxide
Mn	manganese
Li^+ / Na^+	lithium-ion / sodium ion
$LiCoO_2$	lithium cobalt oxide
TiN	titanium nitride
$TiCl_4$	titanium tetrachloride
N_2	nitrogen
Pt	platinum
$MeCpPtMe_3$	trimethyl(methylcyclopentadienyl)platinum(IV)
CNT	carbon nanotube
Co_9S_8	cobalt sulfide

Au	gold
CO	carbon monoxide
$SiTiO_3$	strontium titanate
PVD	physical vapor deposition
H_3PO_4	phosphoric acid
H_2CrO_4	chromic acid
Ni	nickel
3-APTES	3-aminopropyltriethoxysilanc
NCA	nanocone array
DI-water	distilled water
PS	poly-styrene sphere
H_2SO_4	sulfuric acid
H_2O_2	hydrogen peroxide
TCO	transparent conducting oxide
AZO	aluminum-doped zinc oxide
DEZ	diethylzinc
TMA	trimethylaluminum
NT	nanotube
PDMS	polydimethylsiloxane
NaOH	sodium hydroxide
MnO_2	manganese oxide
Ag/AgCl	silver/silver chloride
BC	bacterial cellulose
BCF	bacterial cellulose nanofiber
UV-vis	ultraviolet-visible
I-V	current-voltage
XPS	X-ray photoelectron spectroscopy
FE-SEM	field emission scanning electron microscopy
TEM	transmission electron microscopy
Cu	copper
EDS	energy dispersive X-Ray spectroscopy
Na_2SO_4	sodium sulfate

IPCE	incident photo-to-current efficiency
KCl	potassium chloride
C	carbon
SCE	saturated calomel electrode
RHE	reversible hydrogen electrode
HER	hydrogen evolution reaction
C-V	cyclic voltammetry
iR	interface resistance
FDTD	finite-difference time-domain
IR	infrared
Zn	zinc
PEC	photoelectrochemcial
SPR	surface plasmon resonance
NPs	nanoparticles
3D	three-dimensional
–OH	hydroxy
I-t	current-time
ABPE	photon-to-current efficiency
DL	depletion layer
EIS	electrochemical impedance spectroscopy
PRET	plasmon resonance energy transfer
EM	electromagnetic
SAED	selected area electron diffraction
TMCs	transition metal chalcogenides

1 Introduction

Currently, more than 70 % of the worldwide energy supply is from fossil fuels. The production of fossil energies like oil and natural gas is predicted to peak. Unfortunately, it is still cannot meet the increasing global energy demand in the near future [1,2]. Moreover, the extensive use of fossil fuels would unavoidably release a large amount of pollutants and carbon dioxide to the ambient. Thus, exploring alternative clean energy sources and utilizing it efficiently are of great significance to address these issues. With the magnitude of available energy directing towards the surface of earth, solar power has long been esteemed as the inexhaustible source for generating electricity and clean fuels [3]. So far, a large diversity of devices has been developed to convert solar energy to electricity and clean fuels, including the several kinds of solar cells and water splitting cells [4-7]. Meanwhile, in order to use the electric energy portably in a high power density, storing and utilizing electric energy in an electrochemical way has proven to be a feasible and promising strategy. Such systems for electrochemical energy storage include batteries and supercapacitors [8,9].

Present structures of commercial energy conversion and storage devices are dominated by planar configurations. With the development of advanced techniques in material preparations and device fabrications, the energy conversion and storage efficiencies of these devices have been approaching to the theoretical values. To break through the bottleneck and further improving the energy conversion and storage efficiencies of these devices, large scale of three-dimensional micro/nanoarchitectures are usually introduced [10,11]. The large surface-to-volume ration and large surface area of nanostructures allow the rapid and extensive occurring of energy conversion and storage. However, the realization of functional three-dimensional nanostructures is still one of the most challenging topics in nanotechnology today. The top-down and bottom-up are the two classes of existing strategies [12,13]. The top-down techniques are mainly based on lithography and thus suffer from low through-put and high cost, bottom-up approaches are commonly based on self-assembly and template assisted growth. Generally, these fabrication strategies allow a high through-put, do not need expensive equipment and provide an excellent control of the morphology within the nanometer regime. The advantages that arise from these bottom-up

approaches fabricated three-dimensional nanostructures with respect to energy storage and conversion will be introduced in the following section. Moreover, the beneficial use of atomic layer deposition (ALD) in combination with these three-dimensional nanostructures for energy devices will be discussed.

1.1. Advantage of three-dimensional nanostructures for energy storage and conversion

Nowadays, most of the commercially available energy storage and conversion devices consist of two-dimensional planar thin film structures which experience limitations in conversion efficiency and storage capability. The three-dimensional nanostructure has a high aspect ratio, indicating a large surface-to-volume ratio and the longitudinal continuity of the material. The large surface-to-volume ratio enables the relevant structure to have a huge surface area where the energy conversion and storage reaction could occur extensively and rapidly. The at least one dimension connected structure provides a continuous passway to efficiently transfer charge carriers [11,14,15].

The three-dimensional nanostructures are assembled into large areas, extending millions of nano-units to large-scale arrays for macroscopic energy applications. And these units could raise the scattering and antireflection effects. Meanwhile, the incident radiation could be easily collected, enabling it as an advantageous component in solar energy conversion devices [16,17]. As demonstrated by the finite difference time domain simulations for a conventional semiconductor Cu_2O, when illuminated by photons at 500 nm, the electric-field distribution around the planar Cu_2O film is concentrated on the surface [18]. As to the three-dimensional Cu_2O, the electric field distributing scope is greatly enlarged and a high electric field surrounds the entire nanowire arrays. As a result, the three-dimensional Cu_2O exhibits a dramatic improvement in absorption capability in comparison with the Cu_2O film below 480 nm.

For energy storage devices, the available void volume between adjacent nanostructures results in fast ion transportation, easy electrolyte accessibility to the electrode and tolerance for volume expansion of the active materials [11]. The deterioration problems in the planar batteries with increasing charge/discharge cycles could be largely alleviated by using three-dimensional nanostructures. Moreover, the distance for ion transportation in discharging is dramatically reduced by adopting interdigitated three-dimensional nanostructures [16]. And

such a structure can significantly less susceptible to Ohmic losses and other transport limitations. Thus, the large surface area greatly facilitates energy storage and conversion reactions; the specific three-dimensional surface structure provides an efficient passway for transporting charge carriers or ions; and the optical scattering and antireflection results the overall energy conversion and storage performance.

1.2. Template-directed construction of three-dimensional nanostructures

Over the last decade, numerous researches have sufficiently evidenced the advantages of large scale three-dimensional micro/nanostructures for energy conversion and storage. And various techniques have been shown up to fabricate three-dimensional nanostructures. Among them, template-directed construction of three-dimension nanostructures offers a convenient and versatile approach to produce nanostructure with distinguished advantages for energy-related device applications [17,19-21]. In general, template-directed techniques refer to the techniques that utilize template to regulate the synthesis of the nanomaterials or the dismounting of bulk materials into the desired nanostructures. First, template-directed technique could be used to produce nanostructure of many materials in large scale because of its easiness and maneuverability. Second, template-directed nanostructures have controllable morphological features in nanoscale dimensions, including shape, size, interspace, etc. The flexible structural controllability is highly beneficial for the performance optimization of energy-related devices. Third, the spatial orientation and arrangement of template-directed nanostructure is predefined according to the spatial structure of fixed template, and such structure can be retained to form a self-standing nanostructure on a substrate even after the template removal. The self-standing nanostructure with certain spatial orientation and alignment are promising building blocks for energy storage and conversion [22-25]. By turning the spatial orientation and alignment of these nanostructures, the performance of the corresponding energy devices can be further improved. The last but not the least, template-related process is an efficient way to construct nanostructure with high regularity. Specifically, highly-ordered nanostructure arrays which can be easily achieved based on some highly-ordered templates, including porous anodic aluminum oxide (AAO) template, colloidal crystal template, and so on. They provide opportunities for some exotic optical properties such as anti-reflection, surface plasmon resonance, etc. Based on

the above mentioned advantages, template-directed method has great potentials for constructing three-dimensional nanostructures towards highly efficient energy storage and conversion, including solar water splitting, supercapacitors, and so on.

1.2.1. Porous anodic aluminum oxide template

Since 1995, when Masuda and co-workers reported that well-ordered anodic aluminum oxide nanoporous structure could be attained by anodizing aluminum metal in acidic electrolytes [26], anodic aluminum oxide template has inspired a wave of fashion for fabricating highly-ordered nanostructure arrays. Such AAO template has a self-ordered, honeycomb-like and highly-oriented porous structure in nanoscale, with tunable pore size, density, interpore distance and distribution topologies. By adjusting the anodization conditions (e.g., choosing different electrolytes, applying different anodic biases, etc.), self-ordered anodic aluminum oxide templates with tunable pore diameters of about 10–400 nm and densities in the range 10^{8}–10^{10} pores·cm^{-2} can be prepared [27]. Combining with an imprinting process, long-range order of anodic aluminum oxide templates with tunable pore distributions and profiles could be conveniently realized [28,29]. Thereby, during the last decades, anodic aluminum oxide template has been extensively exploited in the fabrication of diverse nanostructure arrays in the form of nanopores [30], nanodots [31], nanocones [32,33], nanowires [34] and nanotubes [35]. In addition, the developed pulse anodization as well as the alternative usage of mild and hard anodizations for one specimen enable the fabricated anodic aluminum oxide templates with periodically modulated nanopore diameters along the pore axes, supplying another opportunity for tailoring the morphological parameters of the as-fabricated nanostructure arrays [36,37]. Due to the high compatibility of the anodic aluminum oxide template with a broad scope of techniques for material synthesis, many categories of materials can be prepared into nanostructure arrays, like metal, semiconductors, wide band gap oxides, polymers, and organic materials. To be more important, through manipulating the sequences of synthesizing various materials in the anodic aluminum oxide template, nanostructure arrays with multi-components and multi-segments could also be attained [38,39]. Thus, anodic aluminum oxide template provides a good scaffold to prepare nanostructure arrays for real device fabrications (Figure 1-1).

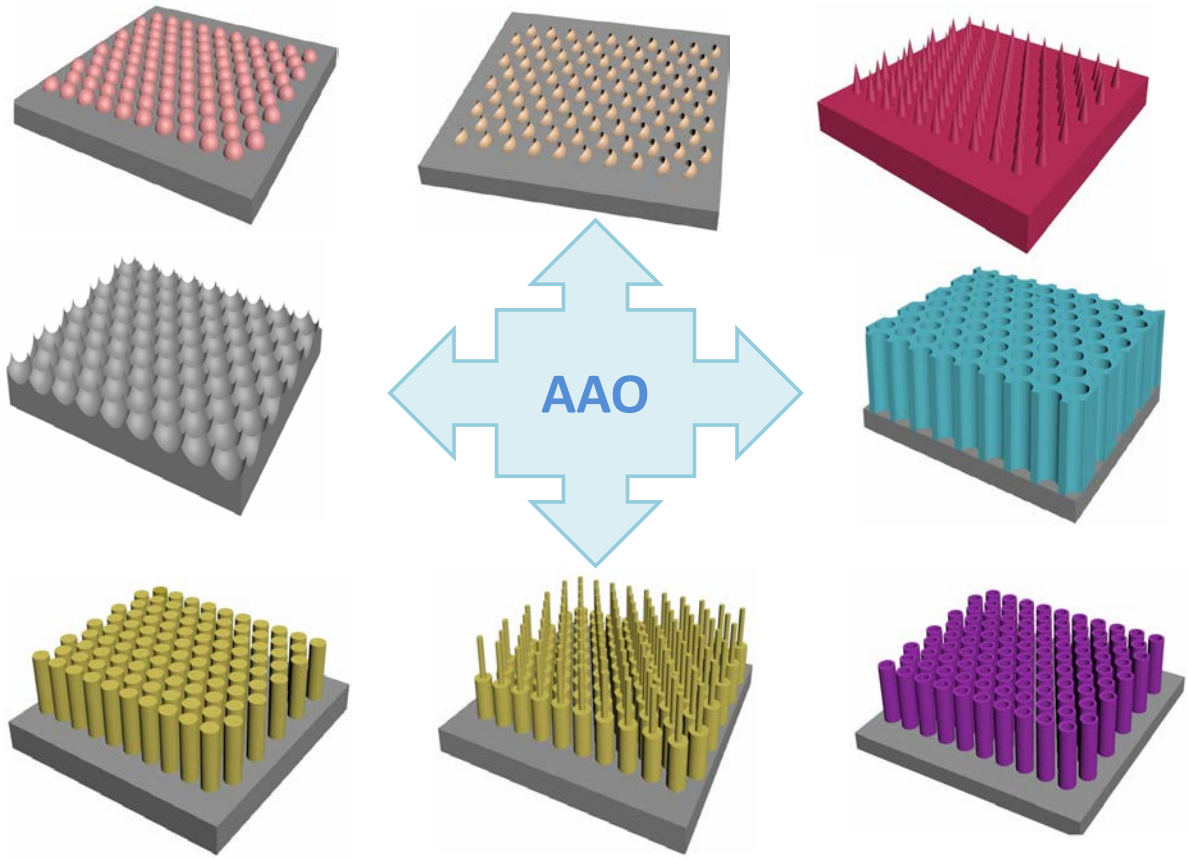

Figure 1-1| Schematic illustration of the basic three-dimensional nanostrucuture constructed base on anodic aluminum oxide template.

Considering the significance of AAO template, it is necessary to understand the formation of AAO in detail. As shown in Figure 1-2a, at the beginning of the anodization, a thin compact oxide layer grows to cover the whole aluminum surface (stage I). Thickening the barrier oxide leads to an increase of local stress. When the thickness of the compact oxide reaches a certain value, local cracks happens, resulting in a path for the acid solution which penetrates to the Al foil under the oxide barrier (stage II). The internal stress resident in the defective oxide barrier promotes the self-organization of the neighboring pores (stage III). As the anodization continues, the regularity of the pore arrays improves. Normally the regularity of anodic alumina is proportional to the anodization time. After about 10 hours, an alumina membrane with disordered pores on the top and ordered pores at the bottom is obtained (stage IV). Due to the disorder nature of the template on the top, we usually etch this layer away and leave aluminum foil being textured with ordered array of semispherical concaves (stage V). Then another procedure for anodizing is performed to acquire well-ordered aluminum oxide porous structure (stage VI). This so called two-step anodization process was

firstly proposed by Masuda and Satoh [26]. The as prepared anodic aluminum oxide as schematically shown in Figure 1-2b, which consists of a large number of parallel pores perpendicular to the aluminum substrate. Each pore cell can be geometrically defined by the pore diameter, pore wall thickness, pore length, interpore distance and porosity. The biggest advantage of the anodic aluminum oxide template is the high turnability of these geometric parameters, which are governed by the anodizing electrolyte, potentials and time.

Considering the time-consuming of the first anodization procedure and the difficulty of manipulating the distribution of nanopores, which are hexagonally distributed in nature, in 1997, Masuda and coworkers developed a so-called ‘‘pretexturing’’ process, which used a silicon carbide (SiC) mold with ordered array of convenes to stamp an Al foil before anodization [40]. In this way, the time-consuming first step anodization process could be omitted and the second anodization step can be directly carried out. More importantly, the profiles and distributions of the resulted aluminum oxide nanoporous array could be highly manipulated by the geometric parameters of the converted in the mold.

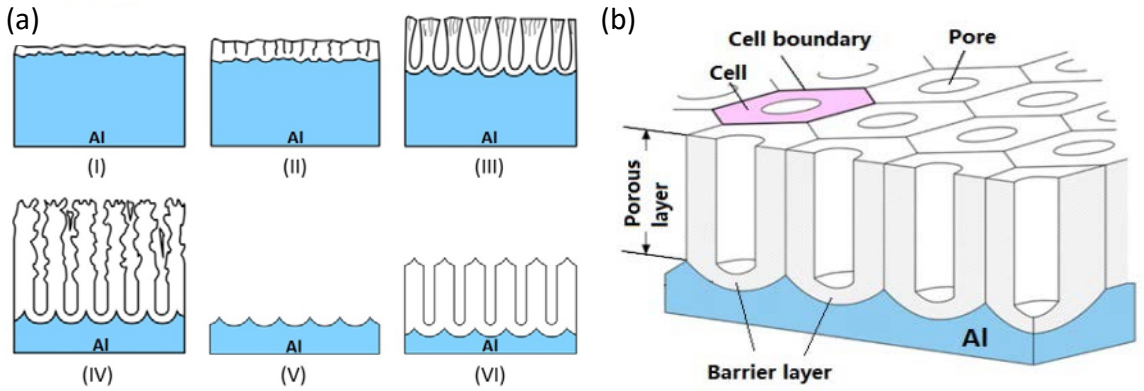

Figure 1-2| (a) Schematic of the two-step anodization process for realizing anodic aluminum oxide template, and (b) Schematic structure of a representative anodic aluminum oxide template, showing the parameter definitions.

It should be mentioned that even using two step anodization processes, it is still tough to get large area of nanopore arrays without defects. In order to obtain larger-area and highly ordered anodic alumina membrane, treatments like annealing and electropolishing the aluminum foil have to be performed. Such treatments are helpful to remove resident stress and defects in the Al foil. To understand the anodization procedure fundamentally, COMSOL Multiphasic software was used to simulate the three-dimensional electric field distribution in the aluminum foil and barrier oxide. The simulation was based on steady-state current

continuity equation, excluding the potential drop in the electrolyte and the electrode double layer at the electrolyte/metal interface. Figure 1-3 a-d show the electric field distribution in aluminum film at the initial stage of the first step anodization, where (a) and (b) indicate that the ideally defect-free sample has a uniform electric field distribution and a relatively small value (1.17×10^8 $V \cdot m^{-1}$) through the whole aluminum foil. In contrast, the defect sample shows a nonuniform electric field (Figure 1-3c and d). The electric field at the corners of the defects is several orders higher than that at other positions. The fluctuant electric field will result in different oxide barrier growth rate and local stress, finally affecting the regularity of the pore arrays.

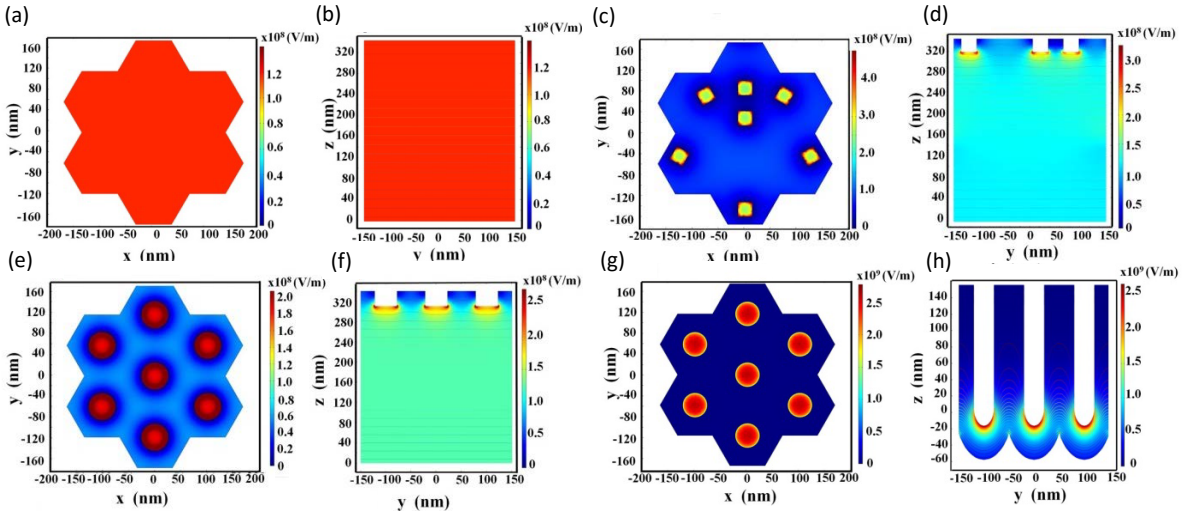

Figure 1-3| (a, b) Top and cross-sectional views of the electric field distribution of polished aluminum foils at the beginning of the first anodization step. (c, d) Top and cross-sectional views of the electric field distribution of unpolished aluminum foils at the beginning of the first anodization step. (e, f) Top and cross-sectional views of the electric field distribution of aluminum foils with nano-textured surface at the beginning of the second anodization step. (g, h) Top and cross-sectional views of the electric field distribution of alumina membrane at the stable stage of hole formation. The voltage applied in all these samples is 40 V and the corresponding interpore distance is about 110 nm.

Figure 1-3 e-h show the electric field distribution in the aluminum foil at the steady pore formation stage of the second step anodization. For this surface-textured aluminum foil, the electric field of each cell at the initial stage is periodic, with the intensity at the bottom of the nanocaves much bigger than that at the top, as shown in Figure 1-3e and f. Such electric field concentration at the bottom of the pores during the pore formation indicates that the oxide dissolution mainly occurs at the bottoms of the pores. According to the field-assistant

oxide dissolution theory [41], the electric field promotes the immigration of ions through the oxide barrier. The electric field along the sidewall and on the top surface of the barrier layer is almost zero, demonstrating that there is almost no dissolution of oxide on the wall and the top surface for the procedures with the same anodizing conditions. This results in a highly-uniform and vertically-distributed aluminum oxide nanoporous arrays (Figure 1-3g and h).

1.2.2. Colloidal crystal template

Colloidal crystal template composed of well-ordered colloidal spheres is another convenient pattern to direct the formation of ordered nanostructure arrays. The colloidal spheres with a uniform size ranging from several micrometers to tens of nanometers could self-assemble into highly-ordered two-dimensional and/or three-dimensional patterns under appropriate conditions [42,43]. The two-dimensional colloidal crystal template pattern is the monolayer of monodispersed colloidal spheres with a well-arranged hexagonal close-packed or non-close packed feature of self-assembly on substrates. Through choosing different approaches to prepare the targeting materials into the 2D pattern, well-ordered nanostructure arrays with various profiles (e.g., nanodots, nanorings, nanocolumns, nanocones, etc.) could be easy-accessibly attained [17][42]. The size of the nanostructure is also tunable, depending on the sizes of colloidal spheres. The three-dimensional colloidal crystal template pattern is multilayer of colloidal spheres that pack into predominantly face-centered cubic arrays on substrates, which is more advantageous in the construction of three-dimensional ordered nanostructure arrays by comparing with the two-dimensional counterpart, particularly good for energy applications. The resulted three-dimensional nanostructure arrays are usually produced by filling the interstitial space of close-packed spheres with the required material and then removing the spheres. These negative replica architectures are usually termed as inverse opals, inverted opals, or three-dimensional ordered macroporous structures. The corresponding open, interconnected macropore structure and nanosized wall components have benefited numerous applications in energy related devices, catalysis, photonics, field emission etc. [17,44-46] Particularly, according to the modified Bragg's law, the photonic stop-band of inverse-opal of semiconductors is determined by the pore size, which is highly tunable by the preparation procedure, thus

providing a good chance to manipulate the photonic properties of the corresponding structures.

Currently, the most common colloidal particles are uniformly sized silica or polymer spheres. Silica spheres could be synthesized by the Stöber process (e.g., via the hydrolysis and condensation of tetraalkoxysilanes in aqueous solution containing alcohol and ammonia) [47]. The resultant silica particles present a uniform size in the range of several tens of nanometers to a few micrometers. Smaller silica particles with size from 10 nm to 40 nm are usually realized by using the basic amino acid L-lysine to control the hydrolysis of tetraethylorthosilicate [48]. Monodispersed polymer spheres include poly-styrene spheres, poly(methyl methacrylate) spheres, and poly(styrene-methylmethacrylate-acrylic acid) spheres. The initiators employed in these emulsion polymerizations govern the surface charge on the polymer spheres, which could influence the interactions with targeting materials in the colloidal crystal template [43].

The silica based colloidal crystal templates, usually called as hard colloidal crystal templates, are of good merit in maintaining the structure in a broad scope of temperatures. This makes the procedure for synthesizing the target materials compatible with the techniques that require a high temperature, like chemical vapor deposition, atomic layer deposition and molecular beam epitaxy. However, the disadvantage of the silica colloidal crystal template is the difficulty of the template removal, which has to be conducted in hydrofluoric acid (toxic and caustic) or hot alkali solution. Such removal treatment could damage the structure of the resultant materials, since most of the metals and oxides are sensitive to such treatment. On the other hand, polymer spheres are easy to be removed by calcination, pyrolysis or extraction with an organic solvent, thus rendering the polymer spheres as versatile template particles. With the increase of the particle size and the multilayer thickness, internal pressure from swelling of the polymer spheres can result in fracture of the particles and generate imperfects to periodicity of the template. Generally, polymer sphere templates are more compatible to the various techniques for nanofabrication and more popular in energy applications, in comparison with the hard sphere template.

Practically, a large diversity of ordered nanostructure arrays could be realized by these template-directed methods. As summarized by Figure 1-4, the profiles, dimensions and distributed regularities of these nanostructure arrays could be well controlled. Even

complicated nanostructure arrays, like multi-segmented and multi-profiled nanostructure arrays, could also be attained by tuning the formation procedure of template and synthetic process of the targeting materials. These ordered nanostructure arrays behave as scaffolds to construct energy-related devices and are of great merit in regulating the energy converting/storing reactions and optimizing the corresponding performances.

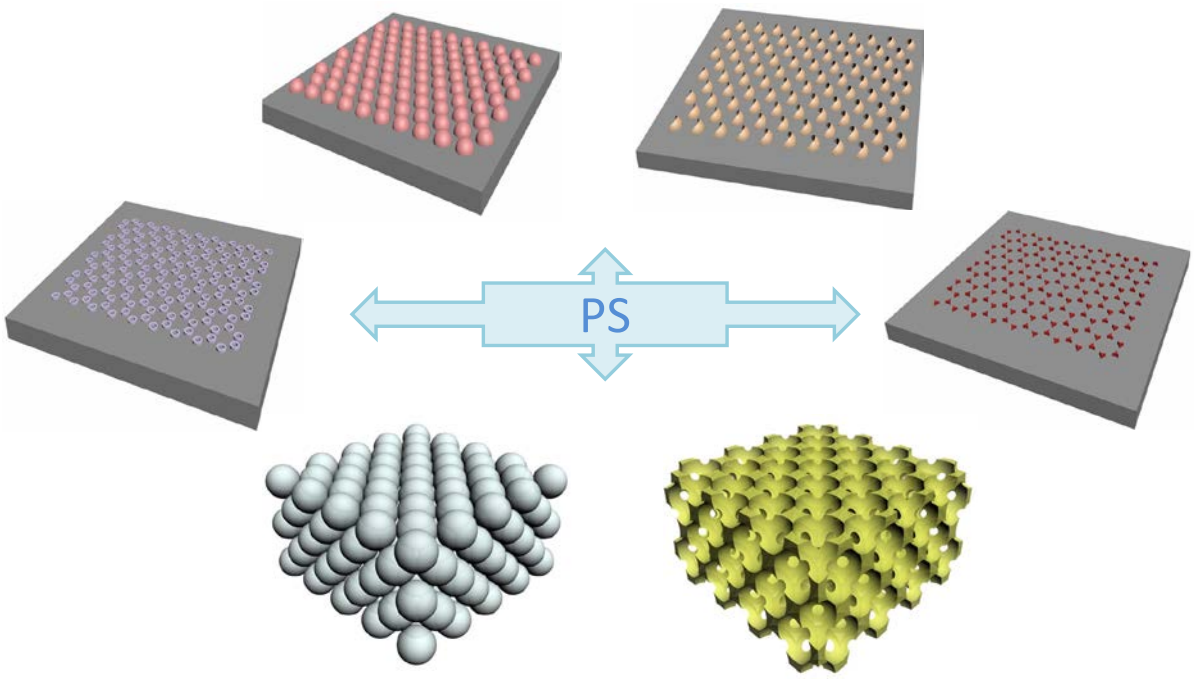

Figure 1-4| Schematic of ordered nanostructure arrays that could be realized via template-directed techniques.

1.3. Atomic layer deposition for constructing three-dimensional nanostructure for energy storage and conversion

1.3.1. Atomic layer deposition

After the construction of three-dimensional nanostructures, the functionalization of those constructed nanostructures turns to be a critical issue that needs to be solved. It requires a synthesis approach that is capable of controlling the decoration or the deposition on the three-dimensional nanostructure substrate at atomic scale, whilst preserving the characteristic properties of the three-dimensional nanostructure support. Amongst various functionality strategies, the atomic layer deposition technique appears to be as one of the

most promising strategy due to its specific characteristics, including simplicity, reproducibility and the high conformity of the obtained samples [49].

Atomic layer deposition is a surface-controlled method that has emerged as an important technique for the deposition of films from gas phase for a variety of applications. ALD is able to meet the needs for atomic layer control and conformal deposition using sequential, self-limiting surface reaction. It was invented in the 1970s by Suntola and Antson, and further developed in the 1980s for the fabrication of a semiconducting light-emitting core surrounded by dielectric layers for electroluminescent flat panel displays. The needs for high-K oxides in microelectronics result the ALD technique to become a success commercial technique. Since then, a wide range of materials, including several oxides, nitrides, sulphides and metals have been deposited by ALD on various substrates [49,50].

Most of the ALD processes are based on binary reaction sequences where two surface reactions occur and deposit a binary compound film, as schematic shown in Figure 1-5, where the thin film growth cycle for a binary compound (Al_2O_3) from gaseous precursors ($Al(CH_3)_3$ and H_2O) is presented as an example. The ALD gaseous reactants are alternately pulsed into the reaction chamber to react on the substrate, and between the reactant pulses the reaction chamber is purged with an inert gas. As shown, a complete ALD cycle process consists of four separate steps [67]: 1) the substrate is exposed to precursor molecules ($Al(CH_3)_3$, precursor 1), which is pulsed into the reaction chamber and absorb ideally as a monolayer on the substrate surface; 2) the excess of $Al(CH_3)_3$ (precursor 1) in the gas phase in reaction chamber is removed by inert gas purging; 3) the substrate is exposed to H_2O (precursor 2) which is pulsed into the reaction chamber and reacts with the adsorbed $Al(CH_3)_3$ (precursor 1) to form a layer of the Al_2O_3 (desired material) and CH_4 (by-product); 4) the excess of H_2O (precursor 2) and the reaction by-products are removed by inert gas purging. The ALD cycle is repeated until the desired thickness of the deposit material is obtained. In the ideal case, a complete monolayer if formed in every deposition cycle and no impurities are introduced to the film. The good quality and excellent conformity of the films deposited by ALD make it a promising technique for a variety of microelectronic applications.

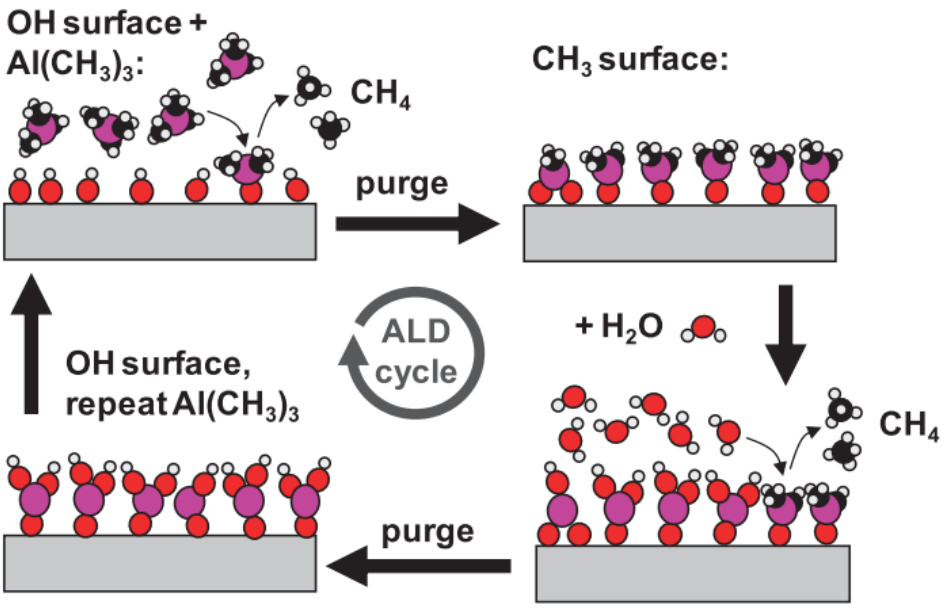

Figure 1-5| Schematic of a binary compound ALD process. One ALD cycle consists of four separate steps: 1) the substrate is exposed to precursor molecules ($Al(CH_3)_3$, precursor 1), which absorb ideally as a monolayer on the substrate surface; 2) the excess of $Al(CH_3)_3$ (precursor 1) in the gas phase in reaction chamber is removed by inert gas purging; 3) the substrate is exposed to H_2O (precursor 2) which reacts with the adsorbed $Al(CH_3)_3$ (precursor 1) to form a layer of the desired material and by-product (CH_4); 4) the excess of H_2O (precursor 2) and the reaction by-products are removed by inert gas purging. The ALD cycle is repeated until the desired thickness of the deposit material is obtained [67].

The ability of ALD to deposit on high aspect ratio structure is the most desirable characteristics for ALD. The miniaturization of semiconductor devices has led to the increasing need of ALD to coat high aspect ratio micro/nanostructures. As the length aspect ratio is expected to increase up to 80 to 1 by the year 2007, ALD is probably the only viable technique for high aspect ratio micro/nanostructure fabrication and modification. The precise control of the deposited layer thickness allows for new strategies in the modification of chemical and physical properties of nan-scaled materials and synthesis routes to novel micro/nanostructures for device fabrication. A number of works report the use of ALD to functionalize complex three-dimensional nanostructures for catalysis, energy storage and conversion, etc. [51,52]

1.3.2. Atomic layer deposition for solar cell

Construction of complex three-dimensional nanostructures is attractive for energy conversion, especially for solar energy conversion, which is the cleanest and most abundant available renewable energy source. So far, the photovoltaic and solar water splitting cells are two major kinds of solar energy conversion devices. For solar cell, including dye-sensitized solar cell (DSSC), quantum dot sensitized solar cell, organic-inorganic hybrid solar cell and thin-film solar cell, to optimize the three main steps of solar energy conversion process: photon absorption, charge carrier generation and charge carrier transport, atomic layer deposition was performed to fabricate nanostructured active electrodes or charge transporter [53,54], form heterojunction and inert surface passivation of trap states, as well as catalytic noble metals [55,56]

Inverse opal is a replicated shell structure with high-specific surface area and porosity (74 % void volume). The periodical three-dimensional inverse opal exhibits photonic crystal properties, thereby providing additional avenues to enhance light-matter interactions by controlling the propagation of light via mirror reflections, slow photons, and surface resonant modes [43]. As such, a challenging issue here is the fabrication of high-quality ideal electrode architecture for solar cell. From the establishment of the effectiveness ALD technique to fabricate inverse opal structure by Karuturi *et al*, high-quality inverse opals with different pore size on fluorine-doped tin-oxide (FTO) coated glass were prepared as a photoanode for DSSCs [57]. The high filling of fractions ensures robust interfacial contact with substrate, thereby providing good electron transport paths. Photosensitization of CdS quantum dots on TiO_2 inverse opal electrode has achieved a promising photocurrent density and incident photon to current conversion efficiency [58]. The light harvesting efficiency of the TiO_2 inverse opal electrode could be further improved by forming a bilayer structure where ZnO nanowire array is grown directly on the top of TiO_2 inverse opal by ZnO seeding layer deposited by ALD [59]. Besides the construction of three-dimensional nanostructures for solar cell devices, functionality of three-dimensional nanostructures by ALD has also investigated. The silica aerogel template, as well as anodic aluminum oxide template deposited either ZnO or TiO_2 layers by ALD for DSSC to impart the desired semiconducting properties [60,61]. Ultrathin layer of surface passivation coated by ALD could improve the photostability or viability of solar cells by isolating photoanode surface from surrounding environments. It is highly required by long-term operation stability and high efficiency solar

cells [62,63]. Not only for DSSCs, but also the ALD layer was reported for the surface passivation of Si solar cells to reduce surface recombination and improve efficiency [64]. The Al_2O_3 passivation layer deposited by ALD realizing up to 23.2 % conversion efficiency of Si solar cell by suppressing surface recombination as well as reflection. Similar work for efficient hole-blocking layer deposited by ALD has also been demonstrated on perovskite solar cells [65].

1.3.3. Atomic layer deposition for solar water splitting

Among the different sources, the high energy density and environment friendliness of hydrogen produced from water splitting does not present the drawback caused by unwanted emissions is regarded as a potential fuel. Thus, efficiently and inexpensively splitting H_2O into H_2 and O_2 is one of the most pressing issues. The discovery of hydrogen evolution through the photoelectronchemical splitting of water on semiconductor electrode (n-type TiO_2 electrode) by Fujishma solves the problem that producing hydrogen requires energy supplied from a high-cost external source [66]. Since then, the technology of semiconductor-based photocatalytic water splitting for the production of hydrogen using solar energy has been considered as one of the most important approaches to solve the world energy crisis. Though the devices for solar energy converting are of large diversity depending on the specific active materials, configuration of the device architecture with complex three-dimensional nanostructure provides a universal methodology to improve the overall efficiency from all the detailed energy converting steps. A large number of studies have been focused on ALD modification and/or fabrication of complex three-dimensional nanostructures for enhancing their solar water splitting efficiency [67].

The complex $TiO_2/TiSi_2$ core/shell nanostructures synthesized by Chemical vapor deposition (CVD) combine with ALD methods provided a structural support with high surface area improving photo absorption [68]. The high electrical conductance structural support enhanced charge transport as well. These features led to a high performance nanostructure for photoelectrochemical water splitting. The ALD growth of WO_3 on indium tin oxide (ITO) or on $TiSi_2$ nanonet, with oxo-bridged Mn dimer adsorbed onto the WO_3 ALD film acting as catalyst, facilitated the hole transfer from the semiconductor to the solution. This heterostructure leads to interesting photocatalytic properties. The thin film of CdS is

conformally deposited onto TiO_2 nanotubes using a modified ALD method to CdS/TiO_2 nanotube array coaxial heterogeneous structures for water splitting devices [59]. The fabricated three-dimensional nanostructure significantly enhances CdS/TiO_2 and CdS/electrolyte contact areas and reduces the distance that holes and electrons must travel to reach the electrolyte or underlying conducing substrate. It results in enhanced photo absorption and photocurrent generation. A five-fold enhancement in photoactivity compares with a bare three-dimensional TiO_2 nanotube array. ALD assist-fabricated three-dimensional ZnO/Si branched nanowire photoelectrodes [69]. The branched nanowire electrode with lightly doped p-Si nanowire core, larger ZnO nanowire branches and longer Si nanowire cores present a higher photocathodic current, while ranched nanowires with heavily doped p-Si nanowire trunks smaller ZnO nanowires and shorter Si nanowires provide a higher photoanodic current. The photoelectrode stability is dramatically improved by coating a thin TiO_2 protection layer by ALD. These results provide useful guidelines in designing photoelectrode for efficient solar water splitting devices.

1.3.4. Atomic layer deposition for battery

Electrochemical energy storage is a crucial technology for portable power needs. Many advances have been made in battery technology, through continued improvement of specific electrochemical system in recent years. Lithium and sodium ion batteries are currently well considered as the power source of choice for high performance rechargeable battery for a wide range of applications, because of their high energy and powder density over other types of batteries [38]. A large variety of nanomaterials and their composites have shown the advantages of increasing the cycling life and charge-discharge rates [11][70]. However, some disadvantages, including undesirable reactions due to high surface area, and low volumetric energy densities because of inferior packing are harmful for batteries. Meanwhile, the batteries consist of thin films with limited thickness due to the low lithium or sodium ions and electron diffusion. Three-dimensional structuring is considered necessary to increase the storage capacity without deteriorating the power capacity. In addressing these various challenges facing batteries, surface coating of electrodes by ALD proved to be a promising strategy. ALD technique not only can be used to accurately design various new high-performance battery components, but also performed to modify the properties of

electrode materials with ultrathin coating films or construct three-dimensional electrode to increase the electrode/electrolyte contact area and short path length for transporting both electrons and lithium or sodium ions [11,71,72].

A passivation or protective thin film coated by ALD can reduce or possibly prevents the decomposition of the electrolyte while have high Li^+ / Na^+ and electron conductivities. A thin layer of Al_2O_3 deposited by ALD improved the stability of $LiCoO_2$ [73]. It also improved the cycle-life of natural graphite anode [71]. Besides the coating of passivation or protective thin film, ALD has also been used in construct three-dimensional electrodes. In which the electrode was specifically designed such that diffusion paths in the materials are short, thus improve the transport of electrons and lithium or sodium ions. It was demonstrated that TiN deposited by ALD from $TiCl_4$ and H_2-N_2 plasma was well-suited as a Li-diffusion barrier and current collector even though the TiN was not fully conformal [70]. The current collectors of Pt were prepared successfully by ALD from $MeCpPtMe_3$ and O_2 gas [74].

1.3.5. Atomic layer deposition for supercapacitor

Supercapacitors are the other one kind of rechargeable electrochemical energy storage devices, which offer a much longer life cycle and higher power density than batteries [72,75]. As such, supercapacitors can replace or complement batteries in various applications. Electrical double-layer capacitors with carbon electrodes and pseudocapacitors with metal-oxide or conducting polymer electrode are the existed two types of supercapacitors. The transition metal-oxides exhibit fast and electrochemically reversible Faradaic redox reactions to store charge in supercapacitors, resulting in high capacitance, but often suffer from low electrical conductivity and low surface area. Thus, researches on large surface area, high electrical conductivity and inexpensive materials and structures for use in supercapacitors is critical to ensure that the demand for high power density energy storage of supercapacitors. Constructing three-dimensional nanostructure is one of the efficient ways to increase the surface area of material used for supercapacitors. Atomic layer deposition is not only benefit for construction three-dimensional nanostructures, but also benefit for modification of constructed three-dimensional nanostructures.

Yushin *et al* conformally deposited various thickness of vanadium oxide on the internal surface area of porous carbon nanotube (CNT) electrodes by ALD for supercapacitors [72].

The ability to precisely control the coating thickness and microstructure by ALD permits systematic studies of the ion intercalation and diffusion into the bulk of the electrode. The electrochemical measurements revealed stable performance of the vanadium oxide coated CNT electrodes with excellent capacitance retention at high current densities or sweep rates. The new promising materials, cobalt sulfide (Co_9S_8) with an ideal layer-by-layer ALD growth behavior could be achieved by ALD process [75]. And it could be conformally deposited into deep narrow trenches with aspect ratio of 10 to 1. As such, Co_9S_8 films conformally coated on nickel form were fabricated for supercapacitor. Benefiting from the merits of ALD for making high-quality uniform Co_9S_8 thin films, the ALD-synthesized electrodes exhibit remarkable electrochemical performance, with high specific capacitance, great rate performance, and long-term cycle ability.

1.3.6. Atomic layer deposition for fuel cell

Electrochemical systems, especial fuel cell devices, represent some of the most efficient and environmentally friendly technologies for energy conversion and storage [6,22,43]. Electrocatalysts play key roles in the chemical processes of fuel cells. It is always applied to modify electrode, in order to overcome the high overpotential or low faradic efficiency of electrode to lower activation energy and increase conversion rate. The electrochemical properties of electrode could be limited by the performance of electrocatalyst. As such, it is a long-standing challenge to develop efficient and durable electrocatalysts at low cost for fuel cell devices. The high surface area and the potential low active material loading of nanostructured catalysts are relevant choice. The deposition of oxide compounds as support as well as deposition and protection of metallic catalysts by ALD process were fantastic for fuel cell device [54,76].

Infiltration of AAO substrate with 1 nm ALD Al_2O_3 before loading it with vanadium oxide by ALD as catalyst was prepared by Feng et al [77]. The ALD-prepared catalyst showed higher specificity toward the oxidative dehydrogenation of cyclohexane. The amorphous silica layer deposited by ALD on Au/TiO_2 showed an improved sintering resistance, maintaining a comparable activity toward CO oxidation. Attributing to the oxide-gold interaction and the improved thermal stability of the porous network, the stabilization of porous gold by Al_2O_3 and TiO_2 ALD showed a three-fold increase of CO oxidation activity [78]. ALD was also used

to directly deposit metal catalyst particles. The uniform 2-3 nm platinum (Pt) nanoparticles with a 4-8 nm interparticle spacing were grown on strontium titanate nanocube. The Pt nanoparticles were stabilized by the strong epitaxy with $SiTiO_3$ nanocube, resulting in improvement of deactivation resistance and inhibiting the complete Pt oxidation [79]. Pt nanoparticles decorated on porous carbon aerogel presented high catalytic activity toward CO oxidation, even with a Pt loading as low as 0.047 $mg \cdot cm^{-2}$, around 2 ALD cycles. Nearly full conversion was reached at temperature as low as 150 ℃ [80].

1.4. Conclusion and perspective

ALD technique rapidly developed in the past two decades. It has emerged as the technique of choice for the fabrication of various complex nanostructurtures due to the ability to coat complex three-dimensional nanostructures and control the thickness at the atomic level. Additionally, ALD is capable of composition control and doping foreign elements. These features make ALD an excellent tool to fabricate both photoactive layers, passivation layers, catalyst layers and performance enhancing layers for energy storage and conversion devices. The examples in this chapter demonstrate ALD is an enabling technique to synthesize, functionalize, or stabilize high-performance nanomaterials used in energy harvesting and storage devices. However, the slow growth rate and the specific chemistry requirement of ALD restrict its industry applications. In such case, ALD is still of key importance as it can serve as a method to construct and functionalize of three-dimensional complex nanostructures for energy storage and conversion.

1.5. Bibliography

[1] Z. Yang, J. Zhang, M.C.W. Kintner-Meyer, X. Lu, D. Choi, J.P. Lemmon, et al., Electrochemical Energy Storage for Green Grid, Chem. Rev. 111 (2011) 3577–3613. doi:10.1021/cr100290v.

[2] Ren 21, Renewables 2014 Global Status Report, 2014.

[3] N.S. Lewis, Solar Energy Use, (2007) 798–802. doi:10.1126/science.1137014.

[4] M.G. Walter, E.L. Warren, J.R. McKone, S.W. Boettcher, Q. Mi, E.A. Santori, et al., Solar Water Splitting Cells, Chem. Rev. 110 (2010) 6446–6473. doi:10.1021/cr1002326.

[5] Y.-J. Cheng, S.-H. Yang, C.-S. Hsu, Synthesis of Conjugated Polymers for Organic Solar Cell Applications, Chem. Rev. 109 (2009) 5868–5923. doi:10.1021/cr900182s.

[6] J. Ronge, T. Bosserez, D. Martel, C. Nervi, L. Boarino, F. Taulelle, et al., Monolithic Cells for Solar Fuels, Chem. Soc. Rev. 43 (2014) 7963–7981. doi:10.1039/C3CS60424A.

[7] K.J. Stevenson, V. Ozoliņš, B. Dunn, Electrochemical Energy Storage, Acc. Chem. Res. 46 (2013) 1051–1052. doi:10.1021/ar400100z.

[8] Y. Zhao, Y. Ding, Y. Li, L. Peng, H.R. Byon, J.B. Goodenough, et al., A Chemistry and Material Perspective on Lithium Redox Flow Batteries Towards High-density Electrical Energy Storage, Chem. Soc. Rev. 44 (2015) 7968–7996. doi:10.1039/C5CS00289C.

[9] D.P. Dubal, O. Ayyad, V. Ruiz, P. Gomez-Romero, Hybrid Energy Storage: The Merging of Battery and Supercapacitor Chemistries, Chem. Soc. Rev. 44 (2015) 1777–1790. doi:10.1039/C4CS00266K.

[10] N. Tétreault, É. Arsenault, L.-P. Heiniger, N. Soheilnia, J. Brillet, T. Moehl, et al., High-Efficiency Dye-Sensitized Solar Cell with Three-Dimensional Photoanode, Nano Lett. 11 (2011) 4579–4584. doi:10.1021/nl201792r.

[11] J.W. Long, B. Dunn, D.R. Rolison, H.S. White, Three-Dimensional Battery Architectures, Chem. Rev. 104 (2004) 4463–4492. doi:10.1021/cr020740l.

[12] J. Wallentin, N. Anttu, D. Asoli, M. Huffman, I. Aberg, M.H. Magnusson, et al., InP Nanowire Array Solar Cells Achieving 13.8 % Efficiency by Exceeding the Ray Optics Limit., Science. 339 (2013) 1057–60. doi:10.1126/science.1230969.

[13] D.C. Dillen, K. Kim, E.-S. Liu, E. Tutuc, Radial Modulation Doping in Core-shell Nanowires, Nat Nano. 9 (2014) 116–120. http://dx.doi.org/10.1038/nnano.2013.301.

[14] A.I. Hochbaum, P. Yang, Semiconductor Nanowires for Energy Conversion, Chem. Rev. 110 (2010) 527–546. doi:10.1021/cr900075v.

[15] M.L. Brongersma, Y. Cui, S. Fan, Light Management for Photovoltaics Using High-index Nanostructures, Nat Mater. 13 (2014) 451–460. http://dx.doi.org/10.1038/nmat3921.

[16] A. Stein, B.E. Wilson, S.G. Rudisill, Design and Functionality of Colloidal-crystal-templated Materials—chemical Applications of Inverse Opals, Chem. Soc. Rev. 42 (2013) 2763–2803. doi:10.1039/C2CS35317B.

[17] H. Zhao, M. Zhou, L. Wen, Y. Lei, Template-directed Construction of Nanostructure Arrays for Highly-efficient Energy Storage and Conversion, Nano Energy. 13 (2015) 790–813. doi:http://dx.doi.org/10.1016/j.nanoen.2015.02.024.

[18] J.M. Foley, M.J. Price, J.I. Feldblyum, S. Maldonado, Analysis of the Operation of Thin Nanowire Photoelectrodes for Solar Energy Conversion, Energy Environ. Sci. 5 (2012) 5203–5220. doi:10.1039/C1EE02518J.

[19] Y. Liu, J. Goebl, Y. Yin, Templated Synthesis of Nanostructured Materials, Chem. Soc. Rev. 42 (2013) 2610–2653. doi:10.1039/C2CS35369E.

[20] W. Lee, S.-J. Park, Porous Anodic Aluminum Oxide: Anodization and Templated Synthesis of Functional Nanostructures., Chem. Rev. 114 (2014) 7487–7556. doi:10.1021/cr500002z.

[21] Y. Xia, B. Gates, Y. Yin, Y. Lu, Monodispersed Colloidal Spheres: Old Materials with New Applications, Adv. Mater. 12 (2000) 693–713. doi:10.1002/(SICI)1521-4095(200005)12:10<693::AID-ADMA693>3.0.CO;2-J.

[22] A.S. Aricò, P. Bruce, B. Scrosati, J. Tarascon, W.V.A.N. Schalkwijk, U. De Picardie, et al., Nanostructured Materials for Advanced Energy Conversion and Storage Devices., Nat. Mater. 4 (2005). doi:10.1038/nmat1368.

[23] J. Maier, Nanoionics: Ion Transport and Electrochemical Storage in Confined Systems., Nat. Mater. 4 (2005) 805–815. doi:10.1038/nmat1513.

[24] P. Simon, Y. Gogotsi, Materials for Electrochemical Capacitors., Nat. Mater. 7 (2008) 845–854. doi:10.1038/nmat2297.

[25] M. Toupin, T. Brousse, D. Bélanger, Charge Storage Mechanism of MnO_2 Electrode Used in Aqueous Electrochemical Capacitor, Chem. Mater. 16 (2004) 3184–3190. doi:10.1021/cm049649j.

[26] H. Masuda, K. Fukuda, Ordered Metal Nanohole Arrays Made by a Two-Step Replication of Honeycomb Structures of Anodic Alumina, Science (80-.). 268 (1995) 1466–1468. doi:10.1126/science.268.5216.1466.

[27] Y. Lei, W. Cai, G. Wilde, Highly Ordered Nanostructures with Tunable Size, Shape and Properties: A New Way to Surface Nano-patterning Using Ultra-thin Alumina Masks, Prog. Mater. Sci. 52 (2007) 465–539. doi:http://dx.doi.org/10.1016/j.pmatsci.2006.07.002.

[28] I. Mikulskas, S. Juodkazis, R. Tomasiunas, J.G. Dumas, Aluminum Oxide Photonic Crystals Grown by a New Hybrid Method, Adv. Mater. 13 (2001) 1574–1577. doi:10.1002/1521-4095(200110)13:20<1574::AID-ADMA1574>3.0.CO;2-9.

[29] Z. Zhan, R. Xu, Y. Mi, H. Zhao, Y. Lei, Highly Controllable Surface Plasmon Resonance

Property by Heights of Ordered Nanoparticle Arrays Fabricated via a Nonlithographic Route, ACS Nano. 9 (2015) 4583–4590. doi:10.1021/acsnano.5b01226.

[30] H. Zhao, C. Wang, R. Vellacheri, M. Zhou, Y. Xu, Q. Fu, et al., Self-Supported Metallic Nanopore Arrays with Highly Oriented Nanoporous Structures as Ideally Nanostructured Electrodes for Supercapacitor Applications, Adv. Mater. 26 (2014) 7654–7659. doi:10.1002/adma.201402766.

[31] K. Furukawa, K. Ebata, M. Fujiki, One-Dimensional Silicon Chain Architecture: Molecular Dot, Rope, Octopus, and Toroid, Adv. Mater. 12 (2000) 1033–1036. doi:10.1002/1521-4095.

[32] Q. Lin, S.-F. Leung, L. Lu, X. Chen, Z. Chen, H. Tang, et al., Inverted Nanocone-Based Thin Film Photovoltaics with Omnidirectionally Enhanced Performance, ACS Nano. 8 (2014) 6484–6490. doi:10.1021/nn5023878.

[33] K.-H. Tsui, Q. Lin, H. Chou, Q. Zhang, H. Fu, P. Qi, et al., Low-Cost, Flexible, and Self-Cleaning 3D Nanocone Anti-Reflection Films for High-Efficiency Photovoltaics, Adv. Mater. 26 (2014) 2805–2811. doi:10.1002/adma.201304938.

[34] C. Wang, L. Wen, T. Kups, Y. Mi, R. Vellacheri, Y. Fang, et al., Growth Control of AgTCNQ Nanowire Arrays by Using a Template-assisted Electro-deposition Method, J. Mater. Chem. C. 1 (2013) 8003–8006. doi:10.1039/C3TC31815J.

[35] A. Al-Haddad, Z. Wang, R. Xu, H. Qi, R. Vellacheri, U. Kaiser, et al., Dimensional Dependence of the Optical Absorption Band Edge of TiO_2 Nanotube Arrays beyond the Quantum Effect, J. Phys. Chem. C. 119 (2015) 16331–16337. doi:10.1021/acs.jpcc.5b02665.

[36] W. Lee, K. Schwirn, M. Steinhart, E. Pippel, R. Scholz, U. Gösele, Structural Engineering of Nanoporous Anodic Aluminium Oxide by Pulse Anodization of Aluminium., Nat. Nanotechnol. 3 (2008) 234–239. doi:10.1038/nnano.2008.54.

[37] W. Lee, J.-C. Kim, U. Gösele, Spontaneous Current Oscillations during Hard Anodization of Aluminum under Potentiostatic Conditions, Adv. Funct. Mater. 20 (2010) 21–27. doi:10.1002/adfm.200901213.

[38] L. Wen, Z. Wang, Y. Mi, R. Xu, S.-H. Yu, Y. Lei, Designing Heterogeneous 1D Nanostructure Arrays Based on AAO Templates for Energy Applications, Small. 11 (2015) 3408–3428. doi:10.1002/smll.201500120.

[39] S. Mubeen, N. Singh, J. Lee, G.D. Stucky, M. Moskovits, E.W. McFarland, Synthesis of

Chemicals Using Solar Energy with Stable Photoelectrochemically Active Heterostructures, Nano Lett. 13 (2013) 2110–2115. doi:10.1021/nl400502u.

[40] D. Crouse, Y.-H. Lo, a E. Miller, M. Crouse, Highly Ordered Nanochannel-arrar architecture in Anodic Alumina, Appl. Phys. Lett. 71 (1997) 2771–2772. doi:10.1063/1.125652.

[41] K.R. Hebert, S.P. Albu, I. Paramasivam, P. Schmuki, Morphological Instability Leading to Formation of Porous Anodic Oxide Films, Nat Mater. 11 (2012) 162–166. http://dx.doi.org/10.1038/nmat3185.

[42] J. Zhang, Y. Li, X. Zhang, B. Yang, Colloidal Self-Assembly Meets Nanofabrication: From Two-Dimensional Colloidal Crystals to Nanostructure Arrays, Adv. Mater. 22 (2010) 4249–4269. doi:10.1002/adma.201000755.

[43] A. Stein, B.E. Wilson, S.G. Rudisill, Design and Functionality of Colloidal-crystal-templated Materials-chemical Applications of Inverse Opals, Chem. Soc. Rev. 42 (2013) 2763–2803. doi:10.1039/C2CS35317B.

[44] H. Arandiyan, H. Dai, K. Ji, H. Sun, J. Li, Pt Nanoparticles Embedded in Colloidal Crystal Template Derived 3D Ordered Macroporous $Ce_{0.6}Zr_{0.3}Y_{0.1}O_2$: Highly Efficient Catalysts for Methane Combustion, ACS Catal. 5 (2015) 1781–1793. doi:10.1021/cs501773h.

[45] Y. Li, X. Fang, N. Koshizaki, T. Sasaki, L. Li, S. Gao, et al., Periodic TiO_2 Nanorod Arrays with Hexagonal Nonclose-Packed Arrangements: Excellent Field Emitters by Parameter Optimization, Adv. Funct. Mater. 19 (2009) 2467–2473. doi:10.1002/adfm.200801857.

[46] S. Yang, F. Xu, S. Ostendorp, G. Wilde, H. Zhao, Y. Lei, Template-Confined Dewetting Process to Surface Nanopatterns: Fabrication, Structural Tunability, and Structure-Related Properties, Adv. Funct. Mater. 21 (2011) 2446–2455. doi:10.1002/adfm.201002387.

[47] W. Stöber, A. Fink, E. Bohn, Controlled Growth of Monodisperse Silica Spheres in the Micron Size Range, J. Colloid Interface Sci. 26 (1968) 62–69. doi:http://dx.doi.org/10.1016/0021-9797(68)90272-5.

[48] W. Fan, M.A. Snyder, S. Kumar, P.-S. Lee, W.C. Yoo, A. V. McCormick, et al., Hierarchical Nanofabrication of Microporous Crystals with Ordered Mesoporosity, Nat. Mater. 7 (2008) 984–991. doi:10.1038/nmat2302.

[49] S.M. George, Atomic Layer Deposition: An Overview, Chem. Rev. 110 (2010) 111–131.

doi:10.1021/cr900056b.

[50] M. Knez, K. Nielsch, L. Niinistö, Synthesis and Surface Engineering of Complex Nanostructures by Atomic Layer Deposition, Adv. Mater. 19 (2007) 3425–3438. doi:10.1002/adma.200700079.

[51] C. Marichy, M. Bechelany, N. Pinna, Atomic Layer Deposition of Nanostructured Materials for Energy and Environmental Applications, Adv. Mater. 24 (2012) 1017–1032. doi:10.1002/adma.201104129.

[52] J.W. Elam, N.P. Dasgupta, F.B. Prinz, ALD for Clean Energy Conversion, Utilization, and Storage, MRS Bull. 36 (2011) 899–906. doi:10.1557/mrs.2011.265.

[53] J. Seidel, D. Fu, S.-Y. Yang, E. Alarcón-Lladó, J. Wu, R. Ramesh, et al., Efficient Photovoltaic Current Generation at Ferroelectric Domain Walls, Phys. Rev. Lett. 107 (2011) 126805. doi:10.1103/PhysRevLett.107.126805.

[54] W. Niu, X. Li, S.K. Karuturi, D.W. Fam, H. Fan, S. Shrestha, et al., Applications of Atomic Layer Deposition in Solar Cells, Nanotechnology. 26 (2015) 064001. doi:10.1088/0957-4484/26/6/064001.

[55] V.O. Williams, N.C. Jeong, C. Prasittichai, O.K. Farha, M.J. Pellin, J.T. Hupp, Fast Transporting ZnO–TiO_2 Coaxial Photoanodes for Dye-Sensitized Solar Cells Based on ALD-Modified SiO_2 Aerogel Frameworks, ACS Nano. 6 (2012) 6185–6196. doi:10.1021/nn3015695.

[56] S.S. Mali, C.S. Shim, H.K. Park, J. Heo, P.S. Patil, C.K. Hong, Ultrathin Atomic Layer Deposited TiO2 for Surface Passivation of Hydrothermally Grown 1D TiO_2 Nanorod Arrays for Efficient Solid-State Perovskite Solar Cells, Chem. Mater. 27 (2015) 1541–1551. doi:10.1021/cm504558g.

[57] S.K. Karuturi, L. Liu, L.T. Su, Y. Zhao, H.J. Fan, X. Ge, et al., Kinetics of Stop-Flow Atomic Layer Deposition for High Aspect Ratio Template Filling through Photonic Band Gap Measurements, J. Phys. Chem. C. 114 (2010) 14843–14848. doi:10.1021/jp1053748.

[58] L. Alibabaei, M.K. Brennaman, M.R. Norris, B. Kalanyan, W. Song, M.D. Losego, et al., Solar Water Splitting in a Molecular Photoelectrochemical Cell, Proc. Natl. Acad. Sci. . 110 (2013) 20008–20013. doi:10.1073/pnas.1319628110.

[59] C. Cheng, S.K. Karuturi, L. Liu, J. Liu, H. Li, L.T. Su, et al., Quantum-Dot-Sensitized TiO_2 Inverse Opals for Photoelectrochemical Hydrogen Generation, Small. 8 (2012) 37–42. doi:10.1002/smll.201101660.

[60] T.W. Hamann, A.B.F. Martinson, J.W. Elam, M.J. Pellin, J.T. Hupp, Aerogel Templated ZnO Dye-Sensitized Solar Cells, Adv. Mater. 20 (2008) 1560–1564. doi:10.1002/adma.200702781.

[61] A.B.F. Martinson, J.W. Elam, J.T. Hupp, M.J. Pellin, ZnO Nanotube Based Dye-Sensitized Solar Cells, Nano Lett. 7 (2007) 2183–2187. doi:10.1021/nl070160+.

[62] H.-J. Son, C. Prasittichai, J.E. Mondloch, L. Luo, J. Wu, D.W. Kim, et al., Dye Stabilization and Enhanced Photoelectrode Wettability in Water-Based Dye-Sensitized Solar Cells through Post-assembly Atomic Layer Deposition of TiO_2, J. Am. Chem. Soc. 135 (2013) 11529–11532. doi:10.1021/ja406538a.

[63] A.K. Chandiran, N. Tetreault, R. Humphry-Baker, F. Kessler, E. Baranoff, C. Yi, et al., Subnanometer Ga2O3 Tunnelling Layer by Atomic Layer Deposition to Achieve 1.1 V Open-Circuit Potential in Dye-Sensitized Solar Cells, Nano Lett. 12 (2012) 3941–3947. doi:10.1021/nl301023r.

[64] K.-S.J. and S.-K.O. and H.-S.S. and H.-J.Y. and S.-H.K. and H.-R.L. and K.-M.H. and H.-Y.P. and H.-D.L. and G.-W. Lee, Novel Silicon Surface Passivation by Al_2O_3/ZnO/Al_2O_3 Films Deposited by Thermal Atomic Layer Deposition, Jpn. J. Appl. Phys. 53 (2014) 04ER19. http://stacks.iop.org/1347-4065/53/i=4S/a=04ER19.

[65] Y.W. and X.Y. and H.C. and K.Z. and C.Q. and J.L. and W.P. and A.I. and E.B. and F.Y. and M.Y. and P.Z. and L. Han, Highly Compact TiO_2 Layer for Efficient Hole-blocking in Perovskite Solar Cells, Appl. Phys. Express. 7 (2014) 52301. http://stacks.iop.org/1882-0786/7/i=5/a=052301.

[66] A. Fujishama, K. Honda, Electrochemical Photolysis of Water at a Semiconductor Electrode, Nature. 238 (1972) 37–38. doi:10.1038/238037a0.

[67] T. Wang, Z. Luo, C. Li, J. Gong, Controllable Fabrication of Nanostructured Materials for Photoelectrochemical Water Splitting via Atomic Layer Deposition, Chem. Soc. Rev. 43 (2014) 7469–7484. doi:10.1039/C3CS60370A.

[68] Y. Lin, S. Zhou, X. Liu, S. Sheehan, D. Wang, TiO_2/$TiSi_2$ Heterostructures for High-Efficiency Photoelectrochemical H_2O Splitting, J. Am. Chem. Soc. 131 (2009) 2772–2773. doi:10.1021/ja808426h.

[69] K. Sun, Y. Jing, C. Li, X. Zhang, R. Aguinaldo, A. Kargar, et al., 3D Branched Nanowire Heterojunction Photoelectrodes for High-efficiency Solar Water Splitting and H_2 Generation, Nanoscale. 4 (2012) 1515–1521. doi:10.1039/C2NR11952H.

[70] L. Baggetto, H.C.M. Knoops, R.A.H. Niessen, W.M.M. Kessels, P.H.L. Notten, 3D Negative Electrode Stacks for Integrated All-solid-state Lithium-ion Microbatteries, J. Mater. Chem. 20 (2010) 3703–3708. doi:10.1039/B926044G.

[71] Y.S. Jung, A.S. Cavanagh, L.A. Riley, S.-H. Kang, A.C. Dillon, M.D. Groner, et al., Ultrathin Direct Atomic Layer Deposition on Composite Electrodes for Highly Durable and Safe Li-Ion Batteries, Adv. Mater. 22 (2010) 2172–2176. doi:10.1002/adma.200903951.

[72] S. Boukhalfa, K. Evanoff, G. Yushin, Atomic Layer Deposition of Vanadium Oxide on Carbon Nanotubes for High-power Supercapacitor Electrodes, Energy Environ. Sci. 5 (2012) 6872. doi:10.1039/c2ee21110f.

[73] I.D. Scott, Y.S. Jung, A.S. Cavanagh, Y. Yan, A.C. Dillon, S.M. George, et al., Ultrathin Coatings on Nano-$LiCoO_2$ for Li-Ion Vehicular Applications, Nano Lett. 11 (2011) 414–418. doi:10.1021/nl1030198.

[74] H.C.M. Knoops, M.E. Donders, M.C.M. van de Sanden, P.H.L. Notten, W.M.M. Kessels, Atomic Layer Deposition for Nanostructured Li-ion Batteries, J. Vac. Sci. Technol. A. 30 (2012) 10801. doi:10.1116/1.3660699.

[75] H. Li, Y. Gao, Y. Shao, Y. Su, X. Wang, Vapor-Phase Atomic Layer Deposition of Co9S8 and Its Application for Supercapacitors, Nano Lett. 15 (2015) 6689–6695. doi:10.1021/acs.nanolett.5b02508.

[76] G.N. Parsons, S.M. George, M. Knez, Progress and Future Directions for Atomic Layer Deposition and ALD-based Chemistry, MRS Bull. 36 (2011) 865–871. doi:10.1557/mrs.2011.238.

[77] H. Feng, J.W. Elam, J.A. Libera, M.J. Pellin, P.C. Stair, Oxidative Dehydrogenation of Cyclohexane over Alumina-supported Vanadium Oxide Nanoliths, J. Catal. 269 (2010) 421–431. doi:http://dx.doi.org/10.1016/j.jcat.2009.11.026.

[78] M.M. Biener, J. Biener, A. Wichmann, A. Wittstock, T.F. Baumann, M. Bäumer, et al., ALD Functionalized Nanoporous Gold: Thermal Stability, Mechanical Properties, and Catalytic Activity, Nano Lett. 11 (2011) 3085–3090. doi:10.1021/nl200993g.

[79] S.T. Christensen, J.W. Elam, F.A. Rabuffetti, Q. Ma, S.J. Weigand, B. Lee, et al., Controlled Growth of Platinum Nanoparticles on Strontium Titanate Nanocubes by Atomic Layer Deposition, Small. 5 (2009) 750–757. doi:10.1002/smll.200801920.

[80] J.S. King, A. Wittstock, J. Biener, S.O. Kucheyev, Y.M. Wang, T.F. Baumann, et al.,

Ultralow Loading Pt Nanocatalysts Prepared by Atomic Layer Deposition on Carbon Aerogels, Nano Lett. 8 (2008) 2405–2409. doi:10.1021/nl801299z.

2. Experiments and methods

All experiments and methods throughout this work are depicted in this chapter. This chapter presents the fabrication processes of three-dimensional nanostructures based on AAO template and carbon nanofiber aerogel derived from bacterial cellulose, with the help of ALD, Physical vapor deposition (PVD) and electrochemical deposition in details. And the analytical methods that utilized to character the morphology, chemical composition, optical properties, conductivity, photoelectrochemical performance, electrochemical performance and electromagnetic field distribution.

2.1. Fabrication of three-dimensional nanostructures

2.1.1. Synthesis of nanoporous anodic aluminum oxide template

The synthesis of nanoporous AAO template was realized via a two-step anodization process initially proposed by Masuda and Satoh [1]. Figure 2-1 presents the required steps and detail experiment conditions in a flow diagram to synthesize AAO template. High purity aluminum foils (99.999%) were used as a starting material. Oxalic acid was using as electrolyte during the anodization process. And the lead electrode was working as a negative electrode. As illuminated in Figure 2-1, the complete synthesis process of AAO template consists of three essential steps. They are the pre-treatment of the aluminum foil, the two-step anodization process and the post-treatment of the AAO, respectively. The high purity aluminum foils were washed in an ultrasonic bath with acetone, water, and ethanol for 10 minutes each to clean and degrease the foils. After that the samples were electrochemically polished in a mixture solution of perchloric acid and ethanol (volume ratio 1:7) for 3 minutes to remove surface asperities. The as pre-treated aluminum foils were then went through the two-step anodization process. The first anodization step was carried out for 6 h with 40 V. Thereafter, the formed anodization product was chemically removed at 60 °C in a solution of 6 wt. % H_3PO_4 and 1.5 wt. % H_2CrO_4. Subsequently, using the same experiment conditions as the first anodization, the treated specimen was anodized again. During this step, the time of the second anodization determines the final thickness of the AAO template, which can be

adjusted from a few hundreds of nanometers to several tens of micrometers. That is to say, the length of nanopore for AAO could be adjusted from a few hundreds of nanometers to several tens of micrometers [2]. Finally, the samples would undergo the post-treatment step, which allows the modification of the AAO template in a way to meet the desired requirements. Such as the aluminum base can be removed, the pore size can be adjusted and the barrier layer can be removed. Here, the AAO templates used in this study were fabricated with a second anodization time of 15 minutes and the pore sizes were widened in a 5 wt. % H_3PO_4 solution for 15 minutes at 30 °C.

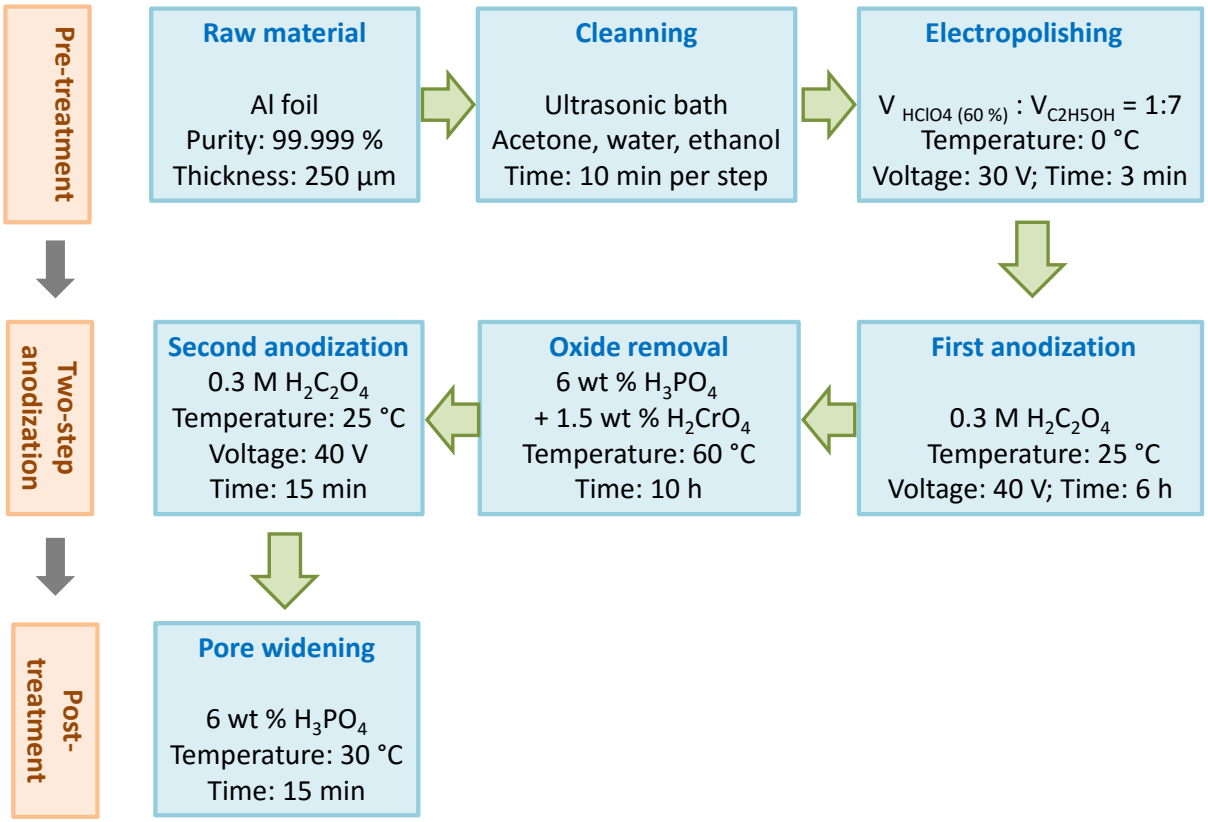

Figure 2-1| The flow diagram presents the fabrication process of nanoporous AAO template by a two-step anodization process, and the details of experiment conditions.

2.1.2. Fabrication of three-dimensional Al nanocone array template

The fabrication of highly ordered nanocone arrays based on AAO template was realized by a special guided one-step anodization and subsequent wet-chemical etching process [3–6] Figure 2-2 shows the flow diagram and experiment conditions to this process in detail.

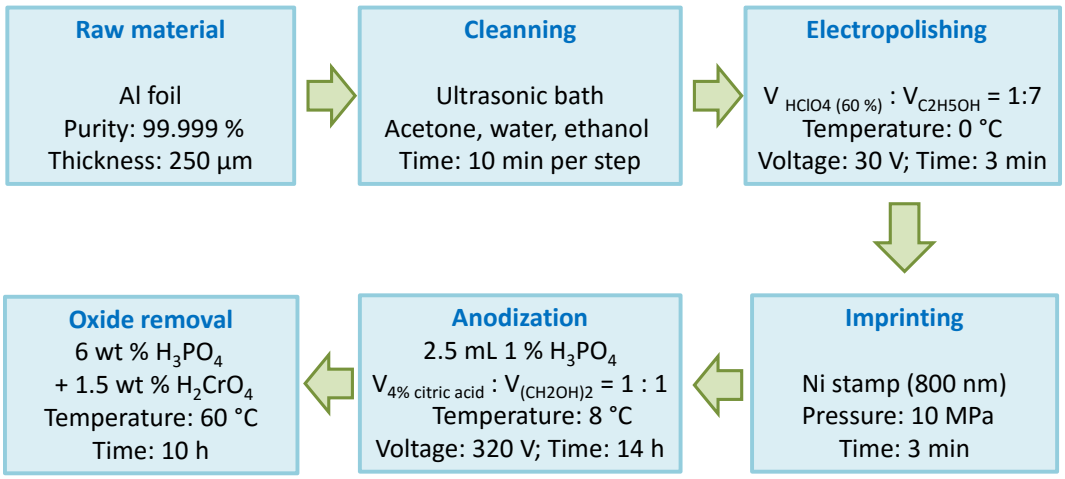

Figure 2-2| The flow diagram presents the fabrication process of highly ordered nanocone array based on AAO template by a special one-step anodization process, and the details of experiment conditions.

2.1.2.1. Preparation of Ni imprinting mold

Ni imprinting molds with squarely order nanopillar array are prepared from a Si master mold with 800 nm spacing shallow array. The Ni imprinting mold is used in the imprinting process on Al foil.

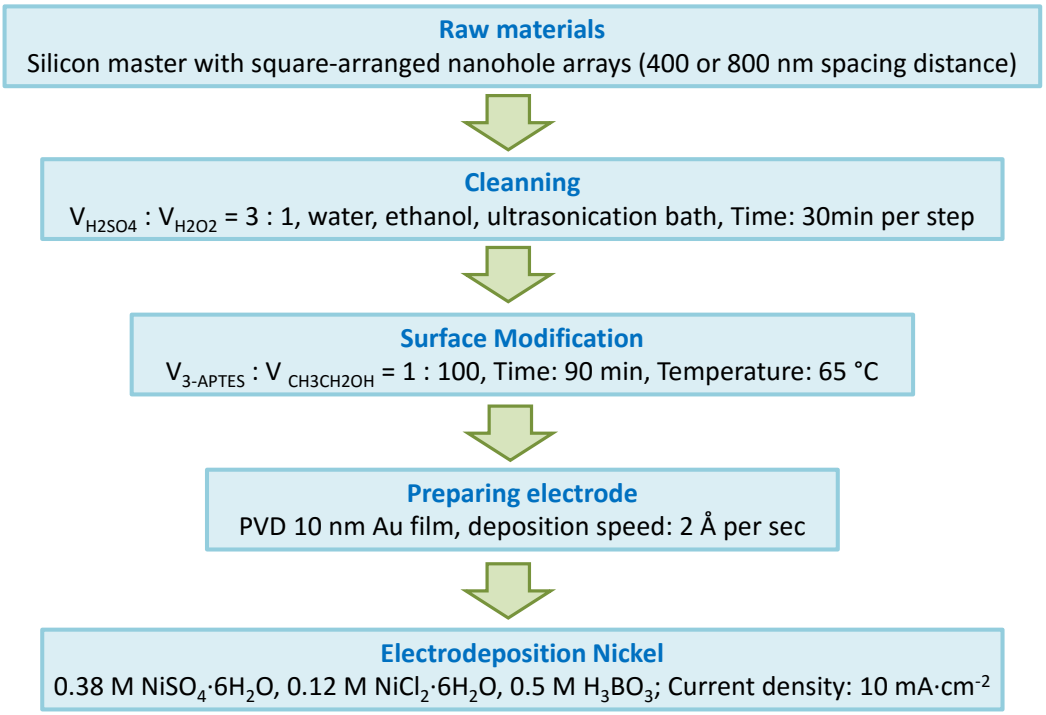

Figure 2-3| The flow diagram presents the fabrication process of nickel stamp, and the detail experiment conditions.

The nickel stamp used in all the experiments was prepared as reported in literature[7,8] Figure 2-3 presents the preparing steps and the detail experiment conditions in a flow diagram to synthesize nickel stamp. Silicon master mold with nanohole array with spacing distance of 400 nm or 800 nm and square-arranged was bought from AMO GmBH. It was firstly cleaned in Piranha solution (V_{H2SO4} : V_{H2O2} = 3 : 1) for 30 min under ultrasonication condition, and subsequently cleaned with water and ethanol with ultrasonication bath. Secondly, the cleaned silicon template was surface modified by 1 vol% of 3-aminopropyltriethoxysilanc (3-APTES) ethanol solution at 65°C for 90 minutes. Then, the modified silicon template was deposited 10 nm Au on the surface by physical vapor deposition with a deposition speed of 2 Å per second. Finally, the pre-treated silicon template was used as the work electrode to deposit a thickness of Ni to form nickel stamp at a current density of 10 mA per square centimeter. The silicon master mold could be recycling used many times.

2.1.2.2. Imprinting and guided anodization of Al foil

The Al nanocone arrays template is the substrate of the subsequent experiments. It is synthesized by a guided anodization on the imprint Al foil and the following precisely controlling wet-chemical etching of AAO templates obtain at 320 V as described below. The all fabrication processes and morphology changes were illustrated in Figure 2-3 and Figure 2-4, respectively.

Firstly, high-purity (99.999 %) aluminum foil with a thickness of 250 µm was used as a starting material. It was cleaned by acetone, deionized water and ethanol in ultrasonic bath for 10 min, separately. Secondly, after the degreasing and clean, the aluminum foil was electrochemically polished in a mixture electrolyte solution with vol. ratio of 1 to 7 of perchloric acid and ethanol for 3 minutes to smooth the surface (Figure 2-3a). Next, the polished aluminum foil was imprinted with 800 nm spacing ordered nanoshallow array by nickel stamp using an oil press under a pressure of 10 MPa for 3 minutes (Figure 2-3b). During the imprint process, the nickel stamps should be kept parallel to the aluminum foil. After that, the imprinted aluminum foil was anodized for 14 hours in a mixture solution of 2.5 mL 1 % H_3PO_4, and vol ration of 1 to 1 of 4 % acidic acid and ethylene glycol at 8 °C and 320 V for different anodization time (Figure 2-3c). The anodization voltage is chose to satisfy

the linear relationship between the interpore spacing and the anodization potential (2.5 $nm \cdot V^{-1}$). In order to expose Al nanocone array, the AAO template is etched away in a mixture of chromium acid (1.5 wt %) and phosphoric acid (6 wt %) solution at 60 °C for 10 h (Figure 2-3d). After the etching, the Al nanocone array (NCA) is cleaned with DI-water and blown dry with air gun for the subsequent materials deposition. The morphology change after the anodization of sample to Al nanocone array was schematically illuminated below in Figure 2-5.

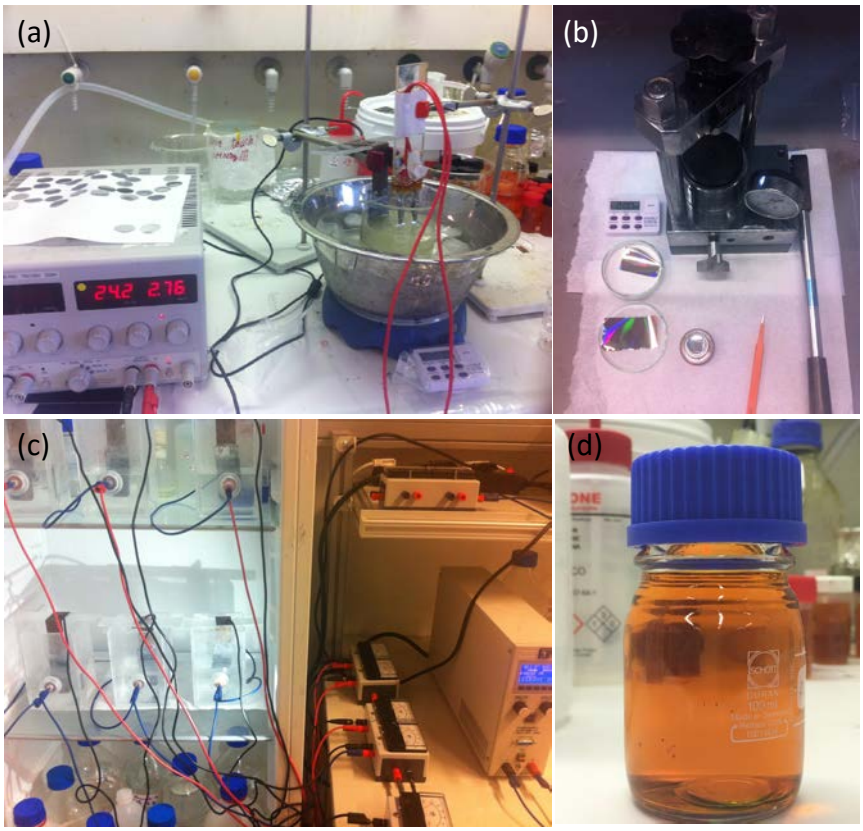

Figure 2-4| The illustrating fabrication process of highly ordered nanocone array based on AAO template by a special one-step anodization process: (a) Electropolishing; (b) Imprinting; (c) Anodization; and (d) Wet-chemical etching.

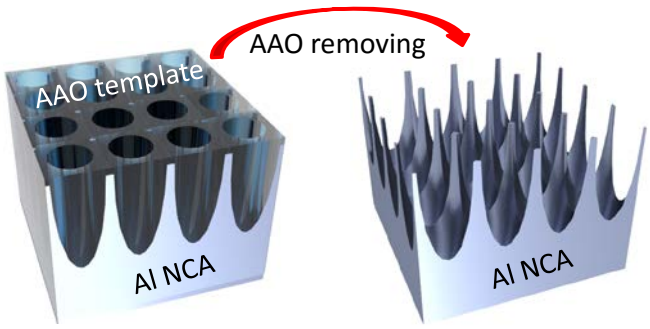

Figure 2-5| The schematic illumination of morphology change for Al nanocone array fabrication.

2.1.3. Assembling of three-dimensional porous poly-styrene sphere template

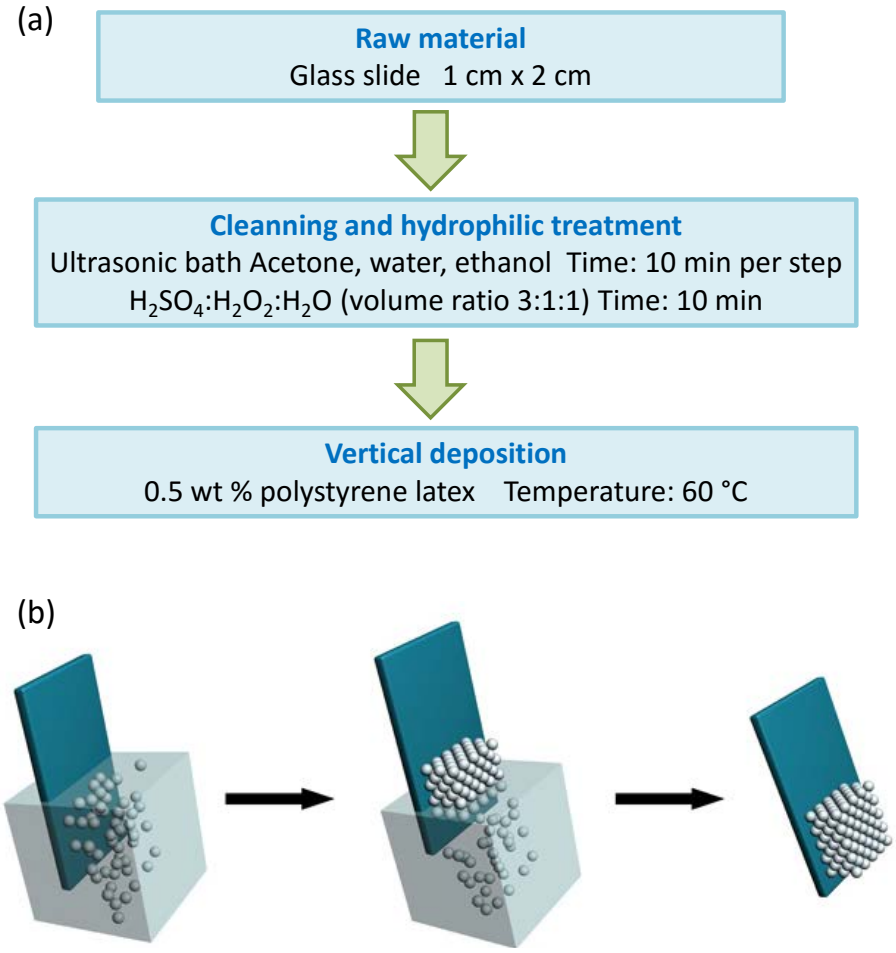

Figure 2-6| (a) The flowchart displays the procedure to fabricate colloidal crystal template by poly-styrene spheres via a vertical deposition process, including required pre-treatments and detail experiment conditions. (b) Schematic illustration of the fabrication of colloidal crystal template by poly-styrene spheres via a vertical deposition process.

Besides the AAO template, poly-styrene sphere (PS) is served as an efficient candidate to construct three-dimensional macro-mesoporous architecture. As intensively researched, the self-assembly of periodic colloidal “opal” template can direct the deposition of functional materials to yield nanoporous “inverse opal” structures [9,10]. The assembled inverse opal architecture can exhibit a high degree of interconnected porosity with extremely uniform size and periodic distributions of pores. Figure 2-6a shows the required steps and detail experiment conditions in a flow diagram to assemble of PS template. As illuminated in Figure 2-6b, the self-assemble of inverse opal template has three sequential steps. They are

assemble of a colloidal crystal template by poly-styrene spheres; deposition of functional materials; and finally selective removal of the colloidal crystal template to yield an inverse porous structures.

Here, in this study, the 500 nm diameter of poly-styrene sphere was selected as a starting material. And in this section, only presents the assembling process of a colloidal crystal template by the selected poly-styrene spheres. Glass was cleaned and degreased under sonication bath with acetone, water, and ethanol for 10 minutes each. And then the glasses were treated with the H_2SO_4:H_2O_2:H_2O (volume ratio 3:1:1) solution for a few seconds to make the surface hydrophilic. The colloidal crystal template comprising poly-styrene spheres arranged on a face-centered cubic lattice was fabricated via the vertical deposition method. The glass substrates were immersed vertically in the 0.5 wt % poly-styrene latex at 60 °C in a vacuum oven. The drying of the sample at very low speed in the presence of moisture prevented the occurrence of cracking on the sample.

2.1.4. Construction of three-dimensional Al doped ZnO transparent electrode

Transparent conducting oxide (TCO) materials are utilized as electrode materials in a wide variety of optoelectronic devices. The most commonly used TCO material is ITO, because of its high conductivity and optical transparency over visible wavelengths. However, the scarcity and high cost of indium limit the industry application. One of the most commonly cited alternative materials is Al-doped ZnO (AZO).

Table 2-1| The experiment details of AZO deposited by ALD

Substrate	Temperature(°C)	Zn:Al (cycle ratio)					
AAO	90	1:0	5:1	10:1	15:a	20:1	25:1
	110	1:0	5:1	10:1	15:a	20:1	25:1
	150	1:0	5:1	10:1	15:a	20:1	25:1
	200	1:0	5:1	10:1	15:a	20:1	25:1
	250	1:0	5:1	10:1	15:a	20:1	25:1
PS	110	1:0	5:1	10:1	15:a	20:1	25:1

Because of its unique ability to conformal coat high-aspect-ratio structures with pin hole free films on a variety of surfaces, atomic layer deposition has arising much attention. The self-limiting surface chemistry of ALD half-reactions, the thickness of films grown by ALD can be controlled with subnanometer precision simply by controlling the number of ALD cycles. This combination of conformality with atomic precision has allowed the development of varieties of new nanofabrication processes and devices.

During my works, the ALD deposition is conducted in a Picosun SUNALE TM R150 ALD System. Diethylzinc (DEZ), trimethylaluminum (TMA), and DI-water were used as the Zn, Al and O precursors, respectively. All the chemicals were purchased from Sigma-Aldrich. And the high purity N_2 (99.999 %) was used as carrying gas. The detailed experiment conditions were illuminated in Table 2-1. Typically, the deposition was performed with reactor chamber temperature at 200 °C. The carrying gas was kept at 100 sccm during the deposition period. The growth process was presented in Figure 2-7. After 20 cycles of ZnO deposition, one cycle of Al_2O_3 was deposited. One complete AZO growth process is: ((0.1 s DEZ pulse – 6 s N_2 purge – 0.1 s DI water pulse – 6 s N_2 purge) x 20 cycles – 0.1 s TMA pulse – 6 s N_2 – 0.1 s DI water – 6 s N_2 purge).The growth rate of AZO is about 1.0 nm per cycle.

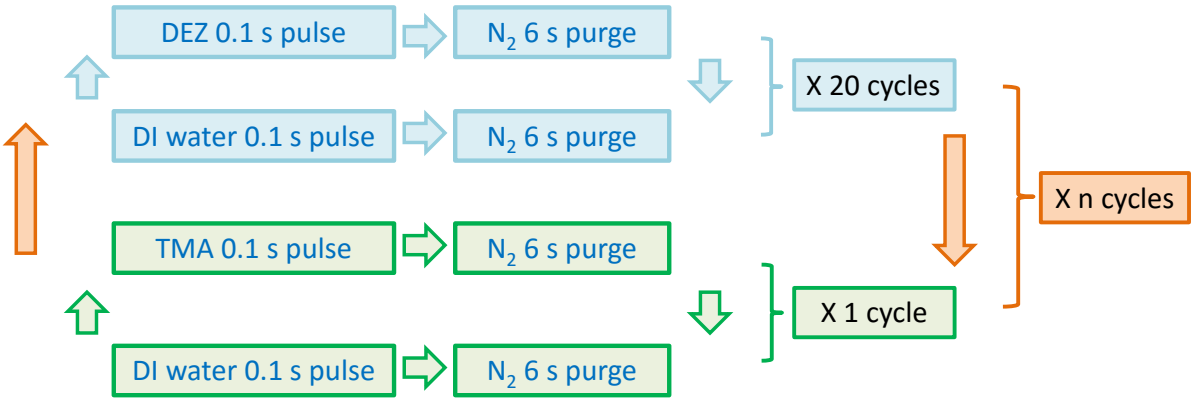

Figure 2-7| The flow diagram presents the ALD growth of AZO transparent electrode and the detail experiment conditions.

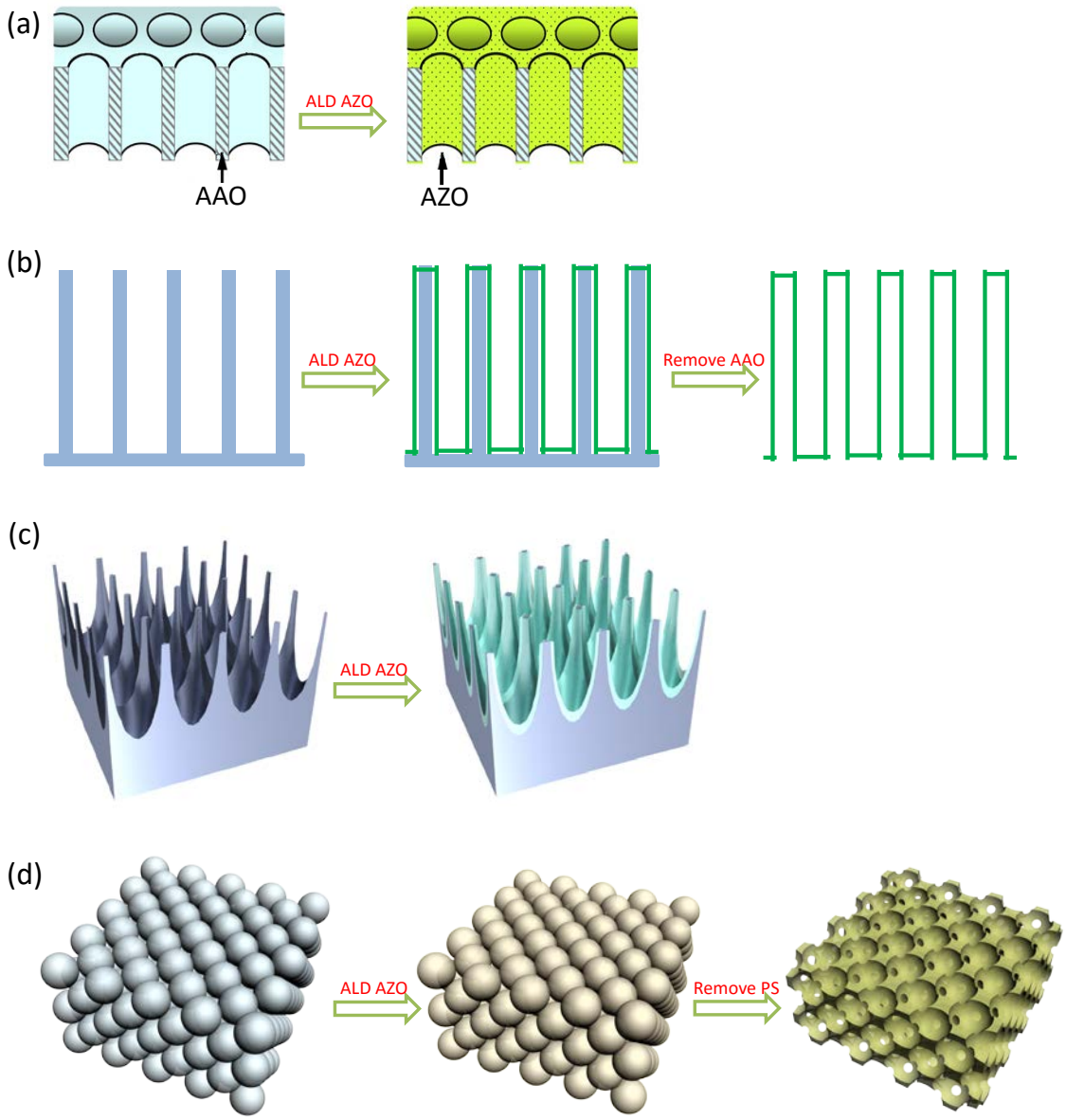

Figure 2-8| Schematic illustration of the three-dimensional AZO fabricated based on anodic aluminum oxide and poly-styrene sphere templates via ALD process: (a) the deposition of AZO on AAO template, (b) the cross-section of deposition AZO and selective removal of AAO, (c) the deposition of AZO on Al nanocone array template which synthesize by unique printing AAO template, and (d) the deposition of AZO and removal of colloidal crystal template vertically deposited by poly-styrene spheres.

Because of its unique ability to conformal coat high-aspect-ratio structures with pin hole free films on a variety of surfaces, atomic layer deposition has been applied to grow three-dimensional AZO transparent electrode for devices. The three-dimensional transparent electrode AZO fabricated by ALD based on anodic aluminum oxide and poly-styrene sphere

(PS) templates was schematically illuminated below in Figure 2-8. The nanostructures of the three-dimensional AZO deposited on AAO were operated at 200 °C with Zn to Al ALD monolayer cycle ratio of 20 to 1. However, because of the unique thermal stability property of poly-styrene sphere, the deposition of AZO based on PS template was operated at 90 °C. The others experiment conditions were the same as that AZO deposited on AAO fabricated nanostructures. After the deposition process, the sample was put into a muffle furnace. And then heating the furnace to 400 °C with a heat rising speed of 2 °C per minute, and kept at 400 °C for 1 hour under atmosphere condition to remove the PS template and crystallize the deposited AZO.

2.1.5. Fabrication of three-dimensional AZO/TiO_2/Au nanocone array

2.1.5.1. Atomic layer deposition of TiO_2 nanocone array

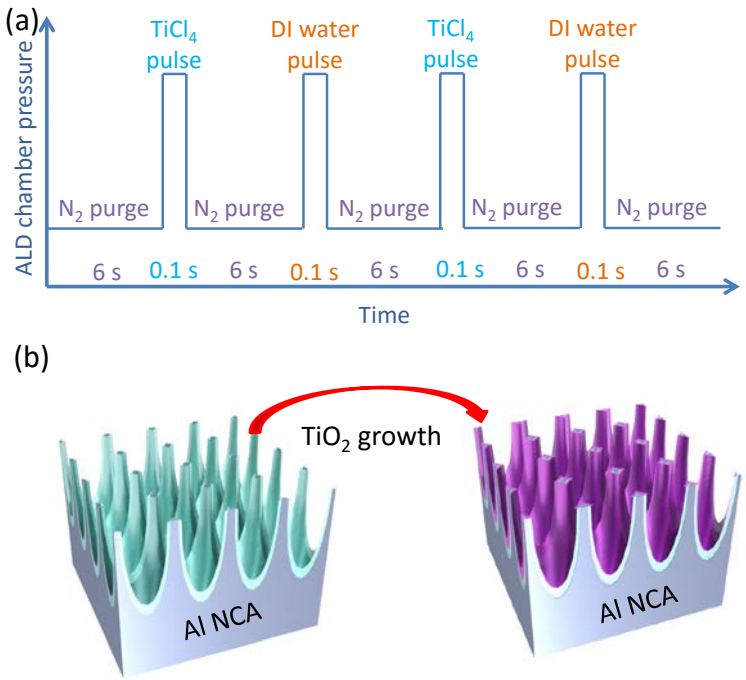

Figure 2-9| (a) The ALD growth of TiO_2 nanocone arrays based on AAO template, and the detail experiment conditions; (b) Schematic illustration of the TiO_2 nanocone arrays grown on three-dimensional AZO surface via ALD process.

The ALD growth of TiO_2 nanocone array on AZO nanocone array is similar to the growth of AZO nanocone array as present in section 2.2.1. $TiCl_4$ and DI-water were acted as Ti and O precursor, separately. The deposition was performed in reactor chamber temperature at

300 °C. The carrying gas was kept at 100 sccm during the deposition period. The growth process and growth condition were presented in Figure 2-9a. One complete TiO_2 growth process is: 0.1 s $TiCl_4$ pulse – 6 s N_2 purge – 0.1 s DI water pulse – 6 s N_2.The growth rate of $TiCl_4$ is about 0.6 nm per cycle. The surface change is schematically illuminated below in Figure 2-9b.

2.1.5.2. Surface modification of Au nanoparticle

Au thin film was evaporated by physical vapor deposition (Kurt J. Lesker). Well-dispersed Au NPs on the surface of the nanocone arrays was obtained after the annealing process at 350 °C for 10 min with a heating rate of 2 °C per minute in muffle furnace and then naturally cooled down to room temperature, as shown in Figure 2-10.

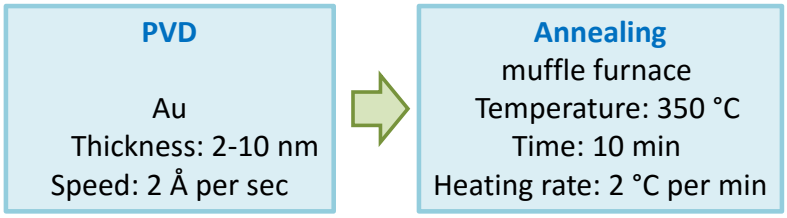

Figure 2-10| The flow diagram presents the decoration of Au nanoparticles.

2.1.6. Construction of three-dimensional Pt/MnO_2 nanotube array

2.1.6.1. Fabrication of regular nanopore array

The fabrication of highly ordered nanopore arrays based on AAO template was realized by a special guided one-step anodization process. It is similar to the fabrication process descripted in Figure 2-1, but the anodization details are different [3,8]. The differences are 1): the nanorod spacing distance of imprint nickel stamp is 400 nm, 2) the anodization voltage is 160 V, 3) temperature is 15 °C and 4) the anodization solution is 0.3 M H_3PO_4. After the anodization process, the formed pore size could be adjusted by opening-pore process with 5 % H_3PO_4 solution at 30 °C for different time. The whole fabrication process was illustrated in Figure 2-11a. The home-made anodization system with automatic linear temperature

controlling programming and the schematic diagram of anodized nanopore array template are shown in Figure 2-11b and c, respectively.

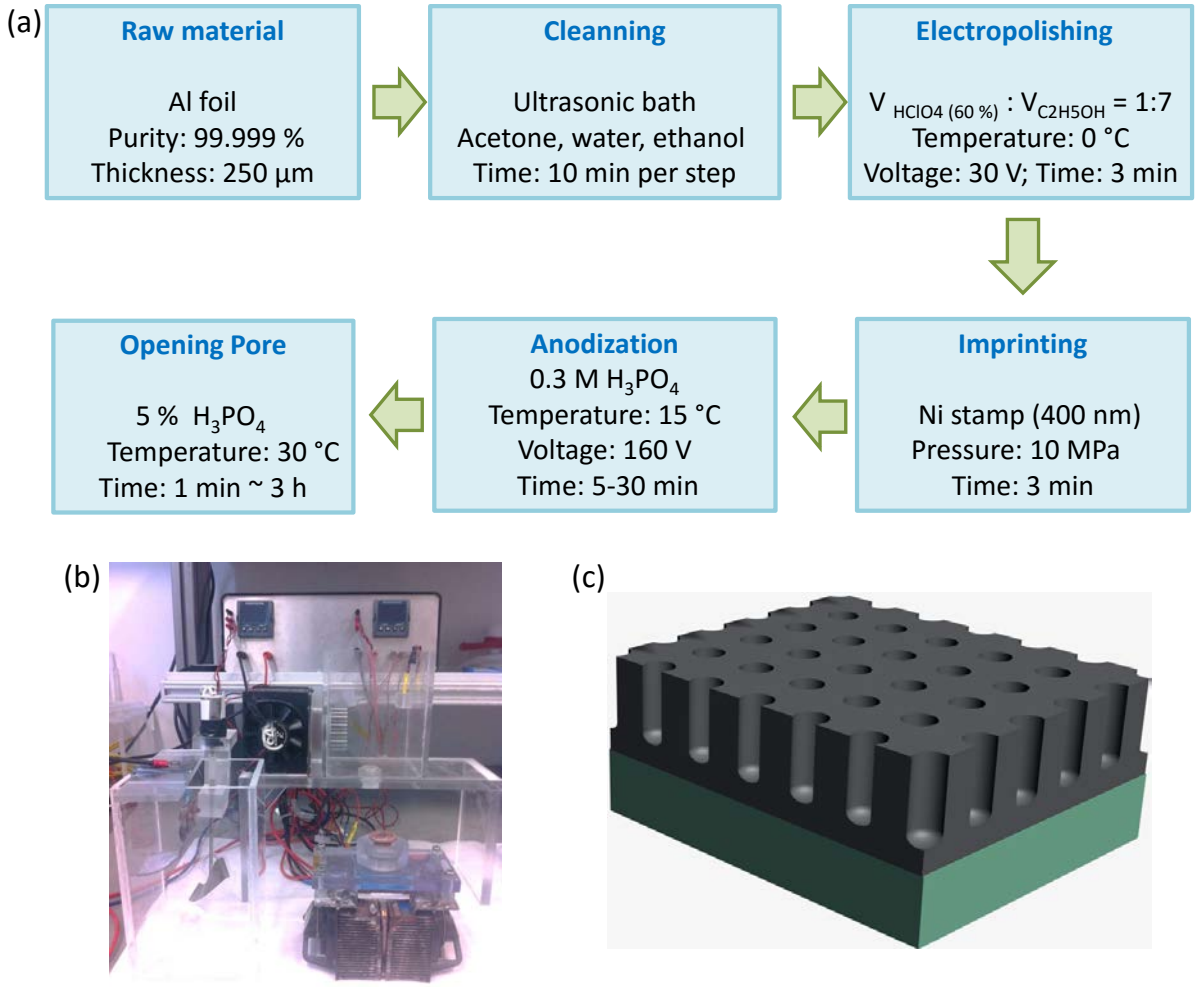

Figure 2-11| (a) The flow diagram presents the fabrication process of highly ordered nanopore arrays based on AAO template, and the detail experiment conditions. (b) The home-made anodization system with automatic linear temperature controlling programming. (c) The schematic diagram of anodized nanopore array template.

2.1.6.2. Atomic layer deposition of Pt nanotube array

The fabrication of Pt NT arrays is conducted in a Picosun SUNALE^{TM} R150 ALD System. And the nanopore array AAO template was prepared in section 2.4.1 used as substrate. The pre-patterned AAO template was further etched in a H_3PO_4 solution (5 wt%) at 30 °C for 90 min

to open the size of the nanopore. The as-prepared template as substrate would be used in the subsequent experiments.

The as-prepared template was put into the ALD reactor chamber. And the ALD reactor chamber was maintained at a temperature of 300 °C and the chamber pressure varied from 8 hPa to 30 hPa under different growth processes. The temperature of $Pt(MeCp)Me_3$ precursor cylinder was held at 80 °C. A typical conventional ALD growth cycle consists of four steps: $Pt(MeCp)Me_3$ pulsing (1.3 s) – N_2 purging (18 s) – O_2 pulsing (1.3 s) – N_2 purging (18 s). The N_2 carrying gases were kept at 100 sccm and the pressure of the reaction chamber was about 8 hPa during the growth. For our innovative ALD growth cycle, it consists of six steps: $Pt(MeCp)Me_3$ pulsing (1.3 s) – low N_2 filling (30 s) -N_2 purging (18 s) – O_2 pulsing (1.3 s) – low N_2 filling (30 s) – N_2 purging (18 s). During the low N_2 filling step, the N_2 carrying gas flows were decreased to 60 sccm and the pressure of the chamber was gradually raised up to about 21 hPa. For the other steps, the N_2 carrying gas flows were still kept at 100 sccm. When 60 s and 90 s low N_2 filling steps were used, the chamber pressure would be increased up to about 24 hPa and 30 hPa, respectively. Figure 2-12 presents the schematic diagram of Pt nanotube array growth by ALD.

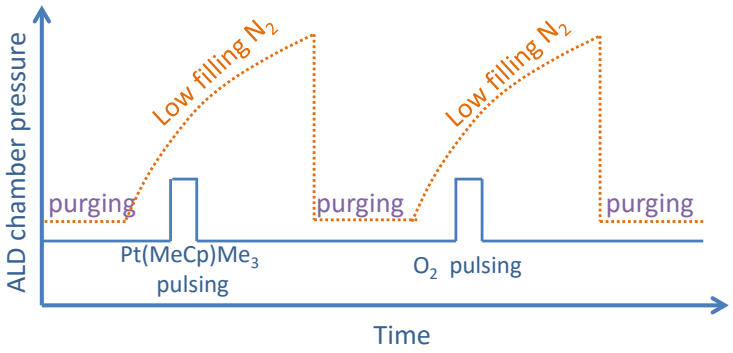

Figure 2-12| Schematic diagram of Pt nanotube array growth by ALD via conventional Pt-ALD process (blue line) and a low filling N_2 process (orange dot line).

2.1.6.3. Electrochemical deposition of MnO_2

The synthesized processes and experiment details were schematically illuminated below in Figure 2-13a. After the growth of Pt nanotube array by ALD, polydimethylsiloxane (PDMS, Sylgard 184 Dow Corning) was poured on the alumina template and was baked at 60 °C for 4

h. The backside aluminum was removed by a mixture solution (3.4 g copper chloride, 100 mL hydrochloric acid and 100 mL deionized water). Pt nanotube arrays were released by dissolving the alumina template in a NaOH solution (1.0 M) for 1 h, followed by a rinsing process with deionized water. Subsequently, manganese oxide (MnO_2) was deposited at a constant potential of 0.7 V using an aqueous solution of manganese acetate (100 mM) and sodium sulfate (100 mM). The potential was measured versus an Ag/AgCl reference electrode. And a Pt foil was used as the counter electrode. The mass of the MnO_2 was determined from the charges passed during electrochemical deposition and assumed 100 % efficiency. The deposition system is present in Figure 2-13b.

(a)

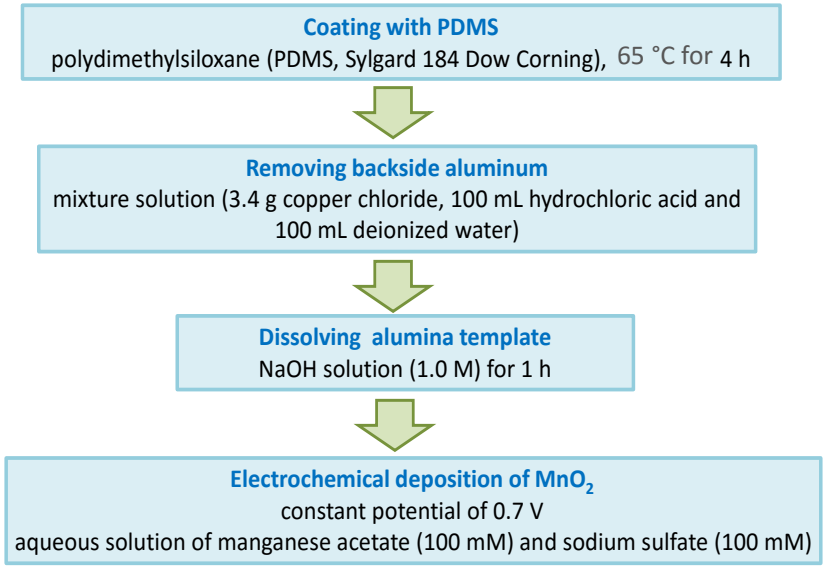

(b)

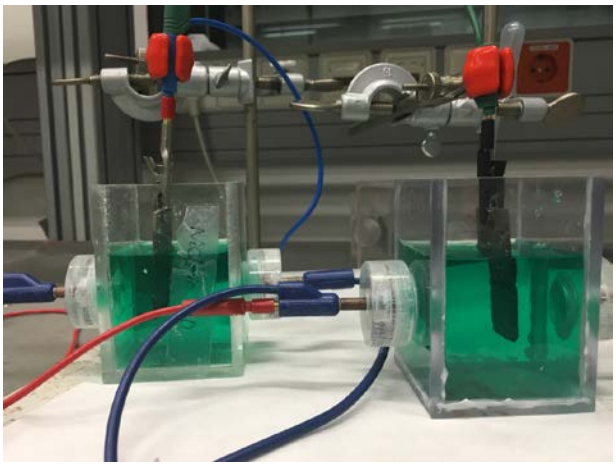

Figure 2-13| (a) The flow diagram presents the fabrication process of electrochemical deposition of MnO_2 on the ordered Pt nanotube arrays based on AAO template, and the detail experiment conditions. (b) The system of electrochemical deposition of MnO_2.

2.1.7. Surface modification of Pt nanoparticles for three-dimensional Pt/Carbon nanofiber aerogel

2.1.7.1. Preparation of three-dimensional carbon nanofibers aerogel derived from bacterial cellulose

Purified bacterial cellulose (BC) pellicle with fiber content of ~1% (vol/vol) was provided by Yu Lab (University of Science and Technology of China) [11,12] As flowing diagramed in Figure 2-14, the wet BC pellicles were first cut into rectangular shape with sharp blade, then frozen in liquid nitrogen and then freeze-dried in a bulk tray dryer at a sublimating temperature of -50 °C and a pressure of 0.04 mbar. The dried BC aerogel was then pyrolysed under flowing N_2 at 800 °C to generate black three-dimensional bacterial cellulose nanofiber (BCF) aerogel.

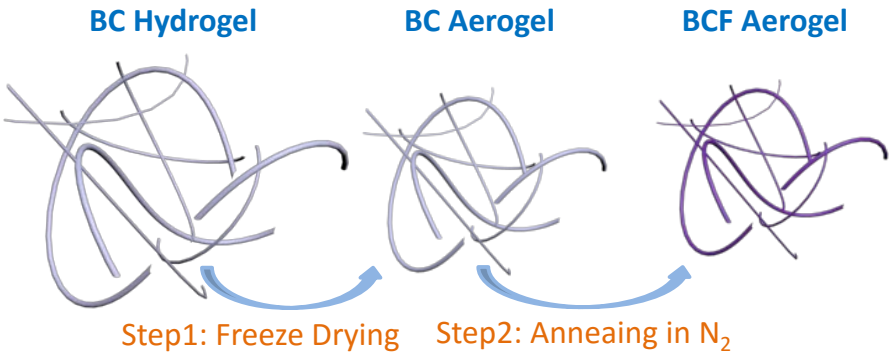

Figure 2-14| Schematic illustration of the preparation of the three-dimensional bacterial cellulose nanofiber aerogel sample.

2.1.7.2. Surface modification of ultra-small Pt nanoparticle by atomic layer deposition

The highly dispersed Pt particles decorated on three dimensional carbon nanofibers aerogel derived from bacterial cellulose, was prepared as the similar process of Pt nanotube array growth by ALD descripted in section 2.1.4. The as-prepared carbon nanofibers aerogel was put into the ALD reactor chamber and the chamber was maintained at a temperature of 220 °C, the chamber pressure value was kept at 26 hPa. The temperature of $Pt(MeCp)Me_3$

precursor cylinder was held at 80 °C. A typical growth process consists of six steps: $Pt(MeCp)Me_3$ pulsing (1.0 s) – low N_2 filling (30 s) -N_2 purging (90 s) – O_2 pulsing (1.0 s) – low N_2 filling (30 s) – N_2 purging (90 s). During the low N_2 filling step, the N_2 carrying gas flows were decreased to 60 sccm and the pressure of the chamber was gradually raised up to about 26 hPa. For the other steps, the N_2 carrying gas flows were still kept at 100 sccm. The growth cycles were less than 10 (Figure 2-15).

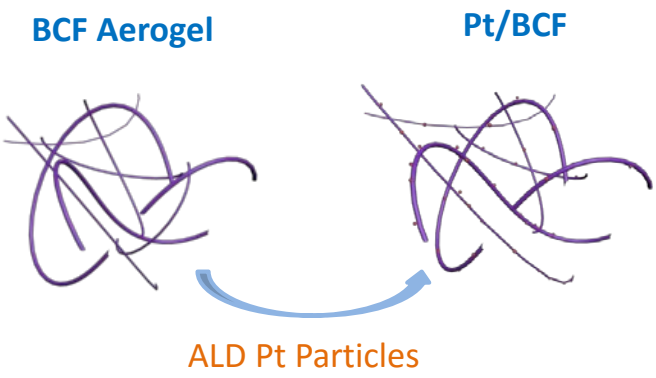

Figure 2-15| Schematic illustration of the surface modification of ultra-small Pt nanoparticles on the three-dimensional bacterial cellulose nanofiber aerogel.

2.2. Characterization of as-prepared specimens

2.2.1. Ultraviolet-visible absorption spectroscopy

The optical properties of prepared samples were investigated by ultraviolet-visible absorption spectroscopy (UV-vis spectroscopy). UV-vis spectroscopy is based on the principle of electronic transition in atoms or molecules upon absorbing suitable energy from an incident light that allows electrons to excite from a lower energy state to higher excited energy state [13]. While interaction with infrared light causes molecules to undergo vibrational transitions, the shorter wavelength with higher energy radiations in the UV (200-400 nm) and visible (400-700 nm) range of the electromagnetic spectrum causes many atoms/molecules to undergo electronic transitions. They were carried out on Varian Cary 5000 UV-VIS-NIR spectrophotometer. The samples were investigated the reflection information. It contains specular reflectance, which is the mirror-like reflection of a sample

surface; and diffuse reflectance, which occurs when the surface reflects light in many different directions, giving a matt appearance surface.

2.2.2. Electroconductivity characterization

2.2.2.1. Four point probe method

A four point probe is a simple apparatus for the measurement of the resistivity of samples. The square resistances of the prepared transparent AZO electrode and Pt nanotube arrays were determined by four point probe method on probe station. As shown in Figure 2-16, the sheet resistivity of the electrode layer was very easy to measure experimentally. A current was passed through the outer probes and induced a voltage in the inner voltage probes. The sheet resistivity was determined as [14]:

$$\rho_{\blacksquare} = \frac{\pi}{\ln(2)} \frac{V}{I}$$

Where $\rho_{\blacksquare}$ is sheet resistivity; $\frac{\pi}{\ln(2)} = 4.53$; V is probe voltage; I is probe current.

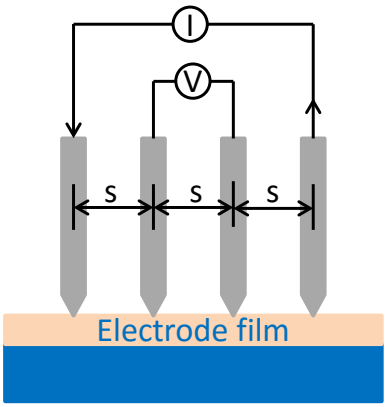

Figure 2-16| The work principle of four point probe method.

2.2.2.2. Probe station

The probe station utilizes manipulators which allow the precise positioning of thin needles on the surface of a semiconductor device to physically acquire signals from the internal

nodes of a semiconductor device. The cuurent-voltage (I-V) curves of the Pt nanotube array were recorded by probe station which connected with the Keithley 2612B.

2.2.3. X-ray photoelectron spectroscopy

X-ray photoelectron spectroscopy (XPS) is a surface-sensitive quantitative spectroscopic technique that measures the elemental composition at the parts per thousand range, empirical formula, chemical state and electronic state of the elements that exist within a material [15]. The spectra are obtained by irradiating a material with a beam of X-rays while simultaneously measuring the kinetic energy and number of electrons that escape from the top 0 to 10 nm of the material being analyzed. It requires high vacuum (P ~ 10^{-8} millibar) or ultra-high vacuum (UHV; P < 10^{-9} millibar) conditions, although a current area of development is ambient-pressure XPS, in which samples are analyzed at pressures of a few tens of millibar. XPS was utilized to verify the chemical states of prepared samples in the whole work. All XPS measurements were recorded on a VG MultiLab 2000 system with a monochromatic Al Kα source operated at 300 W.

2.2.4. Field emission scanning electron microscopy

The field-emission scanning electron microscopy (FE-SEM) is a state-of-the-art electron microscope, which is an analytical method to investigate the morphology of specimen in micro-nanometer regime. The field-emission cathode in the electron gun of microscope provides high electronenergy, while as well as narrower probing beam at low, allowing for ultra-high resolution electron imaging (>10 nm at 1 kV) for samples. Even the conductivity of the samples is not good. And it also minimizes the damage of samples. Therefore, in this work, the FE-SEM images were almost exclusively utilized to investigate the nanostructure morphologies of the prepared samples. All measurements were performed on an ultra-high resolution *Hitachi S4800* FE-SEM and *Auriga Zeiss FIB* at around 5 nm working distance with acceleration voltages in the range of 3-15 kV, and a resolution of 1 to 2 nm. More details on the working principle of a FE-SEM can be found in literatures [16].

2.2.5. Transmission electron microscopy

Transmission electron microscopy (TEM) is a microscopy technique in which a beam of electrons is transmitted through an ultra-thin specimen (the thickness is less than 200 nm), interacting with the specimen as it passes through. An image is formed from the interaction of the electrons transmitted through the specimen; the image is magnified and focused onto an imaging device. Owing to the small Broglie wavelength of electrons, TEM could capable of imaging at a much higher resolution than FE-SEM (sub-nanometer resolution and even single atom resolution). Thus, the TEM and scanning transmission electron microscopy (STEM) of *JEOL JEM-2010F* with an acceleration voltage of 200 kV were used in this work to study fine details, especially the crystal structures of the prepared samples. The more details for the work principles of TEM are widely discussed and can be found in literatures [17]. The TEM samples were prepared on a Quantifoil R 2/2 TEM grid with a Cu 400 mesh and a 12 nm thick holey carbon film (hole size 2 µm, period 4 µm). The sample with ethanol in vessel was placed into an ultrasonic bath for some minutes. After that, a single drop of the solution is dispersed on a TEM grid and dried at ambient condition.

2.2.6. Energy dispersive X-Ray spectroscopy

Energy dispersive X-Ray spectroscopy (EDS) was utilized to study the chemical composition and elements distribution of samples [18]. The EDS system on FE-SEM and TEM detects X-rays emitted from the sample as a result of the high-energy electron beam penetrating into the sample. X-ray spectra can be collected and analyzed, yielding quantitative elemental information about the sample. Most of elements could be detected at concentration on the order of around 0.1 wt%. EDS line scanning and EDS mapping also were performed in this work.

2.2.7. Photoelectrochemical characterization

2.2.7.1. Photocurrent

The photocurrent in this work was characterized by an electrochemical analyser (*BioLogic SP-200*) under solar light irradiation. The solar light was provided by a solar simulator

(*Newport* solar simulator with 300 W Xenon lampe, AM 1.5 global filter). The simulator provides a controllable indoor test facility under laboratory conditions for the testing of solar storage and conversion devices. In this work, it is calibrated to 100 $mW \cdot cm^{-2}$ (1 sun) by a Si photodiode (*Newport Model 818*). The optical filter of 420 nm and 450 nm cut-off were used to cut off the light wavelength small than 420 nm and 450 nm, respectively. And the photocurrents were performed in a standard three-electrode system with prepared samples as working electrodes, a Pt mesh as the counter electrode, and Ag/AgCl as a reference electrode. All three electrodes were placed in a quartz cell. And the 0.1 M Na_2SO_4 aqueous solution was used as the electrolyte which was bubbled by high-purity N_2 thoroughly to remove the dissolved oxygen before the measurement.

2.2.7.2. Incident photo-to-current efficiency

The incident photo-to-current efficiency (IPCE) is a measure of how efficiently the device converts the incident light into electrical energy at a given wavelength. The external quantum efficiency and internal quantum efficiency are two types of efficiency. They are the ratio between the number of collected carriers and the number of all the incident photons on the device active area, or all the absorbed photons by only the active absorber at a given wavelength, respectively. In this work, the IPCE was investigated by QEPVSI-b quantum efficiency measurement system from *Newport* without the applying of bias.

2.2.8. Electrochemical characterization

For the electrochemical characterization of Pt/MnO_2 supercapacitor and Pt/BCF electrocatalyst for hydrogen evolution reaction, all the measurements were performed on a *Bio-Logic VSP* electrochemical work station in ambient condition. The three-electrode measurement system was used during the test period. It contains a working electrode (prepared samples), counter electrode (1 cm^2 platinum foil) and Ag/AgCl reference electrode (3 M KCl). The specific capacitance, cycle stability and impedance spectroscopy were performed via this system. The 1.0 M Na_2SO_4 was used as electrolyte to test the performance of Pt/MnO_2 supercapacitor. Cyclic voltammetry was carried out at scan rates from 5 to 100 $mV \cdot s^{-1}$. Galvanostatic charge/discharge cycling was measured at different

current densities from 2 to 100 $A \cdot g^{-1}$. A potential window in the range of 0-0.9 V was used in all measurements of Pt/MnO_2 supercapacitor.

For the electrocatalytic performance of Pt/C electrodes, 2 mg of as-prepared catalyst (or commercial Pt/C catalyst (10 wt % loading, Sigma-Aldrich)) was dispersed in 0.98 mL of isopropanol and 20 µL Nafion 117 solution (Sigma-Aldrich), followed by sonication till well-dispersed ink, and then 30 µL of the catalyst ink was spin-coated on 1 cm x 1 cm carbon paper (Toray, Japan), and dried under room temperature. The prepared carbon paper was used as the work electrode. Saturated calomel electrode (SCE) and platinum plate were used as reference and counter electrodes, respectively. All potentials in this work were converted to that of reversible hydrogen electrode (RHE) through RHE calibration described in literature [19,20]. In our system, $E_{RHE} = E_{SCE} + 0.272$ V.

Before the electrochemical measurement, the electrolyte (0.5 M H_2SO_4) was degassed by bubbling with high-purity N_2 for 30 min. The polarization curves were obtained by sweeping the potential from -0.7 to -0.2 V versus SCE, with a scan rate of 5 $mV \cdot s^{-1}$. The data were recorded after applying a number of potential sweeps until being stable. The polarization curves were re-plotted as overpoetenial (η) versus log current ($log\ J$) to get Tafel plots for assessing of the HER activities of investigated catalysts. By fitting the linear portion of the plots to the Tafel equation ($\eta = b\ log(j) + a$), the Tafel slope (b) can be obtained. The accelerated stability tests were performed in N_2-satureated 0.5 M H_2SO_4 solution at room temperature by potential cycling between -0.7 to -0.2 V versus SCE at a sweep rate of 100 $mV \cdot s^{-1}$ for 1000 cycles. At the end of the cycles, the resulting electrode was used for HER polarization and CV curves at a sweep rate of 5 $mV \cdot s^{-1}$. All the polarization curves were corrected with iR-compensation.

2.2.9. Finite-difference time-domain simulation

Finite-difference time-domain simulation (FDTD) solutions is a 3D Maxwell solver, capable of analyzing the interaction of UV, visible, and IR radiation with complicated structures employing wavelength scale features [21,22]. FDTD has been identified as the preferred method for performing electromagnetic simulations for photoelectrochemical cells. In this work, in order to identify the light utilization of the prepared nanostructure arrays, the FDTD was applied to simulate the electromagnetic field distribution and the accordingly photo

absorption of simples. It could provide a support to the experiment results as well as a consultant to optimize the structure and composition. The parameters of the AZO/TiO_2 NCA were derived from the SEM image and a sparse density of Au NPs with the size of 18 nm was used for the simulation.

2.3. Bibliography

[1] H. Masuda, K. Fukuda, Ordered Metal Nanohole Arrays Made by a Two-Step Replication of Honeycomb Structures of Anodic Alumina, Science (80-.). 268 (1995) 1466–1468. doi:10.1126/science.268.5216.1466.

[2] Y. Lei, W. Cai, G. Wilde, Highly Ordered Nanostructures with Tunable Size, Shape and Properties: A New Way to Surface Nano-patterning Using Ultra-thin Alumina Masks, Prog. Mater. Sci. 52 (2007) 465–539. doi:http://dx.doi.org/10.1016/j.pmatsci.2006.07.002.

[3] H. Masuda, H. Yamada, M. Satoh, H. Asoh, M. Nakao, T. Tamamura, Highly Ordered Nanochannel-array Architecture in Anodic Alumina, Appl. Phys. Lett. 71 (1997) 2770 – 2772. doi:10.1063/1.120128.

[4] H. Masuda, H. Asoh, M. Watanabe, K. Nishio, M. Nakao, T. Tamamura, Square and Triangular Nanohole Array Architectures in Anodic Alumina, Adv. Mater. 13 (2001) 189–192. doi:10.1002/1521-4095(200102).

[5] W. Lee, R. Ji, C.A. Ross, U. Gösele, K. Nielsch, Wafer-Scale Ni Imprint Stamps for Porous Alumina Membranes Based on Interference Lithography, Small. 2 (2006) 978–982. doi:10.1002/smll.200600100.

[6] H. Oshima, H. Kikuchi, H. Nakao, K.I. Itoh, T. Kamimura, T. Morikawa, et al., Detecting Dynamic Signals of Ideally Ordered Nanohole Patterned Disk Media Fabricated Using Nanoimprint Lithography, Appl. Phys. Lett. 91 (2007) 022508. doi:10.1063/1.2757118.

[7] L. Wen, Y. Mi, C. Wang, Y. Fang, F. Grote, H. Zhao, et al., Cost-effective Atomic Layer Deposition Synthesis of Pt Nanotube Arrays: Application for High Performance Supercapacitor, Small. 10 (2014) 3162–3168. doi:10.1002/smll.201400436.

[8] Y. Qiu, S.-F. Leung, Q. Zhang, B. Hua, Q. Lin, Z. Wei, et al., Efficient Photoelectrochemical Water Splitting with Ultrathin films of Hematite on Three-Dimensional Nanophotonic Structures, Nano Lett. 14 (2014) 2123–2129.

doi:10.1021/nl500359e.

[9] A. Stein, B.E. Wilson, S.G. Rudisill, Design and Functionality of Colloidal-crystal-templated Materials-chemical Applications of Inverse Opals, Chem. Soc. Rev. 42 (2013) 2763–2803. doi:10.1039/C2CS35317B.

[10] B. Hatton, L. Mishchenko, S. Davis, K.H. Sandhage, J. Aizenberg, Assembly of Large-area, Highly Ordered, Crack-free Inverse Opal Films, Proc. Natl. Acad. Sci. . 107 (2010) 10354–10359. doi:10.1073/pnas.1000954107 .

[11] L.-F. Chen, Z.-H. Huang, H.-W. Liang, H.-L. Gao, S.-H. Yu, Three-Dimensional Heteroatom-Doped Carbon Nanofiber Networks Derived from Bacterial Cellulose for Supercapacitors, Adv. Funct. Mater. 24 (2014) 5104–5111. doi:10.1002/adfm.201400590.

[12] H.-W. Liang, Z.-Y. Wu, L.-F. Chen, C. Li, S.-H. Yu, Bacterial Cellulose Derived Nitrogen-doped Carbon Nanofiber Aerogel: An Efficient Metal-free Oxygen Reduction Electrocatalyst for Zinc-air Battery, Nano Energy. 11 (2015) 366–376. doi:http://dx.doi.org/10.1016/j.nanoen.2014.11.008.

[13] P.W. Atkings, Physikalische Chemie, VCH, Weinheim, (1987).

[14] F.M. Smits, Measurements of Sheet Resistivity with the Four-Point Probe, Bell Syst Tech J. 37 (1958) 711–718. doi:10.1002/j.1538-7305.1958.tb03883.x.

[15] S. Hüfner, Introduction and Basic Principles, in: Photoelectron Spectrosc. SE - 1, Springer Berlin Heidelberg, 2003: pp. 1–60. doi:10.1007/978-3-662-09280-4_1.

[16] D. McMullan, Scanning Electron Microscopy 1928–1965, Scanning. 17 (1995) 175–185. doi:10.1002/sca.4950170309.

[17] W.C. Summers, Picture Control: The Electron Microscope and the Transformation of Biology in America, J. Hist. Biol. 32 (n.d.) 566–568. http://www.jstor.org/stable/4331553.

[18] J. Goldstein, Scanning Electron Microscopy and X-Ray Microanalysis, Springer US, 2003.

[19] Y.-F. Xu, M.-R. Gao, Y.-R. Zheng, J. Jiang, S.-H. Yu, Nickel/Nickel(II) Oxide Nanoparticles Anchored onto Cobalt(IV) Diselenide Nanobelts for the Electrochemical Production of Hydrogen, Angew. Chemie Int. Ed. 52 (2013) 8546–8550. doi:10.1002/anie.201303495.

[20] Y.-R. Zheng, M.-R. Gao, Z.-Y. Yu, Q. Gao, H.-L. Gao, S.-H. Yu, Cobalt Diselenide Nanobelts Grafted on Carbon Fiber Felt: an Efficient and Robust 3D Cathode for Hydrogen Production, Chem. Sci. 6 (2015) 4594–4598. doi:10.1039/C5SC01335F.

[21] A. Taflove, Application of the Finite-Difference Time-Domain Method to Sinusoidal Steady-State Electromagnetic-Penetration Problems, Electromagn. Compat. IEEE Trans. EMC-22 (1980) 191–202. doi:10.1109/TEMC.1980.303879.

[22] J. VonNeumann, R.D. Richtmyer, A Method for The Numerical Calculation of Hydrodynamic shocks, J. Appl. Phys. 21 (1950) 232–237. doi:10.1063/1.1699639.

3. Atomic layer deposition fabrication of three-dimensional Al-doped ZnO for transparent electrode

3.1. Introduction

Kapitel 1 Transparent conductive electrodes are optically transparent and electrically conductive electrodes [1][2][3]. In recent years, transparent conductive electrodes are widely used in optical-electronic devices such as solar cells [2][4], displays, organic light-emitting diodes [5][6], and touch screens [7][8]. The fabrication of low-cost thin films and/or complex nanostructures acting as transparent conductive electrodes is one of the most important issues in developing and commercialization of new generations of photovoltaic and optoelectronic devices. The most conventionally and commercially used transparent conductive electrode material is indium tin oxide [9][10], because of its good optical transparency over visible light wavelengths and high conductivity. However, the continuous consumption of the rare indium year by year results the great price increasing of ITO and the depletion of indium in the near future as well [11][12]. Therefore, a lot of research efforts have been put into looking forward an appropriate alternative of ITO.

Kapitel 2 Other transparent conductive oxides [13][14], conductive polymers [15][16], metal grids [17][18], and carbon nanotubes [19][20], graphene [21][22], carbon nanowires [23][24], and ultrathin metal films [25][26] all show possibility in some applications. Amongst the variety of materials investigated for the transparent conducting electrode, aluminum-doped zinc oxide (AZO) is regarded to be one of the most prospective transparent conducting oxides to serve as a replacement of ITO [27][28]. Although the optoelectronic properties of ITO are superior to that of AZO, the abundant and non-toxic as well as inexpensive of Zn and Al are prominent in industry applications. In addition, the electrical and optical properties, such as the conductivity and optical transmittance of AZO could be easily controlled by adjusting the impurity doping concentration of aluminum [29][30].

Kapitel 3 AZO films are easily fabricated using various deposition methods. It has been prepared using various techniques such as chemical vapor deposition [31][32], electron beam evaporation [33][34], pulsed laser deposition [35][36], direct-current and radio-frequency magnetron sputtering [37][38], spray pyrolysis [39][40], solution deposition

[41][42] and so on. The fabricated AZO electrode showed a low resistivity values on the order of 10-4 Ω cm and high transmittance of > 80% for visible light wavelengths. However, the drawbacks such as physical damage to the film surface and the lack of in situ control of the impurity doping concentration of those conventional deposition methods limit the wide application of AZO. Moreover, the new-generation of devices, especially the new generation of optoelectronic devices demand not only flat film transparent conducting films, but also high-aspect-ration transparent conducting micro/nanostructures. It is hard to be achieved by the traditional deposition methods [43]. Thus, it is important and urgent to develop a strategy which could fabrication complex architecture transparent conducting

Recently, the new deposition method, atomic layer deposition has received increasing attention in the fabrication of transparent conducting films. As shown in Table 3-1, with the benefit of sequential, self-limiting and surface controlled gas phase chemical reactions of ALD half-reactions, the dense, crack-, defect- and pinhole-free film could be obtained [36,44–52]. And the thickness, structures and chemical characteristics of ALD films can be precisely controlled on atomic scale. The most significant aspect of ALD is the unique ability to conformal coat high-aspect-ratio structures with pinhole-free films on a variety of surfaces [53–56]. However, the majority of the previously reported works are focus on flat ALD AZO films. The fabrication of complex AZO structures by ALD is rarely reported. Therefore, in this chapter, the detailed fabrication of three-dimensional complex nanostructures AZO based on anodic aluminum oxide and poly styrene sphere (PS) templates, and the corresponding characterization of as-prepared AZO nanostructures were performed.

Table 3-1| AZO films deposited by ALD process

Zn precursor	Al precursor	O precursor	Zn:Al	Temperature (°C)	Ref.
diethyl zinc (DEZ)	dimethylaluminum isopropoxide (DMAI)	water	17:1	150~250	[44]
diethylzinc	trimethylaluminium	water	19:1	200	[45][46]
diethyl zinc	trimethyl aluminum	water	20:a	150	[47]
diethyl zinc	trimethyl aluminum	water	15:1	200	[57]
diethyl zinc	trimethyl aluminum	water	13:1~27:1	140~220	[48]

diethyl zinc	trimethyl aluminum	water	9:1~49:1	200	[49]
diethyl zinc	trimethyl aluminum	water	24:1	110, 140	[50]
diethyl zinc	trimethyl aluminum	water	20:1	150~325	[51]
diethyl zinc	aluminum isopropoxide	water	19:1	200	[52]

3.2. Results and discussion

In this section, the three-dimensional AZO nanostructures were fabricated based on AAO and PS template by ALD. The thicknesses, optical and electronic properties of AZO were controlled by adjusting the growth temperature, ALD growth cycle numbers and doping concentration of Al. The experiment operated as described in section 2.1.4.

3.2.1. Morphology analysis

In this section, the morphology characteristics of the three-dimensional AZO nanostructure fabricated by ALD process based on AAO and PS template were investigated by SEM.

3.2.1.1. Three-dimensional AZO nanostructure based on AAO

Figure 3-1 shows the three-dimensional AZO nanostructure fabricated based on AAO template by ALD process. As can be seen in Figure 3-1a, the as-prepared fresh AAO template with a pore size around 50 nm. After post-treated with 5 wt % of H_3PO_4 solution at 30 °C for 15 min, the pore size enlarged to around 70 nm (Figure 3-1 b and c). These post-treated AAO samples were used as substrate to deposit AZO by ALD technique. As presented in Figure 3-1d, after deposition of AZO as described in section 2.1.4 with Zn to Al monocycle ratio of 20 to 1 at 200 °C for 10 repeat ALD cycles, the cross-section of sample presented tube like morphologies. After selective removal of AAO substrate, they are top-connected three-dimensional AZO nanotube array (Figure 3-1e). The broken area in Figure 3-1f clearly presents the tube morphology of AZO fabricated by ALD process.

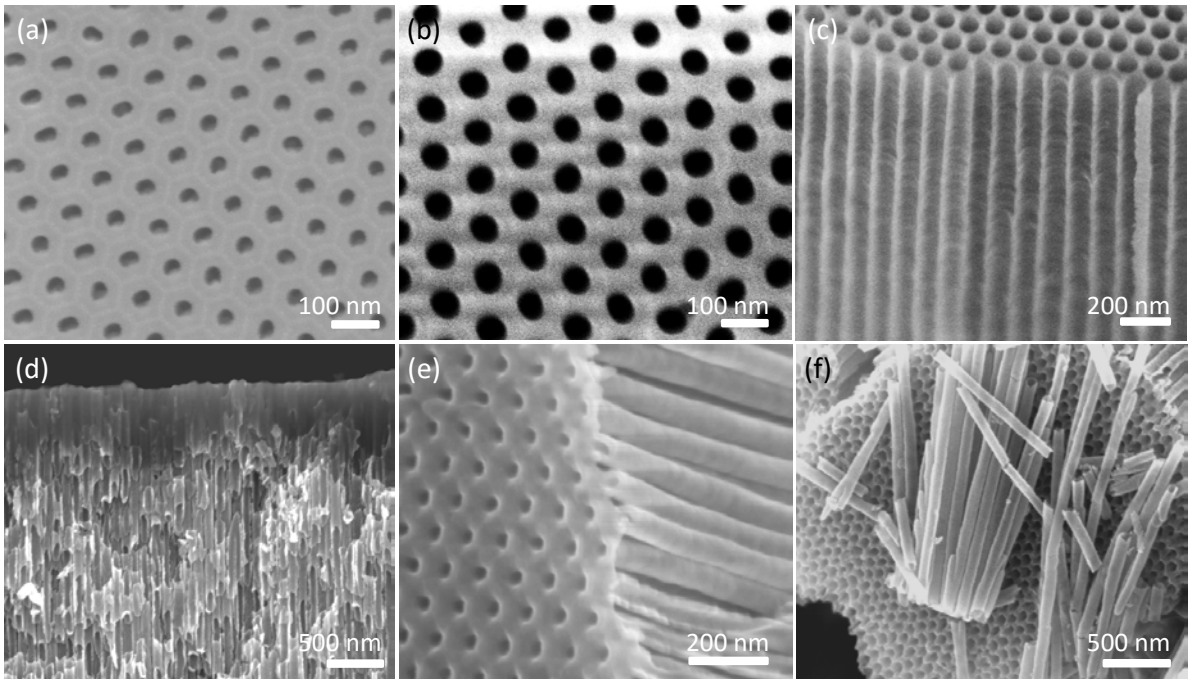

Figure 3-1| The SEM images of the as-prepared and post-treated AAO template, and the fabricated three-dimensional AZO tube array based on the prepared AAO template. (a) Fresh AAO template, (b) 15 min wide-pore treatment of AAO template, (c) the cross-section SEM image of post-treated AAO template, (d) the cross-section SEM image of post-treated AAO template deposited AZO by ALD, (e) side-view of the AZO nanostructure selectively removed AAO of sample in (d), (d) the AZO nanotubes.

The precise control of the thickness of deposited materials is one of the main unique properties of ALD technique. The thickness of AZO fabricated based on AAO template also could be precisely controlled by changing the deposition ALD repeat cycle numbers. The morphology changes were presented in Figure 3-2. As can be found in the presented SEM images, with the increase of repeat cycle numbers, the thickness of AZO nanotube in AAO pores increased as well.

From the SEM images, it can be calculated that the growth speed of AZO at the deposition condition is about 1 Å per cycle. That is to say, for each repeat cycle, the AZO has a thickness of 2 nm. The morphology of three-dimensional AZO nanocone array which fabricated based on Al nanocone template presents in chapter 4.

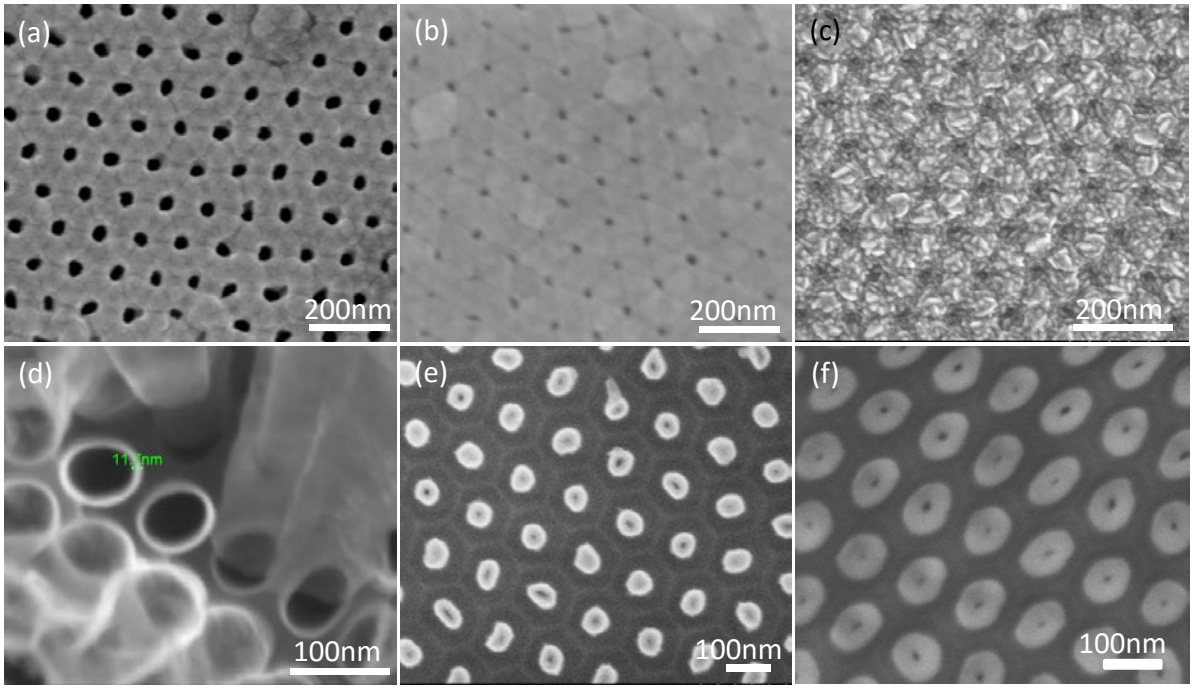

Figure 3-2| The SEM images of the as-prepared three-dimensional AZO tube array based on the prepared AAO template with different deposition ALD repeat cycle numbers: (a) 5 repeat cycles, (b) 10 repeat cycles, and (c) 20 repeat cycles. And the corresponding AZO tube array after selectively removed AAO: (d) 5 repeat cycles, (e) 20 repeat cycles, and (f) 30 repeat cycles.

3.2.1.2. Three-dimensional AZO nanostructure based on PS

Besides the AAO template fabricated three-dimensional nanostructures, the colloidal crystal template vertically deposited by poly-styrene spheres also used as one of the fabrication templates. The morphology of the three-dimensional AZO nanostructure fabricated via PS template was displayed in Figure 3-3. As shown in Figure 3-3a, the poly-styrene spheres constructed colloidal crystal template has a smooth surface. And those poly-styrene spheres were regularly self-assembled. After the deposition of AZO by ALD process at 90 °C, the morphology of the colloidal crystal template was still as before (Figure 3-3b). But the surface was not as smooth as bare colloidal crystal template deposited by poly-styrene spheres (Figure 3-3c and d).

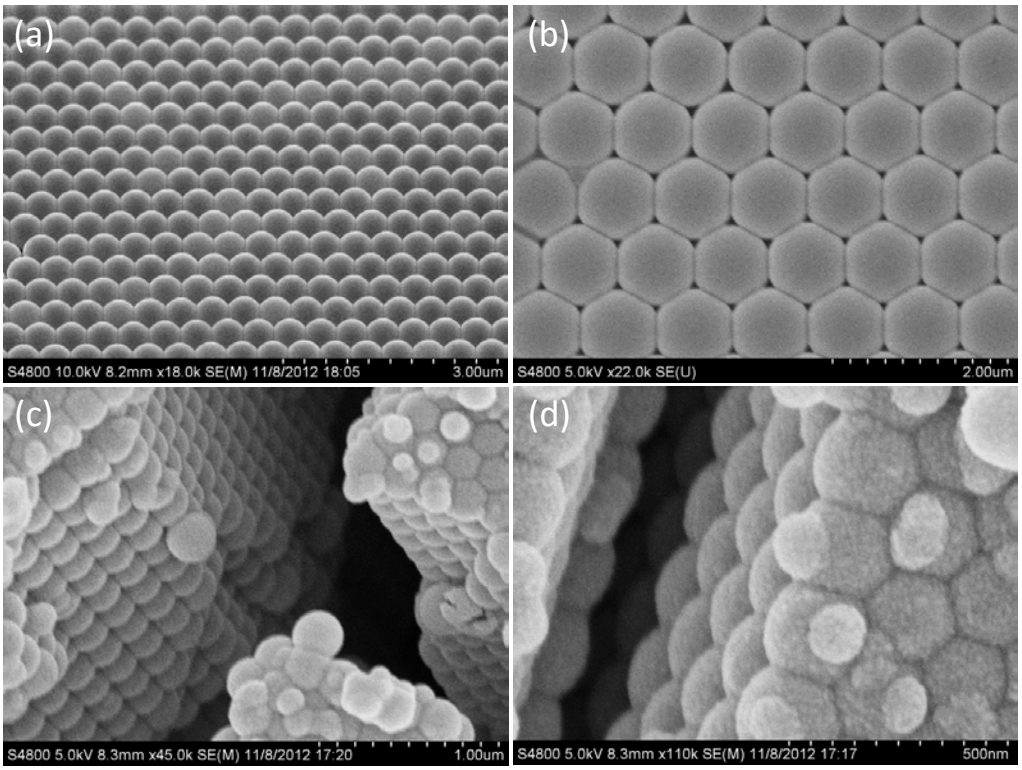

Figure 3-3| (a) The SEM images of the as-prepared three-dimensional colloidal crystal template vertically deposited by poly-styrene spheres. (b) The top view of colloidal crystal template coated with 10 repeat cycles of AZO. (c-d) The SEM images of the chapped area of colloidal crystal template deposited with 10 repeat cycles of AZO.

As described in section 2.1.4 and schematic illustrated in Figure 2-8d, after the ALD deposition of AZO on three-dimensional colloidal crystal template vertically deposited by poly-styrene spheres, the poly-styrene spheres were removed via thermal treatment to obtain the three-dimensional nanoporous structures. As displayed in Figure 3-4, after the high temperature thermal treatment at atmosphere condition, the regular appearance of the colloidal crystal template still maintained. Compering with the fresh ALD deposited colloidal crystal template, the surface of the template was smoother after thermal treatment. After the thermal treatment, the poly-styrene spheres were disappeared left the porous AZO shell. It is demonstrated by the chapped area and broken area SEM images shown in Figure 3-4b, c and d. From the SEM images in Figure 3-4 e and f, the poly-styrene spheres connected areas of the colloidal crystal template were not coated by AZO. After the removal of the poly-styrene spheres under high temperature thermal treatment, those areas were shown to be nanoporous. It means that each of the nanoporous AZO shell was not

isolated AZO shell. They were constructed into three-diemensional interconnected nanoporous AZO macroarchitecture.

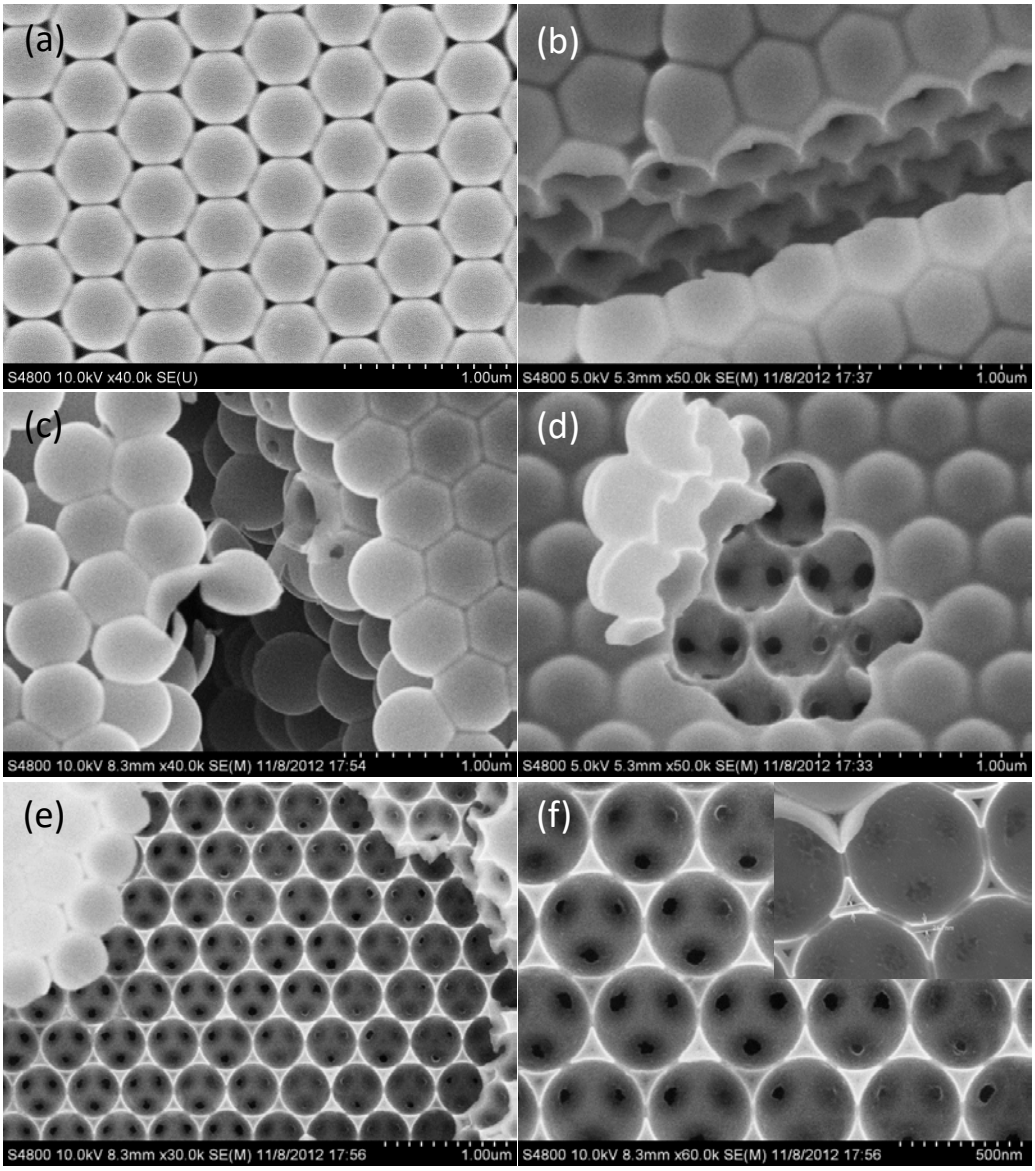

Figure 3-4| (a) The Top-view SEM image of the as-prepared three-dimensional colloidal crystal template deposited with AZO by ALD process after thermal removal of poly-styrene spheres. (b) The SEM image of the chapped area of sample in (a). (c-d) The SEM images of the broken area of sample in (a). (e-f) The SEM images of sample in (a) partly remove the top layer AZO film.

3.2.2. Chemical and structure information

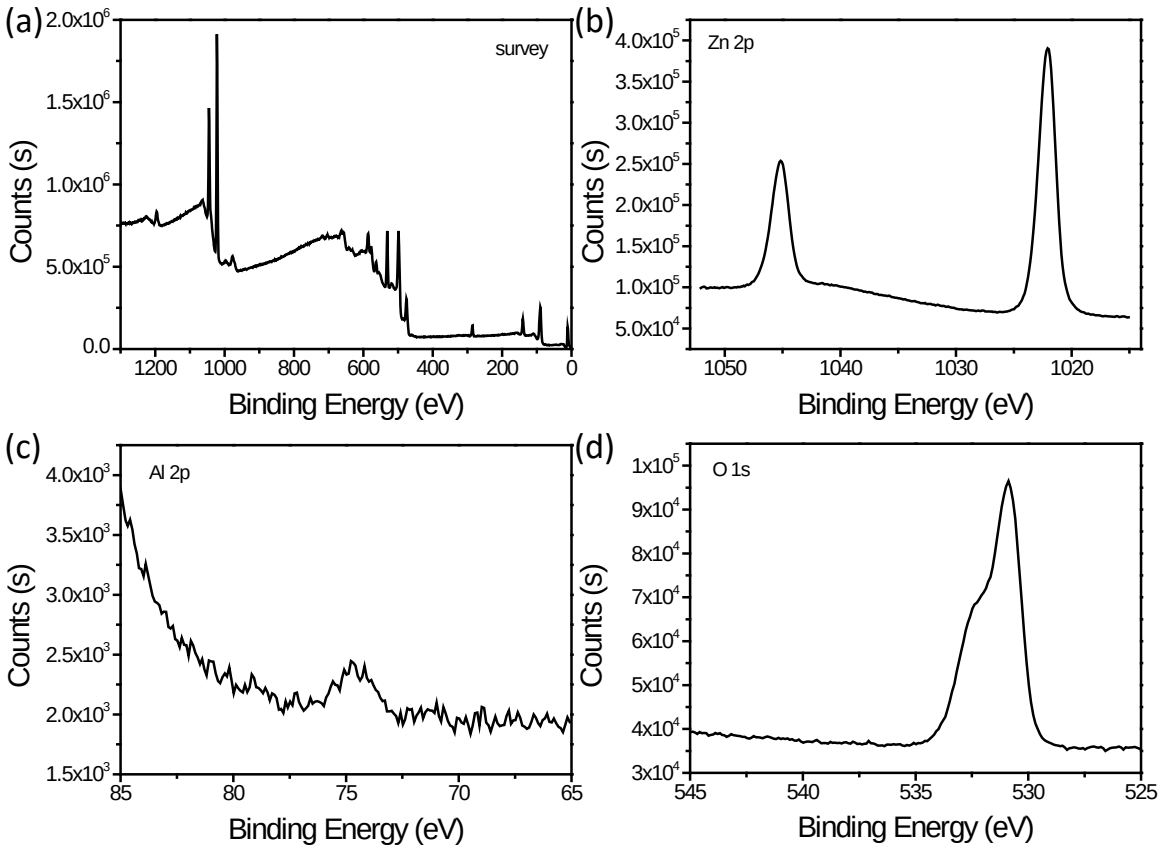

Figure 3-5| EDS spectra of AZO deposited on poly-styrene spheres constructed three-dimensional substrate: (a) Survey, (b) Zn 2p, (c) Al 2p and (d) O 1s.

The EDS spectra were used to investigate the elements information of the ALD deposited three-dimensional AZO nanostructures. To avoid the interference signal from AAO template, the EDS spectra were performed on AZO deposited on glass substrate. The results were shown in Figure 3-5. The peaks at 1045.15 eV and 1022.08 eV in Figure 3-5b spectra can be assigned to Zn $2p_{1/2}$ and Zn $2p_{3/2}$, respectively [30]. The signal present in Figure 3-5c has been fitted to AlOx. The O 1s signal in Figure 3-5d has been fitted to two components of 532.32 eV and 530.89 eV, which are associated with the Zn-O groups.

3.2.3. Electroconductivity Property

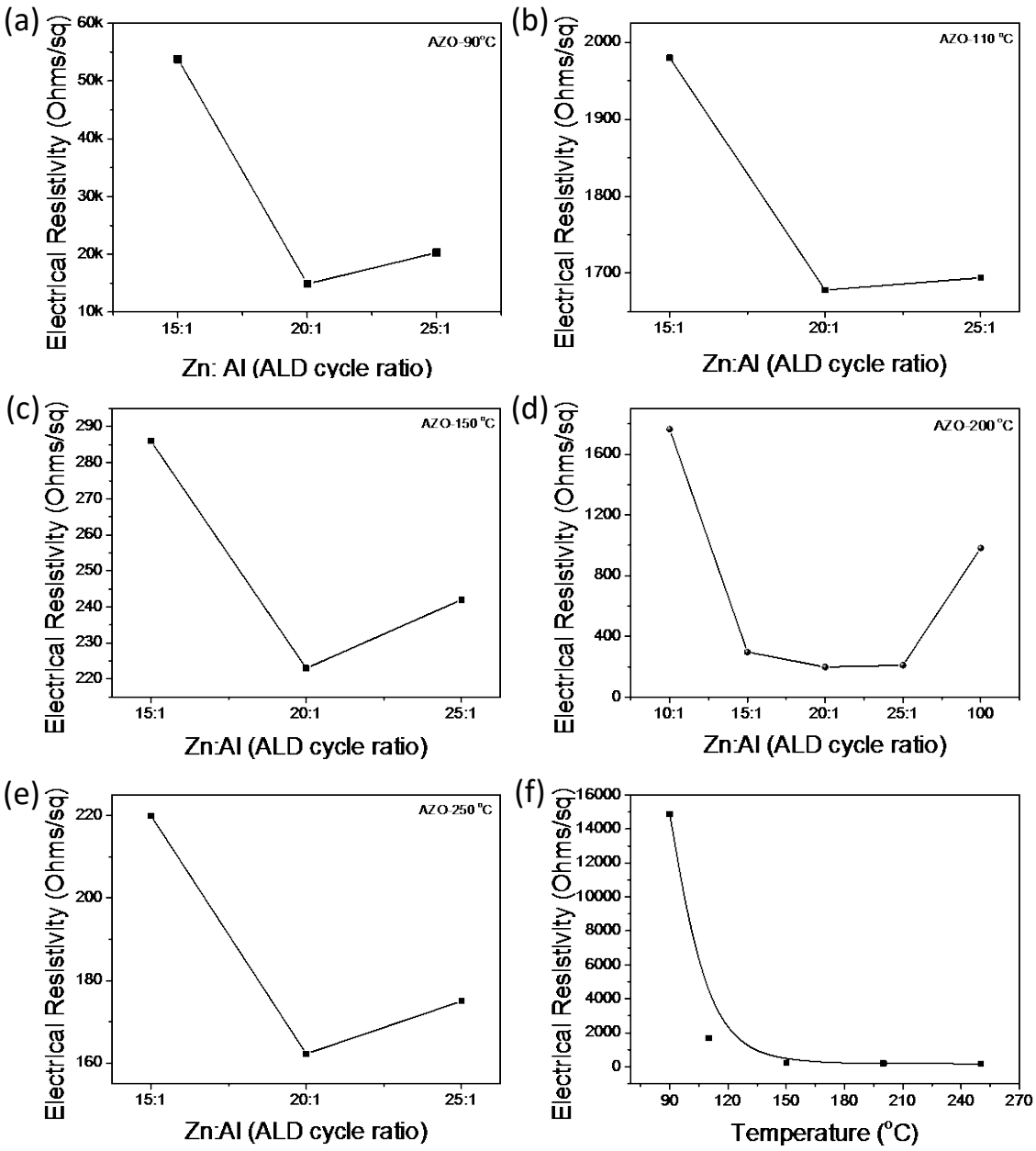

Figure 3-6| The electroconductivity of AZO deposited at different temperature: (a), (b), (c), (d) and (e) for 90 °C, 110 °C, 150 °C, 200 °C and 250 °C, respectively. (f) The electroconductivity of AZO deposited with different Zn to Al ratio at 200 °C.

The electroconductivity is the most important factors of AZO to be severed as an electrode instead of ITO. The electroconductivity of the prepared samples was investigated by four probe stage. The results were shown below in Figure 3-6. As shown in Figure 3-6a-e, at different deposition conditions, with the similar thickness of deposited AZO film, the electroconductivity of the prepared sample firstly increased with the increasing of Zn ALD

cycles. After the Zn ALD cycle ratio increased to 5 %, the electroconductivity of prepared samples started to decrease.

Meanwhile, as the data shown in Figure 3-6f, the electroconductivity of the AZO films with the similar thickness deposited at Zn to Al ALD cycle ratio 20 to 1 enhanced with the increasing of ALD deposition temperature. As shown in the data image, it is clear that when the temperature increased to 150 °C, the electroconductivity of deposited AZO obviously enhanced. After the temperature increased to more than 200 °C, the electroconductivity has a negligible increasing. Therefore, considering the price, the Zn to Al with ALD cycle ratio of 20 to 1, and the deposition temperature of 200 °C was selected as the AZO deposition condition in whole experiments.

3.2.4. Optical property

The AZO is fabricated to be served as the substitute of ITO transparent electrode in the new generation devices, especially the photoelectric devices. One of the other important factors of AZO is the transparency of the sample. The samples used for transparency investigation were prepared by deposition of AZO on quart glasses with the same growth condition as that on AAO and PS contracted three-dimensional substrates. And the transparency of the samples was investigated by UV-vis spectroscopy. As shown in Figure 3-7a-e, with the same thickness, the transparencies of AZO deposited at different condition were not the same. Even thought, all of the ALD deposited AZO samples had good transparent property in the visible light range. Comparing with the bare ZnO film, the samples deposited with Al have better transparency. As shown in Figure 3-7f, when the Zn to Al ALD cycle ratio fixed at 20 to 1, the AZO samples obtained at 150 °C, 200 °C and 250 °C had transmittances around 90 % during the visible light range.

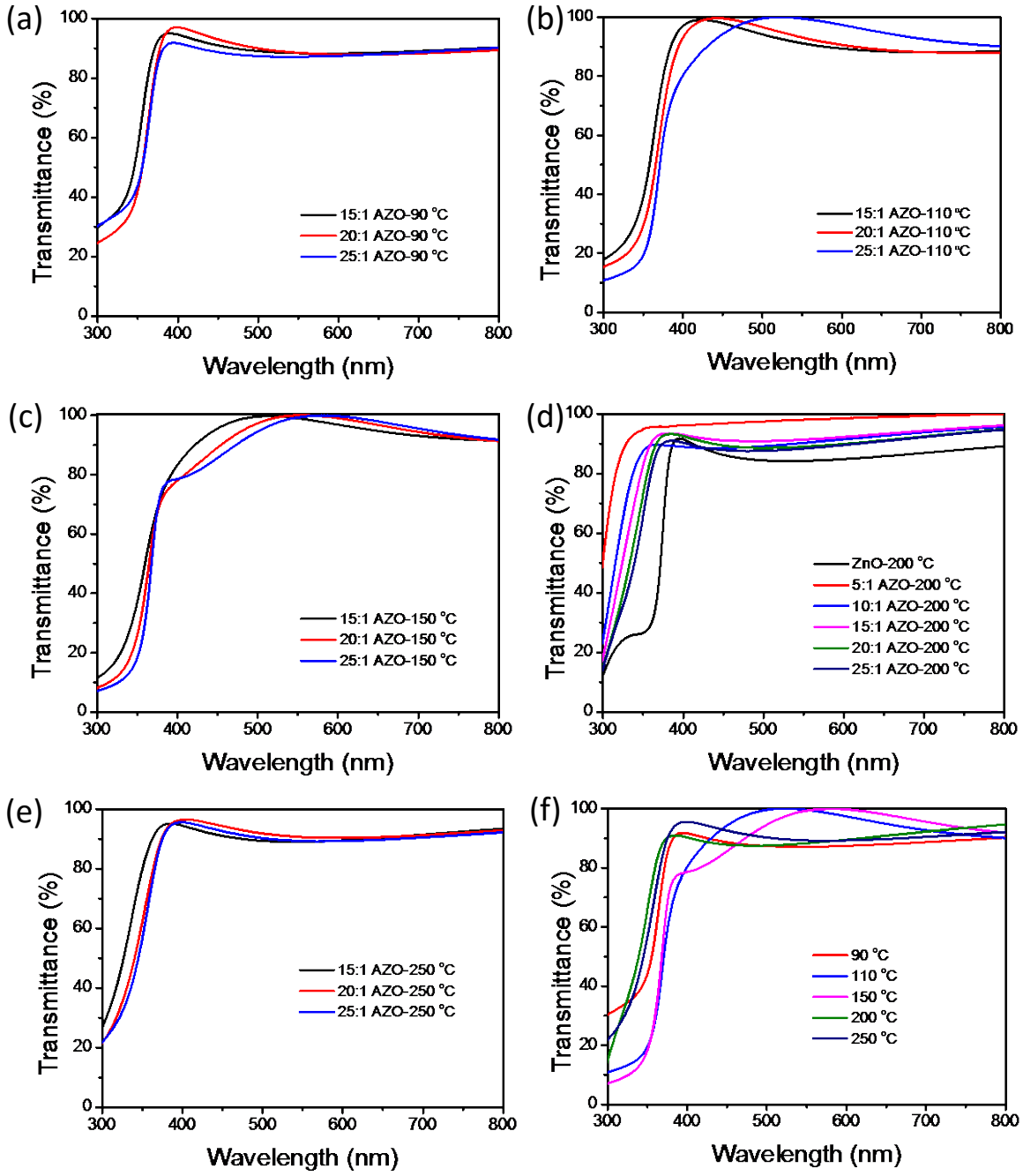

Figure 3-7| The transparency of AZO deposited at different temperature with different Zn to Al ALD cycle ratios: (a), (b), (c), (d) and (e) for 90 °C, 110 °C, 150 °C, 200 °C and 250 °C, respectively. (f) The transparency of AZO deposited with different Zn to Al ALD cycle ratio at 20 to 1 under 200 °C.

3.3. Conclusions

In summary, throughout this chapter, it has been shown that the three-dimensional AZO transparent electrode which could be served as the substitute for ITO can be achieved by ALD deposition technique. From the analyses, it could be found that the electroconductivity and transmittance of the AZO deposited by ALD could be controlled. In this chapter, the three-dimensional nanopore, nanocone and nanoporous architectures that fabricated from AAO and PS constructed template were used as substrates. The corresponding three dimensional AZO nanopore, nanocone and nanoporous architectures were obtained. And the obtained three-dimensional AZO architectures presented an electroconductivity as low as 165 ohms per sq, and a transmittance as high as 90 % during the visible light range. That is to say, the fabricated three-dimensional AZO architecture could be served as one of the substitutes for ITO as transparent electrode in the new generation device.

3.4. Bibliography

[1] H. Wu, D. Kong, Z. Ruan, P.-C. Hsu, S. Wang, Z. Yu, et al., A Transparent Electrode Based on a Metal Nanotrough Network, Nat Nano. 8 (2013) 421–425. http://dx.doi.org/10.1038/nnano.2013.84.

[2] X. Wang, L. Zhi, K. Müllen, Transparent, Conductive Graphene Electrodes for Dye-Sensitized Solar Cells, Nano Lett. 8 (2008) 323–327. doi:10.1021/nl072838r.

[3] H. Kang, S. Jung, S. Jeong, G. Kim, K. Lee, Polymer-metal Hybrid Transparent Electrodes for Flexible Electronics, Nat Commun. 6 (2015). http://dx.doi.org/10.1038/ncomms7503.

[4] P. Dong, Y. Zhu, J. Zhang, C. Peng, Z. Yan, L. Li, et al., Graphene on Metal Grids as the Transparent Conductive Material for Dye Sensitized Solar Cell, J. Phys. Chem. C. 118 (2014) 25863–25868. doi:10.1021/jp505735j.

[5] E.C.-W. Ou, L. Hu, G.C.R. Raymond, O.K. Soo, J. Pan, Z. Zheng, et al., Surface-Modified Nanotube Anodes for High Performance Organic Light-Emitting Diode, ACS Nano. 3 (2009) 2258–2264. doi:10.1021/nn900406n.

[6] J.-H. Chang, W.-H. Lin, P.-C. Wang, J.-I. Taur, T.-A. Ku, W.-T. Chen, et al., Solution-Processed Transparent Blue Organic Light-emitting Diodes with Graphene as the Top Cathode, Sci. Rep. 5 (2015) 9693. http://dx.doi.org/10.1038/srep09693.

[7] D.J. Lipomi, M. Vosgueritchian, B.C.-K. Tee, S.L. Hellstrom, J.A. Lee, C.H. Fox, et al.,

Skin-like Pressure and Strain Sensors Based on Transparent eElastic Films of Carbon Nanotubes, Nat Nano. 6 (2011) 788–792. http://dx.doi.org/10.1038/nnano.2011.184.

[8] J. Li, J. Liang, L. Li, F. Ren, W. Hu, J. Li, et al., Healable Capacitive Touch Screen Sensors Based on Transparent Composite Electrodes Comprising Silver Nanowires and a Furan/Maleimide Diels–Alder Cycloaddition Polymer, ACS Nano. 8 (2014) 12874–12882. doi:10.1021/nn506610p.

[9] A. Jakubec, V. Tvarozek, I. Novotny, V. Rehacek, V. Breternitz, C. Knedlik, et al., Characterization of Indium-Tin-Oxide Thin Film Microelectrodes for Biomedical Use, Materwiss. Werksttech. 34 (2003) 662–665. doi:10.1002/mawe.200390132.

[10] H.S. Jeong, H.-J. Jeon, Y.H. Kim, M.B. Oh, P. Kumar, S.-W. Kang, et al., Bifunctional ITO Layer with a High Resolution, Surface Nano-pattern for Alignment and Switching of LCs in Device Applications, NPG Asia Mater. 4 (2012) e7. http://dx.doi.org/10.1038/am.2012.12.

[11] W.P. Bolen, 2013 Minerals Yearbook - Salt, 2015. http://minerals.usgs.gov/minerals/pubs/commodity/myb/.

[12] A. Kumar, C. Zhou, The Race To Replace Tin-Doped Indium Oxide: Which Material Will Win?, ACS Nano. 4 (2010) 11–14. doi:10.1021/nn901903b.

[13] E.S. Ates, S. Kucukyildiz, H.E. Unalan, Zinc Oxide Nanowire Photodetectors with Single-Walled Carbon Nanotube Thin-Film Electrodes, ACS Appl. Mater. Interfaces. 4 (2012) 5142–5146. doi:10.1021/am301402y.

[14] D.S. Bhachu, G. Sankar, I.P. Parkin, Aerosol Assisted Chemical Vapor Deposition of Transparent Conductive Zinc Oxide Films, Chem. Mater. 24 (2012) 4704–4710. doi:10.1021/cm302913b.

[15] M. Vosgueritchian, D.J. Lipomi, Z. Bao, Highly Conductive and Transparent PEDOT:PSS Films with a Fluorosurfactant for Stretchable and Flexible Transparent Electrodes, Adv. Funct. Mater. 22 (2012) 421–428. doi:10.1002/adfm.201101775.

[16] J. Langecker, H. Ritter, A. Fichini, P. Rupper, M. Faller, B. Hanselmann, Ultrathin, Flexible, and Transparent Polymer Multilayer Composites for the Protection of Silver Surfaces, ACS Appl. Mater. Interfaces. 4 (2012) 619–627. doi:10.1021/am2015684.

[17] A. Wang, L. Jiang, X. Li, Y. Liu, X. Dong, L. Qu, et al., Mask-Free Patterning of High-Conductivity Metal Nanowires in Open Air by Spatially Modulated Femtosecond Laser Pulses, Adv. Mater. (2015) n/a–n/a. doi:10.1002/adma.201503289.

[18] K. Zilberberg, F. Gasse, R. Pagui, A. Polywka, A. Behrendt, S. Trost, et al., Highly Robust Indium-Free Transparent Conductive Electrodes Based on Composites of Silver Nanowires and Conductive Metal Oxides, Adv. Funct. Mater. 24 (2014) 1671–1678. doi:10.1002/adfm.201303108.

[19] J. Du, S. Pei, L. Ma, H.-M. Cheng, 25th Anniversary Article: Carbon Nanotube- and Graphene-Based Transparent Conductive Films for Optoelectronic Devices, Adv. Mater. 26 (2014) 1958–1991. doi:10.1002/adma.201304135.

[20] Q. Liu, T. Fujigaya, H.-M. Cheng, N. Nakashima, Free-Standing Highly Conductive Transparent Ultrathin Single-Walled Carbon Nanotube Films, J. Am. Chem. Soc. 132 (2010) 16581–16586. doi:10.1021/ja1067367.

[21] Y. Wu, X. Zhang, J. Jie, C. Xie, X. Zhang, B. Sun, et al., Graphene Transparent Conductive Electrodes for Highly Efficient Silicon Nanostructures-Based Hybrid Heterojunction Solar Cells, J. Phys. Chem. C. 117 (2013) 11968–11976. doi:10.1021/jp402529c.

[22] J. Wu, M. Agrawal, H.A. Becerril, Z. Bao, Z. Liu, Y. Chen, et al., Organic Light-Emitting Diodes on Solution-Processed Graphene Transparent Electrodes, ACS Nano. 4 (2010) 43–48. doi:10.1021/nn900728d.

[23] L.J. Brennan, M.T. Byrne, M. Bari, Y.K. Gun'ko, Carbon Nanomaterials for Dye-Sensitized Solar Cell Applications: A Bright Future, Adv. Energy Mater. 1 (2011) 472–485. doi:10.1002/aenm.201100136.

[24] F.S. Gittleson, D. Hwang, W.-H. Ryu, S.M. Hashmi, J. Hwang, T. Goh, et al., Ultrathin Nanotube/Nanowire Electrodes by Spin–Spray Layer-by-Layer Assembly: A Concept for Transparent Energy Storage, ACS Nano. (2015). doi:10.1021/acsnano.5b03578.

[25] K. V Rajani, S. Daniels, P.J. McNally, F.O. Lucas, M.M. Alam, Ultrathin Chromium Transparent Metal Contacts by Pulsed dc Magnetron Sputtering, Phys. Status Solidi. 207 (2010) 1586–1589. doi:10.1002/pssa.200983732.

[26] M. Maragkou, Transparent electrodes: Fractal Future, Nat Phot. 8 (2014) 817. http://dx.doi.org/10.1038/nphoton.2014.257.

[27] A. Paracchino, V. Laporte, K. Sivula, M. Grätzel, E. Thimsen, Highly Active Oxide Photocathode for Photoelectrochemical Water Reduction, Nat Mater. 10 (2011) 456–461. http://dx.doi.org/10.1038/nmat3017.

[28] A.K. Pradhan, R.M. Mundle, K. Santiago, J.R. Skuza, B. Xiao, K.D. Song, et al., Extreme

Tunability in Aluminum Doped Zinc Oxide Plasmonic Materials for Near-infrared Applications, Sci. Rep. 4 (2014) 6415. http://dx.doi.org/10.1038/srep06415.

[29] N. Zhang, X. Wang, Z. Ye, Y. Jin, A Quantitative Study of Chemical Kinetics for The Synthesis of Doped Oxide Nanocrystals Using FTIR, Sci. Rep. 4 (2014) 4353. http://dx.doi.org/10.1038/srep04353.

[30] R. Buonsanti, A. Llordes, S. Aloni, B.A. Helms, D.J. Milliron, Tunable Infrared Absorption and Visible Transparency of Colloidal Aluminum-Doped Zinc Oxide Nanocrystals, Nano Lett. 11 (2011) 4706–4710. doi:10.1021/nl203030f.

[31] J. Nishino, S. Ohshio, K. Kamata, Preparation of Aluminum-Doped Zinc Oxide Films by a Normal-Pressure CVD Method, J. Am. Ceram. Soc. 75 (1992) 3469–3472. doi:10.1111/j.1151-2916.1992.tb04452.x.

[32] J. Hu, R.G. Gordon, Textured Aluminum-doped Zinc Oxide Thin Films from Atmospheric Pressure Chemical-vapor Deposition, J. Appl. Phys. 71 (1992) 880–890. doi:10.1063/1.351309.

[33] M. Ruth, J. Tuttle, J. Goral, R. Noufi, Aluminum Doped Zinc Oxide Thin Films Deposited by Ion Beam Sputtering, J. Cryst. Growth. 96 (1989) 363–368. doi:http://dx.doi.org/10.1016/0022-0248(89)90534-4.

[34] A. Kuroyanagi, Properties of Aluminum-Doped ZnO Thin Films Grown by Electron Beam Evaporation, Jpn. J. Appl. Phys. 28 (1989) 219. http://stacks.iop.org/1347-4065/28/i=2R/a=219.

[35] Y. Liu, L. Zhao, J. Lian, Al-doped ZnO Films by Pulsed Laser Deposition at Room Temperature, Vacuum. 81 (2006) 18–21. doi:http://dx.doi.org/10.1016/j.vacuum.2006.02.001.

[36] Y. Liu, Q. Li, H. Shao, Optical and Photoluminescent Properties of Al-doped Zinc Oxide Thin Films by Pulsed Laser Deposition, J. Alloys Compd. 485 (2009) 529–531. doi:http://dx.doi.org/10.1016/j.jallcom.2009.06.019.

[37] Z.-C. Jin, I. Hamberg, C.G. Granqvist, Optical Properties of Sputter-deposited ZnO:Al Thin Films, J. Appl. Phys. 64 (1988) 5117. doi:10.1063/1.342419.

[38] M. Van Gompel, B. Conings, K.L. Jiménez Monroy, J. D'Haen, K. Gilissen, M. D'Olieslaeger, et al., Preparation of Epitaxial Films of the Transparent Conductive oxide Al:ZnO by Reactive High-pressure Sputtering in Ar/O_2 Mixtures, Phys. Status Solidi. 210 (2013) 1013–1018. doi:10.1002/pssa.201200986.

[39] D.G. and P.S. and B.M. and M.T. and V. Bhide, Deposition of Aluminum-Doped Zinc Oxide Thin Films by Spray Pyrolysis, Jpn. J. Appl. Phys. 31 (1992) 361. http://stacks.iop.org/1347-4065/31/i=2R/a=361.

[40] S. Rahmane, M.S. Aïda, A. Chala, H. Ben Temam, A. Djouadi, Elaboration of Transparent Undoped ZnO and Al-Doped ZnO Thin Films by Spray Pyrolysis and their Properties, Plasma Process. Polym. 4 (2007) S356–S358. doi:10.1002/ppap.200730908.

[41] H. Hagendorfer, K. Lienau, S. Nishiwaki, C.M. Fella, L. Kranz, A.R. Uhl, et al., Highly Transparent and Conductive ZnO: Al Thin Films from a Low Temperature Aqueous Solution Approach, Adv. Mater. 26 (2014) 632–636. doi:10.1002/adma.201303186.

[42] M. Ohyama, H. Kozuka, T. Yoko, Sol-Gel Preparation of Transparent and Conductive Aluminum-Doped Zinc Oxide Films with Highly Preferential Crystal Orientation, J. Am. Ceram. Soc. 81 (1998) 1622–1632. doi:10.1111/j.1151-2916.1998.tb02524.x.

[43] A.M. Schwartzberg, D. Olynick, Complex Materials by Atomic Layer Deposition, Adv. Mater. 27 (2015) 5778–5784. doi:10.1002/adma.201500699.

[44] C.R. Ellinger, S.F. Nelson, Selective Area Spatial Atomic Layer Deposition of ZnO, Al_2O_3, and Aluminum-Doped ZnO Using Poly(vinyl pyrrolidone), Chem. Mater. 26 (2014) 1514–1522. doi:10.1021/cm402464z.

[45] B.H. Kong, M.K. Choi, H.K. Cho, J.H. Kim, S. Baek, J.-H. Lee, Conformal Coating of Conductive ZnO:Al Films as Transparent Electrodes on High Aspect Ratio Si Microrods, Electrochem. Solid-State Lett. 13 (2010) K12. doi:10.1149/1.3267051.

[46] A. Illiberi, R. Scherpenborg, Y. Wu, F. Roozeboom, P. Poodt, Spatial Atmospheric Atomic Layer Deposition of AlxZn1–xO, ACS Appl. Mater. Interfaces. 5 (2013) 13124–13128. doi:10.1021/am404137e.

[47] L. Rovelli, S.D. Tilley, K. Sivula, Optimization and Stabilization of Electrodeposited Cu2ZnSnS4 Photocathodes for Solar Water Reduction, ACS Appl. Mater. Interfaces. 5 (2013) 8018–8024. doi:10.1021/am402096r.

[48] N.P. Dasgupta, S. Neubert, W. Lee, O. Trejo, J.-R. Lee, F.B. Prinz, Atomic Layer Deposition of Al-doped ZnO Films: Effect of Grain Orientation on Conductivity, Chem. Mater. 22 (2010) 4769–4775. doi:10.1021/cm101227h.

[49] D.-J. Lee, H.-M. Kim, J.-Y. Kwon, H. Choi, S.-H. Kim, K.-B. Kim, Structural and Electrical Properties of Atomic Layer Deposited Al-Doped ZnO Films, Adv. Funct. Mater. 21 (2011) 448–455. doi:10.1002/adfm.201001342.

[50] G. Luka, B.S. Witkowski, L. Wachnicki, R. Jakiela, I.S. Virt, M. Andrzejczuk, et al., Electrical and Mechanical Stability of Aluminum-doped ZnO Films Grown on Flexible Substrates by Atomic Layer Deposition, Mater. Sci. Eng. B. 186 (2014) 15–20. doi:http://dx.doi.org/10.1016/j.mseb.2014.03.002.

[51] T. Dhakal, A.S. Nandur, R. Christian, P. Vasekar, S. Desu, C. Westgate, et al., Transmittance from Visible to Mid Infra-red in AZO Films Grown by Atomic Layer Deposition System, Sol. Energy. 86 (2012) 1306–1312. doi:http://dx.doi.org/10.1016/j.solener.2012.01.022.

[52] X. Qian, Y. Cao, B. Guo, H. Zhai, A. Li, Atomic Layer Deposition of Al-doped ZnO Films Using Aluminum Isopropoxide as the Al Precursor, Chem. Vap. Depos. 19 (2013) 180–185. doi:10.1002/cvde.201207051.

[53] J.W. Elam, D. Routkevitch, P.P. Mardilovich, S.M. George, Conformal Coating on Ultrahigh-Aspect-Ratio Nanopores of Anodic Alumina by Atomic Layer Deposition, Chem. Mater. 15 (2003) 3507–3517. doi:10.1021/cm0303080.

[54] X. Chen, E. Pomerantseva, P. Banerjee, K. Gregorczyk, R. Ghodssi, G. Rubloff, Ozone-Based Atomic Layer Deposition of Crystalline V_2O_5 Films for High Performance Electrochemical Energy Storage, Chem. Mater. 24 (2012) 1255–1261. doi:10.1021/cm202901z.

[55] A. Rugge, J.S. Becker, R.G. Gordon, S.H. Tolbert, Tungsten Nitride Inverse Opals by Atomic Layer Deposition, Nano Lett. 3 (2003) 1293–1297. doi:10.1021/nl034362r.

[56] L. Wen, Y. Mi, C. Wang, Y. Fang, F. Grote, H. Zhao, et al., Cost-effective Atomic Layer Deposition Synthesis of Pt Nanotube Arrays: Application for High Performance Supercapacitor, Small. 10 (2014) 3162–3168. doi:10.1002/smll.201400436.

[57] Y.-J. Choi, S.C. Gong, C.-S. Park, H.-S. Lee, J.G. Jang, H.J. Chang, et al., Improved Performance of Organic Light-Emitting Diodes Fabricated on Al-Doped ZnO Anodes Incorporating a Homogeneous Al-Doped ZnO Buffer Layer Grown by Atomic Layer Deposition, ACS Appl. Mater. Interfaces. 5 (2013) 3650–3655. doi:10.1021/am400140c.

4. Construction of three-dimensional core/shell AZO/TiO_2/Au nanocone array based on atomic layer deposition for enhancing photoelectrochemcial water splitting

4.1. Introduction

By converting sunlight to fuel-hydrogen, photoelectrochemcial (PEC) water splitting has been proven to be one of the most effective approaches to utilize the unlimited solar energy economically and environmentally [1–4] Considering the broad spectrum of solar radiations, a key point for PEC water splitting is to explore photoelectrode materials with a high-efficient solar light utilization. Since the pioneering work demonstrated by Fujishima and Honda in 1972, TiO_2 has been extensively investigated as a photoanode material, attributing to its advantages of high photochemical stability, cost effectiveness and non-toxicity [5–10]. However, in view of the large band gap (3.2 eV for anatase and 3.0 eV for rutile), low electron mobility (1 $cm^2 V^{-1} s^{-1}$) and short minority carrier (hole) diffusion length (10-100 nm) of TiO_2, its practical application for PEC is restricted [10]. Thus, many efforts have been devoted to address this issue [11–13].

In particular, owning to the significant capability of decoupling light absorption and charge carrier collection, and shortening minority carrier diffusion distance compared to bulk structures, one-dimensional nanostructures (e.g., nanorod [13,14] nanowire [7,15] and nanotube [6,16,17]) of TiO_2 have been intensively studied. Additionally, rational construction of complex hierarchical TiO_2 nanostructures, such as branched nanowire array [18–20] and nanotube photonic crystal [21], can further increase the light absorption efficiency and contact surface areas, thus enhances the PEC performance accordingly. Although the TiO_2 nanostructuring could efficiently transfer the holes at the TiO_2/electrolyte interface via diffusing across the axial direction of the nanostructures, the low mobility of electrons in TiO_2 is still an obstacle because they must transport along the radial direction to reach to the current collector [18] As previously demonstrated, core/shell nanostructures, in which the core acts as a conductive path, could be an excellent candidate to facilitate the electrons separation and transportation simultaneously in the axial direction [22–26]. Furthermore, in order to promote the solar light utilization of the TiO_2-based core/shell nanostructures,

introducing surface plasmon resonance (SPR) of Au nanoparticles (NPs) is a promising approach, ascribing to the advantages of its visible light absorption and good stability [27–32] However, most of the existing TiO_2-based core/shell nanostructures require complex multi-step fabrication processes and the structure could only be roughly adjusted, which make it difficult to quantitatively optimize the charge carrier collection [33]. Meanwhile, although the Au NPs have been introduced into TiO_2 nanostructures by a few attempts [17,34,35], the poor management of the Au NPs distribution over the TiO_2 surfaces is unfavorable for the efficient utilization of the SPR effect. Therefore, it is highly desirable to explore a strategy, which is capable of achieving TiO_2-based core/shell nanostructures with precise structure and composition tuning to maximize the light harvesting and charge carrier collection.

In this regard, we propose a feasible route to realize a well-defined regular array of Al doped ZnO /TiO_2 core/shell nanocones arrays (AZO/TiO_2 NCA) with surface coating of uniformly dispersed Au NPs (AZO/TiO_2/Au NCA). The structure and composition of the AZO/TiO_2/Au NCA can be modulated to maximize the solar light utilization, such as the height of the Al nanocone array (Al NCA), the conductive of the AZO core, the thickness of TiO_2 shell, and the size and density of the Au NPs. Therefore, the probable paths that the charge carriers could be effectively collected in the AZO/TiO_2/Au NCA should include the charge carriers generated inside the diffusion layer and the depletion layer of TiO_2, as well as the hot-carrier injected from the Au NPs to TiO_2. The photocurrent density of the AZO/TiO_2/Au NCA electrode reaches up to 1.1 mA·cm^{-2} at 1.23 V versus reversible hydrogen electrode (RHE) in neutral environment, which is five times of that from flat AZO/TiO_2 electrode (0.22 mA·cm^{-2}). Meanwhile, the photoconversion of the AZO/TiO_2/Au NCA electrode approaches to 0.72 % at 0.21 V versus RHE, which is one of the highest values with the lowest external potential that ever reported in Au/TiO_2 photoelectrochemical systems. The promising strategy demonstrated here shall be easily to be extended in other metal/semiconductor composites for optimizing the performance of the PEC electrodes.

4.2. Results and discussion

4.2.1. Morphology and structure analysis for the three-dimensional core/shell AZO/TiO_2/Au nanocone array

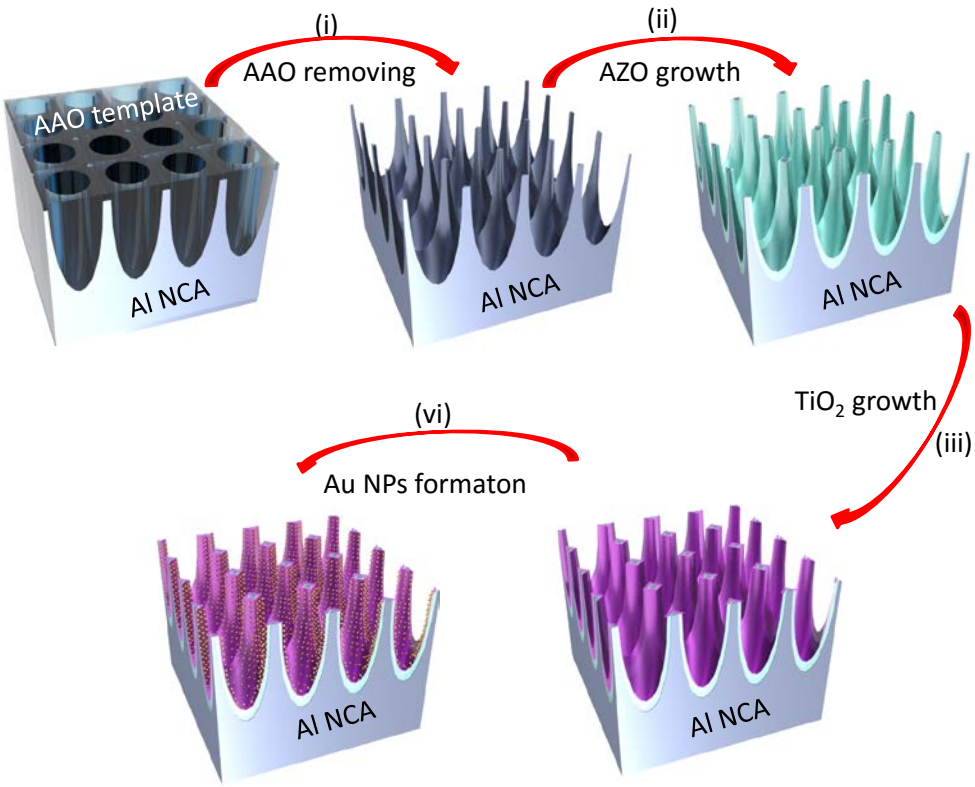

Figure 4-1| Schematic diagram of the procedure for realizing the AZO/TiO_2/Au NCA. From regular nano-porous AAO templates (step i) to aluminum nanocone arrays, and to AZO nanocone arrays by ALD of Al doped ZnO (step ii), and further to AZO/TiO_2 nanocone arrays by conformal ALD deposition of TiO_2 on bare AZO nanocone arrays (step iii). Finally, different thickness of Au film was deposited on the surface of AZO/TiO_2 nanocone arrays by physic vapor deposition process (step vi).

Figure 4-1 illustrates the fabrication process from regular nano-porous AAO templates (step i) to aluminum nanocone arrays, and to AZO nanocone arrays by ALD of Al doped ZnO (step ii), and further to AZO/TiO_2 nanocone arrays by conformal ALD deposition of TiO_2 on bare AZO nanocone arrays (step iii). Finally, different thickness of Au film was deposited on the surface of AZO/TiO_2 nanocone arrays by physic vapor deposition process (step vi). The proposed synthesis strategy facilitates the fabrication of Al nanocone arrays by selective anodization and precisely controlled AAO template etching. It was systematically described in section 2.1.2.2.

In this chapter, the results of the fabricated 3D core/shell AZO/TiO_2/Au nanocone arrays with the help of nanocone arrays Al template by ALD are systematically studied with reference to their morphologies as well as the structures of the 3D nanostructured PEC electrode. The morphology and structure information of the as fabricated 3D TiO_2/AZO NCA nanostructure and modified with Au NPs on the surface of 3D TiO_2/AZO NCA nanostructure were investigated by SEM and TEM.

4.2.1.1. Al nanocone array template

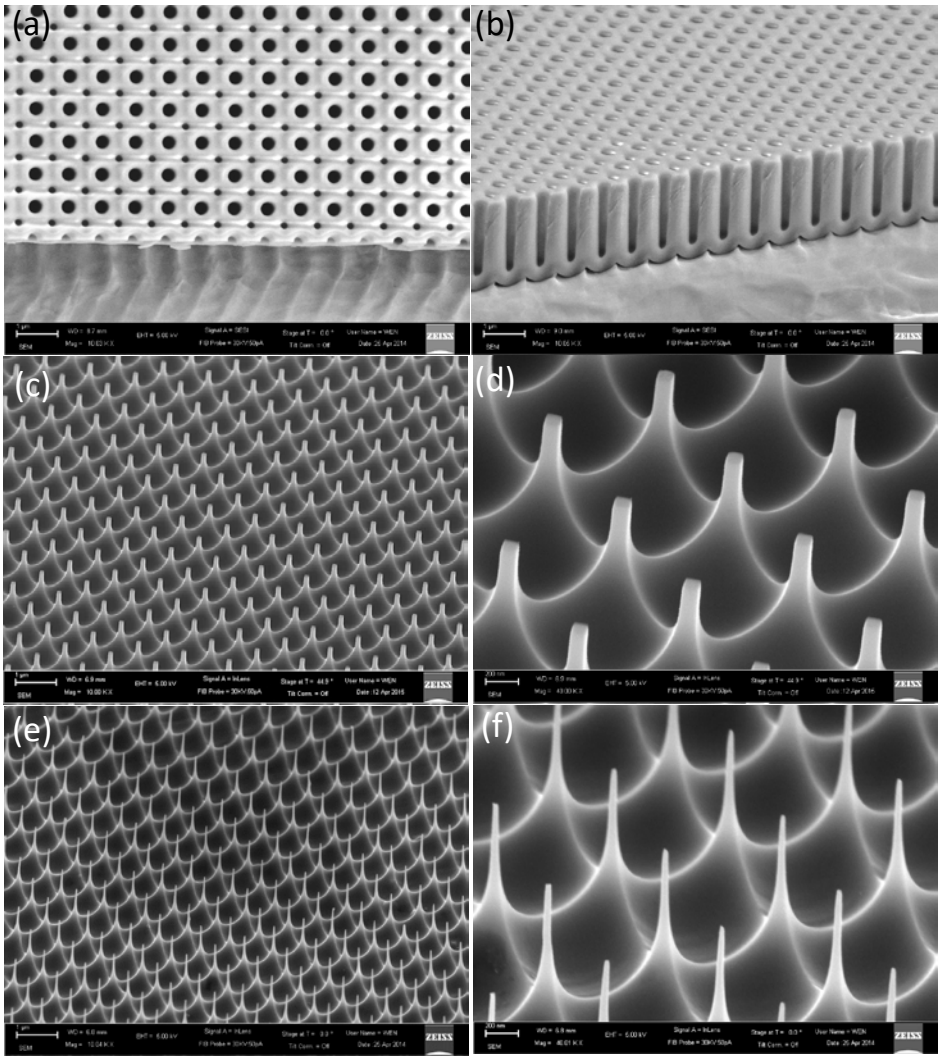

Figure 4-2| (a) Top view and (b) side-view SEM images of AAO template obtained at 320 V. (c) (d) the enlarged magnification SEM image of Figure c. (e) SEM image of Al nanocone

obtained after chemical etching the Al_2O_3 nanopore which anodized at 320 V for 14 hours, (d) the enlarged magnification SEM image of Figure e.

The morphology of obtained Al nanocone arrays is investigated and presented in Figure 4-2. As the SEM images shown in Figure 4-2a and b, the AAO template obtained at 320 V anodization has a spacing distance of 800 nm, and nanopore with a diameter of around 300 nm. After the wet-chemical etching by the mixture of chromium acid (1.5 wt %) and phosphoric acid (6 wt %) solution at 60 °C for 10 h, the anodized Al_2O_3 nanopores are disappeared, left nanocone arrays on Al substrate. The height of the Al nanocone could be adjusted by changing the time of anodization process. As shown in Figure 4-2c-d, with different anodization time, the nanocones present different heights.

4.2.1.2. AZO nanocone array

As intensively discussed in chapter 3, AZO electrode has been considerably developed due to its abundance in natural resources, easy production procedure, low cost, non-toxicity, high thermal stability and chemical stability [36–38]. It is extensively researched and presented as transparent electrode in PEC cells and solar cells. The AZO nanocone arrays transparent electrode is prepared by ALD deposition on Al nanocone arrays template as described in section 2.1.2.2. An optimized ALD process is used for AZO deposition at 200 °C and one typical growth cycle consists of: DEZ-N_2 purge-H_2O-N_2 purge (20 cycle ZnO)-TMA-N_2 purge-H_2O-N_2 purge. The growth rate of ZnO and Al_2O_3 is about 1.0 nm per cycle.

The morphology of the sample was investigated by SEM and presented in Figure 4-3. The AZO nanocone with a height of more than 800 nm, and a thickness of around 100 nm could be measured. The thickness of AZO could be easily adjusted by the change of the ALD growth cycle numbers.

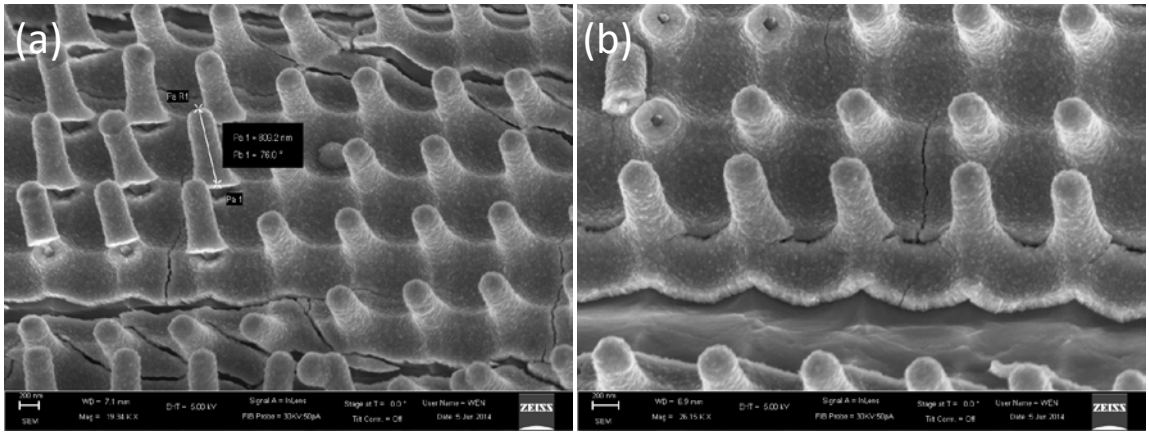

Figure 4-3| (a) Side-view and (d) Enlarged magnification side-view SEM images of bended AZO nanocone array.

4.2.1.3. Core/shell AZO/TiO_2 nanocone array

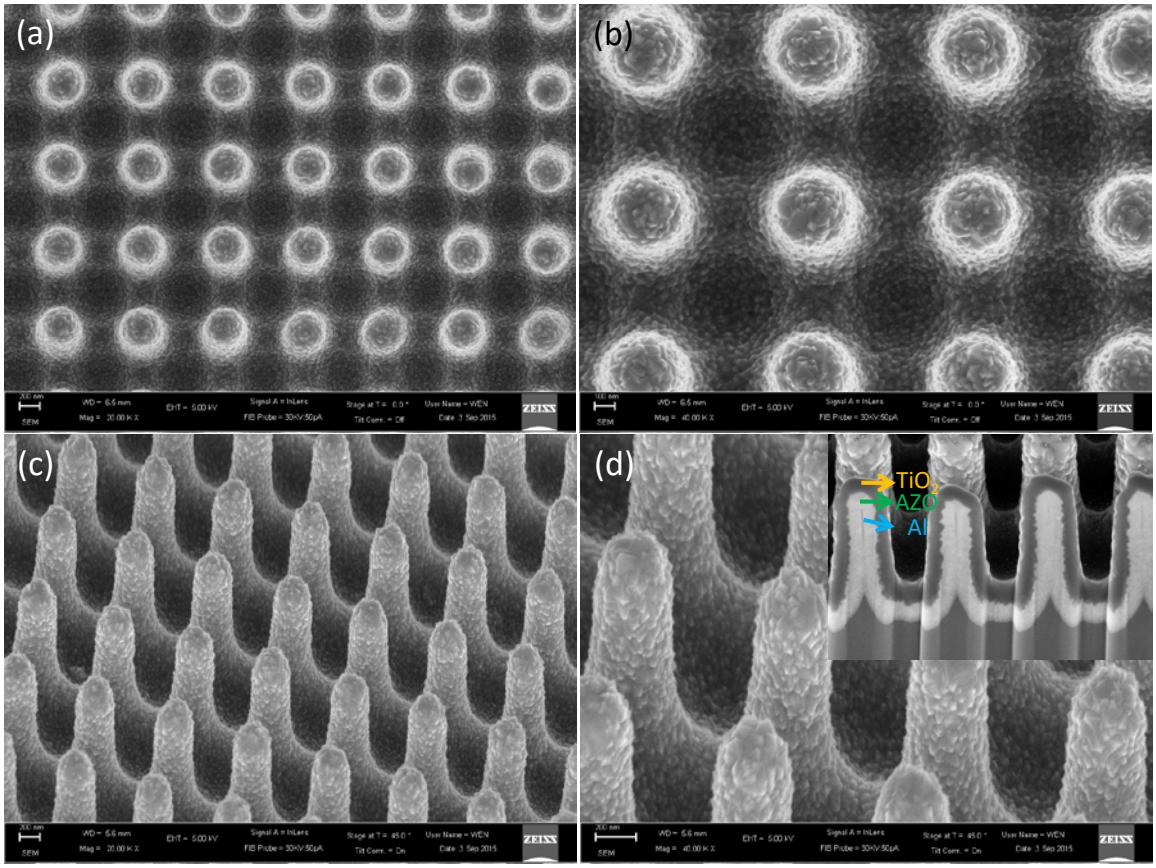

Figure 4-4| (a) Top-view SEM image of TiO_2/AZO NCA; (b) Enlarge magnification SEM image of (a). (c) Side-view SEM image of TiO_2/AZO NCA; (d) Enlarge magnification SEM image of (c), inset in Figure (d) is the cross-section SEM image of TiO_2/AZO NCA.

After the fabrication of 3D transparent electrode, the photocurrent response material TiO_2 was grew on the electrode by ALD. The TiO_2 deposition was carried out at 300°C and one typical cycle consists of: $TiCl_4$-N_2 purge-H_2O-N_2 purge (1 cycle). The growth rate of TiO_2 is about 0.6 nm per cycle. The morphology and structure information after the growth of TiO_2 on AZO NCA nanostructure were determined by SEM, as shown in Figure 4-4. From Figure 4-4a and the enlarge-magnification SEM image (Figure 4-4b), the side-view (Figure 4-4c) and corresponding enlarge magnification SEM images (Figure 4-4d), it can be seen that the TiO_2 film coat on the whole surface of 3D AZO NCA with a uniform thickness distribution. The cross-section SEM image of 3D TiO_2/AZO NCA which obtains by Ga ion beam cut the 3D TiO_2/AZO NCA is shown in the inset image of Figure 4-4d. It is clearly present the core-shell structure of nanocone, and the uniform thickness of ALD growth AZO and TiO_2 films on the Al cone.

4.2.1.4. Three-dimensional core/shell AZO/TiO_2/Au nanocone array

The large band gap of TiO_2 only has the light absorption property during UV light range. Thus, the Au NPs that could induce the visible light absorption via the SPR of Au NPs was introduced on the surface of 3D TiO_2/AZO NCA electrode to increase the light absorption and utilization. Accordingly increase the photocurrent response of bare TiO_2 electrode. After the deposition of Au film by PVD and the subsequent annealing treatment at 350 °C for 10 min with a heating rate of 2 °C per minute and then naturally cooling down to room temperature, the morphology and structure information of the decoration of Au nanoparticles on 3D TiO_2/AZO NCA nanostructure were determined by SEM and TEM, as shown in Figure 4-5 and Figure 4-7, respectively.

As can be seen in Figure 4-5a, and the step by step enlargement magnification SEM images in Figure 4-5b and c, the Au nanoparticles decorated on 3D TiO_2/AZO NCA nanostructure have a uniform size distribution on the whole 3D surface. The uniformity Au nanoparticles well-distributed decorated on the top and bottom surfaces of the nanocone, as well as on the side surface of nanocone (Figure 4-5d).

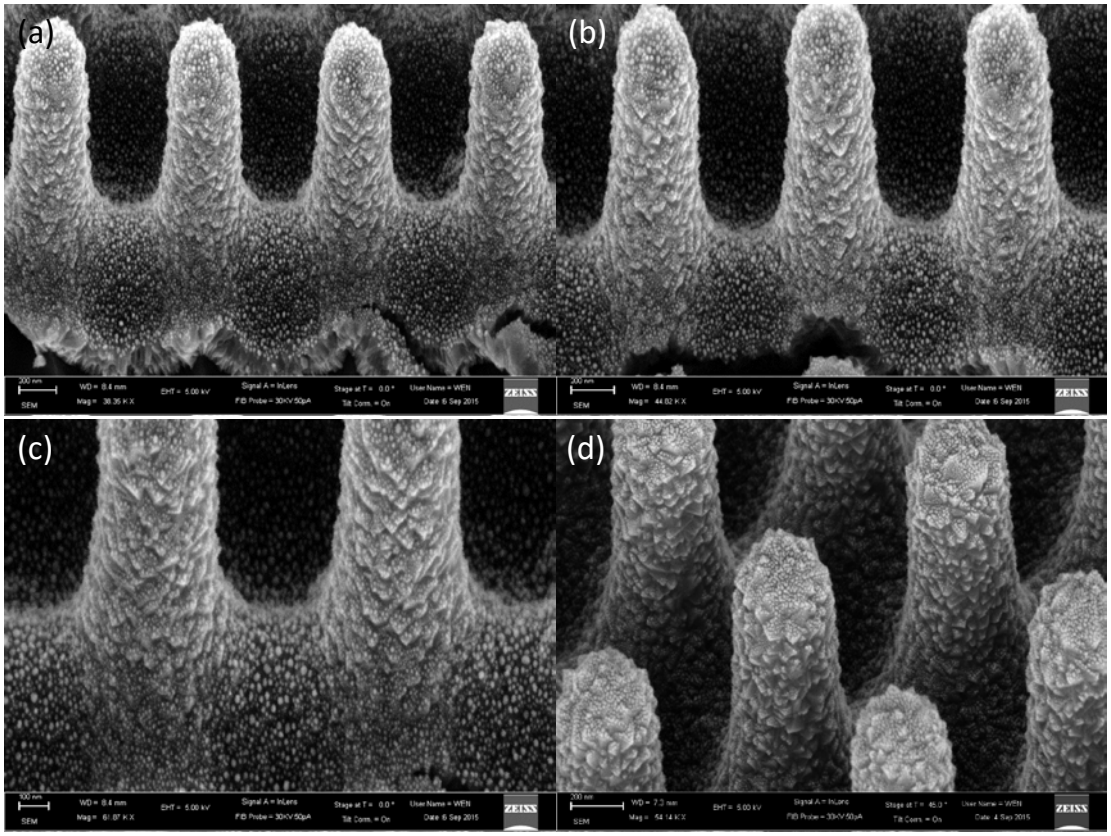

Figure 4-5| (a) Side-view SEM image of bended Au/TiO_2/AZO NCA, (b-c) the corresponding enlarge magnification SEM images, (d) Side-view SEM image of bended Au/TiO_2/AZO NCA with a rotation angle.

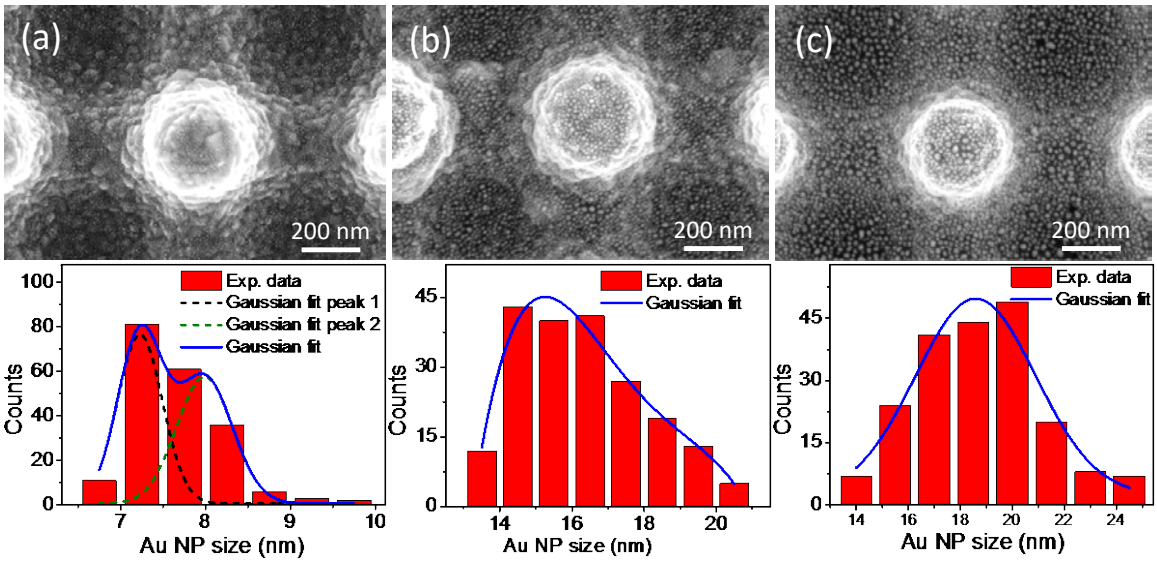

Figure 4-6| The SEM images and particle size distribution of deposition Au on the surface of TiO_2/AZO NCA after annealing process; (a) 2 nm, (b) 5 nm and (c) 10 nm Au film, respectively.

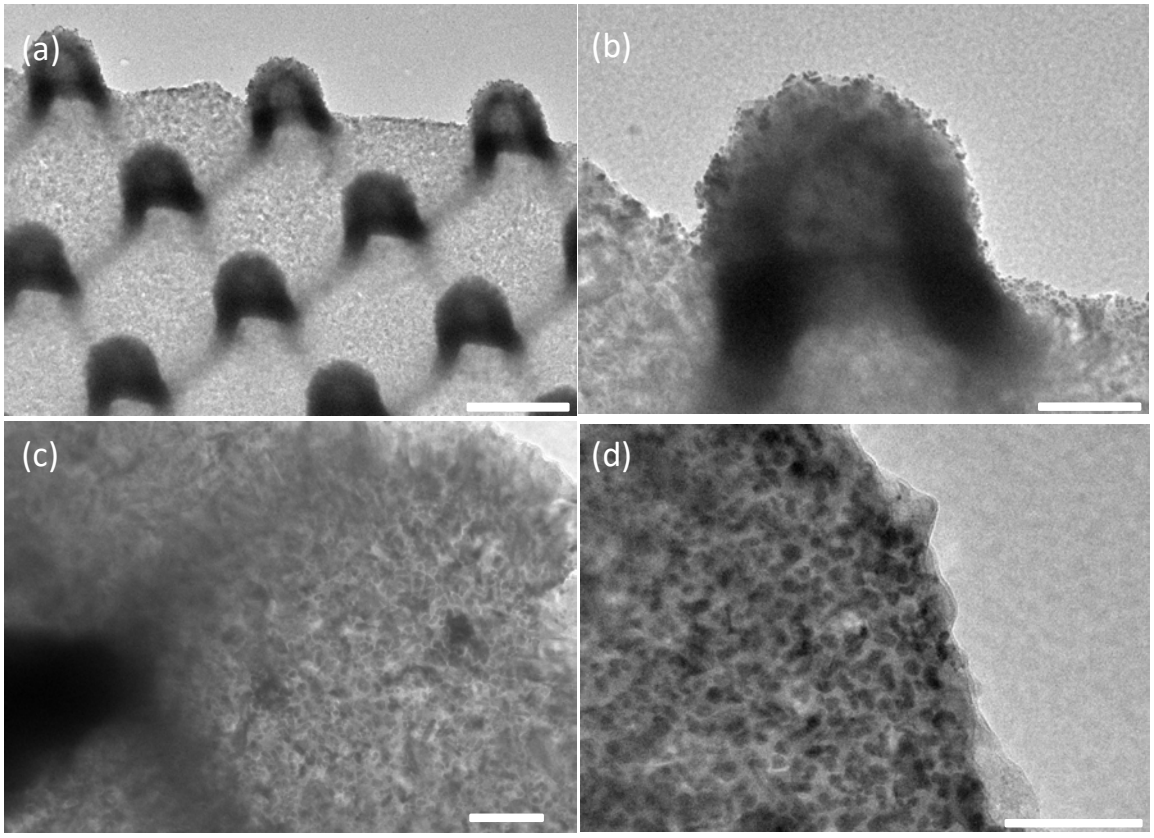

Figure 4-7| TEM images of Au/TiO_2 NCA, the scale bar are 500, 200, 100 and 100 nm for a, b, c and d, respectively. (a) The distribution of Au nanoparticles on the curved surface of TiO_2 nanocone, (d) the corresponding enlargement SEM image of (a). (c) The distribution of Au nanoparticles on the flat surface of TiO_2 NCA, (d) the corresponding enlargement SEM image of (c).

In order to adjust the parameter of the Au NPs and the resultant SPR effect, different thickness of Au film is intentionally evaporated on AZO/TiO_2 NCA surface, followed by the annealing treatment. The film-to-particles evolution is largely attributed to thermally activated Ostwald ripening process that larger particles will consume smaller particles by atom migration and become larger; the driving force of this process is to reduce surface energy [39]. Meanwhile, the roughness surface and the annealing condition could also affect this evolution. The particle size distribution on the surface was evaluated by Gaussian distribution.

Figure 4-6 shows the SEM images and the relevant size distributions of the Au NPs for the evaporated Au film as 2 nm (Figure 4-6a), 5 nm (Figure 4-6b) and 10 nm (Figure 4-6c),

respectively. For the 2 nm Au film (No.1), the size of the obtained Au NPs is limited in the range of 6-9 nm (Figure 3a1). For the 5 nm (No.2) and 10 nm Au film (No.3), the size of the obtained Au NPs increases to the range of 13-21 nm and 14-24 nm, respectively. These Au NPs with different parameter could offer a good chance to optimize the capability of light absorption.

For the further investigation of the dispersion of Au NPs, the TEM image of Au/TiO_2 which scrapped off AZO and Al template from 3D TiO_2/AZO NCA nanostructure. As can be seen in Figure 4-7, the Au NPs with diameter of less than 10 nm uniformly dispersed on the surface of continuous TiO_2 nanocone film. It is uniformly dispersed on the surface of plat surface (Figure 4-7c-d), as well as uniformly dispersed on the cone surface (Figure 4-7 a-b).

4.2.2. Chemical and element composition

Besides the structure and morphology information that performed by SEM and TEM, the EDS spectroscopy, the corresponding EDS and the XPS spectroscopy were performed to investigate the elements composition and chemical states properties of the prepared Au/TiO_2/AZO NCA.

4.2.2.1. Elements composition of Au/TiO_2/AZO NCA

The elements composition determined by EDS is present in Figure 4-8. As shown in the EDS spectroscopy, there have elements of Ti, Zn, Al, O and Au. The total and the individual EDS mapping clearly present the dispersion and distribution of each element on the 3D nanostructure. From the EDS mapping of Au, it is clear that the Au NPs uniformly dispersed on the whole surface of TiO_2/AZO NCA.

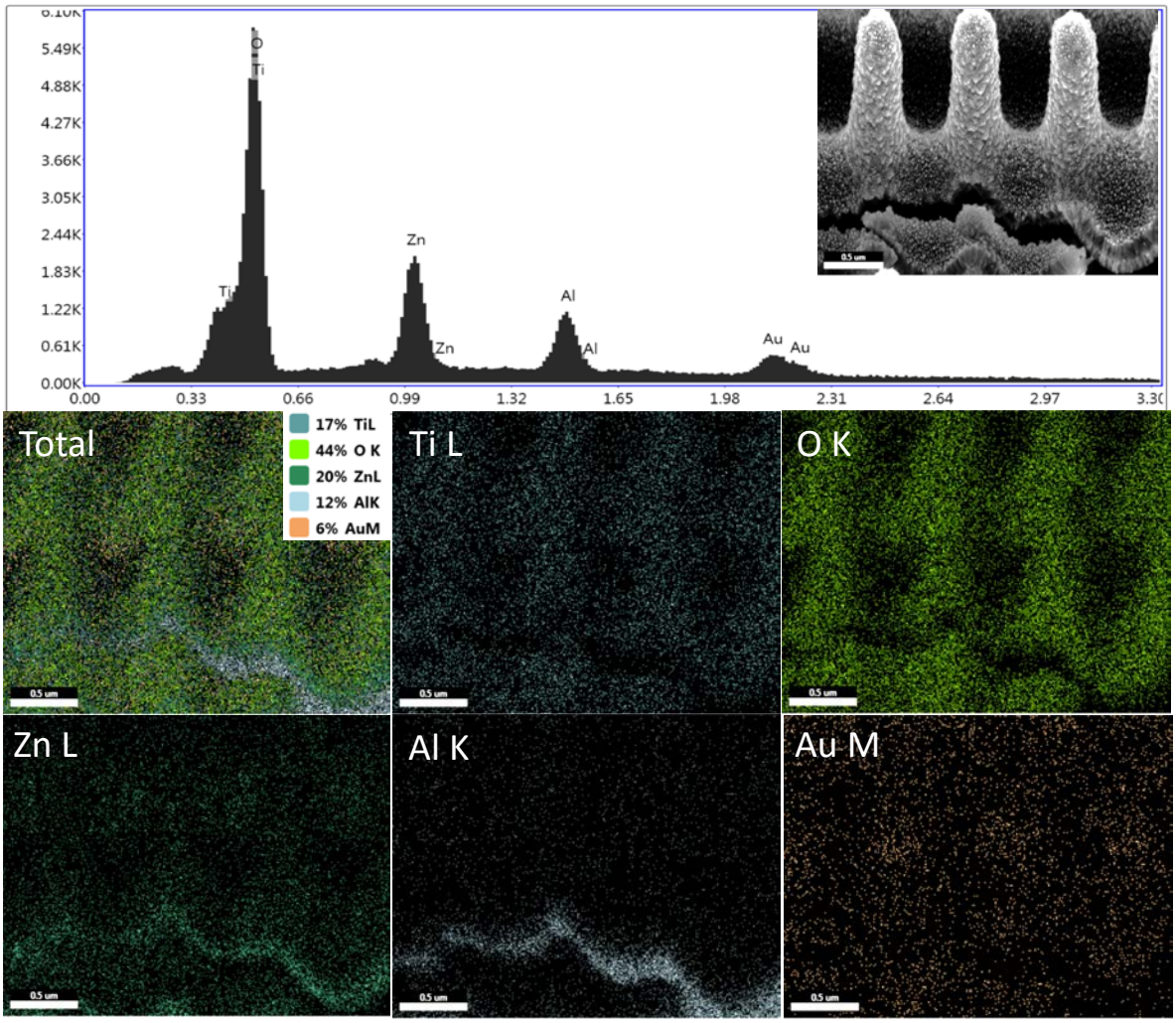

Figure 4-8| EDS spectrum and mappings of a cross-sectional AZO/TiO_2/Au NCA from the inset SEM image, which confirm the elements of O, Zn, Ti, Al, Au and the relevant distributions.

4.2.2.2. Chemical state property of Au/TiO_2/AZO NCA

The chemical state of those composed element in this structure was performed by XPS results. As can be seen in Figure 4-9a, the full XPS spectrum of an AZO/TiO_2/Au NCA confirm the presences of Ti, O and Au [40,41]. Because the XPS only collected the signals of the top 10 nm thickness of samples, the signals of Al and Zn cannot be detected. High-resolution Ti 2p XPS spectra shown in Figure 4-9b present the Ti $2p_{3/2}$ and Ti $2p_{1/2}$ centered at binding energies of 458.9 and 464.6 eV, respectively, and are consistent with the typical values of the TiO_2. The high-resolution O 1s core-level XPS spectra in Figure 4-9c shows one peak

centered at 530.0 eV, which corresponds to the characteristic peak of Ti-O-Ti. And one shoulder centered at 531.8 eV, which is assigned to –OH bond, such as adsorbed water molecules on the surface. The high-resolution Au 4f core-level XPS spectra shown in Figure 4-9d has two single peaks of Au $4f_{7/2}$ and Au $4f_{5/2}$ centered at 83.5 and 87.2 eV, which reveal the existence of metal Au.

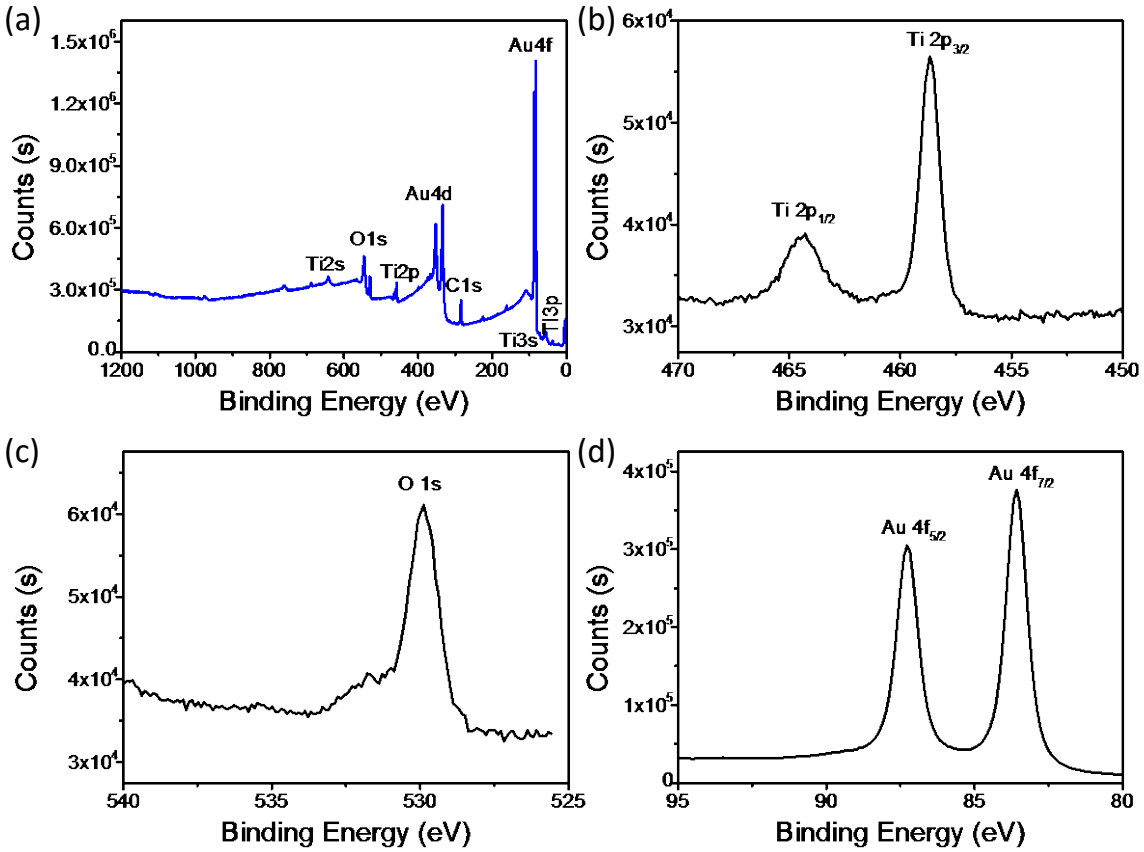

Figure 4-9| (a) Full XPS spectrum of an AZO/TiO_2/Au NCA, which confirms the presences of Ti, O and Au. (b) High-resolution Ti 2p XPS spectra. The Ti $2p_{3/2}$ and Ti $2p_{1/2}$ centered at binding energies of 458.9 and 464.6 eV, respectively, and are consistent with the typical values of the TiO_2. (c) High-resolution O 1s core-level XPS spectra with one peak centered at 530.0 eV, which corresponds to the characteristic peak of Ti-O-Ti; and one shoulder centered at 531.8 eV, which is assigned to –OH bond, such as adsorbed water molecules on the surface. (d) High-resolution Au 4f core-level XPS spectra with two single peaks of Au $4f_{7/2}$ and Au $4f_{5/2}$ centered at 83.5 and 87.2 eV, which reveal the existence of metal Au.

4.2.3. Light absorption performance

The light absorption performance is one of the key factors determine the light absorption and light utilization ability of photoresponse materials in PEC system. The large band-gap of TiO_2 only could absorb the light in the UV light range. The deposited Au NPs with different parameter on the surface of TiO_2/AZO NCA could offer a good chance to optimize the capability of light absorption, because of the visible light absorption which induced by the SPR of Au NPs.

The light absorption properties of the prepared samples were investigated by the UV-vis diffuse reflectance spectra. Figure 4-10a shows the absorption spectra of the prepared samples, which are measured in the diffuse reflectance mode. As can be seen, the bare TiO_2 film deposited on the surface of AZO/Al flat substrate only has light absorption at UV light range. In comparison with the flat AZO/TiO_2 film, AZO/TiO_2 NCA exhibits a distinct absorption enhancement in the range of 300 nm to 800 nm, which is attributed to the anti-reflection characteristic of the NCA structure. Both of the two spectra possess an absorption onset at 390 nm, in consistence with the band gap of bulk TiO_2 anatase (Eg = 3.2 eV). Meanwhile, the absorption spectra of the AZO/TiO_2/Au NCAs are also included in Figure 4-10a, which present pronounced absorption in the visible region, comparing to that of the bare AZO/TiO_2 NCA. These absorption peaks are centered at around 540 nm, indicating that the absorptions are originated from the SPR of Au NPs. In particular, due to the optimal size and density of the Au NPs, the AZO/TiO_2/Au NCA (No.2) demonstrates the largest absorption enhancement, about 30 %-40 % in the entire range of 300 nm to 800 nm.

From the photo shown in Figure 4-10b, it shows that the color of the AZO/TiO_2/Au NCA varies largely from the different Au NPs. Comparing to the NCA area of No.1 and the flat edge area of No.2 and No.3, the NCA area of No.2 and No.3 present dark green and dark blue, respectively. Thus, the strong light trapping of the AZO/TiO_2/Au NCA should ascribe to both of the NCA structure and the SPR effect of Au NPs.

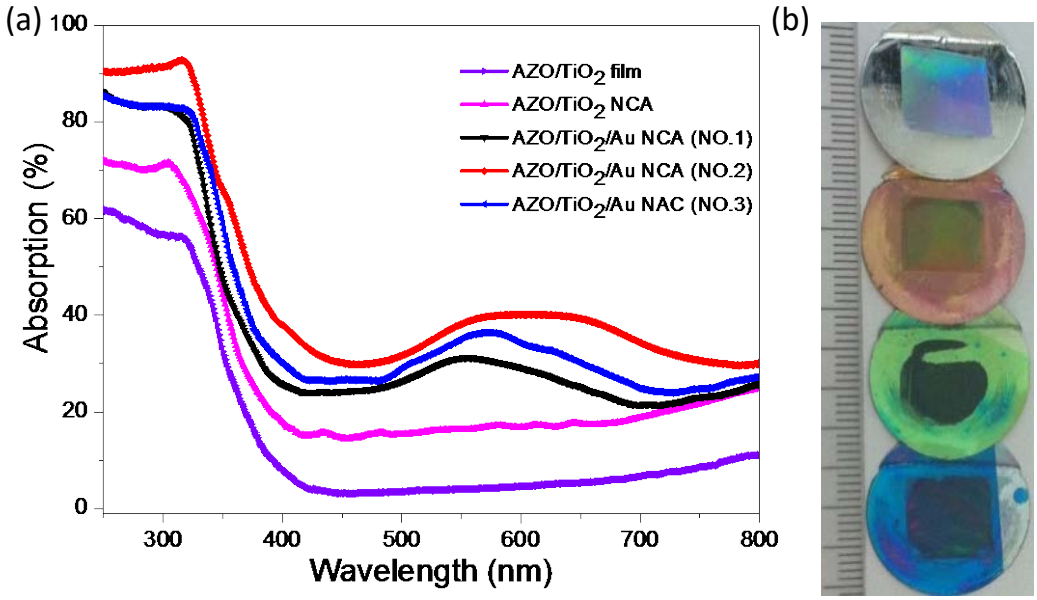

Figure 4-10| (a) Diffused reflectance UV-Vis spectra of the flat AZO/TiO_2 film, AZO/TiO_2 NCA, and AZO/TiO_2/Au NCA (No.1, No.2 and No.3). (b) The photo of the corresponding four samples (from top to bottom): AZO/TiO_2 NCA and AZO/TiO_2/Au NCA (No.1, No.2 and No.3), respectively.

4.2.4. Photoelectrochemical performance

The photoelectrochemical properties of NCA electrodes are studied in a three-electrode cell with Ag/AgCl as the reference electrode and a Pt wire as the counter electrode. It is worth to note that all of the measurements are conducted in 0.1 M Na_2SO_4 neutral aqueous solution (pH = 6.8). The applied biases are measured versus the Ag/AgCl reference electrode and are subsequently converted to the RHE scale using the Nernst equation:[42]

$$E_{RHE} = E_{Ag/AgCl} + E^{\circ}_{Ag/AgCl} + 0.059\ pH$$

Where the E_{RHE} is the converted bias versus RHE, the $E_{Ag/AgCl}$ is the applied bias measured against the Ag/AgCl reference electrode, and the $E^{\circ}_{Ag/AgCl}$ is the standard potential of Ag/AgCl at 25° C (0.1976 V).

4.2.4.1. Photocurrent

In order to maximize the collection of the photo-generated carriers and minimize the carrier recombination in AZO/TiO_2 NCA, the effect of TiO_2 shell thickness on PEC performance is particularly examined. Figure 4-11a shows the photocurrent density versus applied bias curves under chopped white light illumination (AM 1.5G, 100 mW·cm^{-2}) for the AZO/TiO_2 NCA electrodes with different TiO_2 shell thickness (indicated with ALD cycles).

In comparison with the dark current, the photocurrents of all these electrodes increase with the positive scanning of the bias, indicating a standard n type feature of TiO_2. Moreover, the value of the photocurrent varies largely according to the thickness of TiO_2, suggesting the obvious impact of the thickness on the photo-generation of carriers and carrier collection. As the dependence of photocurrent density (at 1.23 V vs. RHE) on the thickness of TiO_2 shown in Figure 4-11b, the photocurrent displays an increasing tendency up to 0.65 mA/cm^2 when the thickness is broadened from about 18 nm (300 cycles) to 90 nm (1400 cycles). With the further increase of TiO_2 thickness, the photocurrent decreases. On one hand, the increasing TiO_2 thickness would enhance photon-absorption, which contributes to the generation of more charge carriers that could be separated by the band bending at the interface of TiO_2/electrolyte. On the other hand, the band bending is also sensitive to the TiO_2 shell thickness in nanometer range. When only about 18 nm TiO_2 layer is grown (300 cycles), the entire TiO_2 layer is completely depleted and the band bending is limited. In this case, the driving force for separating the charge carriers is very weak. Thus the carriers have to travel to the interface in an inefficient drift mode.

With the TiO_2 thickness increasing, the band bending could be enlarged until the TiO_2 thickness matches the length of the depletion layer. Accordingly, the driving force would become influential gradually and we could attain an increasing efficiency of charge separation. After that, we observe a decreasing photocurrent with the increase of TiO_2 thickness more than 90 nm (1400 cycles). The reason is that though thicker TiO_2 layer could absorb more photos, significant portion of the generated carriers are produced outside and those carriers have higher chance to dissipate via the recombination.

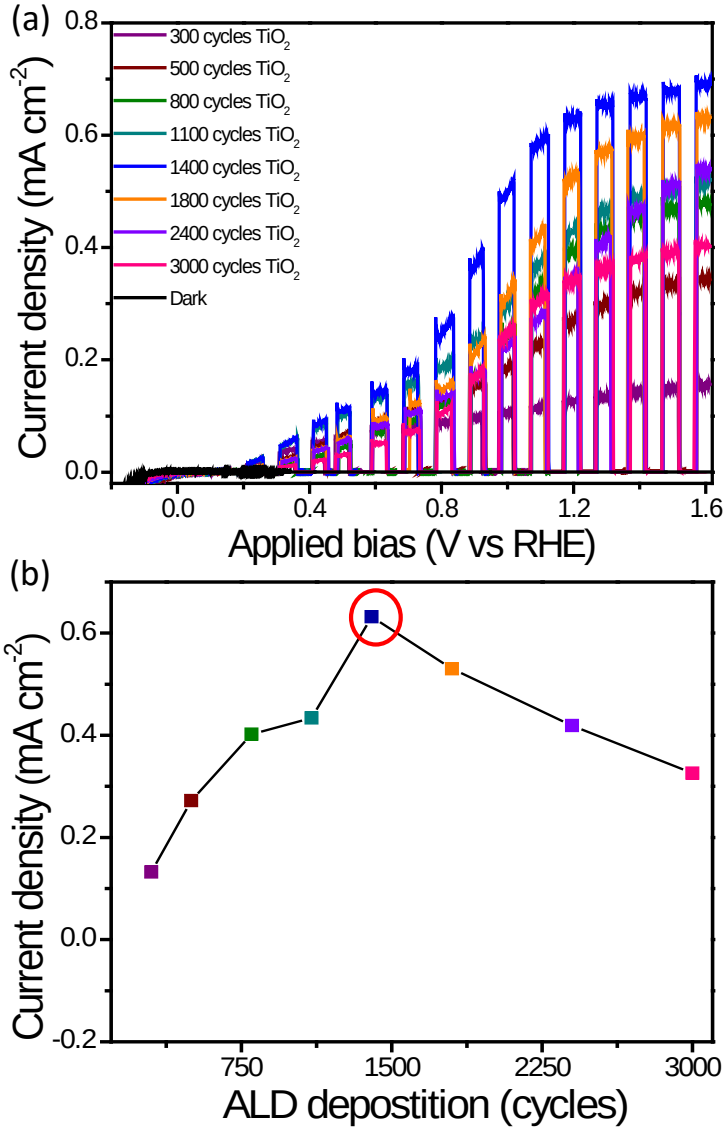

Figure 4-11| (a) Photocurrent densities of the AZO/TiO_2 NCA electrodes with different TiO_2 shell thickness (indicated with ALD cycles) under chopped white light (AM 1.5G, 100 mW·cm^{-2}) from -0.2 V to 1.6 V vs RHE. (b) Plot of photocurrent densities vs the TiO_2 shell thickness at 1.23 V vs RHE.

In addition, the advantage of the three-dimensional NAC structure is clearly demonstrated in Figure 4-12, in which the photocurrent density from the AZO/TiO_2 NCA electrode is about three times of that from the flat AZO/TiO_2 electrode with the optimal TiO_2 thickness.

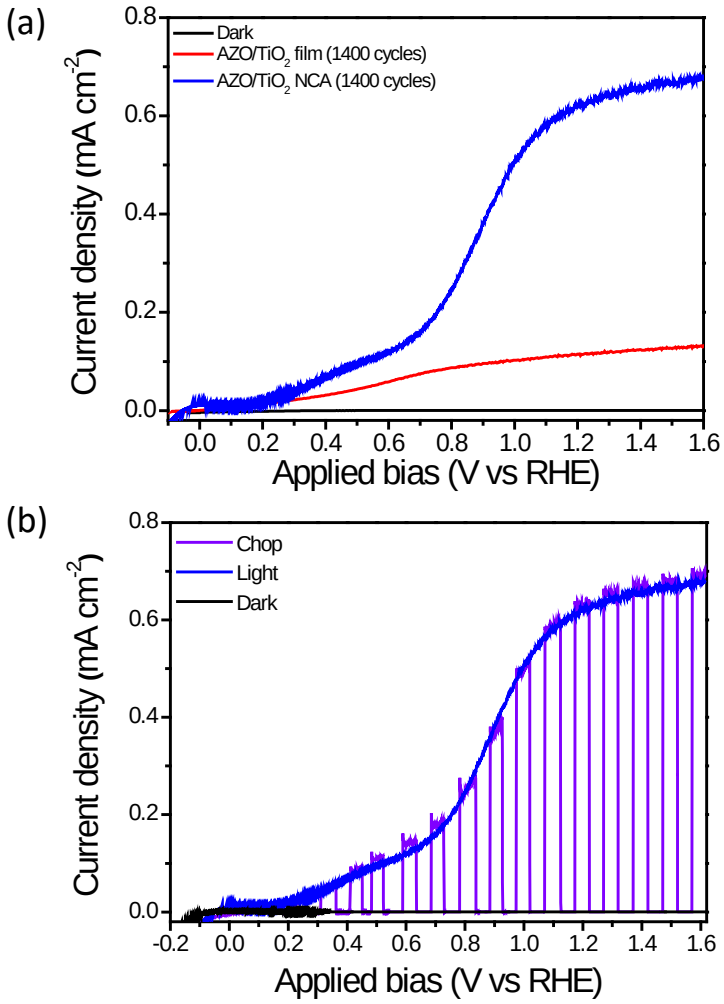

Figure 4-12| (a) Photocurrent density comparison of flat AZO/TiO_2 and AZO/TiO_2 NCA electrodes with the optimal TiO_2 thickness (90 nm). (b) Photocurrent densities of the AZO/TiO_2 NCA electrodes with the optimal TiO_2 thickness (90 nm) under chopped white light (AM 1.5G, 100 mW·cm^{-2}) from -0.2 V to 1.6 V vs RHE.

Though the PEC performance of the AZO/TiO_2 electrode could be maximized by using optimal NCA structure, AZO core and TiO_2 shell, the solar light utilization is still limited by the wide bandgap of TiO_2. Therefore, the Au NPs is integrated into AZO/TiO_2 NCA for introduction of SPR effect. The SPR effect is strongly related to the size, morphology and density of the Au NPs [43]. Figure 4-13 shows a set of photocurrent densities under AM 1.5G sunlight. All of the AZO/TiO_2/Au NCA (No.1, No.2 and No.3) electrodes exhibit larger photocurrent densities than that from the bare AZO/TiO_2 NCA electrode. Significantly, the

No.2 electrode achieves the highest photocurrent density (1.1 mA·cm^{-2}) at 1.23 V vs. RHE, which is almost double of that from the bare AZO/TiO_2 NCA electrode (0.63 mA·cm^{-2}) at the same applied bias. Those results confirm the positive role of the uniformly dispersed Au NPs in boosting the photoactivity of the AZO/TiO_2 NCA electrode under illumination. Meanwhile, for the No.1 electrode, because of the small size (about 8 nm) and the low density of Au NPs, the photocurrent enhancement from the SPR is scant. For the No.3 electrode, owing to the size and density of Au NPs is larger than that of No.2, the surface area of TiO_2 that the photo flux reaching and the surface area of TiO_2 that directly contact with the aqueous solution are both reduced. This is similar as the previous reported that over-loading of Au NPs would compromise the contribution of SPR in Au/TiO_2 systems [34,35].

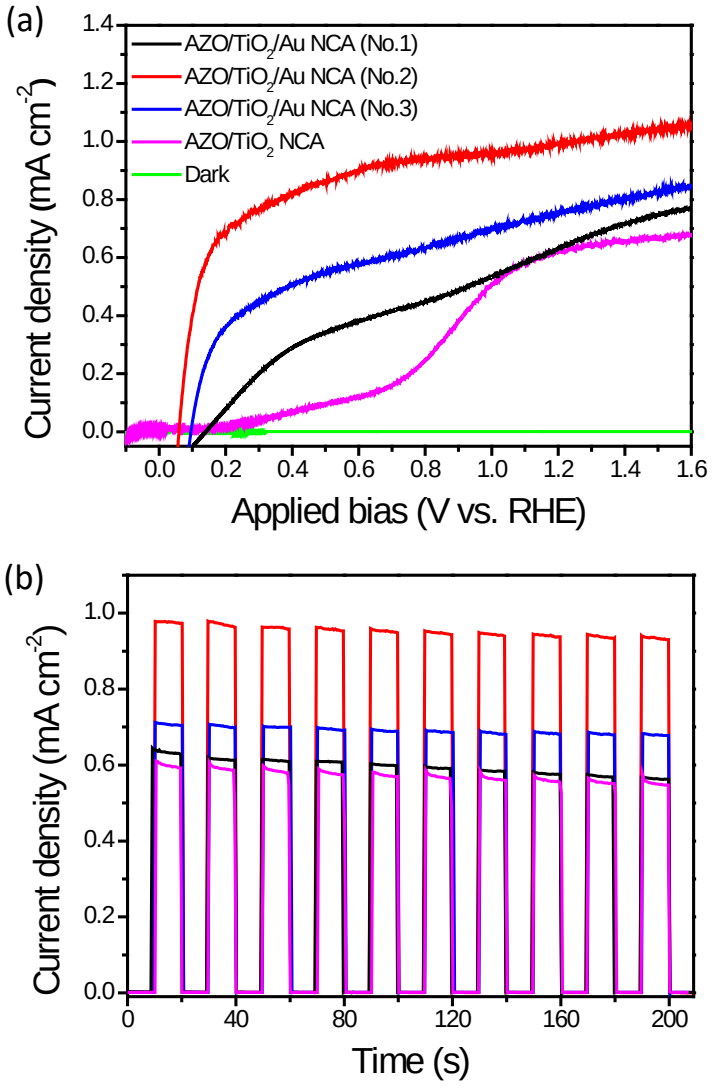

Figure 4-13| (a) Photocurrent densities of the bare AZO/TiO_2 NCA and AZO/TiO_2/Au NCA (No.1, No.2 and No.3) electrodes recorded in the dark and under AM 1.5G sunlight. The scans are collected from -0.2 to 1.6 V vs. RHE. (b) The corresponding amperometric I–t curves of the electrodes measured at 0.2 V vs. RHE with chopped on–off cycles under AM 1.5G sunlight.

Besides the photocurrent enhancement, obvious cathodic shift of the onset potential are also observed from the AZO/TiO_2/Au NCA electrodes, along with the photocurrent saturation at more negative. The No.2 electrode displays the lowest onset potential of 0.06 eV vs. RHE, comparing to 0.09 eV vs. RHE of No.3, 0.12 eV vs. RHE of No.1, and 0.15 eV vs. RHE of bare AZO/TiO_2 NCA electrodes (Figure 4-13a). This benefit is attributed to the catalytic effect of the Au NPs.

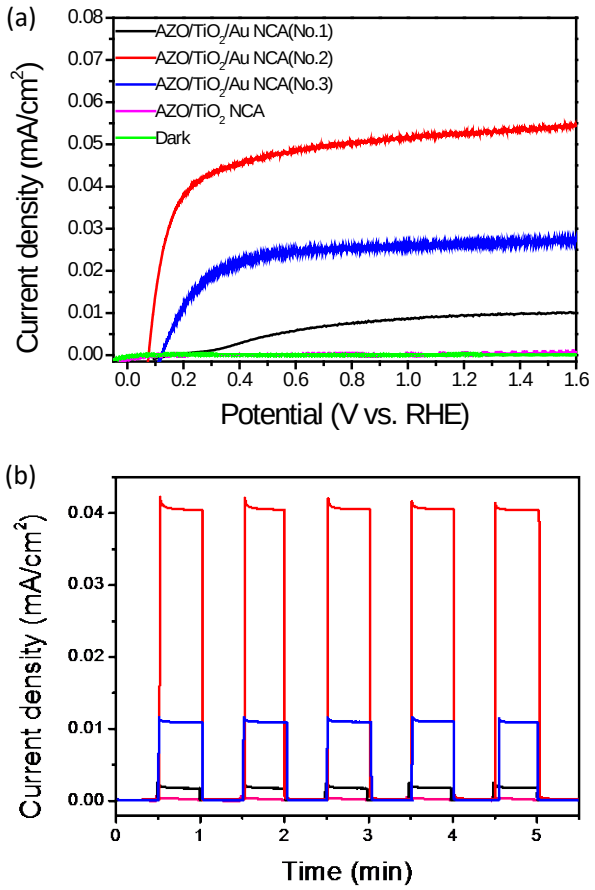

Figure 4-14| (a) Photocurrent densities of the bare AZO/TiO_2 NCA and AZO/TiO_2/Au NCA (No.1, No.2 and No.3) electrodes recorded in the dark and under AM 1.5G sunlight coupled with a 455 nm cut-off optical filter. The scans are collected from -0.2 to 1.6 V vs. RHE. (b)

The corresponding amperometric I–t curves of the electrodes measured at 0.2 V vs. RHE with chopped on–off cycles under AM 1.5G sunlight coupled with a 455 nm cut-off optical filter.

To clarify the responsibility of TiO_2 and Au in this work, an optical filter with 455 nm cut-off is used to rule out the impact from band gap transition of TiO_2. The photoelectrochemical properties of the prepared samples with 455 nm cut-off filter was investigated. As presented in Figure 4-14a, with a 455 nm cut-off filter, the occurrence of photocurrent is similar to that shown in Figure 4-13a. Further, amperometric current-time (I-t) characterization results for the four electrodes illuminated with chopped visible light ($\lambda \geq$ 455 nm) at 0.2 V vs. RHE with chopped on–off cycles under AM 1.5G sunlight coupled with a 455 nm cut-off optical filter are also shown here (Figure 4-14b).

As can be seen from those Figures, all the electrodes with the Au NPs present remarkably higher photocurrents than that from the bare AZO/TiO_2 NCA electrode. In particular, the No.2 electrode possesses a highest photocurrent of 0.041 mA·cm^{-2}. While the bare AZO/TiO_2 NCA electrode presents an ignorable photocurrent with 455 nm cut-off filter. Thus, the occurrences of photocurrents in the visible range are certainly attributed to the Au NPs on AZO/TiO_2 NCA electrodes instead of the TiO_2, which indicates that the SPR effect of the Au NPs is the origin of the occurrence of photocurrent in visible light range.

4.2.4.2. Applied bias photon-to-current efficiency

In this work, it is clearly that the Au NPs could significantly enhance the electron mobility by reducing the recombination of electron−hole pairs, and the No.2 electrode has the lowest resistance owing to the optimal size and density of Au NPs. To investigate the conversion efficiency of electrodes under different external applied bias, we performed the photoconversion efficiency "η". The efficiency is also called applied bias photon-to-current efficiency (ABPE) [42,44,45]. It is defined as:

$$\eta = I\left(1.23 - V_{app}\right)\Big/P_{light}$$

Where the V_{app} is the applied bias vs. RHE, I is the externally measured current density, and P_{light} is the power density of the illumination. As can be seen from the equation, the photoconversion efficiency is a function of applied bias versus reversible hydrogen electrode. It is done based on an assumption ideal condition that all photons are absorbed, and that 100 % of the absorbed photons are converted to electron-hole pairs that contribute to the photocurrent.

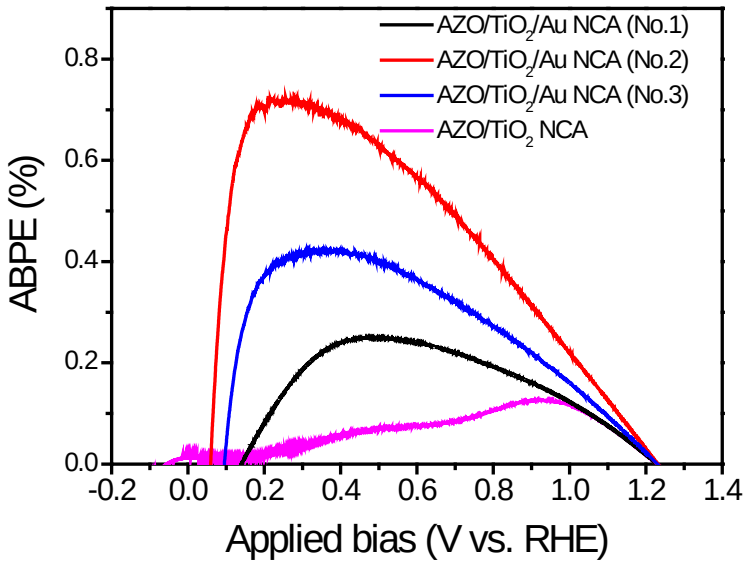

Figure 4-15| ABPEs of the bare AZO/TiO_2 NCA and AZO/TiO_2/Au NCA (No.1, No.2 and No.3) electrodes recorded in the dark and under AM 1.5G sunlight obtained from Figure 4-13a.

Therefore, the data in Figure 4-15 presents the ABPE of electrodes under different applied bias based on all photons are absorbed by electrodes and 100 % of the absorbed photos are converted to electron-hole pairs. It could obviously reveal the conversion efficiency with different applied bias. Figure 4-15 shows the calculated ABPEs from the results in Figure 4-13a. The maximum ABPEs for the bare AZO/TiO_2 NCA and AZO/TiO_2/Au NCA (No.1, No.2 and No.3) electrodes are 0.13 % (at 0.94 V vs. RHE), 0.25 % (at 0.47 V vs. RHE), 0.73 % (at 0.21 V vs. RHE), and 0.33 % (at 0.42 V vs. RHE), respectively. More important, the ABPE of the No.2 electrode is one of the highest values with the lowest external applied bias that ever reported in Au/TiO_2 PEC systems. From those results, it shows that, comparing with bare AZO/TiO_2 NCA electrode, the NCA electrodes with Au NPs have higher conversion efficiency

at much lower applied bias. It is demonstrated that the Au NPs on NCA electrode could enhance the conversion efficiency while lowering the demands of applied bias.

4.2.4.3. Incident photon-to-current efficiency

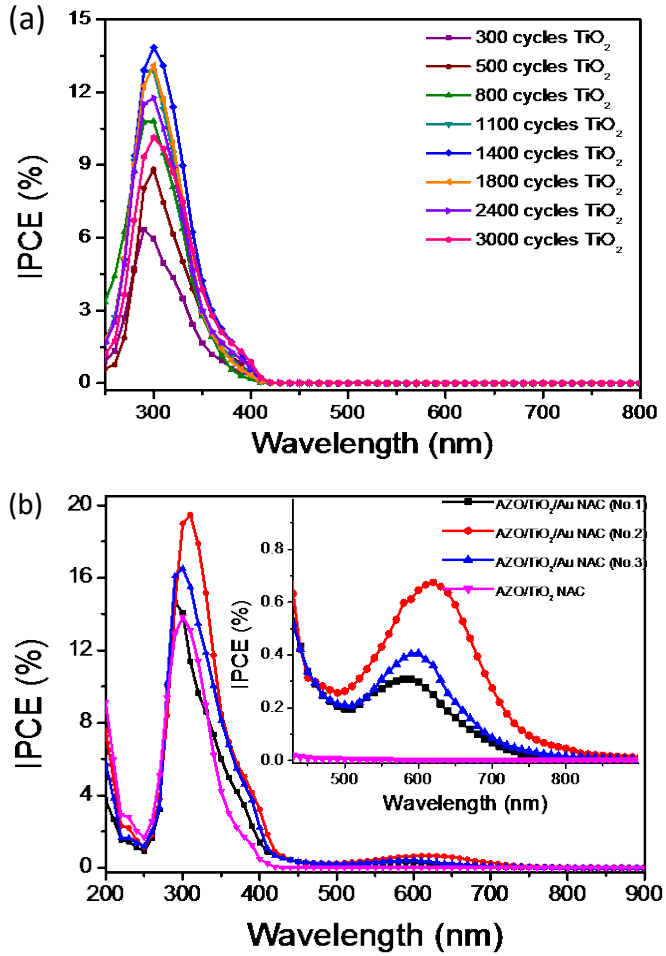

Figure 4-16| (a) IPCE (without applying external bias) of the relevant AZO/TiO_2 NCA electrodes with different shell thickness of TiO_2 in Figure 4-11a. (b) IPCE of the prepared electrodes measured without applying an external applied bias, inset is the enlarged IPCE result of (b) in the visible light range.

Incident photon-to-current efficiency (IPCE) is a measure of how efficiently the device converts the incident light into electrical energy at a given wavelength [42,45]. Figure 4-16 presents IPCE measurement of the all prepared electrodes without applying external bias. As can be seen in Figure 4-16a, the AZO/TiO_2 NCA electrode with different shell thickness of TiO_2 are particularly examined. In which the maximum value of 14 % is obtained from the

AZO/TiO_2 NCA electrode with the optimal TiO_2 thickness (90 nm, 1400 cycles). Meanwhile, the IPCE peak values of those electrodes versus TiO_2 shell thicknesses show the same tendency as that revealed in Figure 4-11b, supporting the observation from another aspect.

The Au NPs is integrated into AZO/TiO_2 NCA for introduction of SPR effect to increase the light absorption and light utilization. To further elucidate the role of Au NPs, the IPCE spectra of the bare AZO/TiO_2 NCA and AZO/TiO_2/Au NCA (No.1, No.2 and No.3) electrodes are collected without applying external bias, as shown in Figure 4-16b. First, for all the electrodes, the observed photoconversion is dominated by the photoactivity of TiO_2 in the ultraviolet (UV) region, and the IPCE spectra of the AZO/TiO_2/Au NCA electrodes are higher and broader than that of the bare AZO/TiO_2 NCA electrode in the UV region. This indicates that the presence of Au NPs promotes the photon absorption and collection via the band gap transitions of TiO_2. The highest value comes from the No.2 electrode, in consistent with the highest absorption curve in Figure 4-10. Second, as given by the inset of Figure 4-16b, we could also observe a series of IPCE peaks in the visible region for the AZO/TiO_2 NCA electrodes with Au NPs. The profiles of these peaks are in good agreement with those of the SPR peaks from the absorption spectra in Figure 4-10, and the highest IPCE of 0.71 % is obtained from the No.2 electrode.

4.2.4.4. Mott- Schottky measurement

With the TiO_2 thickness increasing, the band bending could be enlarged until the TiO_2 thickness matches the length of the depletion layer (DL_1). Accordingly, the driving force would become influential gradually and we could attain an increasing efficiency of charge separation. After that, we observe a decreasing photocurrent with the increase of TiO_2 thickness more than 90 nm (1400 cycles). The reason is that though thicker TiO_2 layer could absorb more photos, significant portion of the generated carriers are produced outside of the DL_1 and those carriers have higher chance to dissipate via the recombination. From the calculation based on the Mott-Schottky plot, the DL_1 thickness of our prepared TiO_2 is about 59 nm (Figure 4-17) [42,46].

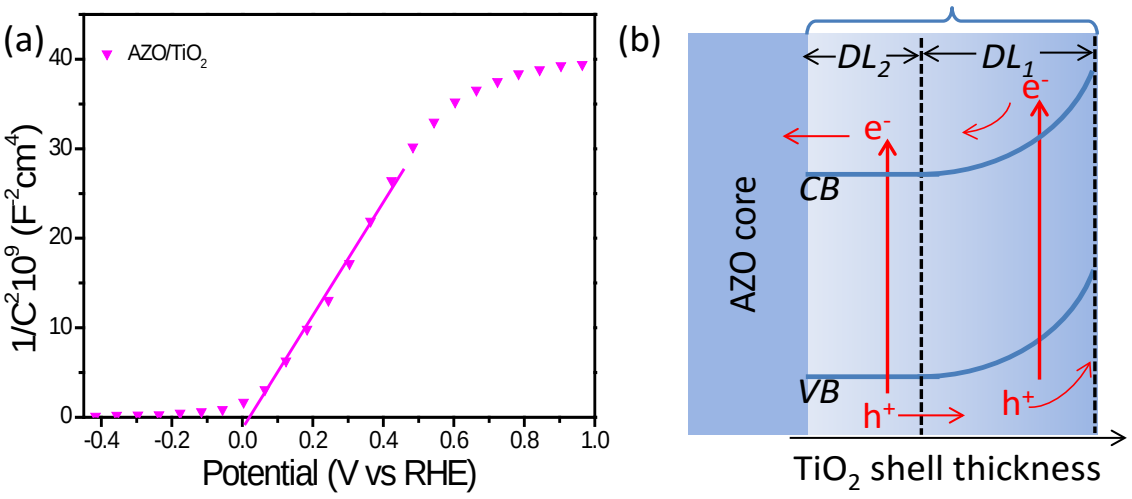

Figure 4-17| (a) Mott-Schottky plots of ALD-TiO_2 at a fixed frequency of 5 kHz in the dark. (b) The band bending at the interface of TiO_2/electrolyte, in which the optimal TiO_2 thickness includes the depletion layer (*DL_1*) and the diffusion layer (*DL_2*) that the photo-generated carriers could be efficiently collected.

To estimate the thickness of TiO_2 depletion layer, 90 nm thick TiO_2 (1400 cycles) film on ITO substrate is prepared for capacitance measurement; which is conducted on the electrode/electrolyte with the Mott−Schottky equation: [47]

$$\frac{1}{C^2} = \frac{2}{N_D e \varepsilon_0 \varepsilon}\left(E - E_{FB} - \frac{kT}{e}\right) \qquad \text{(Equation 4-1)}$$

where C is the space charge capacitance in the semiconductor, N_D is the electron carrier density, e is the elemental charge, ε_0 is the permittivity of vacuum, ε is the relative permittivity of the semiconductor, E is the applied bias, E_{FB} is the flat band potential, T is the temperature, and k is the Boltzmann constant. Figure 4-17 displays the Mott−Schottky plots of $1/C^2$ as a function of the applied bias, from which the positive slope is observed, suggesting n-type semiconductor. Furthermore, the plots are extrapolated to $1/C^2 = 0$ to estimate the value of E_{FB} (Equation 4-1), indicating 0.02 V for TiO_2. In addition, the carrier density N_D can also be calculated from using the following equation (Equation 4-2):

$$N_D = \frac{2}{e\varepsilon_0\varepsilon}\left(\frac{dE}{d\left(\frac{1}{C^2}\right)}\right) \quad \text{(Equation 4-2)}$$

As e = 1.6 × 10^{-19} C, ε_0 = 8.86 × 10^{-12} F·m^{-1}, and ε = 35 for the TiO_2 film [48] the N_D values of TiO_2 is determined to be 6.12 × 10^{17} cm^{-3}.

The thickness of depletion layer (ω) at TiO_2 surface can be calculated by (Equation 4-3) [44]:

$$\omega = \sqrt{\frac{2\varepsilon\varepsilon_0 E_B}{eN}} \quad \text{(Equation 4-3)}$$

E_B is the amount of band bending in the depletion layer, which has to be at least 50 mV in order to help the light-induced charge separation efficiently [43]. The calculated ω is about 59 nm.

Considering the uniform AZO/TiO_2 core/shell NCA structure, it means that about 31 nm diffusion layer (DL_2) from the DL_1 is the maximum distance that the photo-generated carriers can effectively collected at the TiO_2/electrode interface, as the illustration shown in Figure 4-17b.

4.2.4.5. Electrochemical impedance spectroscopy

Electrochemical impedance spectroscopy (EIS) measures the dielectric properties of a medium as a function of frequency [49,50]. It is based on the interaction of an external field with the electric dipole moment of the sample, often expressed by permittivity. It is also an experimental method of characterizing electrochemical systems. This technique measures the impedance of a system over a range of frequencies, and therefore the frequency response of the system, including the energy storage and dissipation properties, is revealed. Ordinarily, data obtained by EIS is expressed graphically in a Bode plot or a Nyquist plot. EIS reveals information about the reaction mechanism of an electrochemical process: different

reaction steps will dominate at certain frequencies, and the frequency response shown by EIS can help identify the rate limiting step.

The EIS of the prepared electrodes are shown in Figure 4-18. It is clearly that the Au NPs could significantly enhance the electron mobility by reducing the recombination of electron−hole pairs, and the No.2 electrode has the lowest resistance owing to the optimal size and density of Au NPs.

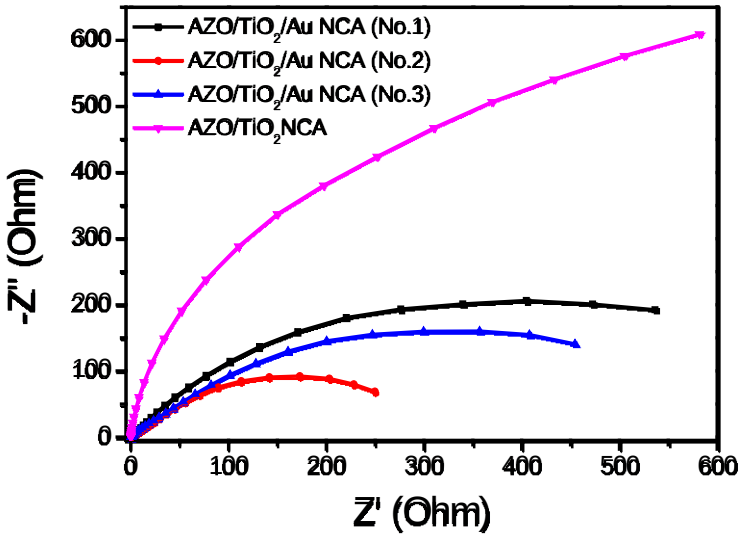

Figure 4-18| Nyquist plot of electrochemical impedance spectra of AZO/TiO_2 NCA and AZO/TiO_2/Au NCA (No.1, No.2, and No.3) electrodes at high frequencies. The Impedance measurements are performed under dark in 0.1 M Na_2SO_4 solution at open circuit voltage over a frequency range from 10^5 to 10^{-1} Hz with an AC voltage at 10 mV. The impedance data are analyzed by Potentiostat/.Galvanostat (BioLogic, Inc.). A semicircle (i.e., the arch in the present study) in the Nyquist plot at high frequency represents the charge-transfer process, while the diameter of the semicircle reflects the charge-transfer resistance.

4.2.4.6. Photoelectrochemical stability

The photoelectrochemical stability determines the possibility of industry application for the prepared NCA electrodes. As shown below in Figure 4-19a, the amperometric I-t stability test for more than 5 hours without chopping the light at 0.2 V (vs. RHE) under AM 1.5G sunlight irradiation for AZO/TiO_2/Au NCA (No.2) electrode. The photocurrent decreased from 0.7209 mA to 0.6973 mA. It decreased only around 3 % during the testing period. After that,

the other more than 5 hours amperometric I-t stability test of the same sample without chopping the light at 0.2 V (vs. RHE) with a 455 nm cut-off filter was performed under the same test condition, as shown below in Figure 4-19b. Without the 455 nm cut-off filter, the photocurrent decreased less than 5 %, from 0.0411 mA to 0.0391 mA. The results demonstrated that the prepared electrode is stable under the testing condition.

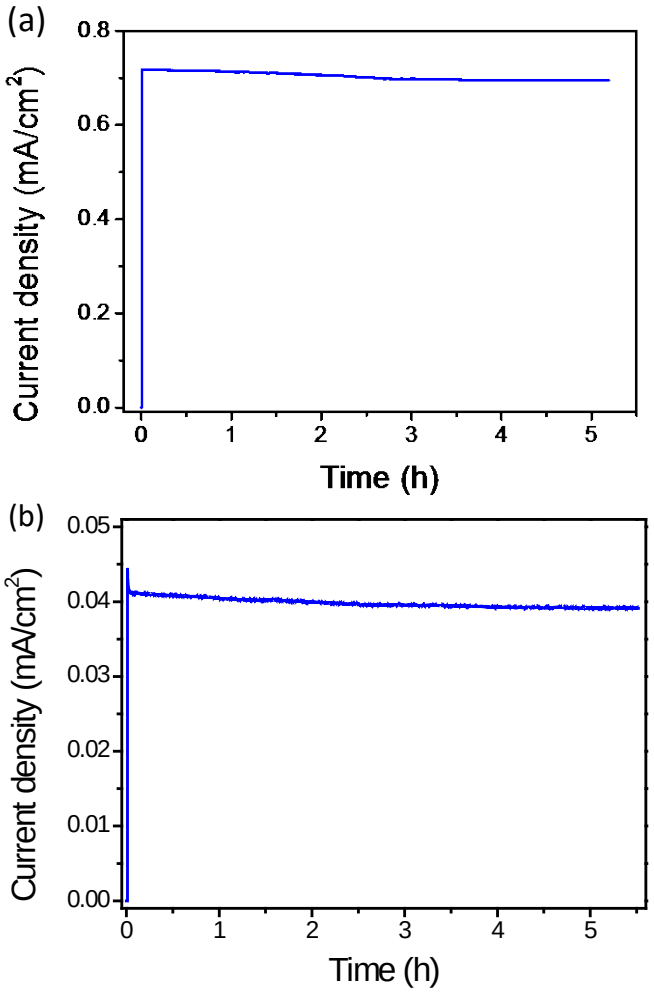

Figure 4-19| (a) Amperometric I–t curves of the electrodes measured at 0.2 V vs. RHE under AM 1.5G sunlight for more than five hours. (b) Amperometric I–t curves of the electrodes measured at 0.2 V vs. RHE under AM 1.5G sunlight coupled with a 455 nm cut-off optical filter for more than five hours.

4.2.5. Finite-difference time-domain simulation

Several different roles of the SPR effect in enhancing the photoactivity of semiconductors has been proposed, which includes plasmon resonance energy transfer (PRET), scattering and anti-reflection, and hot electron transfer [51]. For both of the PRET and light scattering, the enhancement could be observed at wavelengths where the plasmon resonance and semiconductor resonance overlap. As noted in previous reports that smaller NPs have lower scattering rates [52], so the photo scattering can be excluded in our electrodes because of the small size of Au NPs. The PRET describes the interaction of TiO_2 with the SPR induced electric-field amplification localized nearby at the Au NPs. This interaction promotes the photon absorption of TiO_2 and thus the photo-generated charge carriers of TiO_2.

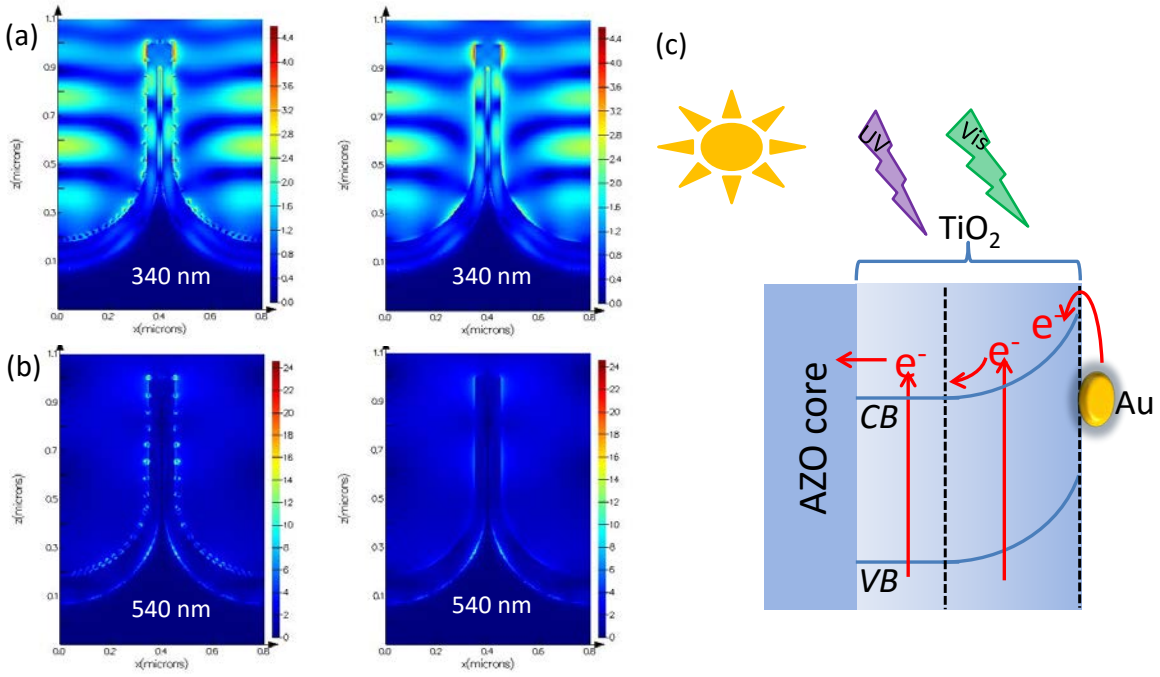

Figure 4-20| Simulated cross-sectional EM wave distributions of the AZO/TiO_2 NCA with or without Au NPs at the wavelength of (a) 340 nm, (b) 540 nm, respectively. (c) Schematic of the probable paths that the charge carriers could be effectively collected in the AZO/TiO_2/Au NCA.

On the other hand, from the simulated electromagnetic (EM) wave at 540 nm for the AZO/TiO_2 NCA with or without Au NPs, it is obviously that the magnitude of electric field intensity at the interface of Au NPs and TiO_2 shell is increased by 24 times, and the relevant

photon absorption rate is enhanced by 576 times (Figure 4-20b). This increased electric field could be the reason for the observed enhancement of the visible light photoactivity, though there is no spectral overlap between the amplified electric field and the absorption edge of TiO_2. It has been suggested that if the hot electrons possess sufficient energy and are in contact with TiO_2, then they can be injected into the conduction band of TiO_2 via Schottky junction, leaving energetic positive charges at Au NPs as holes for water oxidation. In this way, the Au NP acts as a sensitizer to light absorption, in analogy to a dye in the dye sensitized solar cell.

Therefore, we believe that the enhanced photoactivity of AZO/TiO_2/Au NCA in the visible region is mainly ascribed to the hot-carrier generation upon SPR excitation. Therefore, the probable paths that the charge carriers could be effectively collected in our AZO/TiO_2/Au NCA electrodes is shown in Figure 4-20c, including the charge carriers that generated inside the diffusion layer and the depletion layer of TiO_2, as well as the hot-carrier injection from the Au NPs to TiO_2. Most important, each of the paths can be optimized at the relevant steps.

In order to better understand how UV light absorption is enhanced and its possible contribution to the photoactivity, finite-difference-time-domain (FDTD) simulations are performed at the wavelength of 340 nm for the AZO/TiO_2 NCA with or without Au NPs, respectively. The cross-sectional EM wave distributions are plotted in Figure 4-20a. In both simulations, EM plane waves propagate downward and the color index at the specific location in the simulations reflects the magnitude of electric field at that point, normalized with that of the source EM wave if propagating in free space. It can be observed that both of the NCA structures show much low reflectance at 340 nm. More important, the electric field intensity at the interface of the Au NPs and TiO_2 is increased by 4 times the magnitude, which means that the photon absorption rate is enhanced by 16 times in this local area (absorption is proportional to square of electric field) compared with the bare AZO/TiO_2 NCA. The increased photo absorption in the UV region could overlap with the TiO_2 absorption, therefore, the PRET of Au NPs might be the major contributor of the UV absorption increasing and thus the corresponding enhancement of IPCE that shown in Figure 4-16a and b.

4.3. Conclusions

In this work, the Au SPR is the origin of the improve photo-performance with water splitting. It was proved from different aspects in manuscript and the added investigation results in supporting information. As presented in Figure 4-16, the AZO/TiO_2 NCA electrode shows negligible IPCE percent in the visible light range. While the electrodes with Au NPs have distinct IPCE percent in the same range (455-800 nm). And the profiles of these peaks are in good agreement with those of the Au SPR peaks from the absorption spectra in Figure 4-10. It indicates that the photo absorption and collection origin from Au SPR result the IPCE percent in the visible light range.

On the other hand, the photocurrents under visible light irradiation ($\geqslant$455 nm) (Figure 4-14) shows that there is almost no photocurrent for AZO/TiO_2 NCA electrode with applied bias from -0.05 to 1.6 V versus HER. While the electrodes with Au NPs present obvious photocurrent with the same applied bias. It is demonstrated that the Au SPR results the distinct photocurrent responses under the visible light irradiation. Finally, from the FDTD simulation, the electric field intensity of the AZO/TiO_2 NCA at 540 nm with Au NPs is 24 times than that without Au NPs, which further confirms the result (shown in Figure 4-20). Besides the SPR effect, the small Au NPs also act as the catalyst to largely lower the onset potential of electrodes as well (Figure 4-15).

Thus, the well-defined regular array of AZO/TiO_2 core/shell nanocones with uniformly dispersed Au nanoparticles is successfully realized with three sequential steps of ALD, PVD and annealing processes. The photo-generated charge carriers in the depletion layer and diffusion layer are maximally collected with an optimal thickness of TiO_2 shell (90 nm). The consequent formation of uniformly dispersed Au NPs further amplifies the light utilization and the according photocurrent density increases up to 1.1 mA·cm^{-2} at 1.23 V vs. RHE. Moreover, the photoconversion of the AZO/TiO_2/Au NCA electrode approaches to 0.73 % at 0.21 V versus RHE. The IPCE measurements and FDTD simulations reveal that the enhanced light utilization in the UV region is due to the optimal size and density of the Au NPs with strong electric field amplification, while the enhanced light utilization in the visible region is mainly caused by the hot-carrier generation upon SPR excitation. Moreover, the scalable fabrication route used in this work is highly feasible and repeatable, and can be easily applied to other metal/semiconductor systems.

4.4. Bibliography

[1] M.G. Walter, E.L. Warren, J.R. McKone, S.W. Boettcher, Q. Mi, E.A. Santori, et al., Solar Water Splitting Cells, Chem. Rev. 110 (2010) 6446–6473. doi:10.1021/cr1002326.

[2] F. Li, K. Fan, B. Xu, E. Gabrielsson, Q. Daniel, L. Li, et al., Organic Dye-Sensitized Tandem Photoelectrochemical Cell for Light Driven Total Water Splitting, J. Am. Chem. Soc. 137 (2015) 9153–9159. doi:10.1021/jacs.5b04856.

[3] D. Mersch, C.-Y. Lee, J.Z. Zhang, K. Brinkert, J.C. Fontecilla-Camps, A.W. Rutherford, et al., Wiring of Photosystem II to Hydrogenase for Photoelectrochemical Water Splitting, J. Am. Chem. Soc. 137 (2015) 8541–8549. doi:10.1021/jacs.5b03737.

[4] W. Yang, Y. Yu, M.B. Starr, X. Yin, Z. Li, A. Kvit, et al., Ferroelectric Polarization-Enhanced Photoelectrochemical Water Splitting in TiO_2–$BaTiO_3$ Core–Shell Nanowire Photoanodes, Nano Lett. 15 (2015) 7574–7580. doi:10.1021/acs.nanolett.5b03988.

[5] A. FUJISHIMA, K. HONDA, Electrochemical Photolysis of Water at a Semiconductor Electrode, Nature. 238 (1972) 37–38. doi:10.1038/238037a0.

[6] I.S. Cho, J. Choi, K. Zhang, S.J. Kim, M.J. Jeong, L. Cai, et al., Highly Efficient Solar Water Splitting from Transferred TiO2 Nanotube Arrays, Nano Lett. 15 (2015) 5709–5715. doi:10.1021/acs.nanolett.5b01406.

[7] G. Wang, H. Wang, Y. Ling, Y. Tang, X. Yang, R.C. Fitzmorris, et al., Hydrogen-Treated TiO2 Nanowire Arrays for Photoelectrochemical Water Splitting, Nano Lett. 11 (2011) 3026–3033. doi:10.1021/nl201766h.

[8] S. Srivastava, J.P. Thomas, M.A. Rahman, M. Abd-Ellah, M. Mohapatra, D. Pradhan, et al., Size-Selected TiO_2 Nanocluster Catalysts for Efficient Photoelectrochemical Water Splitting, ACS Nano. 8 (2014) 11891–11898. doi:10.1021/nn505705a.

[9] D. Regonini, A.C. Teloeken, A.K. Alves, F.A. Berutti, K. Gajda-Schrantz, C.P. Bergmann, et al., Electrospun TiO_2 Fiber Composite Photoelectrodes for Water Splitting, ACS Appl. Mater. Interfaces. 5 (2013) 11747–11755. doi:10.1021/am403437q.

[10] A.L. Linsebigler, G. Lu, J.T. Yates, Photocatalysis on TiO_2 Surfaces: Principles, Mechanisms, and Selected Results, Chem. Rev. 95 (1995) 735–758. doi:10.1021/cr00035a013.

[11] K. Lee, A. Mazare, P. Schmuki, One-Dimensional Titanium Dioxide Nanomaterials: Nanotubes, Chem. Rev. 114 (2014) 9385–9454. doi:10.1021/cr500061m.

[12] L. Sang, Y. Zhao, C. Burda, TiO_2 Nanoparticles as Functional Building Blocks, Chem. Rev. 114 (2014) 9283–9318. doi:10.1021/cr400629p.

[13] X. Wang, Z. Li, J. Shi, Y. Yu, One-Dimensional Titanium Dioxide Nanomaterials: Nanowires, Nanorods, and Nanobelts, Chem. Rev. 114 (2014) 9346–9384. doi:10.1021/cr400633s.

[14] B. Liu, E.S. Aydil, Growth of Oriented Single-Crystalline Rutile TiO_2 Nanorods on Transparent Conducting Substrates for Dye-Sensitized Solar Cells, J. Am. Chem. Soc. 131 (2009) 3985–3990. doi:10.1021/ja8078972.

[15] J.-Z. Chen, W.-Y. Ko, Y.-C. Yen, P.-H. Chen, K.-J. Lin, Hydrothermally Processed TiO_2 Nanowire Electrodes with Antireflective and Electrochromic Properties, ACS Nano. 6 (2012) 6633–6639. doi:10.1021/nn300787r.

[16] J.H. Park, S. Kim, A.J. Bard, Novel Carbon-Doped TiO_2 Nanotube Arrays with High Aspect Ratios for Efficient Solar Water Splitting, Nano Lett. 6 (2006) 24–28. doi:10.1021/nl051807y.

[17] Z. Zhang, L. Zhang, M.N. Hedhili, H. Zhang, P. Wang, Plasmonic Gold Nanocrystals Coupled with Photonic Crystal Seamlessly on TiO_2 Nanotube Photoelectrodes for Efficient Visible Light Photoelectrochemical Water Splitting, Nano Lett. 13 (2013) 14–20. doi:10.1021/nl3029202.

[18] J. Shi, Y. Hara, C. Sun, M.A. Anderson, X. Wang, Three-Dimensional High-Density Hierarchical Nanowire Architecture for High-Performance Photoelectrochemical Electrodes, Nano Lett. 11 (2011) 3413–3419. doi:10.1021/nl201823u.

[19] W. Guo, C. Xu, X. Wang, S. Wang, C. Pan, C. Lin, et al., Rectangular Bunched Rutile TiO2 Nanorod Arrays Grown on Carbon Fiber for Dye-Sensitized Solar Cells, J. Am. Chem. Soc. 134 (2012) 4437–4441. doi:10.1021/ja2120585.

[20] G.K. Mor, K. Shankar, M. Paulose, O.K. Varghese, C.A. Grimes, Enhanced Photocleavage of Water Using Titania Nanotube Arrays, Nano Lett. 5 (2005) 191–195. doi:10.1021/nl048301k.

[21] Z. Zhang, P. Wang, Optimization of Photoelectrochemical Water Splitting Performance on Hierarchical TiO_2 Nanotube Arrays, Energy Environ. Sci. 5 (2012) 6506–6512.

doi:10.1039/C2EE03461A.

[22] J. Hong Noh, B. Ding, H. Soo Han, J. Seong Kim, J. Hoon Park, S. Baek Park, et al., Tin Doped Indium Oxide Core-TiO_2 Shell Nanowires on Stainless Steel Mesh for Flexible Photoelectrochemical Cells, Appl. Phys. Lett. 100 (2012) 084104. doi:10.1063/1.3684805.

[23] D. Guo, J. Wang, C. Cui, P. Li, X. Zhong, F. Wang, et al., ZnO@TiO_2 Core–shell Nanorod Arrays with Enhanced Photoelectrochemical Performance, Sol. Energy. 95 (2013) 237–245. doi:http://dx.doi.org/10.1016/j.solener.2013.06.003.

[24] L. Alibabaei, B.H. Farnum, B. Kalanyan, M.K. Brennaman, M.D. Losego, G.N. Parsons, et al., Atomic Layer Deposition of TiO_2 on Mesoporous nano ITO: Conductive Core–Shell Photoanodes for Dye-Sensitized Solar Cells, Nano Lett. 14 (2014) 3255–3261. doi:10.1021/nl5006433.

[25] S. Hernández, V. Cauda, A. Chiodoni, S. Dallorto, A. Sacco, D. Hidalgo, et al., Optimization of 1D ZnO@TiO_2 Core–Shell Nanostructures for Enhanced Photoelectrochemical Water Splitting under Solar Light Illumination, ACS Appl. Mater. Interfaces. 6 (2014) 12153–12167. doi:10.1021/am501379m.

[26] A.W. Maijenburg, J. Veerbeek, R. de Putter, S.A. Veldhuis, M.G.C. Zoontjes, G. Mul, et al., Electrochemical Synthesis of Coaxial TiO_2-Ag Nanowires and Their Application in Photocatalytic Water Splitting, J. Mater. Chem. A. 2 (2014) 2648–2656. doi:10.1039/C3TA14551D.

[27] Y. Tian, T. Tatsuma, Mechanisms and Applications of Plasmon-Induced Charge Separation at TiO_2 Films Loaded with Gold Nanoparticles, J. Am. Chem. Soc. 127 (2005) 7632–7637. doi:10.1021/ja042192u.

[28] A. Furube, L. Du, K. Hara, R. Katoh, M. Tachiya, Ultrafast Plasmon-Induced Electron Transfer from Gold Nanodots into TiO_2 Nanoparticles, J. Am. Chem. Soc. 129 (2007) 14852–14853. doi:10.1021/ja076134v.

[29] S. Linic, P. Christopher, D.B. Ingram, Plasmonic-metal Nanostructures for Efficient Conversion of Solar to Chemical Energy, Nat Mater. 10 (2011) 911–921. http://dx.doi.org/10.1038/nmat3151.

[30] Z. Liu, W. Hou, P. Pavaskar, M. Aykol, S.B. Cronin, Plasmon Resonant Enhancement of Photocatalytic Water Splitting Under Visible Illumination, Nano Lett. 11 (2011) 1111–

1116. doi:10.1021/nl104005n.

[31] Z.W. Seh, S. Liu, M. Low, S.-Y. Zhang, Z. Liu, A. Mlayah, et al., Janus Au-TiO_2 Photocatalysts with Strong Localization of Plasmonic Near-Fields for Efficient Visible-Light Hydrogen Generation, Adv. Mater. 24 (2012) 2310–2314. doi:10.1002/adma.201104241.

[32] L. Liu, S. Ouyang, J. Ye, Gold-Nanorod-Photosensitized Titanium Dioxide with Wide-Range Visible-Light Harvesting Based on Localized Surface Plasmon Resonance, Angew. Chemie Int. Ed. 52 (2013) 6689–6693. doi:10.1002/anie.201300239.

[33] L. Wen, Z. Wang, Y. Mi, R. Xu, S.-H. Yu, Y. Lei, Designing Heterogeneous 1D Nanostructure Arrays Based on AAO Templates for Energy Applications, Small. 11 (2015) 3408–3428. doi:10.1002/smll.201500120.

[34] X. Zhang, Y. Liu, S.-T. Lee, S. Yang, Z. Kang, Coupling Surface Plasmon Resonance of Gold Nanoparticles with Slow-photon-effect of TiO_2 Photonic Crystals for Synergistically Enhanced Photoelectrochemical Water Splitting, Energy Environ. Sci. 7 (2014) 1409–1419. doi:10.1039/C3EE43278E.

[35] Y.-C. Pu, G. Wang, K.-D. Chang, Y. Ling, Y.-K. Lin, B.C. Fitzmorris, et al., Au Nanostructure-Decorated TiO_2 Nanowires Exhibiting Photoactivity Across Entire UV-visible Region for Photoelectrochemical Water Splitting, Nano Lett. 13 (2013) 3817–3823. doi:10.1021/nl4018385.

[36] C. Agashe, O. Kluth, J. Hüpkes, U. Zastrow, B. Rech, M. Wuttig, Efforts to Improve Carrier Mobility in Radio Frequency Sputtered Aluminum Doped Zinc Oxide Films, J. Appl. Phys. 95 (2004) 1911–1917. doi:10.1063/1.1641524.

[37] J.K. Sheu, M.L. Lee, C.J. Tun, S.W. Lin, Ultraviolet Band-pass Schottky Barrier Photodetectors Formed by Al-doped ZnO Contacts to n-GaN, Appl. Phys. Lett. 88 (2006) 043506. doi:10.1063/1.2167796.

[38] T. Minami, Substitution of Transparent Conducting Oxide Thin Films for Indium Tin Oxide Transparent Electrode Applications, Thin Solid Films. 516 (2008) 1314–1321. doi:http://dx.doi.org/10.1016/j.tsf.2007.03.082.

[39] a. Sundar, R. a. Hughes, P. Farzinpour, K.D. Gilroy, G. a. Devenyi, J.S. Preston, et al., Manipulating the Size Distribution of Supported Gold Nanostructures, Appl. Phys. Lett. 100 (2012) 013111. doi:10.1063/1.3675569.

[40] M.M. Ottakam Thotiyl, S.A. Freunberger, Z. Peng, Y. Chen, Z. Liu, P.G. Bruce, A Stable Cathode for the Aprotic Li–O_2 Battery, Nat Mater. 12 (2013) 1050–1056. http://dx.doi.org/10.1038/nmat3737.

[41] N. Kruse, S. Chenakin, XPS characterization of Au/TiO_2 Catalysts: Binding Energy Assessment and Irradiation Effects, Appl. Catal. A Gen. 391 (2011) 367–376. doi:http://dx.doi.org/10.1016/j.apcata.2010.05.039.

[42] Z. Chen, T.F. Jaramillo, T.G. Deutsch, A. Kleiman-Shwarsctein, A.J. Forman, N. Gaillard, et al., Accelerating Materials Development for Photoelectrochemical Hydrogen Production: Standards for Methods, Definitions, and Reporting Protocols, J. Mater. Res. 25 (2010) 3–16.

[43] N.J. Halas, S. Lal, W.-S. Chang, S. Link, P. Nordlander, Plasmons in Strongly Coupled Metallic Nanostructures, Chem. Rev. 111 (2011) 3913–3961. doi:10.1021/cr200061k.

[44] A.J. Nozik, Photoelectrochemistry: Applications to Solar Energy Conversion, Annu. Rev. Phys. Chem. 29 (1978) 189–222. doi:10.1146/annurev.pc.29.100178.001201.

[45] Q. Jia, K. Iwashina, A. Kudo, Facile Fabrication of an Efficient $BiVO_4$ Thin Film Electrode for Water Splitting Under Visible Light Irradiation, Proc. Natl. Acad. Sci. 109 (2012) 11564–11569. doi:10.1073/pnas.1204623109 .

[46] M. Zhou, J. Bao, Y. Xu, J. Zhang, J. Xie, M. Guan, et al., Photoelectrodes Based upon Mo:$BiVO_4$ Inverse Opals for Photoelectrochemical Water Splitting, ACS Nano. 8 (2014) 7088–7098. doi:10.1021/nn501996a.

[47] K. Gelderman, L. Lee, S.W. Donne, Flat-Band Potential of a Semiconductor: Using the Mott–Schottky Equation, J. Chem. Educ. 84 (2007) 685. doi:10.1021/ed084p685.

[48] D. Wei, T. Hossain, N.Y. Garces, N. Nepal, H.M. Meyer, M.J. Kirkham, et al., Influence of Atomic Layer Deposition Temperatures on TiO_2/n-Si MOS Capacitor, ECS J. Solid State Sci. Technol. 2 (2013) N110–N114. doi:10.1149/2.010305jss .

[49] M. Adachi, M. Sakamoto, J. Jiu, Y. Ogata, S. Isoda, Determination of Parameters of Electron Transport in Dye-Sensitized Solar Cells Using Electrochemical Impedance Spectroscopy, J. Phys. Chem. B. 110 (2006) 13872–13880. doi:10.1021/jp061693u.

[50] S.-M. Park, J.-S. Yoo, Peer Reviewed: Electrochemical Impedance Spectroscopy for Better Electrochemical Measurements, Anal. Chem. 75 (2003) 455 A–461 A. doi:10.1021/ac0313973.

[51] S.C. Warren, E. Thimsen, Plasmonic Solar Water Splitting, Energy Environ. Sci. 5 (2012) 5133–5146. doi:10.1039/C1EE02875H.

[52] C. Sönnichsen, T. Franzl, T. Wilk, G. von Plessen, J. Feldmann, O. Wilson, et al., Drastic Reduction of Plasmon Damping in Gold Nanorods, Phys. Rev. Lett. 88 (2002) 77402. http://link.aps.org/doi/10.1103/PhysRevLett.88.077402.

5. Fabrication of three-dimensional Pt/MnO_2 nanotube arrays for supercapacitor

Three-dimensional Pt nanostructures play an important role in fuel cells and microelectronics, due to the unique advantages of them. Considering the fact that Pt is an expensive metal, a major challenging point nowadays is how to realize efficient utilization of Pt. In this chapter, a cost-effective atomic layer deposition process with a low N_2 filling step is introduced for realizing well-defined Pt nanotube arrays in anodic alumina nano-porous templates. Compared to the conventional ALD growth of Pt, originates from the low N_2 filling step, much fewer ALD cycles and a shorter precursor pulsing time are required. To achieve similar Pt nanotubes, about half cycles and 10 % Pt precursor pulsing time is needed using our ALD process. Meanwhile, the Pt nanotube array is explored as a current collector for supercapacitors based on core/shell Pt/MnO_2 nanotubes. This nanotube-based electrode exhibits high gravimetric and areal specific capacitance (810 $F \cdot g^{-1}$ and 75 $mF \cdot cm^{-2}$ at a scan rate of 5 $mV \cdot s^{-1}$) as well as an excellent rate capability (68 % capacitance retention from 2 to 100 $A \cdot g^{-1}$). Additionally, a negligible capacitance loss is observed after 8000 cycles of random charging-discharging from 2 to 100 $A \cdot g^{-1}$.

5.1. Introduction

Metal nanostructures with high regularity, complex architectures and large specific surface areas have been extensively utilized in various application fields [1–8]. Due to the unique advantages of Pt including high catalytic ability, chemical stability against oxidation and high work function of 5.6 eV, it plays an especially important role in fuel cells and microelectronics [9–17]. Considering the fact that Pt is a very expensive metal, a major challenge nowadays is how to realize cost-effective utilization of Pt. To meet this challenge, an approximate fivefold reduction of Pt content is necessary at the present state of industrial development [4,5] Meanwhile, the trend of device miniaturization requires efficient techniques enabling Pt fabrication at nano-scale range so as to increase the overall surface-to-volume ratio and hence to reduce the Pt loading. Recently, intensive interests have been raised for synthesizing different configurations of Pt nanostructures, especially for nanowires and nanotubes [9,18–20] Anodic alumina nano-porous templates have been

widely used for fabricating ordered arrays of diverse nanostructures [20–26] including Pt nanowires and nanotubes [27–31]. Comparing to dispersed Pt nanoparticles that usually have agglomeration problems, Pt nanowires and nanotubes are highly desirable for applications as catalytic materials and micro-electrodes [9,28].

Atomic layer deposition, which allows conformal and homogenous three-dimensional nano-fabrication with high structural controllability at atomic level, becomes a promising alternative approach for realizing Pt nanostructures [32–38]. To date, Pt has been deposited by ALD process on various substrates [35,37,39–41]. Suffering from poor nucleation and inland growth, dispersed Pt nanoparticles usually appeared at the beginning of the ALD process [38]. And a real layer-by-layer atomic growth can only be achieved when the dispersed Pt nanoparticles coalesce together and finally forms a continuous film, which requires a large number of ALD cycles and hence makes the ALD growth of Pt nanostructures high costly. Meanwhile, owing to the reaction limitation and the large molecular mass of Pt precursors ($MeCpPtMe_3$), the diffusion and transportation of the precursors in nano-pores are very slow [29,30,42,43] which require a sufficient long pulsing time so as to accomplish the precursor diffusion and reaction process within the nano-pores. Just recently, increasing Pt precursor pulsing time up to 30 seconds has been tried to obtain high Pt coverage inside alumina templates [30], in which a large amount of Pt precursor was consumed and hence further increases the cost of the ALD growth of Pt nanostructures. This is also the reason why most of the Pt ALD growth so far is limited to nanoparticles or low aspect ratio structures. Therefore, how to realize a cost-effective ALD process for high aspect ratio Pt nanostructures presents a timely topic for advanced electronic devices such as energy storage elements, transistors and sensors.

Herein, we achieve a highly cost-effective ALD technique for synthesising pre-defined Pt nanotube (NT) arrays within alumina nano-porous templates. This low Pt consuming advantage is attributed to a low N_2 filling step of the ALD process, by which much fewer cycles and a shorter Pt precursor pulsing time are required comparing to the conventional ALD growth. It is demonstrated that about half ALD cycles and 10 % Pt precursor pulsing time is necessary for obtaining similar Pt NTs using the low N_2 filling step, enabling Pt nanostructures more practicable for device utilizations such as superior current collectors. Therefore, starting from these Pt NTs, core/shell Pt/MnO_2 NT arrays are fabricated for realizing a high performance supercapacitor. The presented approach shall be applicable for

fabricating other noble metal nanostructures, since the ALD processes of these materials are ruled by the similar reaction mechanisms to that of Pt.

5.2. Results and discussion

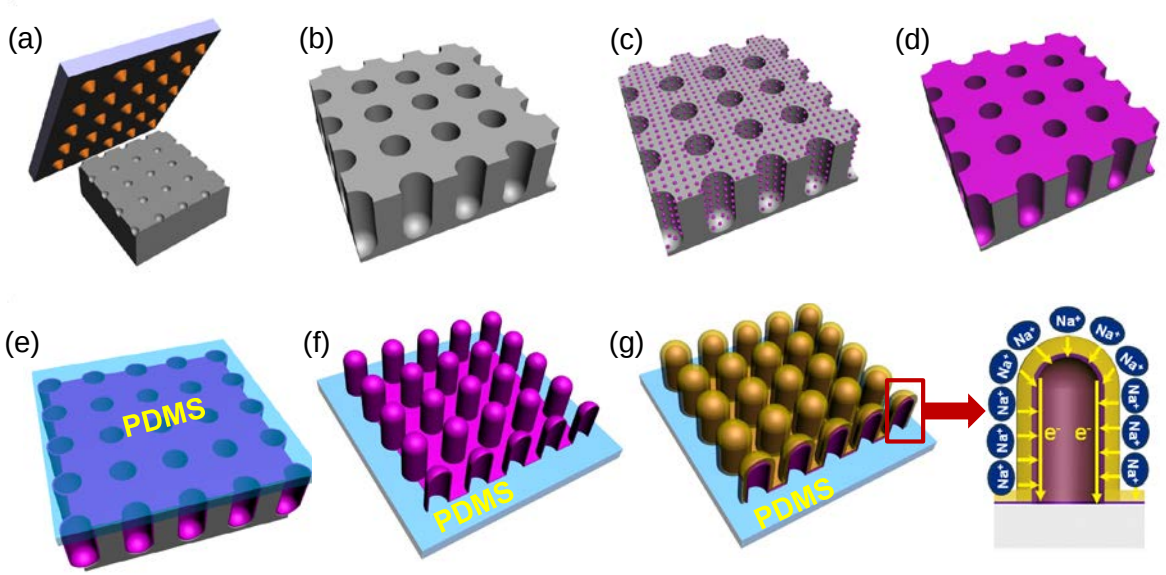

Figure 5-1| Schematic illustration of the fabrication process of Pt and Pt/MnO_2 nanotube array: (a) surface imprinting on an aluminum foil using a Ni nano-piller stamp; (b) anodization for preparing alumina template followed by a chemical etching process; (c) dispersed Pt nanoparticles formed on template after a few ALD growth cycles; (d) continuous Pt nanotue array obtained after more ALD growth cycles; (e) a mixed PDMS solution poured on alumina template; (f) removal of alumina template and resulting in a Pt nanotube array on PDMS substrate; (g) electrodeposition of MnO_2 to form Pt/MnO_2 nanotube array for supercapacitor.

The fabrication procedure is described and schematically shown in section 2.1.6. During the fabrication process, a Pt nanotube array is grown on a pre-patterned alumina template, as schematically demonstrated in Figure 5-1a-d. After that, a mixed polydimethylsiloxane (PDMS) solution is poured on the surface of the template, followed by dissolving the backside alumina template (Figures 5-1e and f). Finally, a thin MnO_2 layer is deposited on the Pt nanotubes, resulting in a supercapacitor electrode based on core/shell Pt/MnO_2 nanotube array (Figure 5-1g). For this core/shell structure, the core Pt nanotube with high electrical conductivity is used as a current collector to provide paths for charge storage and delivery.

Meanwhile, the construction of the nanotubes can also offer a large surface area to increase mass loading of the active material (i.e., MnO_2).

The detail morphology changes of the synthesized regular AAO template, the fabricated Pt nanotube arrays by ALD deposition process, and the electrodeposition of MnO_2 shell active materials were carefully investigated by SEM. The elements composition and chemical states of the prepared sample, as well as the chemical and physical properties were detailed determined in this section.

5.2.1. Morphology and structure analysis for the three-dimensional Pt/MnO_2 nanotube array

5.2.1.1. Regular AAO template

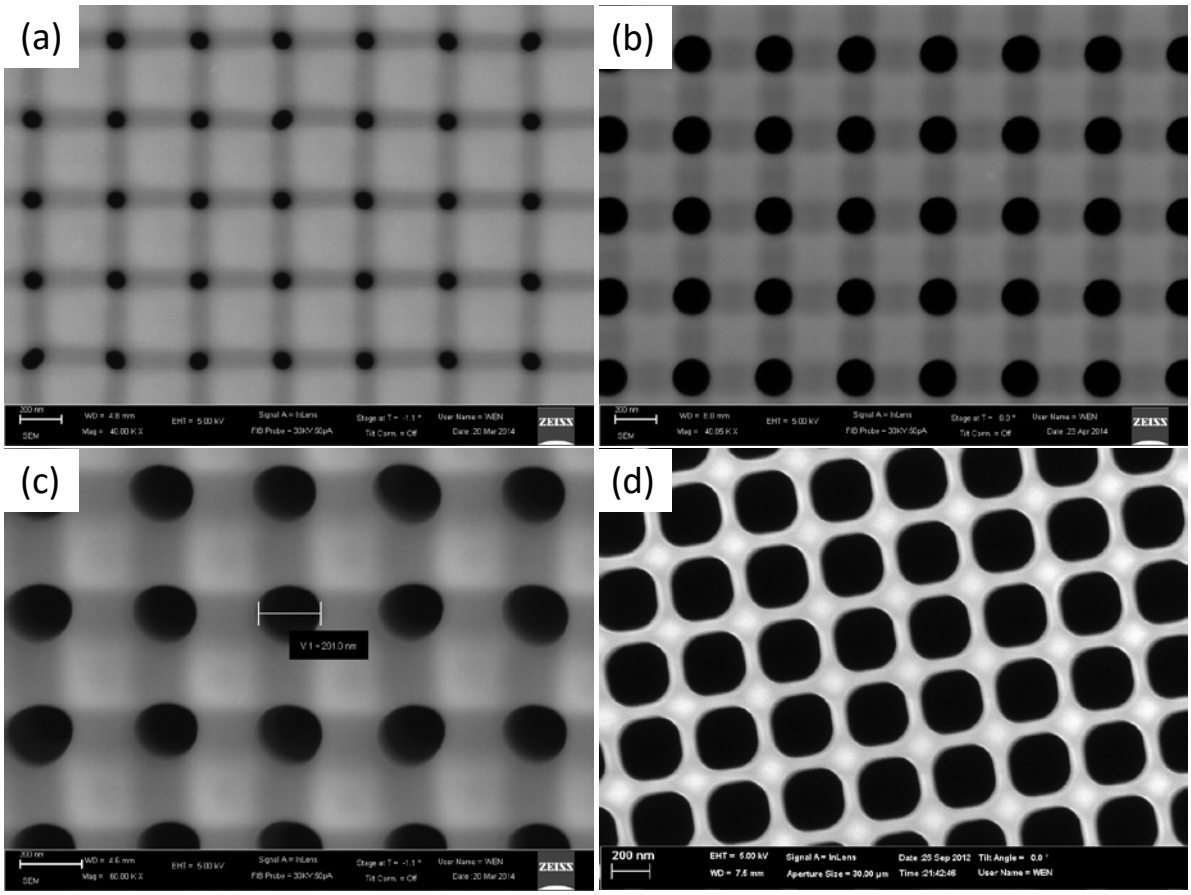

Figure 5-2| (a) Top-view SEM image of the fresh anodized regular AAO template. And the top-view SEM images of AAO templates with different time of post-treatment by 5 % of H_3PO_4 solution at 30 ^oC: (b), (c), and (d) for 30 min, 60 min, and 120 min, respectively.

The three-dimensional Pt/MnO_2 nanotube array was fabricated based on regular AAO template, which was prepared as describe in section 2.1.6.1. The thickness of AAO template (the length of nanopore) could be very easily controlled by the anodizaiton time. And the diameter of nanopore could be very easily adjusted by the post-treatment process. As shown in Figure 5-2a, the prepared AAO template with a regular pore structure, each of the pore with a diameter larger than 100 nm. And four of the neighboring pores composed a square shape with 400 nm of side length of the square. After 15 min of anodization at 160 V during 15 ^{o}C, the nanopore of AAO template has a length of around 2 µm (Figure 5-2b). Applied with different post-treatment time of anodized AAO template by 5 % of H_3PO_4 solution at 30 ^{o}C, could obtain different diameter pore size of AAO template (Figure 5-2c-e). Different anodization conditions and wet-chemical post-treatment were applied to obtain the desirable pre-patterned alumina templates

5.2.1.2. Pt nanotube array

After the fabrication of regular AAO template, a 100-cycle conventional ALD process (the blue line in Figure 2-12) was used for the Pt growth. Dispersed Pt nanoparticles were formed on the surface of the template (Figure 5-3a). After 200 ALD cycles, the dispersed Pt nanoparticles coalesce into a porous film (Figure 5-3b), and this behavior is consistent with the Volmer-Weber island growth model of metal films on oxide surfaces [38]. With 200 ALD cycles, the infiltration depth of Pt in the AAO template was less than 2 µm (Figure 5-3c).

Instead of using the conventional process, we introduce an innovative ALD process for Pt growth, where a low N_2 filling step is used after pulsing (as illustrated in the orange dot line of Figure 2-12). Figure 5-3d shows the template surface after 100 cycles with a 60 s of low-filling-N_2 step, where Pt porous film already appeared. This demonstrated that the nucleation delay phenomenon of the Pt ALD growth in our process is largely decreased and about half of the Pt precursor can be saved to obtain a similar Pt film. When the cycle number was increased to 200 (Figure 5-3e), the porous Pt film further transforms to a compact film. Importantly, the infiltration depth of the Pt NTs inside the template pores reaches about 5 µm, which is approximately 2.5 times of the infiltration depth in the conventional process presented in Figures 5-3c.

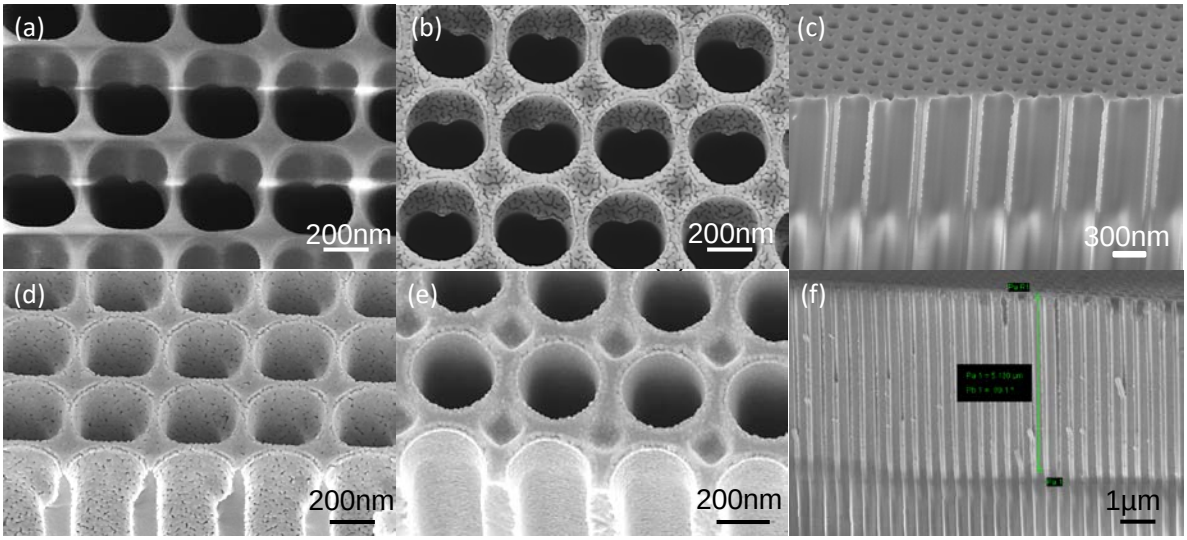

Figure 5-3| Top-view SEM image of ALD growth of Pt nanotube based on regular AAO template with different conventional ALD cycle numbers :(a) 100 ALD cycles, (b) 200 ALD cycles, and (c) the cross-section SEM image of (b). Top-view SEM image of ALD growth of Pt nanotube based on regular AAO template with different low-filling-N_2 ALD cycle numbers :(d) 100 ALD cycles, (e) 200 ALD cycles, and (f) the cross-section SEM image of (e).

The surface morphology and the length of ALD deposited Pt nanotubes could further adjusted by the ALD growth conditions. To investigate the influence of the low N_2 filling step on the Pt infiltration depth inside the pores, a series of experiments were conducted in which the low N_2 filling time was adjusted in the range of 0 – 90 s. It was revealed in Figures 5-4a-d that the infiltration depth increases with the increment of the low N_2 filling time, where a maximum depth of about 6 µm was obtained when the time was increased to 90 s (Figure 5-4d). Since the pore diameter was about 260 nm, the aspect ratio of Pt NTs increases about 3.5 times (from 7 to 23) with the same Pt precursor pulsing time of 1.3s. Based on previous reports, the Pt infiltration depth in nanopores versus the Pt precursor pulsing time shows a square root dependence (Pt infiltration depth $\propto$ Pt pulsing time$^{1/2}$), which belongs to the diffusion-limited regime of ALD coating on nanopores [29,43]. However, differs from the above-mentioned relationship, the Pt infiltration depth versus the low N_2 filling time shows good square root dependence (Pt infiltration depth $\propto$ Low N_2 filling time$^{1/2}$) in our ALD process (Figure 5-4e). In the conventional ALD process, about 12 s of Pt precursor pulsing was required to obtain Pt nanotubes with an infiltration depth of 6 µm. This assumption was also supported by previous experiment results, where up to 30 s of Pt

precursor pulsing time was used for growing about 10 µm Pt NTs inside the alumina template [30]. However, when a 90 s of low N_2 filling step was introduced into ALD process, only 10 % Pt precursor pulsing time was required for the similar Pt infiltration depth. It clearly indicates that the Pt precursor pulsing time can be largely shortened with the additional low N_2 filling step in the Pt nanotube growth.

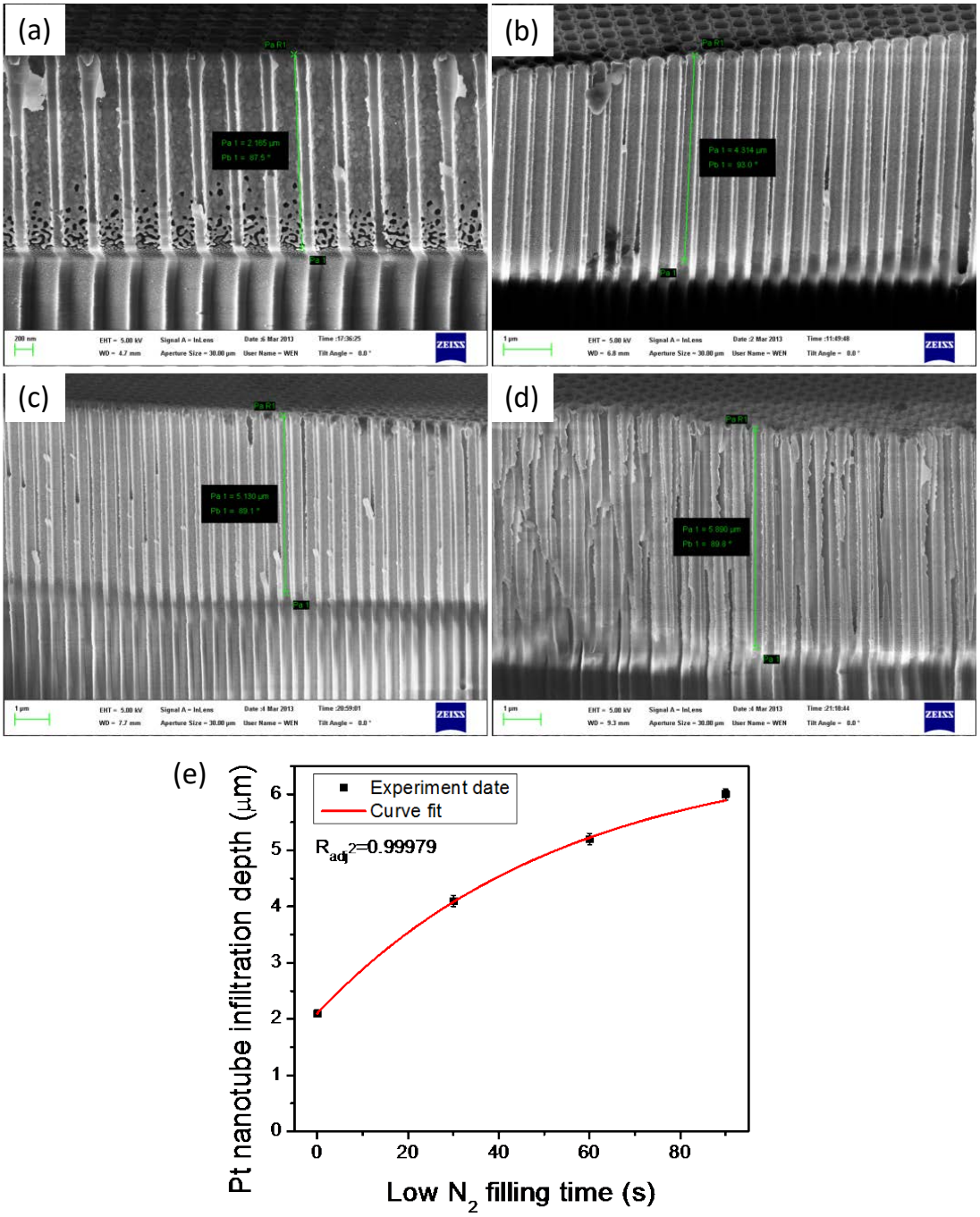

Figure 5-4| SEM images of Pt NTs after different ALD processes: (a) Pt pulsing (1.3 s) - N_2 purging (18 s); (b) Pt pulsing (1.3 s) - low N_2 filling (30 s) - N_2 purging (18 s); (c) Pt pulsing

(1.3 s) - low N_2 filling (60 s) - N_2 purging (18 s); (d) Pt pulsing (1.3 s) - low N_2 filling (90 s) - N_2 purging (18 s); and (e) dependence of the Pt infiltration depth on the low N_2 filling time.

Besides the low N_2 filling time, the Pt precursor pulsing time is also one of the main influences for the Pt infiltration depth. Therefore, the influence of Pt precursor pulsing time on Pt infiltration depth was also studied. When the Pt pulsing time increased from 0.5 to 2.1 s with the same N_2 low filling step of 30 s, the Pt infiltration depth only extends to about 5.3 µm (as shown in Figure 5-5a and b). Even so, this value was still less than that of the Pt NTs obtained from a shorter pulsing (1.3 s) but a longer low N_2 filling (90 s) process.

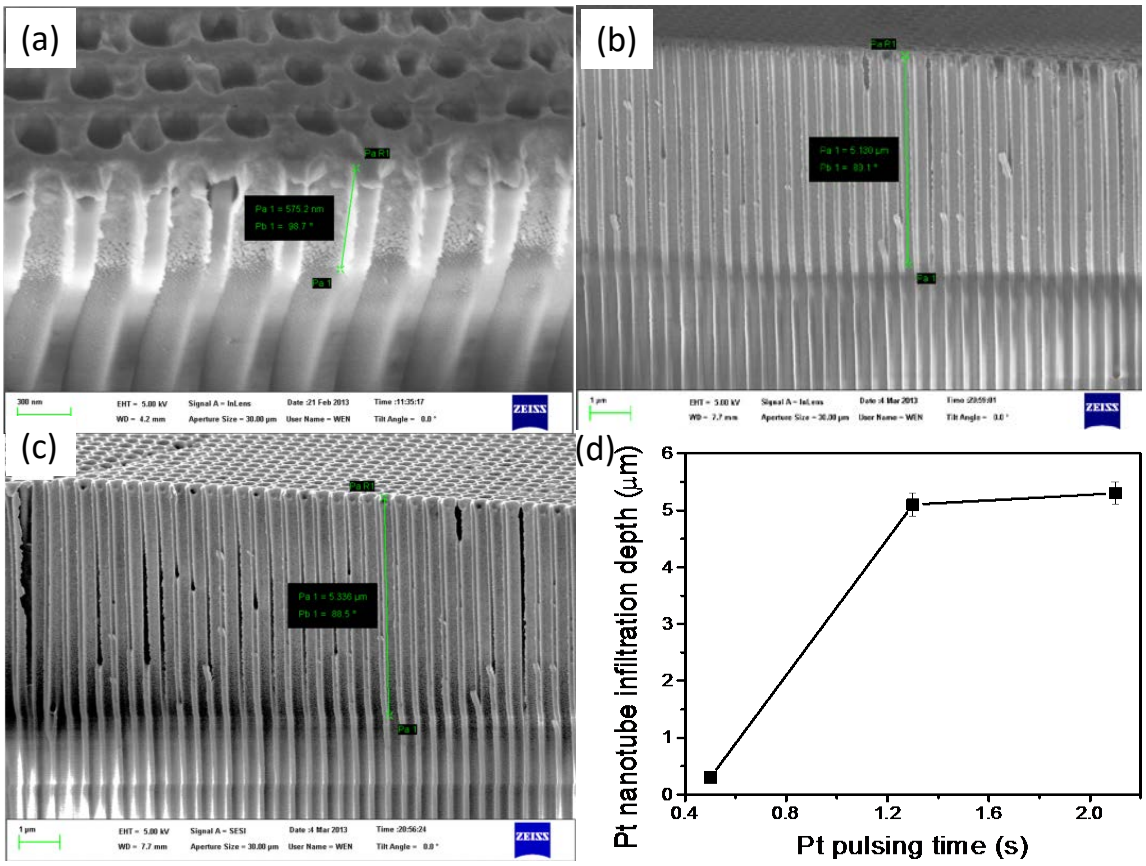

Figure 5-5| SEM images of Pt NTs after different ALD processes: (a) Pt pulsing (0.5 s) - low N_2 filling (30 s) - N_2 purging (18 s); (b) Pt pulsing (1.3 s) - low N_2 filling (60 s) - N_2 purging (18 s); (c) Pt pulsing (2.1 s) - low N_2 filling (30 s) - N_2 purging (18 s). And (d) the relationship of the Pt infiltration depth to the Pt precursor pulsing time.

It is well known that there are two main requirements for the thermal ALD growth of Pt on oxide substrates: (i) adsorption of the Pt precursor ($MeCpPtMe_3$) and (ii) elimination of the

precursor ligands. For the Pt growth within a nano-porous template, the Pt coverage is typically determined by the material surface, the applied pressure and the precursor pulsing time [42,43]. Whereas using the same Pt precursor pulsing time and the same template, the low N_2 filling step builds up a higher Pt precursor partial pressure. The higher-pressure condition not only enhances the Pt precursor diffusion and adsorption inside the pores, but also largely extends the nucleation time of the Pt nanoparticles on oxide surfaces, as shown in Figure 5-5c Therefore, instead of extending Pt precursor pulsing time, introducing a low N_2 filling step in Pt ALD process is an efficient choice for realizing high aspect ratio Pt nanotubes with an ultra-less Pt precursor consumption. The growth conditions and the relevant length of Pt nanotubes fabricated by ALD were summarized in Table 5-1.

Table 5-1| The growth conditions and the relevant lengths of Pt nanotubes by ALD

Pt deposition at constant purge time: 30 s, pulse time: 1.3 s				
Pt precursor fill time	0 s	30 s	60 s	90 s
Pt nanotubes length	2.1 ±0.1 µm	4.4 ±0.2 µm	5.0 ±0.2 µm	5.9 ±0.2 µm
Pt deposition at constant purge time: 30 s, pulse fill time: 60 s				
Pt precursor pulse time	0.5 s	1.3 s	2.1 s	
Pt nanotubes length	0.3 ±0.05 µm	5.0 ±0.2 µm	5.3 ±0.2 µm	

According to the above mentioned results, here, a pre-patterned alumina template with a thickness of about 6.0 µm was used to prepare continuous Pt nanotube array with the 90 s of low N_2 filling step. The SEM images in Figure 5-6 presented the appearances of the fabricated Pt nanotube array. Figure 5-6a was the cross-sectional view of the prepared sample. It can be seen that the whole surface of the template was covered with continuous Pt film after 200 cycles of ALD growth. The right two images (Figure 5-6b and c) were the enlarged views of the top and bottom part of the sample, respectively. It is clear that the inside surface of Pt nanotubes at the top was more compact and smooth than those at the bottom part. Even so, the Pt nanotube was still a continuous film.

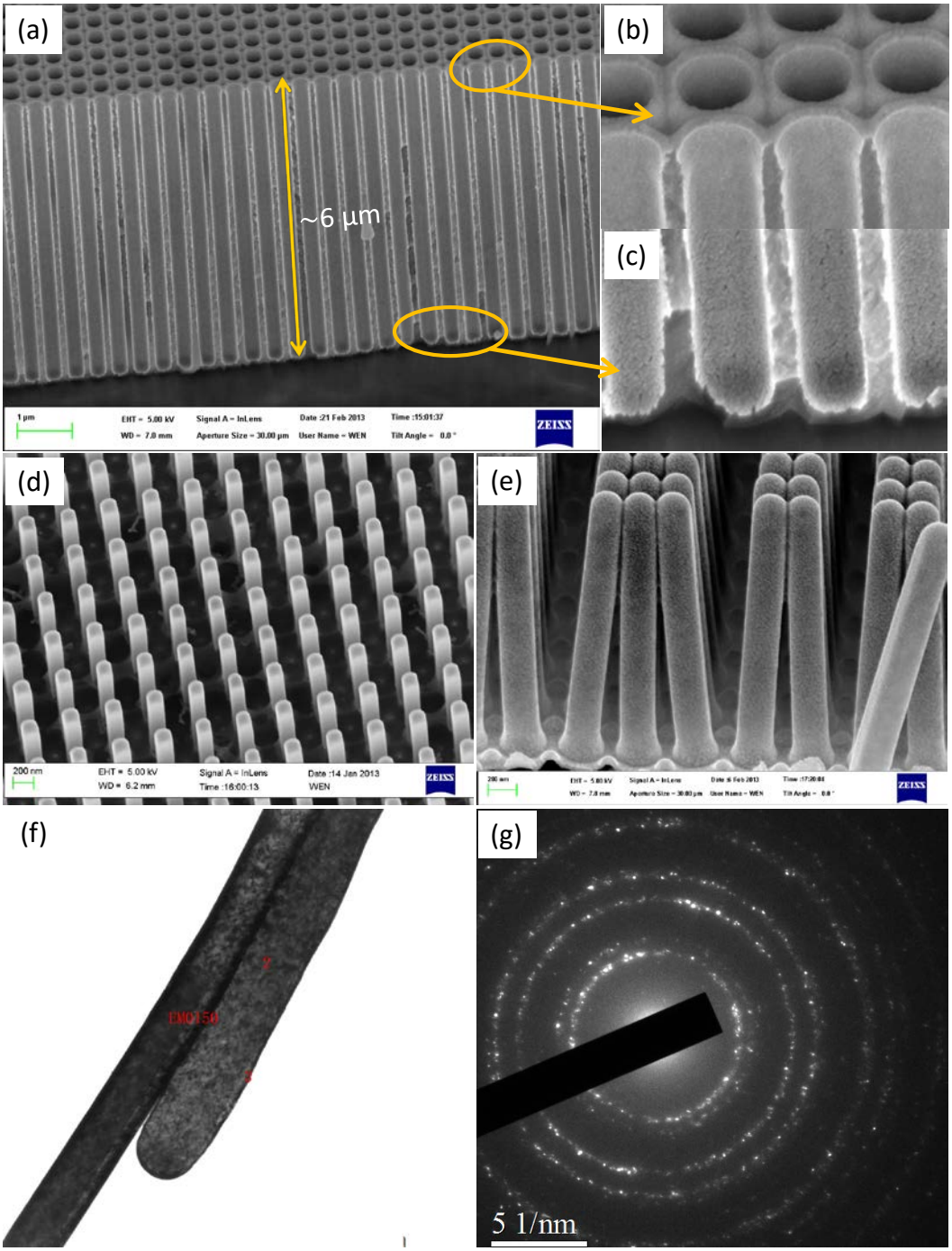

Figure 5-6| (a) The cross section SEM image of Pt nanotubes after 200 cycles of ALD growth using the innovative process. The enlarged SEM images of the top (b), and bottom part (c) of sample was shown in (a). SEM images of the free-standing Pt nanotube array after the AAO template was partly (d) and completed (e) removed. (f) The TEM image of the bottom part of individual Pt nanotube, and (g), the corresponding selected area electron diffraction (SAED) of number 2 in (f).

The continuity of the deposited Pt nanotubes was further verified by the SEM images free-standing Pt nanotubes after remove of the AAO template. As can be seen in Figure 5-6d,

after partly removal of AAO template from back side of template, they were free-standing regular Pt nanotube array, with smooth and continuous closed tube bottom. After totally removal of the AAO template, they were top connected nanotube array (Figure 5-6d). The outside surface of nanotube was smooth and continuous (Figure 5-6e). Those results were further confirmed by the TEM image of the bottom part for an individual Pt nanotube (Figure 5-6f). Furthermore, the structure information of the growth Pt nanotube was investigated by the selected area electron diffraction (SAED) pattern. As can be seen in Figure 5-6g, the SAED pattern shows circular diffraction pattern. And those cycle ring were composed by bright spots. That means the fabricated Pt nanotube by ALD is polycrystalline.

5.2.1.3. Three-dimensional Pt/MnO_2 nanotube array

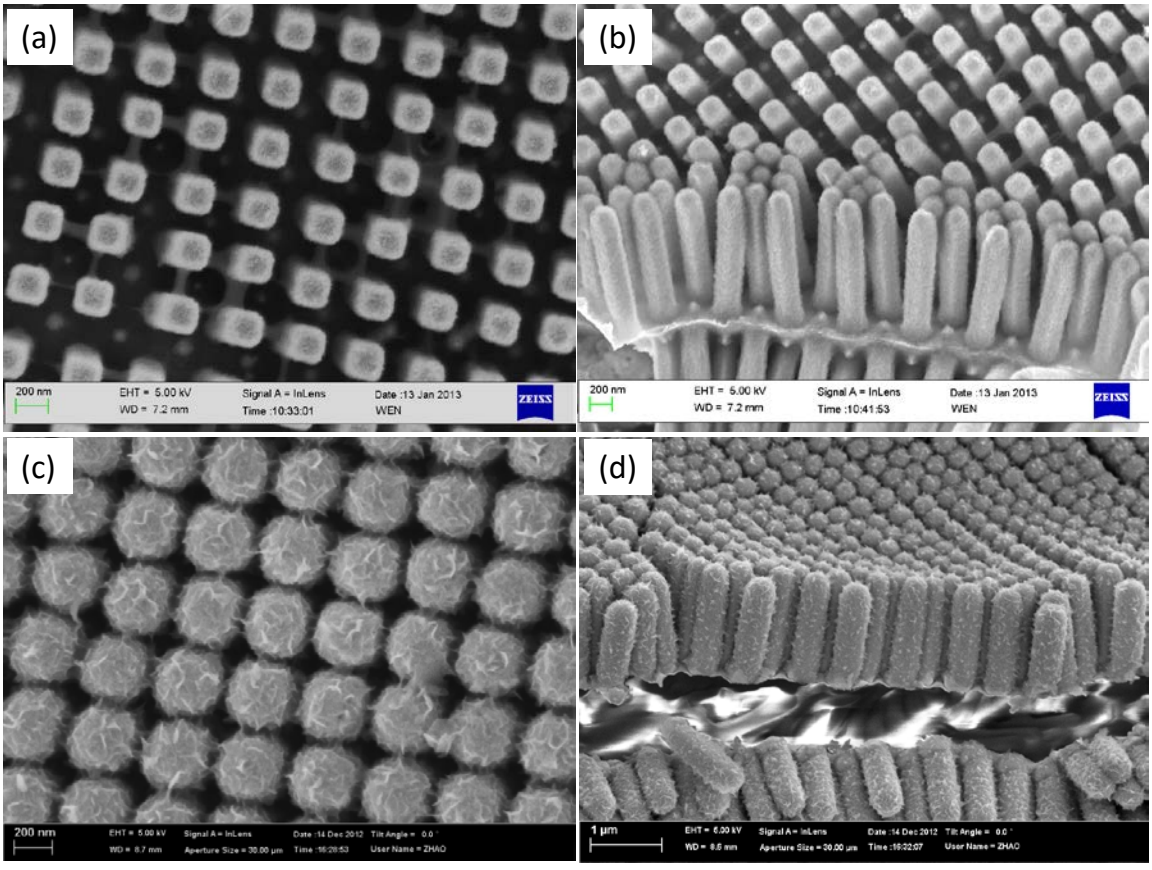

Figure 5-7| (a) and (b), the top view and cross section SEM images of MnO_2 shell on Pt nanotubes after 30 s of deposition, respectively. (c) and (d), the top view and cross section SEM images of MnO_2 shell on Pt nanotubes after 90 s of deposition, respectively.

The above mentioned Pt nanotube array fabricated based on regular AAO template with a length of around 2 µm was chosen for the following construction of three-dimensional Pt/MnO_2 nanotube array, to avoid the top connect of each nanotubes.

Pt nanotubs with about 180 nm tube diameter and 2 µm length were used for growing core/shell Pt/MnO_2 nanotubes for supercapacitor application. MnO_2 shells were electrodeposited on Pt cores [44–46]. The overall core-shell nanotube diameter (and hence the thickness of MnO_2 shell) can be adjusted by controlling the MnO_2 deposition time: the tube diameter and the shell thickness were about 240 and 30 nm when the deposition time was 30 s (Figure 5-7a and b), while the diameter and thickness reach up to about 340 and 80 nm respectively for 90 s of deposition time (Figure 5-7c and d). These pre-defined core-shell Pt/MnO_2 nanotube array was used to construct supercapacitor electrodes.

5.2.2. Chemical and element composition

Besides the structure and morphology information that studied by SEM, the corresponding EDS and XPS spectroscopy were performed to investigate the elements composition and chemical states properties of the prepared three-dimensional core/shell Pt/MnO_2 nanotube array.

5.2.2.1. Elements composition

The element composition was studied by EDS present in Figure 5-8a. As shown in the EDS spectroscopy, there have elements of Pt, O, Mn, C and Si. The Figure 5-8b presented the SEM image of EDS mapping area (20 µm × 20 µm) and corresponding individual EDS mapping of platinum, oxygen and manganese elements in that area. It clearly presents the dispersion and distribution of each element on the three-dimensional nanotube array nanostructure. The EDS line-scanning across a single Pt/MnO_2 nanotube also be investigated. And the result further confirmed the structure and elements composition of Pt/MnO_2 nanotube.

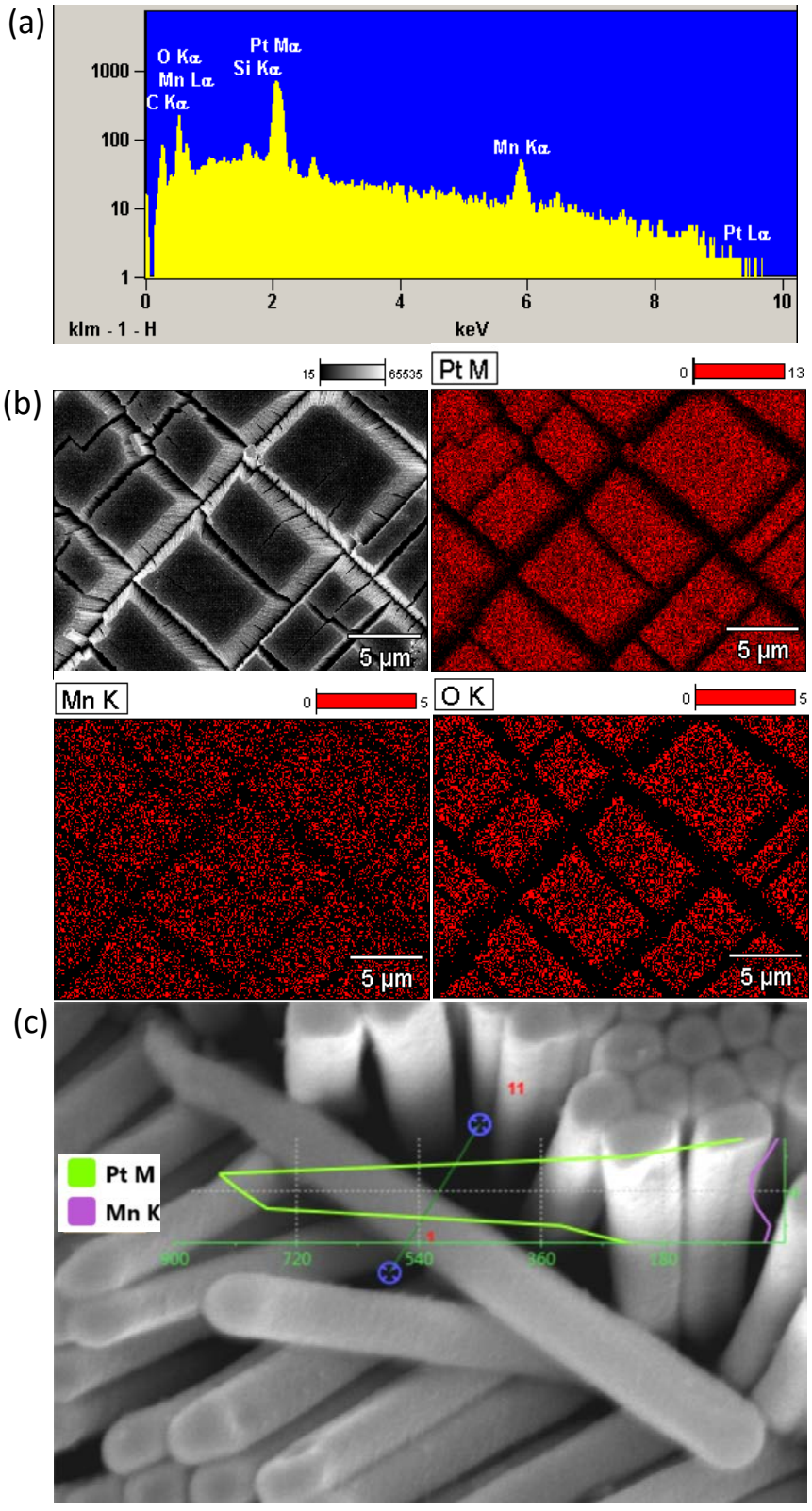

Figure 5-8| (a) the EDS spectrum of prepared three-dimensional Pt/MnO_2 nanotube array; (b) EDS mapping of the platinum, oxygen and manganese elements on a 20 µm × 20 µm area; (c) EDS line scan of a single Pt/MnO_2 nanotube.

5.2.2.2. Chemical states analysis

The chemical states information of the fabricated three-dimensional Pt/MnO_2 nanotube based on regular AAO template was performed by XPS measurement. As displayed in Figure 5-9, there only has the signal from Pt. Since the penetrating depth of XPS measurement is about 10 nm, the lack of the Al_2O_3 XPS signal from the underlying alumina template agrees for the continuous characteristic of the Pt nanotubes [47,48].

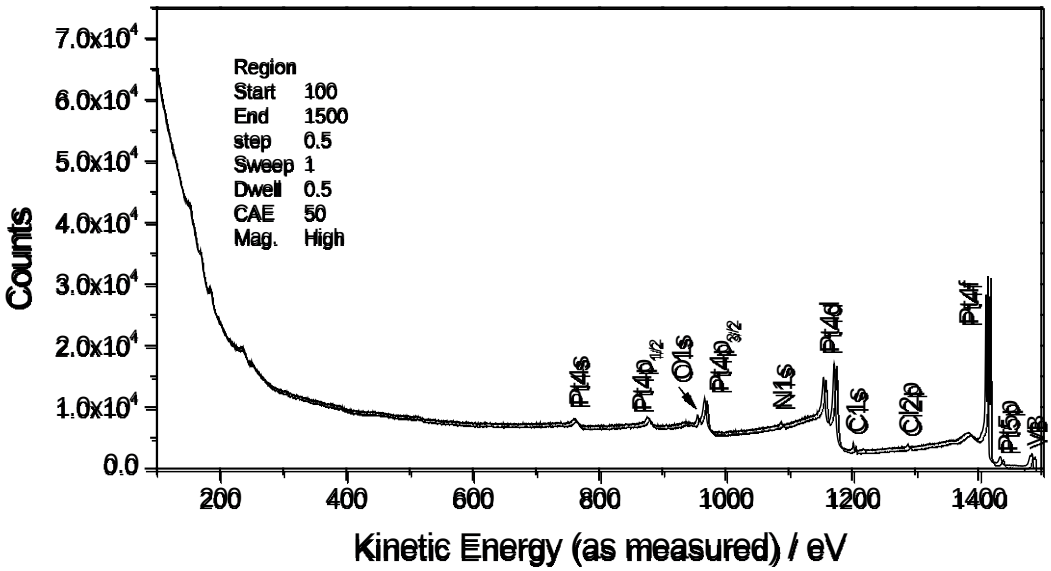

Figure 5-9| XPS data of the Pt nanotubes after 200 cycles of ALD growth using the innovative process.

5.2.3. Conductivity

Pt nanotube array with about 180 nm nanotube diameter and 2 µm nanotube length was used for growing core/shell Pt/MnO_2 nanotube array for supercapacitor applications. Therefore, the conductivity of the Pt nanotube is important to device fabrication. Thus, the conductivity of the fabricated Pt nanotube array was investigated by a four-probe station.

Four silver pastes (denoted as electrode a, b, c and d) were connected to the four edges of the sample, constructing two pairs of measuring electrodes (Figure 5-10a). The sheet

electrical resistance of the continuous Pt nanotube film was as low as 3.4 Ω·cm^{-2}. And there was only small variation between the two different pairs (Figure 5-10b).

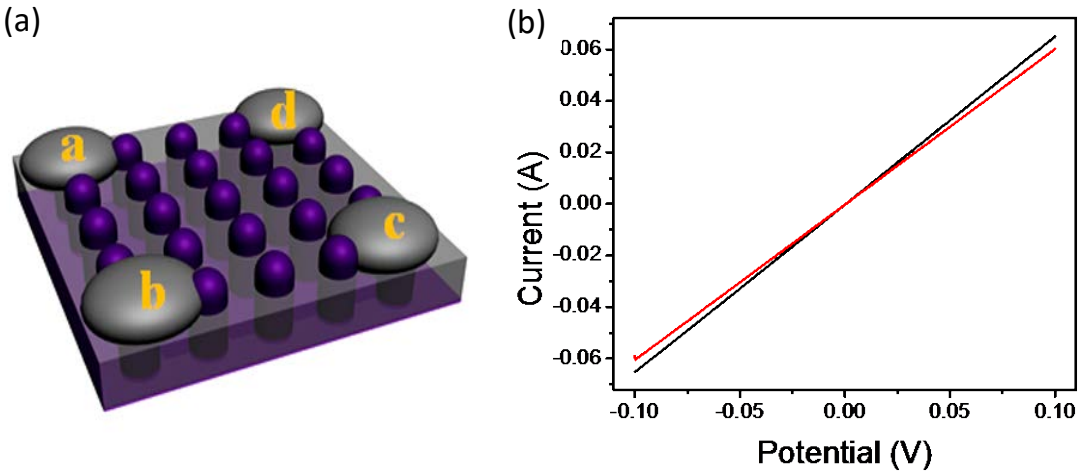

Figure 5-10| (a) The schematic of the conductivity measurement setup with two pairs of electrodes (a and c, b and d) the inter-electrode distance is about 0.7 cm. (b) I-V curves of Pt nanotube array after partially etching the backside template.

5.2.4. Electrochemical performance

In order to study the performance of the core/shell Pt/MnO_2 nanotube array for electrochemical energy storage, cyclic voltammetry (CV) and galvanostatic charge-discharge were measured in a voltage window of 0-0.9 V. And the mass of the MnO_2 was determined from the charge passed during electrochemical deposition and assumes 100% efficiency. The calculated mass of MnO_2 was ~ 0.094 mg·cm^{-2} and ~ 0.216 mg·cm^{-2} for 30 s and 90 s MnO_2 deposition electrodes, respectively.

The CV tests were performed on four samples at a scan rate of 20 mV·s^{-1} in 1.0 M Na_2SO_4: bare Pt nanotube array (denoted as NT electrode), 30 s deposition of Pt/MnO_2 nanotube array (denoted as 30s-NT electrode), 90 s deposition of Pt/MnO_2 nanotube array (denoted as 90s-NT electrode), MnO_2 on a Pt planar film (denoted as PF electrode) with same mass loading of the 30s-NT sample (Figure 5-11a). The enclosed areas of the CV curves became much larger after MnO_2 loading, which revealed that the Pt electrode contribution to the capacitance can be ignored. The CV curves of the 30s-NT and 90s-NT electrodes had a clear quasi-rectangular shape, indicating their ideal electrical double-layer capacitance behaviors.

On the contrary, the CV curve of the PF electrode was much worse compared to the NT electrodes.

Meanwhile, the rate-dependent CVs of the typical 30s-NT electrode were investigated from 5 to 100 mV·s^{-1} (Figure 5-11b). All the curves maintained a nearly ideal capacitive CV shape with only small distortions, showing remarkable rate capabilities of the electrode.

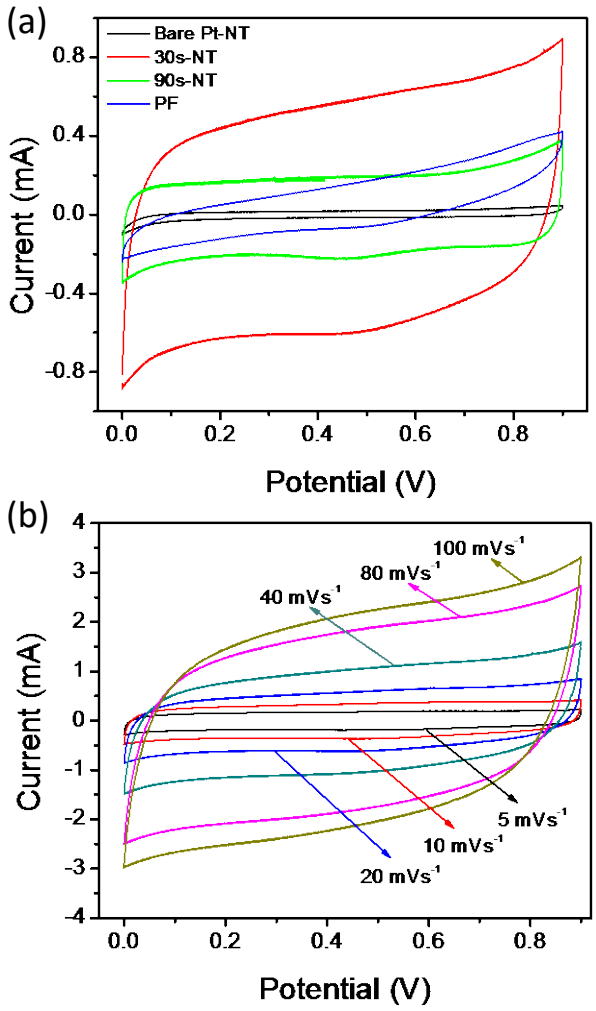

Figure 5-11| (a) The CVs of bare Pt-NT, 30s-NT, 90s-NT and PF electrode at a scan rate of 20 mV·s^{-1}. (b) Typical CVs of the 30s-NT electrode at different scan rates from 5 to 100 mV·s^{-1}.

The gravimetric specific capacitance (Csp) of core/shell MnO_2/Pt nanotube array electrode was calculated from CV in 1.0 M Na_2SO_4 using Equation 5-1[32,49,50]:

$$C_{sp} = \frac{Q}{\Delta V * m} \qquad \text{(Equation 5-1)}$$

Where C_{sp} is specific capacitance, Q is the total charge integrated from the CVs, ΔV is the width of potential window 0.9 V, and m is the mass of deposited MnO_2.

The specific capacitance, energy density (d_e), and power density (d_p) were also calculated from the chronopotentiometric curves according to Equations 5-2 to 5-4:

$$C_{sp} = \frac{I\Delta t}{m\Delta V} \quad \text{(Equation 5-2)}$$

$$d_e = \frac{1}{2} C_{sp} (\Delta \mathrm{V})^2 \quad \text{(Equation 5-3)}$$

$$d_p = \frac{d_e}{\Delta t} \quad \text{(Equation 5-4)}$$

Where the I is the charge/discharge current, Δt is the time for a full charge or discharge, m is the mass of the active MnO_2 electrodes, and ΔV is the voltage change after a full charge or discharge.

And the areal specific capacitance (*Casp*) can be calculated as

$$C_{asp} = \frac{Q}{\Delta V * a} or \frac{I\Delta t}{a\Delta V} \quad \text{(Equation 5-5)}$$

Where the a is the area of the MnO_2 active electrodes (about 0.50 cm^2) and the other values are the same as before described.

After the measurement of rate-dependent CVs, the (*Csp*) versus the scan rate was summarized in Figure 5-12a. It demonstrated that the capacitance of the 30s-NT electrode reaches to 810 $F \cdot g^{-1}$ at the scan rate of 5 $mV \cdot s^{-1}$ (Equation 5-1). Meanwhile, the areal specific capacitance (*Casp*) also reached up to 75 $mF \cdot cm^{-2}$ (Equation 5-5). Even when the deposition time increases to 90 s, the electrode *Csp* still kept at 550 $F \cdot g^{-1}$ (119 $mF \cdot cm^{-2}$). The *Csp* of the 30s-NT electrode and 90s-NT electrode yield much better performance at all scan rates compared with the PF electrode. For the 30s-NT electrode, the typical one-cycle charging-discharging behavior from the current density of 20 to 100 $A \cdot g^{-1}$ (Figure 5-12b) and the representative linear voltage-time profiles at 2 $A \cdot g^{-1}$ (Figure 5-12c) showed high symmetric natures in all current densities. The summary plot of *Csp* versus current density

demonstrates that the 30s-NT electrode reached up to 793 F·g^{-1} (73 mF·cm^{-2}) at 2 A·g^{-1} and this value is still at 530 F·g^{-1} (114 mF·cm^{-2}) when the deposition time was increased to 90 s (Figure 5-12d and Equation 5-2 to 5-5). And both the NT-electrodes had a much better performance than that of the PF electrode in all current densities.

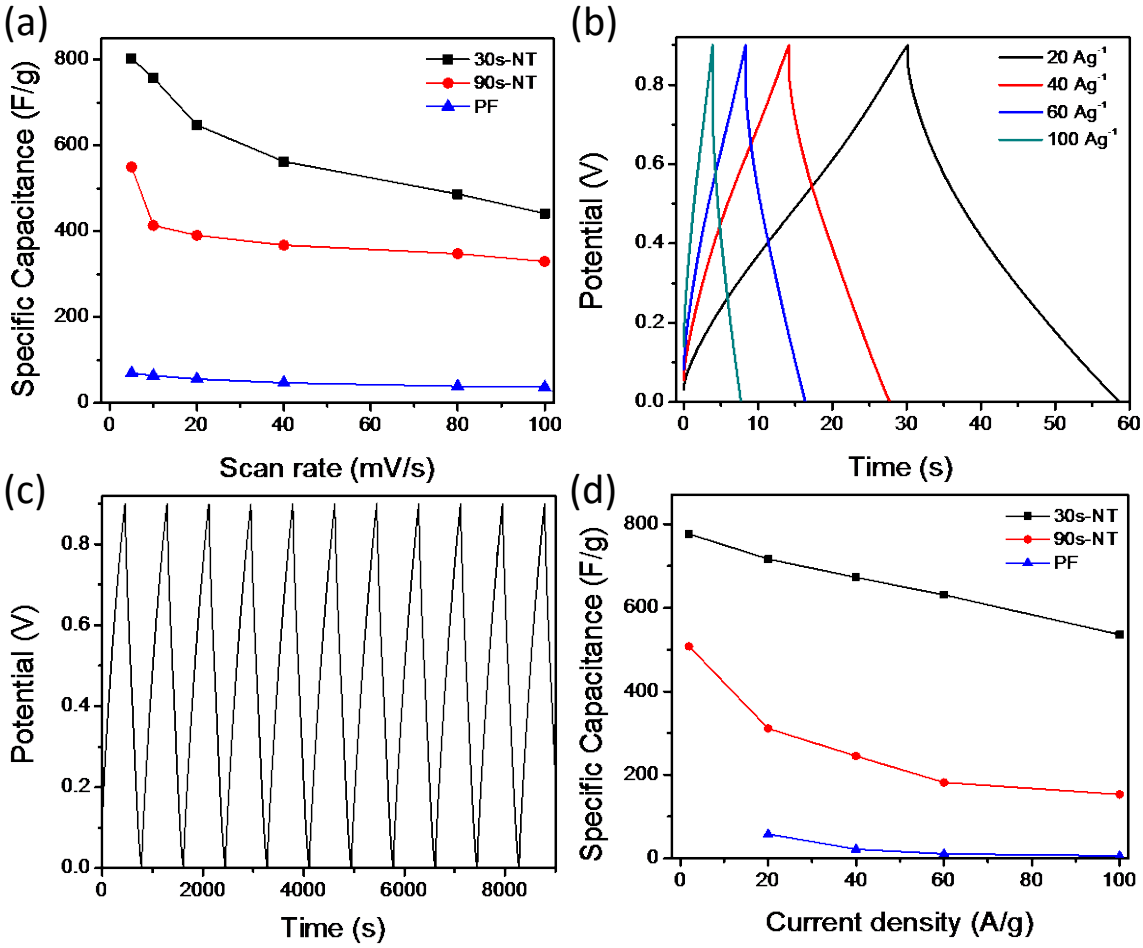

Figure 5-12| (a) Specific capacitance curves of the 30s-NT, 90s-NT and PF electrodes at the different scan rates. (b) Representative linear voltage-time profiles for the charging and discharging of the 30s-NT electrode at high current densities from 20 to 100 A·g^{-1}. (c) The representative linear voltage-time profiles of the 30s-NT electrode for the charging and discharging at a current density of 2 A·g^{-1}. (d) The summary plot of *Csp* versus current density of the 30s-NT, 90s-NT and PF electrodes.

Most importantly, when the current density of the 30s-NT electrode increases to 100 A·g^{-1}, the *Csp* still keeps at 542 F·g^{-1} (50 mF·cm^{-2}), which retains at about 68 % capacitance of the *Csp* at 2 A·g^{-1}. For most of the previously reported core/shell and hybrid nanostructures (e.g., Au/MnO_2 nanopores [3], Au/MnO_2 nanowires [51] and AuPd/MnO_2 nanorods [52]), the *Csp*

were very high at low current densities while it decreased dramatically at high current densities. The good rate capability of our Pt/MnO_2 NT arrays electrodes can be attributed to the superior Pt NT collector, which provides not only a highly accessible surface area but also appropriate gaps among the adjacent NTs for fast and reversible Faradic reactions and short ion diffusion paths.

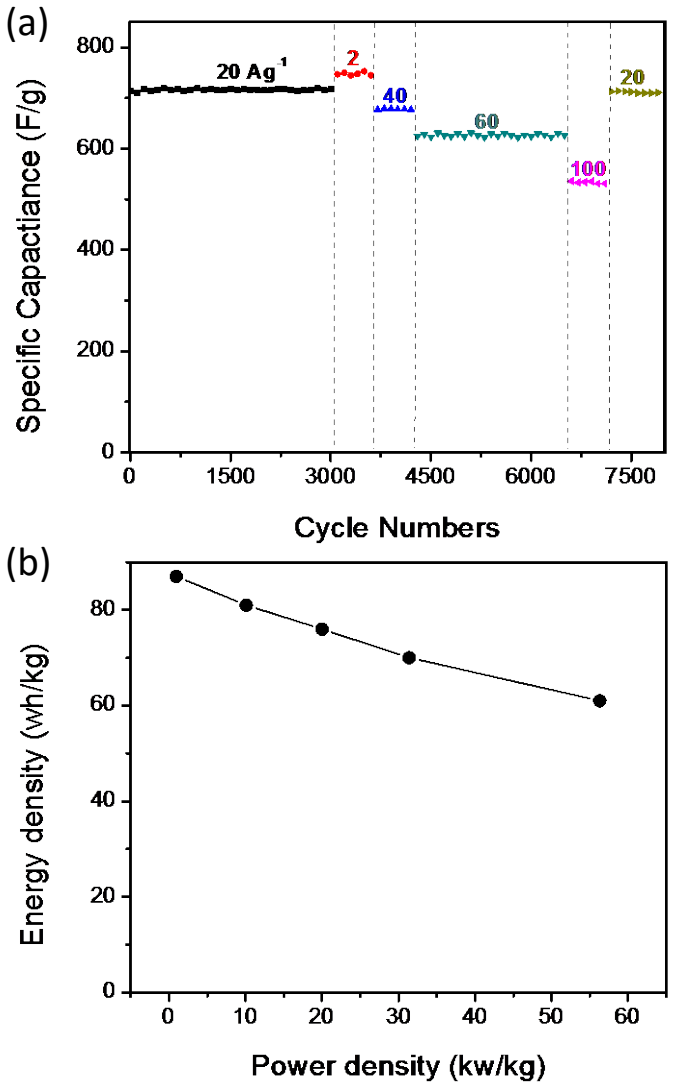

Figure 5-13| (a) Cycling stability of the 30s-NT electrode at random current densities up to 8000 cycles. (b) Ragone plots (energy density vs power density) of 30s-NT electrode at various current densities.

The long-term cycle stability of the 30s-NT electrode was also evaluated. The *Csp* as a function of cycle number was presented in Figure 5-13a, where a negligible *Csp* loss at 20

A·g^{-1} was observed over the first 3000 cycles. After that, random charging and discharging with current densities from 2 to 100 A·g^{-1} was carried out up to 8000 cycles and the electrode still presented a high cycle stability and a negligible capacitance loss after such a sudden variation.

Moreover, the Ragone plot (power density vs energy density) of the electrode at various current densities was shown in Figure 5-13b, which delivered a high power density of about 56 kW·kg^{-1} at the energy density of about 61 kW·h·kg^{-1}. The energy and power density in this study revealed that our Pt/MnO_2 NT-based electrodes fulfil the power requirement (15 kW·kg^{-1}) for PNGV (Partnership for a New Generation of Vehicles).

5.3. Conclusions

In summary, in this chapter, it successfully established an innovative ALD process to grow regular arrays of Pt nanotube array on pre-patterned alumina templates, in which a low N_2 filling step was introduced. It was demonstrated that with the low N_2 filling step, half Pt precursor ALD cycles can be saved for growing similar Pt films. Additionally, Pt NTs with an infiltration depth up to 6 µm were achieved and the aspect ratio of Pt nanotubes increased about 3.5 times (from 7 to 23) with the same Pt precursor pulsing time of 1.3 s. For obtaining an identical infiltration depth in the conventional process, about ten times of Pt precursor pulsing time was required. The presented approach here should be applicable to obtain other noble metal nanostructures, since they have the similar ALD reaction mechanisms to that of Pt.

Meanwhile, the fabricated three-dimensional Pt/MnO_2 core/shell nanotube array on a PDMS substrate was explored for high-performance supercapacitor application. This core-shell nanotube electrode exhibited a high gravimetric and areal specific capacitance (810 F·g^{-1} and 75 mF·cm^{-2} at 5 mV·s^{-1}) as well as an excellent rate capability (68 % capacitance retention from 2 to 100 A·g^{-1}). A negligible capacitance loss was observed after 8000 random charging-discharging cycles from 2 to 100 A·g^{-1}. These good performances can be attributed to the well-defined Pt nanotube array, which provided a high accessible surface area and inter-tube gaps for fast and reversible Faradic reactions and short ion diffusion paths. Overall, the Pt nanotube array demonstrated here provided a desirable candidate structure for high-

performance supercapacitors as well as for other Pt-based nano-devices such as energy storage elements, transistors and sensors.

5.4. Bibliography

[1] M.E. Stewart, C.R. Anderton, L.B. Thompson, J. Maria, S.K. Gray, J.A. Rogers, et al., Nanostructured Plasmonic Sensors, Chem. Rev. 108 (2008) 494–521. doi:10.1021/cr068126n.

[2] H. Zhang, X. Yu, P. V Braun, Three-dimensional Bicontinuous Ultrafast-charge and -discharge Bulk Battery Electrodes, Nat Nano. 6 (2011) 277–281. http://dx.doi.org/10.1038/nnano.2011.38.

[3] X. Lang, A. Hirata, T. Fujita, M. Chen, Nanoporous Metal/oxide Hybrid Electrodes for Electrochemical Supercapacitors, Nat Nano. 6 (2011) 232–236. http://dx.doi.org/10.1038/nnano.2011.13.

[4] D.F. van der Vliet, C. Wang, D. Tripkovic, D. Strmcnik, X.F. Zhang, M.K. Debe, et al., Mesostructured Thin Films as Electrocatalysts with Tunable Composition and Surface Morphology, Nat Mater. 11 (2012) 1051–1058. http://dx.doi.org/10.1038/nmat3457.

[5] M.K. Debe, Electrocatalyst Approaches and Challenges for Automotive Fuel Cells, Nature. 486 (2012) 43–51. doi:10.1038/nature11115.

[6] K. Yoshioka, Y. Minami, K. Shudo, T.D. Dao, T. Nagao, M. Kitajima, et al., Terahertz-Field-Induced Nonlinear Electron Delocalization in Au Nanostructures, Nano Lett. 15 (2015) 1036–1040. doi:10.1021/nl503916t.

[7] Z. Weng, W. Liu, L.-C. Yin, R. Fang, M. Li, E.I. Altman, et al., Metal/Oxide Interface Nanostructures Generated by Surface Segregation for Electrocatalysis, Nano Lett. 15 (2015) 7704–7710. doi:10.1021/acs.nanolett.5b03709.

[8] G. Schatz, Metal Nanostructures, J. Phys. Chem. Lett. 1 (2010) 2980–2981. doi:10.1021/jz101284n.

[9] E.P. Lee, Z. Peng, D.M. Cate, H. Yang, C.T. Campbell, Y. Xia, Growing Pt Nanowires as a Densely Packed Array on Metal Gauze, J. Am. Chem. Soc. 129 (2007) 10634–10635. doi:10.1021/ja074312e.

[10] X. Yu, S. Ye, Recent Advances in Activity and Durability Enhancement of Pt/C catalytic Cathode in PEMFC: Part I. Physico-chemical and Electronic Interaction between Pt and

Carbon Support, and Activity Enhancement of Pt/C Catalyst, J. Power Sources. 172 (2007) 133–144. doi:http://dx.doi.org/10.1016/j.jpowsour.2007.07.049.

[11] E.P. Lee, Z. Peng, W. Chen, S. Chen, H. Yang, Y. Xia, Electrocatalytic Properties of Pt Nanowires Supported on Pt and W Gauzes, ACS Nano. 2 (2008) 2167–2173. doi:10.1021/nn800458p.

[12] S. Sun, F. Jaouen, J.-P. Dodelet, Controlled Growth of Pt Nanowires on Carbon Nanospheres and Their Enhanced Performance as Electrocatalysts in PEM Fuel Cells, Adv. Mater. 20 (2008) 3900–3904. doi:10.1002/adma.200800491.

[13] J. Shui, J.C.M. Li, Platinum Nanowires Produced by Electrospinning, Nano Lett. 9 (2009) 1307–1314. doi:10.1021/nl802910h.

[14] H.-W. Liang, X. Cao, F. Zhou, C.-H. Cui, W.-J. Zhang, S.-H. Yu, A Free-Standing Pt-Nanowire Membrane as a Highly Stable Electrocatalyst for the Oxygen Reduction Reaction, Adv. Mater. 23 (2011) 1467–1471. doi:10.1002/adma.201004377.

[15] M.S. Saha, V. Neburchilov, D. Ghosh, J. Zhang, Nanomaterials-supported Pt Catalysts for Proton Exchange Membrane Fuel Cells, Wiley Interdiscip. Rev. Energy Environ. 2 (2013) 31–51. doi:10.1002/wene.47.

[16] B.Y. Xia, W.T. Ng, H. Bin Wu, X. Wang, X.W. (David) Lou, Self-Supported Interconnected Pt Nanoassemblies as Highly Stable Electrocatalysts for Low-Temperature Fuel Cells, Angew. Chemie. 124 (2012) 7325–7328. doi:10.1002/ange.201201553.

[17] L. Su, W. Jia, C.-M. Li, Y. Lei, Mechanisms for Enhanced Performance of Platinum-Based Electrocatalysts in Proton Exchange Membrane Fuel Cells, ChemSusChem. 7 (2014) 361–378. doi:10.1002/cssc.201300823.

[18] A. Chen, P. Holt-Hindle, Platinum-Based Nanostructured Materials: Synthesis, Properties, and Applications, Chem. Rev. 110 (2010) 3767–3804. doi:10.1021/cr9003902.

[19] M. Carmo, R.C. Sekol, S. Ding, G. Kumar, J. Schroers, A.D. Taylor, Bulk Metallic Glass Nanowire Architecture for Electrochemical Applications, ACS Nano. 5 (2011) 2979–2983. doi:10.1021/nn200033c.

[20] Y. Li, Q. Wu, S. Jiao, C. Xu, L. Wang, Single Pt Nanowire Electrode: Preparation, Electrochemistry, and Electrocatalysis, Anal. Chem. 85 (2013) 4135–4140. doi:10.1021/ac400331w.

[21] W. Lee, S.-J. Park, Porous Anodic Aluminum Oxide: Anodization and Templated Synthesis of Functional Nanostructures., Chem. Rev. 114 (2014) 7487–7556. doi:10.1021/cr500002z.

[22] Y. Lei, C.H. Liang, Y.C. Wu, L.D. Zhang, Y.Q. Mao, Preparation of Highly Ordered Nanoporous Co Membranes Assembled by Small Quantum-sized Co Particles, J. Vac. Sci. Technol. B Microelectron. Nanom. Struct. 19 (2001) 1109–1114. doi:10.1116/1.1378011.

[23] Y.L. and W.K.C. and J.W. and G.W. and H.P.S. and X.Q. Pan, Ordered Arrays of Highly Oriented Single-crystal Semiconductor Nanoparticles on Silicon Substrates, Nanotechnology. 16 (2005) 1892. http://stacks.iop.org/0957-4484/16/i=9/a=079.

[24] M. Wu, L. Wen, Y. Lei, S. Ostendorp, K. Chen, G. Wilde, Ultrathin Alumina Membranes for Surface Nanopatterning in Fabricating Quantum-Sized Nanodots, Small. 6 (2010) 695–699. doi:10.1002/smll.200902038.

[25] L. Wen, Z. Shao, Y. Fang, K.M. Wong, Y. Lei, L. Bian, et al., Selective Growth and Piezoelectric Properties of Highly Ordered Arrays of Vertical ZnO Nanowires on Ultrathin Alumina Membranes, Appl. Phys. Lett. 97 (2010) 053106. doi:10.1063/1.3474615.

[26] S.R. Gowda, A. Leela Mohana Reddy, X. Zhan, H.R. Jafry, P.M. Ajayan, 3D Nanoporous Nanowire Current Collectors for Thin Film Microbatteries, Nano Lett. 12 (2012) 1198–1202. doi:10.1021/nl2034464.

[27] G.-Y. Zhao, C.-L. Xu, D.-J. Guo, H. Li, H.-L. Li, Template Preparation of Pt–Ru and Pt Nanowire Array Electrodes on a Ti/Si Substrate for Methanol Electro-oxidation, J. Power Sources. 162 (2006) 492–496. doi:http://dx.doi.org/10.1016/j.jpowsour.2006.06.082.

[28] K.S. Napolskii, P.J. Barczuk, S.Y. Vassiliev, A.G. Veresov, G.A. Tsirlina, P.J. Kulesza, Templating of Electrodeposited Platinum Group Metals as a Tool to Control Catalytic Activity, Electrochim. Acta. 52 (2007) 7910–7919. doi:http://dx.doi.org/10.1016/j.electacta.2007.06.043.

[29] D.J. Comstock, S.T. Christensen, J.W. Elam, M.J. Pellin, M.C. Hersam, Tuning the Composition and Nanostructure of Pt/Ir Films via Anodized Aluminum Oxide Templated Atomic Layer Deposition, Adv. Funct. Mater. 20 (2010) 3099–3105. doi:10.1002/adfm.201000389.

[30] D. Gu, H. Baumgart, K. Tapily, P. Shrestha, G. Namkoong, X. Ao, et al., Precise Control of Highly Ordered Arrays of Nested Semiconductor/metal Nanotubes, Nano Res. 4 (2011) 164–170. doi:10.1007/s12274-010-0066-9.

[31] H. Schlörb, V. Haehnel, M.S. Khatri, A. Srivastav, A. Kumar, L. Schultz, et al., Magnetic Nanowires by Electrodeposition within Templates, Phys. Status Solidi. 247 (2010) 2364–2379. doi:10.1002/pssb.201046189.

[32] L. Wen, Y. Mi, C. Wang, Y. Fang, F. Grote, H. Zhao, et al., Cost-effective Atomic Layer Deposition Synthesis of Pt Nanotube Arrays: Application for High Performance Supercapacitor, Small. 10 (2014) 3162–3168. doi:10.1002/smll.201400436.

[33] S.T. Christensen, J.W. Elam, F.A. Rabuffetti, Q. Ma, S.J. Weigand, B. Lee, et al., Controlled Growth of Platinum Nanoparticles on Strontium Titanate Nanocubes by Atomic Layer Deposition, Small. 5 (2009) 750–757. doi:10.1002/smll.200801920.

[34] X. Jiang, T.M. Gür, F.B. Prinz, S.F. Bent, Atomic Layer Deposition (ALD) Co-Deposited Pt−Ru Binary and Pt Skin Catalysts for Concentrated Methanol Oxidation, Chem. Mater. 22 (2010) 3024–3032. doi:10.1021/cm902904u.

[35] H.-B.-R. Lee, S.F. Bent, Microstructure-Dependent Nucleation in Atomic Layer Deposition of Pt on TiO_2, Chem. Mater. 24 (2012) 279–286. doi:10.1021/cm202764b.

[36] H.-B.-R. Lee, K.L. Pickrahn, S.F. Bent, Effect of O_3 on Growth of Pt by Atomic Layer Deposition, J. Phys. Chem. C. 118 (2014) 12325–12332. doi:10.1021/jp502596n.

[37] I.J. Hsu, D.A. Hansgen, B.E. McCandless, B.G. Willis, J.G. Chen, Atomic Layer Deposition of Pt on Tungsten Monocarbide (WC) for the Oxygen Reduction Reaction, J. Phys. Chem. C. 115 (2011) 3709–3715. doi:10.1021/jp111180e.

[38] S.M. George, Atomic Layer Deposition: An Overview, Chem. Rev. 110 (2010) 111–131. doi:10.1021/cr900056b.

[39] H.-B.-R. Lee, S.H. Baeck, T.F. Jaramillo, S.F. Bent, Growth of Pt Nanowires by Atomic Layer Deposition on Highly Ordered Pyrolytic Graphite, Nano Lett. 13 (2013) 457–463. doi:10.1021/nl303803p.

[40] J. Lu, J.W. Elam, P.C. Stair, Synthesis and Stabilization of Supported Metal Catalysts by Atomic Layer Deposition, Acc. Chem. Res. 46 (2013) 1806–1815. doi:10.1021/ar300229c.

[41] A.J.M. Mackus, M.A. Verheijen, N. Leick, A.A. Bol, W.M.M. Kessels, Influence of Oxygen Exposure on the Nucleation of Platinum Atomic Layer Deposition:

Consequences for Film Growth, Nanopatterning, and Nanoparticle Synthesis, Chem. Mater. 25 (2013) 1905–1911. doi:10.1021/cm400562u.

[42] R.G. Gordon, D. Hausmann, E. Kim, J. Shepard, A Kinetic Model for Step Coverage by Atomic Layer Deposition in Narrow Holes or Trenches, Chem. Vap. Depos. 9 (2003) 73–78. doi:10.1002/cvde.200390005.

[43] J.W. Elam, D. Routkevitch, P.P. Mardilovich, S.M. George, Conformal Coating on Ultrahigh-Aspect-Ratio Nanopores of Anodic Alumina by Atomic Layer Deposition, Chem. Mater. 15 (2003) 3507–3517. doi:10.1021/cm0303080.

[44] J. Duay, S.A. Sherrill, Z. Gui, E. Gillette, S.B. Lee, Self-Limiting Electrodeposition of Hierarchical MnO_2 and $M(OH)_2/MnO_2$ Nanofibril/Nanowires: Mechanism and Supercapacitor Properties, ACS Nano. 7 (2013) 1200–1214. doi:10.1021/nn3056077.

[45] A.L.M. Reddy, M.M. Shaijumon, S.R. Gowda, P.M. Ajayan, Multisegmented Au-MnO_2/Carbon Nanotube Hybrid Coaxial Arrays for High-Power Supercapacitor Applications, J. Phys. Chem. C. 114 (2010) 658–663. doi:10.1021/jp908739q.

[46] G. Yu, L. Hu, N. Liu, H. Wang, M. Vosgueritchian, Y. Yang, et al., Enhancing the Supercapacitor Performance of Graphene/MnO_2 Nanostructured Electrodes by Conductive Wrapping, Nano Lett. 11 (2011) 4438–4442. doi:10.1021/nl2026635.

[47] F. Sedona, G.A. Rizzi, S. Agnoli, F.X. Llabrés i Xamena, A. Papageorgiou, D. Ostermann, et al., Ultrathin TiO_x Films on Pt(111): A LEED, XPS, and STM Investigation, J. Phys. Chem. B. 109 (2005) 24411–24426. doi:10.1021/jp0543173.

[48] C. Dablemont, P. Lang, C. Mangeney, J.-Y. Piquemal, V. Petkov, F. Herbst, et al., FTIR and XPS Study of Pt Nanoparticle Functionalization and Interaction with Alumina, Langmuir. 24 (2008) 5832–5841. doi:10.1021/la7028643.

[49] H. Zhao, C. Wang, R. Vellacheri, M. Zhou, Y. Xu, Q. Fu, et al., Self-Supported Metallic Nanopore Arrays with Highly Oriented Nanoporous Structures as Ideally Nanostructured Electrodes for Supercapacitor Applications, Adv. Mater. 26 (2014) 7654–7659. doi:10.1002/adma.201402766.

[50] F. Grote, R.S. Kühnel, A. Balducci, Y. Lei, Template Assisted Fabrication of Free-standing MnO2 Nanotube and Nanowire Arrays and Their Application in Supercapacitors, Appl. Phys. Lett. 104 (2014) 10–14. doi:10.1063/1.4864285.

[51] W. Yan, J.Y. Kim, W. Xing, K.C. Donavan, T. Ayvazian, R.M. Penner, Lithographically Patterned Gold/Manganese Dioxide Core/Shell Nanowires for High Capacity, High

Rate, and High Cyclability Hybrid Electrical Energy Storage, Chem. Mater. 24 (2012) 2382–2390. doi:10.1021/cm3011474.

[52] Z. Yu, B. Duong, D. Abbitt, J. Thomas, Highly Ordered MnO_2 Nanopillars for Enhanced Supercapacitor Performance, Adv. Mater. 25 (2013) 3302–3306. doi:10.1002/adma.201300572.

6. Surface modification of three-dimensional Carbon nanofiber aerogel with ultrasmall Pt nanoparticles by ALD for electrocatalytic hydrogen evolution

6.1. Introduction

Because of the deteriorating environment and depleting of fossil fuels, as a high-energy-density carrier of clean energy, hydrogen has attracted tremendous attention recently [1–8]. The direct generation of hydrogen from the environmental-friendly electrolysis of water is one attractive strategy [1,9–18]. While the hydrogen evolution reaction (HER) of direct electrochemical splitting of water requires an efficient and robust catalyst to reduce the reaction overpotential and to increase the catalytic current density [1,18]. Currently, among various catalyst materials, noble metals, especially platinum has been regarded as the best electrocatalyst that provides the highest electrochemical activity towards the HER [19–24]. However, the high cost of Pt limits the according economic viability and hinders the widespread utilization. Though alternative electrocatalysts based on earth-abundant elements such as transition metal chalcogenides (TMCs) have been explored to reduce the costs [12,14], the electrochemical catalytic performances of these developed materials are still lag behind Pt in terms of the HER. Thus, feasible option approaches, which could reduce the loading amount of Pt while retaining the electrocatalytic activity for HER, become very urgent.

Besides Pt utilization, the use of large-surface-area conductive supports for a given catalyst is another way to increase the catalytic activity of HER, such as carbon nanotubes, graphene [25–30] and carbon nanofibers [31–33]. In particular, three-dimensional (3D) carbon nanofiber aerogel that derived from biologic bacterial cellulose (BC) has been explored for HER, owing to the environmental friendliness, cost effectiveness, light-weight, high inertness in harsh electrochemical conditions, large surface area as well as good conductivity for intermediation transport [31,34]. However, it is still challenging to achieve low-loading and high dispersion of Pt nanoparticles on the surface of BCF by the traditional chemical deposition, electrodepositing or physical vapor deposition processes. Therefore, a strategy based on low-loading amount of Pt nanoparticles highly-dispersed on high-surface-area of supports to minimize the overall raw material cost is imperative.

Recently, as a modified chemical vapor deposition technique, Atomic layer deposition allows conformal and homogenous coating on large-surface 3D structures with precise controllable thickness at atomic level [35–44]. For the Pt ALD process, the certain chemical reaction results in the nucleation of isolated islands on the support surface. The islands grow with increasing ALD cycles and finally coalesce into a film [45–47]. The growth process of the isolated islands has been used for direct depositing Pt particles with diameters less than 10 nm [47]. Combining with our modified ALD process [45], the conformal Pt isolated-islands could highly disperse Pt nanoparticles on large surfaces of conductive supports, while decreasing the utilization of Pt for HER application.

Herein, to minimize the loading amount of Pt while maintaining their catalytic performance, we grafted ultra-low loading amount of Pt (0.87 %) nanoparticles with diameters ranging from 1 to 3 nm on surfaces of 3D carbon nanofibers, via only 5 cycles of ALD process. With the intervening of low nitrogen filling steps, the Pt nanoparticles were highly dispersed on nanofiber surfaces with a high surface-to-bulk atomic ratio. Electrochemical measurements showed that the as-prepared ultra-low mass loading Pt nanoparticles on BCF catalyst has as good electrocatalytic activity as commercial Pt/C catalyst for HER. The present investigations demonstrate that the combination of low-nitrogen-filling ALD process and large-surface BCF is a powerful strategy that could efficiently minimize the Pt demands for efficient hydrogen evolution.

6.2. Results and discussion

6.2.1. Morphology and structure analysis

BCF aerogel was chosen as a support because the low-cost carbon nanofibers have advantages of high inertness in harsh electrochemical conditions, large surface area as well as good conductivity for intermediation transport. The purified wet BC pellicle with controllable thickness was firstly cut into small pieces (Figure 6-1a), and then lyophilized to form dry BC aerogels (Figure 6-1b) via freeze-dry process. The dried BC aerogels were then loaded to pyrolysis under a high-purity N_2 atmosphere at 800 °C for 2 h to form the BCF aerogels (Figure 6-1c). Finally, the as-prepared BCF aerogels were put into ALD reactor chamber to deposit Pt nanoparticles according to our previous work (Figure 6-1d).

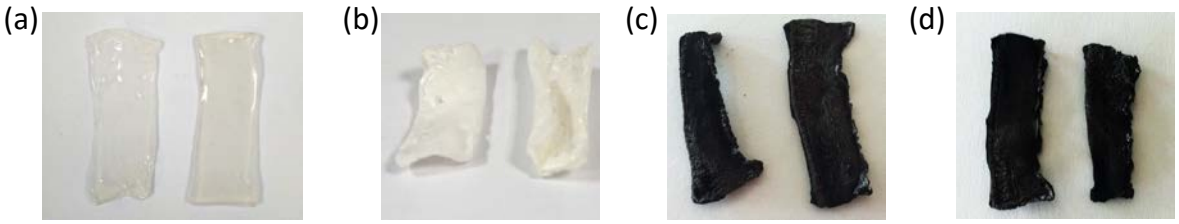

Figure 6-1| The photographs for the preparation of sample: (a) BC Hydrogel, (b) BC Aerogel, BCF Aerogel, and (d) Pt/BCF.

The morphology of the BCF aerogel as well as the morphology of Pt particles on BCF aerogels was further characterized by TEM. After high-temperature pyrolysis and ALD deposition process, the macroscopic volumes of BCF aerogels (photograph in Figure 6-1a and d) and the nanofibers gradually shrink to about half of their original size. However, the nanofibrous network structure of original BC precursors maintained well (Figure 6-2). As shown in Figure 2a and b, the BCF composes of random-orientated carbon nanofibers.

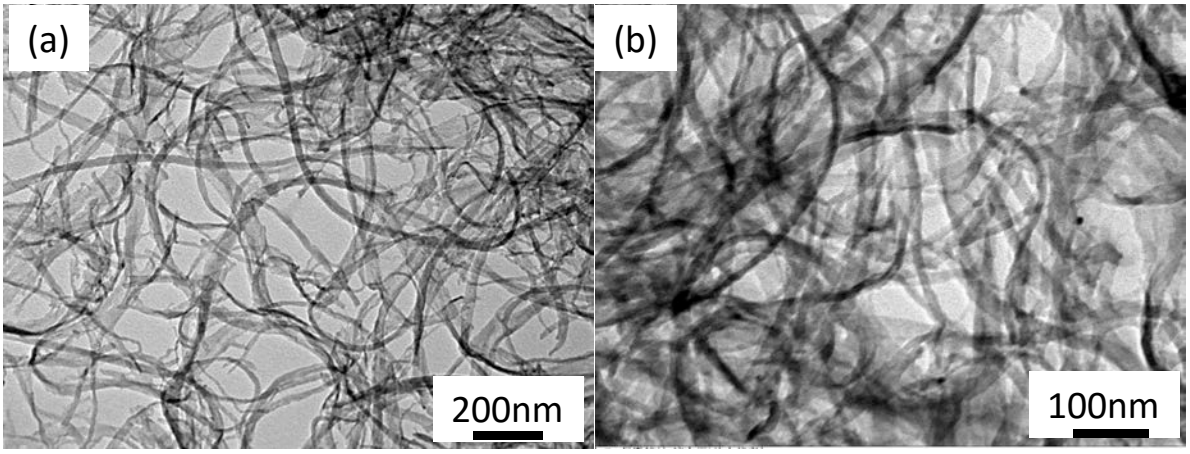

Figure 6-2| (a) The TEM image of the as-prepared three-dimensional BCF aerogel. (b) The enlarged magnification TEM images of sample in (a).

After only 5 cycles of low-nitrogen-filling ALD processes, the appearance of the sample was the same as that of BCF aerogel. Under TEM investigation, it could found that the Pt particles were highly dispersed on the surface of carbon nanofibers, even at the inner central surface

of BCF aerogel (Figure 6-3a).The magnified TEM image (Figure 6-3b and c) further demonstrated the dispersity of Pt particles. And the particle size distribution based on several TEM images was shown in Figure 6-3d. It was presented that the average Pt particle diameter was 2 nm.

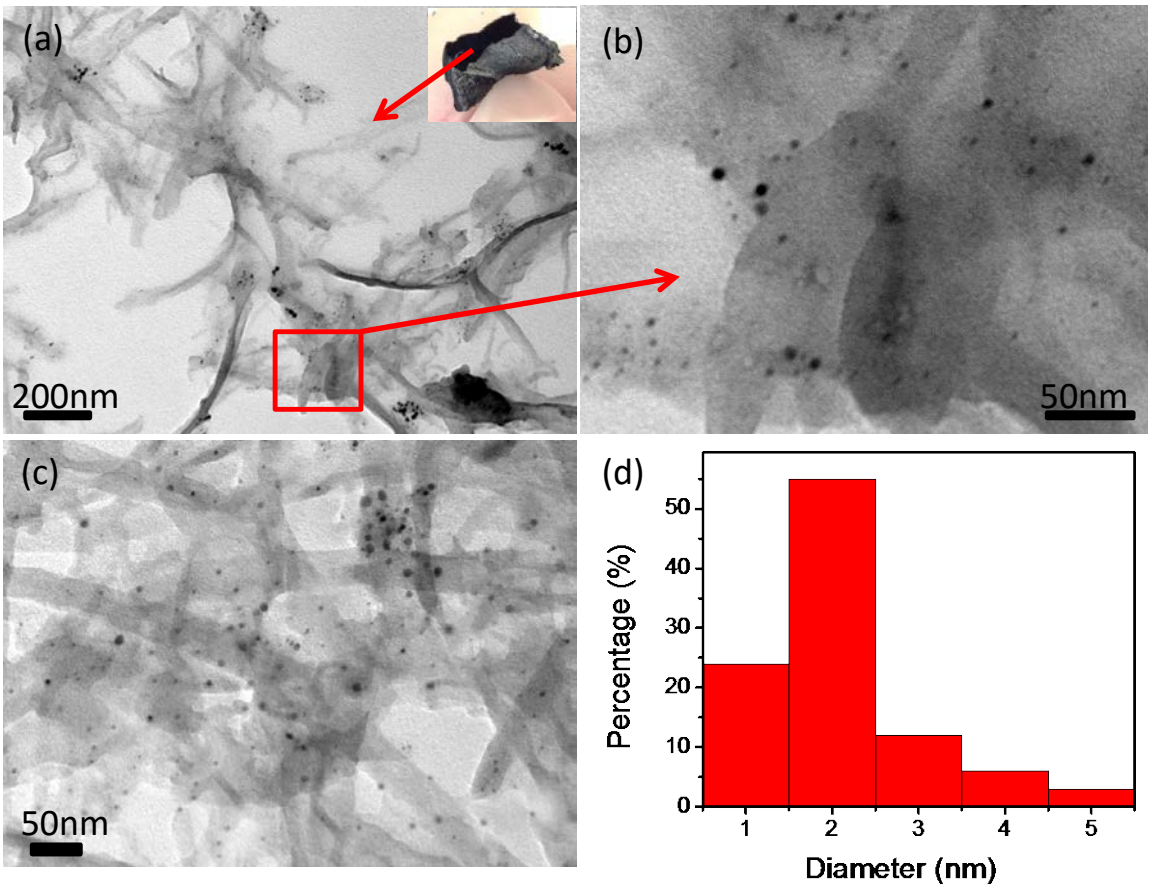

Figure 6-3| (a) The TEM image of the as-prepared three-dimensional Pt/BCF aerogel. (b) and (c) The enlarged magnification TEM images of the as-prepared three-dimensional Pt/BCF aerogel. (d) The Pt particle size distribution on three-dimensional BCF aerogel via 5 cycles of modified ALD process.

6.2.2. Chemical state analysis

The chemical state of the surface modification Pt by 5 cycles of low-filling-N_2 step ALD process on the as-prepared three-dimensional BCF aerogel was investigated by XPS spectra. As presented in Figure 6-4, the spectrum marked in blue line, the Pt/BCF sample presented

obviously Pt $4f_{5/2}$ and Pt $4f_{7/2}$ peaks, both of them were fitted well with the Pt^0state, confirming the presence of Pt [47,48].

Besides the identification of chemical state, the weight percent calculations also done based on XPS spectroscopy. It is obvious that the comparison bare BCF sample does not show Pt 4f peaks (Figure 6-4 marked in black line). Accordingly, the Pt loading on BCF was detected to be about 0.87 wt% by XPS analysis. The high-level of disperse and low-level of loading of Pt nanoparticles over high-surface-area 3D carbon networks is difficult to be achieved by normal Pt deposition process, allowing the feasibility to break the Pt loading limits for HER process.

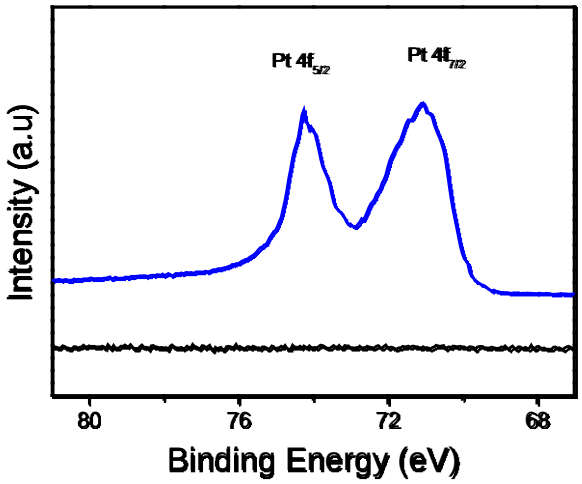

Figure 6-4| The Pt 4f XPS spectra of the bare three-dimensional BCF aerogel and the three-dimensional Pt/BCF samples.

6.2.3. Electrochemical performance

6.2.3.1. Electrocatalytic performance for hydrogen evolution reaction

The electrocatalytic performance of the three-dimensional Pt/BCF was investigated in 0.5 M H_2SO_4 solution with a typical three-electrode system for HER. The catalytic performance of the bare three-dimensional BCF and the commercial Pt/C electrodes were tested for comparison. As shown in Figure 6-5a, the Pt/C catalyst shows a distinctly high HER catalytic activity, with a very low overpotential (-19 mV) as H_2 evolution (J = 10 mA·cm^{-2}), near to zero overpotential. The bare BCF presents almost negligible HER catalytic activity, with a high

overpotential of about -350 mV at the same current density condition. The overpotential of three-dimensional Pt/BCF with as low as 0.87 wt% Pt loading was only -55 mV at the cathodic current density of 10 mA cm^{-2}, which is comparable with that of commercial Pt/C catalyst. Meanwhile, the loading of Pt nanoparticles had lowered the onset potential of three-dimensional bare BCF electrode. Both of them suggested the good catalytic activity of three-dimensional Pt/BCF catalyst. The catalytic activity is similar to that in previously reported 7 wt% Pt carbon system [48].

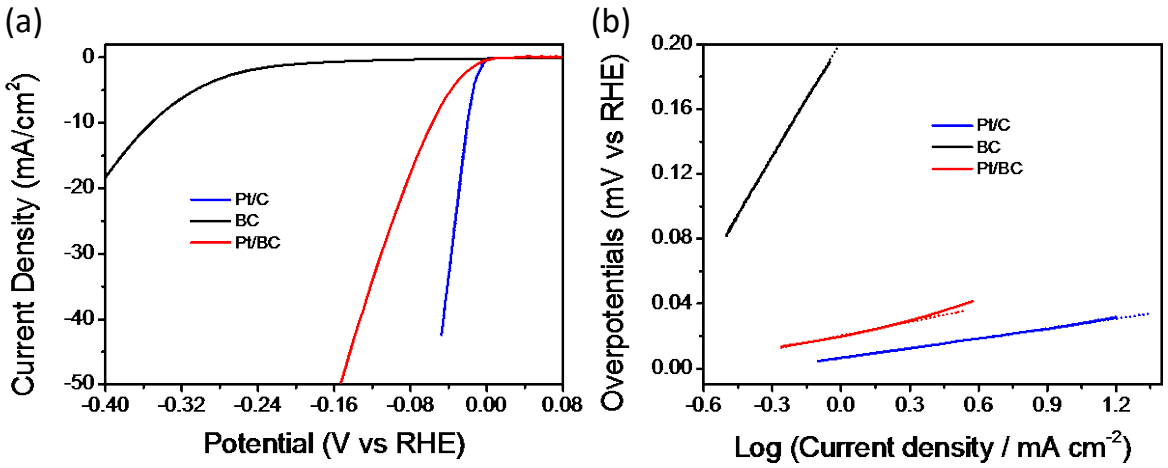

Figure 6-5| Electrochemical performance of electrodes in 0.5 M H_2SO_4 solution: (a) iR-corrected polarization curves; and (b) Tafel plots for HER on bare three-dimensional BCF, three-dimensional Pt/BCF and commercial Pt/C electrodes, respectively.

Moreover, the HER kinetics of the catalysts were probed by the corresponding Tafel slopes (overpotential versus log current) for further evaluating the electrochemical performance of samples. As shown in Figure 6-5b, the linear regions of the Tafel plots were fitted into the Tafel equation, getting values of 32 and 24 mV per decade for the three-dimensional Pt/BCF and the commercial Pt/C catalyst, respectively. The small Tafel slope of the three-dimensional Pt/BCF demonstrated its superior catalytic activity, because of the fast increase of HER velocity while overpotential increasing. Generally, there are three principal steps that may participate for the HER in acidic media [49–51]. Under a specific set of condition, Tafel slopes of about 120, 40 and 30 mV per decade will be achieved if the Volmer (electrochemical hydrogen adsorption : $H_3O^+ + e^- \rightarrow H_{ads} + H_2O$),the Heyrovsky (electrochemical desorption: $H_{ads} + H_3O^+ + e^- \rightarrow H_2\uparrow + H_2O$), or the Tafel (chemical desorption: $H_{ads} + H_{ads} \rightarrow H_2\uparrow$) step is the rate-determining step, respectively. The obtained

Tafel slope of about 32 mV per decade for the three-dimensional Pt/BCF indicated that the HER takes place by the Volmer-Heyrovsky mechanism [49,50].

6.2.3.2. Electrochemical impedance spectroscopy

To understand the electrochemical activation behavior of the corresponding catalysts, the electrochemical impedance spectroscopy (EIS) tests were carried out. The Nyquist plots were presented in Figure 6-6. It could be found that the Pt/BCF possesses a small arc, indicating a low charge transfer resistance, which is beneficial to achieve a high reaction rate of HER. The small charge transfer resistance of the Pt/BCF was attributed to the high conductivity of BCF support, and the incorporation of tiny Pt nanoparticles.

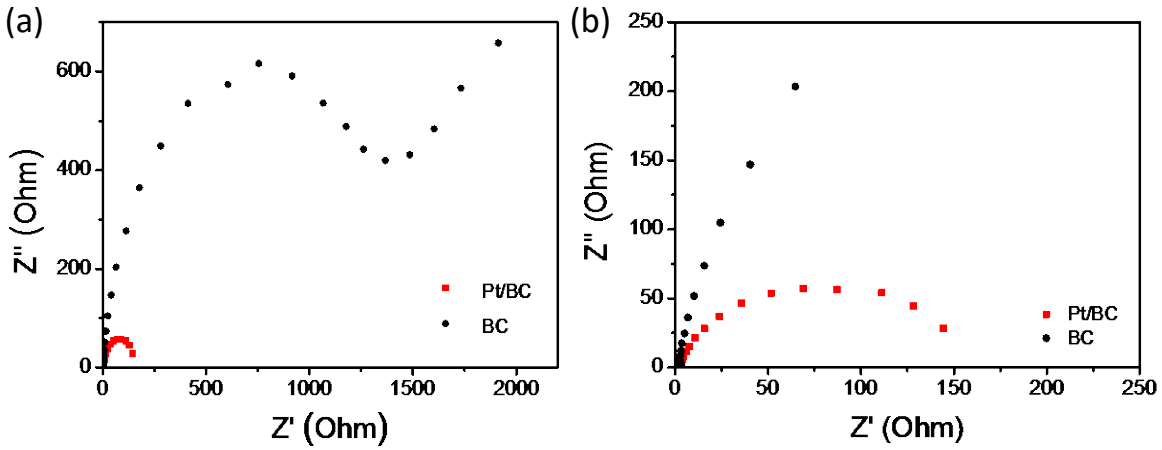

Figure 6-6| (a) Nyquist plots of electrochemical impedance spectra for bare three-dimensional BCF and three-dimensional Pt/BCF electrodes in 0.5 M H_2SO_4 solution; and (b) the enlarged part of (a).

6.2.3.3. Long-term stability

The good stability is another crucial factors for a good HER catalyst. The accelerated durability test of Pt/BCF was performed by taking continuous potential cycling at 100 $mV \cdot s^{-1}$ for 1000 cycles in 0.5 M H_2SO_4 solution. As shown in Figure 6-7a, the polarization curve of the three-dimensional Pt/BCF electrode has a negligible loss of cathodic current, and the curve was almost the same as the original one. Thus, the as-prepared three-dimensional

Pt/BCF had excellent stability in HER process. To further verify the long-term stability of Pt/BCF, at the applied potential of -0.124 V (vs RHE), more than 10 h of current-time plot was performed. As present in Figure 6-7b, the loss of current density during the test period was negligible. Thus, the three-dimensional Pt/BCF had good stability in long-term electrocatalytic process. We considered that the good stability of the three-dimensional Pt/BCF was owing to the strong chemical bond between small Pt nanoparticles deposited by low-filling-N_2 ALD process and three-dimensional BCF aerogel, and to the high inertness of the three-dimensional BCF support that protected the catalyst during the continuous potential cycling process.

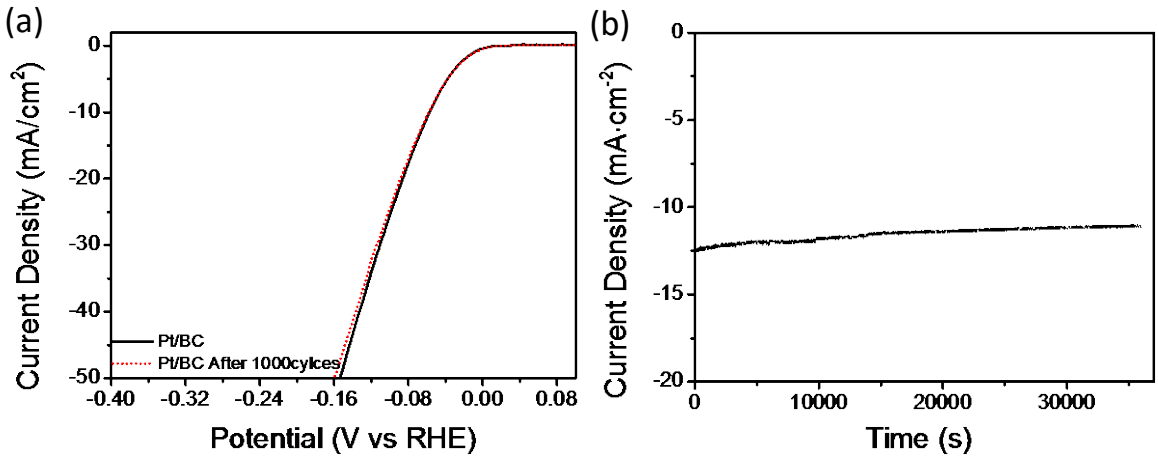

Figure 6-7| (a) Accelerated durability test for the three-dimensional Pt/BCF electrode before and after 1000 cycles. (b) Current-time response of the three-dimensional Pt/BCF electrode at the applied potential of -0.124 V (vs RHE).

6.3. Conclusions

In this work, we have prepared the efficient three-dimensional Pt/BCF HER catalyst system, with as low as 0.87 wt% Pt mass loading on low-cost bacterial cellulose derived three-dimensional carbon nanofibers aerogel by a modified low-nitrogen-filling ALD process, and quantitatively analyzed its performance. The morphological characterizations presented that the Pt nanoparticles were highly dispersed on the three-dimensional BCF aerogel with an average Pt particle size of 2 nm.

With the ultra-low mass loading of ultra-small Pt nanoparticles, the prepared sample exhibited a low overpotential of -55 mV at the cathodic current density of 10 $mA \cdot cm^{-2}$, a small Tafel slope of 32 mV per decade, and a good long-term stability property. The investigations and results suggested that the modified Pt ALD process is a promising strategy to highly disperse tiny Pt particles on large-surface-area three-dimensional BCF aerogel with ultra-low mass loading of Pt nanoparicles. It could dramatically reduce the demands of expensive noble metals while maintaining their high catalytic activity.

6.4. Bibliography

[1] Y. Li, H. Wang, L. Xie, Y. Liang, G. Hong, H. Dai, MoS2 Nanoparticles Grown on Graphene: An Advanced Catalyst for the Hydrogen Evolution Reaction, J. Am. Chem. Soc. 133 (2011) 7296–7299. doi:10.1021/ja201269b.

[2] Z. Wei, J. Sun, Y. Li, A.K. Datye, Y. Wang, Bimetallic Catalysts for Hydrogen Generation, Chem. Soc. Rev. 41 (2012) 7994–8008. doi:10.1039/C2CS35201J.

[3] H.-P. Wang, K. Sun, S.Y. Noh, A. Kargar, M.-L. Tsai, M.-Y. Huang, et al., High-Performance a-Si/c-Si Heterojunction Photoelectrodes for Photoelectrochemical Oxygen and Hydrogen Evolution, Nano Lett. 15 (2015) 2817–2824. doi:10.1021/nl5041463.

[4] V.S. Thoi, Y. Sun, J.R. Long, C.J. Chang, Complexes of Earth-abundant Metals for Catalytic Electrochemical Hydrogen Generation under Aqueous Conditions, Chem. Soc. Rev. 42 (2013) 2388–2400. doi:10.1039/C2CS35272A.

[5] X. Chen, S. Shen, L. Guo, S.S. Mao, Semiconductor-based Photocatalytic Hydrogen Generation, Chem. Rev. 110 (2010) 6503–6570. doi:10.1021/cr1001645.

[6] X. Zou, Y. Zhang, Noble Metal-free Hydrogen Evolution Catalysts for Water Splitting, Chem. Soc. Rev. 44 (2015) 5148–5180. doi:10.1039/C4CS00448E.

[7] L. Shang, B. Tong, H. Yu, G.I.N. Waterhouse, C. Zhou, Y. Zhao, et al., CdS Nanoparticle-Decorated Cd Nanosheets for Efficient Visible Light-Driven Photocatalytic Hydrogen Evolution, Adv. Energy Mater. (2015) n/a–n/a. doi:10.1002/aenm.201501241.

[8] C.G. Morales-Guio, L.-A. Stern, X. Hu, Nanostructured Hydrotreating Catalysts for Electrochemical Hydrogen Evolution, Chem. Soc. Rev. 43 (2014) 6555–6569.

doi:10.1039/C3CS60468C.

[9] R. Wu, J. Zhang, Y. Shi, D. Liu, B. Zhang, Metallic WO_2–Carbon Mesoporous Nanowires as Highly Efficient Electrocatalysts for Hydrogen Evolution Reaction, J. Am. Chem. Soc. 137 (2015) 6983–6986. doi:10.1021/jacs.5b01330.

[10] Y. Yu, S.-Y. Huang, Y. Li, S.N. Steinmann, W. Yang, L. Cao, Layer-Dependent Electrocatalysis of MoS_2 for Hydrogen Evolution, Nano Lett. 14 (2014) 553–558. doi:10.1021/nl403620g.

[11] J. Guo, F. Li, Y. Sun, X. Zhang, L. Tang, Oxygen-incorporated MoS_2 Ultrathin Nanosheets Grown on Graphene for Efficient Electrochemical Hydrogen Evolution, J. Power Sources. 291 (2015) 195–200. doi:http://dx.doi.org/10.1016/j.jpowsour.2015.05.034.

[12] D. Voiry, M. Salehi, R. Silva, T. Fujita, M. Chen, T. Asefa, et al., Conducting MoS_2 Nanosheets as Catalysts for Hydrogen Evolution Reaction, Nano Lett. 13 (2013) 6222–6227. doi:10.1021/nl403661s.

[13] B. Seo, G.Y. Jung, Y.J. Sa, H.Y. Jeong, J.Y. Cheon, J.H. Lee, et al., Monolayer-Precision Synthesis of Molybdenum Sulfide Nanoparticles and Their Nanoscale Size Effects in the Hydrogen Evolution Reaction, ACS Nano. 9 (2015) 3728–3739. doi:10.1021/acsnano.5b00786.

[14] B. Hinnemann, P.G. Moses, J. Bonde, K.P. Jørgensen, J.H. Nielsen, S. Horch, et al., Biomimetic Hydrogen Evolution: MoS_2 Nanoparticles as Catalyst for Hydrogen Evolution, J. Am. Chem. Soc. 127 (2005) 5308–5309. doi:10.1021/ja0504690.

[15] Y. Yan, B. Xia, Z. Xu, X. Wang, Recent Development of Molybdenum Sulfides as Advanced Electrocatalysts for Hydrogen Evolution Reaction, ACS Catal. 4 (2014) 1693–1705. doi:10.1021/cs500070x.

[16] Q. Gong, L. Cheng, C. Liu, M. Zhang, Q. Feng, H. Ye, et al., Ultrathin $MoS_{2(1-x)}Se_{2x}$ Alloy Nanoflakes For Electrocatalytic Hydrogen Evolution Reaction, ACS Catal. 5 (2015) 2213–2219. doi:10.1021/cs501970w.

[17] J. Benson, M. Li, S. Wang, P. Wang, P. Papakonstantinou, Electrocatalytic Hydrogen Evolution Reaction on Edges of a Few Layer Molybdenum Disulfide Nanodots, ACS Appl. Mater. Interfaces. 7 (2015) 14113–14122. doi:10.1021/acsami.5b03399.

[18] X. Yan, L. Tian, M. He, X. Chen, Three-Dimensional Crystalline/Amorphous Co/Co_3O_4 Core/Shell Nanosheets as Efficient Electrocatalysts for the Hydrogen Evolution

Reaction, Nano Lett. 15 (2015) 6015–6021. doi:10.1021/acs.nanolett.5b02205.

[19] L. Wang, C. Lin, D. Huang, J. Chen, L. Jiang, M. Wang, et al., Optimizing the Volmer Step by Single-Layer Nickel Hydroxide Nanosheets in Hydrogen Evolution Reaction of Platinum, ACS Catal. 5 (2015) 3801–3806. doi:10.1021/cs501835c.

[20] S.H. Sun, D.Q. Yang, D. Villers, G.X. Zhang, E. Sacher, J.P. Dodelet, Template- and Surfactant-free Room Temperature Synthesis of Self-Assembled 3D Pt Nanoflowers from Single-Crystal Nanowires, Adv. Mater. 20 (2008) 571–574. doi:10.1002/adma.200701408.

[21] G.-F. Wei, Z.-P. Liu, Restructuring and Hydrogen Evolution on Pt Nanoparticle, Chem. Sci. 6 (2015) 1485–1490. doi:10.1039/C4SC02806F.

[22] S. Bai, C. Wang, M. Deng, M. Gong, Y. Bai, J. Jiang, et al., Surface Polarization Matters: Enhancing the Hydrogen-Evolution Reaction by Shrinking Pt Shells in Pt–Pd–Graphene Stack Structures, Angew. Chemie Int. Ed. 53 (2014) 12120–12124. doi:10.1002/anie.201406468.

[23] C. Wang, M. Chi, D. Li, D. Strmcnik, D. van der Vliet, G. Wang, et al., Design and Synthesis of Bimetallic Electrocatalyst with Multilayered Pt-Skin Surfaces, J. Am. Chem. Soc. 133 (2011) 14396–14403. doi:10.1021/ja2047655.

[24] F. Su, Z. Tian, C.K. Poh, Z. Wang, S.H. Lim, Z. Liu, et al., Pt Nanoparticles Supported on Nitrogen-Doped Porous Carbon Nanospheres as an Electrocatalyst for Fuel Cells, Chem. Mater. 22 (2010) 832–839. doi:10.1021/cm901542w.

[25] H. Jin, H. Huang, Y. He, X. Feng, S. Wang, L. Dai, et al., Graphene Quantum Dots Supported by Graphene Nanoribbons with Ultrahigh Electrocatalytic Performance for Oxygen Reduction, J. Am. Chem. Soc. 137 (2015) 7588–7591. doi:10.1021/jacs.5b03799.

[26] J. Zhang, F. Li, shu-feng zhao, L. Chen, A. Khan, D. MacFarlane, Polyethylenimine Promoted Electrocatalytic Reduction of CO_2 to CO in Aqueous Medium by Graphene-Supported Amorphous Molybdenum Sulphide, Energy Environ. Sci. (2015). doi:10.1039/C5EE02879E.

[27] L. Nan, W. Yue, Y. Jiang, Fabrication of Graphene-porous Carbon-Pt Nanocomposites with High Electrocatalytic Activity and Durability for Methanol Oxidation, J. Mater. Chem. A. 3 (2015) 22170–22175. doi:10.1039/C5TA06854A.

[28] S. Chen, S.-Z. Qiao, Hierarchically Porous Nitrogen-Doped Graphene–$NiCo_2O_4$ Hybrid

Paper as an Advanced Electrocatalytic Water-Splitting Material, ACS Nano. 7 (2013) 10190–10196. doi:10.1021/nn404444r.

[29] W. Zhou, K. Zhou, D. Hou, X. Liu, G. Li, Y. Sang, et al., Three-Dimensional Hierarchical Frameworks Based on MoS_2 Nanosheets Self-Assembled on Graphene Oxide for Efficient Electrocatalytic Hydrogen Evolution, ACS Appl. Mater. Interfaces. 6 (2014) 21534–21540. doi:10.1021/am506545g.

[30] Z. Jiang, X. Zhao, X. Tian, L. Luo, J. Fang, H. Gao, et al., Hydrothermal Synthesis of Boron and Nitrogen Codoped Hollow Graphene Microspheres with Enhanced Electrocatalytic Activity for Oxygen Reduction Reaction, ACS Appl. Mater. Interfaces. 7 (2015) 19398–19407. doi:10.1021/acsami.5b05585.

[31] Y.-R. Zheng, M.-R. Gao, Z.-Y. Yu, Q. Gao, H.-L. Gao, S.-H. Yu, Cobalt Diselenide Nanobelts Grafted on Carbon Fiber Felt: An Efficient and Robust 3D Cathode for Hydrogen Production, Chem. Sci. 6 (2015) 4594–4598. doi:10.1039/C5SC01335F.

[32] Z. Yang, J. Ren, Z. Zhang, X. Chen, G. Guan, L. Qiu, et al., Recent Advancement of Nanostructured Carbon for Energy Applications, Chem. Rev. 115 (2015) 5159–5223. doi:10.1021/cr5006217.

[33] M. Kang, Y. Lee, H. Jung, J.H. Shim, N.-S. Lee, J.M. Baik, et al., Single Carbon Fiber Decorated with RuO_2 Nanorods as a Highly Electrocatalytic Sensing Element, Anal. Chem. 84 (2012) 9485–9491. doi:10.1021/ac302334t.

[34] L.-F. Chen, Z.-H. Huang, H.-W. Liang, H.-L. Gao, S.-H. Yu, Three-Dimensional Heteroatom-Doped Carbon Nanofiber Networks Derived from Bacterial Cellulose for Supercapacitors, Adv. Funct. Mater. 24 (2014) 5104–5111. doi:10.1002/adfm.201400590.

[35] H. Li, Y. Gao, Y. Shao, Y. Su, X. Wang, Vapor-Phase Atomic Layer Deposition of Co_9S_8 and Its Application for Supercapacitors, Nano Lett. 15 (2015) 6689–6695. doi:10.1021/acs.nanolett.5b02508.

[36] V.O. Williams, N.C. Jeong, C. Prasittichai, O.K. Farha, M.J. Pellin, J.T. Hupp, Fast Transporting ZnO–TiO_2 Coaxial Photoanodes for Dye-Sensitized Solar Cells Based on ALD-Modified SiO_2 Aerogel Frameworks, ACS Nano. 6 (2012) 6185–6196. doi:10.1021/nn3015695.

[37] S.M. George, Atomic Layer Deposition: An Overview, Chem. Rev. 110 (2010) 111–131. doi:10.1021/cr900056b.

[38] X. Chen, E. Pomerantseva, P. Banerjee, K. Gregorczyk, R. Ghodssi, G. Rubloff, Ozone-Based Atomic Layer Deposition of Crystalline V_2O_5 Films for High Performance Electrochemical Energy Storage, Chem. Mater. 24 (2012) 1255–1261. doi:10.1021/cm202901z.

[39] K.L. Pickrahn, A. Garg, S.F. Bent, ALD of Ultrathin Ternary Oxide Electrocatalysts for Water Splitting, ACS Catal. 5 (2015) 1609–1616. doi:10.1021/cs501532b.

[40] Q. Li, C. Dong, A. Nie, J. Liu, W. Zhou, H. Wang, Microstructure-Dependent Conformal Atomic Layer Deposition on 3D Nanotopography, Langmuir. 28 (2012) 15809–15815. doi:10.1021/la302391u.

[41] J. Ye, A.C. Baumgaertel, Y.M. Wang, J. Biener, M.M. Biener, Structural Optimization of 3D Porous Electrodes for High-Rate Performance Lithium Ion Batteries, ACS Nano. 9 (2015) 2194–2202. doi:10.1021/nn505490u.

[42] S.K. Cheah, E. Perre, M. Rooth, M. Fondell, A. Hårsta, L. Nyholm, et al., Self-Supported Three-Dimensional Nanoelectrodes for Microbattery Applications, Nano Lett. 9 (2009) 3230–3233. doi:10.1021/nl9014843.

[43] E. Kim, Y. Vaynzof, A. Sepe, S. Guldin, M. Scherer, P. Cunha, et al., Gyroid-Structured 3D ZnO Networks Made by Atomic Layer Deposition, Adv. Funct. Mater. 24 (2014) 863–872. doi:10.1002/adfm.201302238.

[44] V. Brizé, T. Prieur, P. Violet, L. Artaud, G. Berthomé, E. Blanquet, et al., Developments of TaN ALD Process for 3D Conformal Coatings, Chem. Vap. Depos. 17 (2011) 284–295. doi:10.1002/cvde.201100045.

[45] L. Wen, Y. Mi, C. Wang, Y. Fang, F. Grote, H. Zhao, et al., Cost-effective Atomic Layer Deposition Synthesis of Pt Nanotube Arrays: Application for High Performance Supercapacitor, Small. 10 (2014) 3162–3168. doi:10.1002/smll.201400436.

[46] H.-B.-R. Lee, S.F. Bent, Microstructure-Dependent Nucleation in Atomic Layer Deposition of Pt on TiO_2, Chem. Mater. 24 (2012) 279–286. doi:10.1021/cm202764b.

[47] N.P. Dasgupta, C. Liu, S. Andrews, F.B. Prinz, P. Yang, Atomic Layer Deposition of Platinum Catalysts on Nanowire Surfaces for Photoelectrochemical Water Reduction, J. Am. Chem. Soc. 135 (2013) 12932–12935. doi:10.1021/ja405680p.

[48] T. Yang, M. Du, H. Zhu, M. Zhang, M. Zou, Immobilization of Pt Nanoparticles in Carbon Nanofibers: Bifunctional Catalyst for Hydrogen Evolution and Electrochemical Sensor, Electrochim. Acta. 167 (2015) 48–54.

doi:http://dx.doi.org/10.1016/j.electacta.2015.03.077.

[49] Y.-F. Xu, M.-R. Gao, Y.-R. Zheng, J. Jiang, S.-H. Yu, Nickel/Nickel(II) Oxide Nanoparticles Anchored onto Cobalt(IV) Diselenide Nanobelts for the Electrochemical Production of Hydrogen, Angew. Chemie Int. Ed. 52 (2013) 8546–8550. doi:10.1002/anie.201303495.

[50] B.E. Conway, B. V Tilak, Interfacial Processes Involving Electrocatalytic Evolution and Oxidation of H_2, and the Role of Chemisorbed H, Electrochim. Acta. 47 (2002) 3571–3594. doi:http://dx.doi.org/10.1016/S0013-4686(02)00329-8.

[51] Z. Chen, D. Cummins, B.N. Reinecke, E. Clark, M.K. Sunkara, T.F. Jaramillo, Core–shell MoO_3–MoS_2 Nanowires for Hydrogen Evolution: A Functional Design for Electrocatalytic Materials, Nano Lett. 11 (2011) 4168–4175. doi:10.1021/nl2020476.

7. Summary and outlook

In summary, the works throughout this thesis have shown that the atomic layer deposition is a very important and useful technique in fabrication and surface modification of three-dimensional nanostructures for the new generation of energy storage and conversion devices construction. The ALD combination with AAO and PS templates can precisely control the structural parameters of active materials within the nanometer regime, including length, spacing, and thickness and so on. The results in this thesis have shown that the energy storage and conversion efficiency can be enhanced by 1) constructing a three-dimensional transparent conductive electrode as core to improve the collection and transfer of photo generated electrons and holes in TiO_2 shell; meanwhile, precise control of the thickness of photoactive TiO_2 optimizing the utilization of photo generated charge carries in the depletion layer and diffusion layer of TiO_2; 2) developing a cost-effective ALD process to realize three-dimensional Pt nanostructures with ultralow demands of Pt source; the constructed 3D Pt nanostructures can be used in many energy storage device to greatly increase the current collection; 3) further developing a cost-effective ALD process to modify complex three-dimensional nanostructure with ultra-small Pt nanoparticles, the minimizing demands of precious metal via the modification process maintaining the high catalytic performance of precious metal for energy conversion reactions.

The works within this thesis have profiled that in order to realize a new generation of energy storage and conversion devices with high performance, nano-engineered multifunctionalization of three-dimensional complex nanoarchitectures, as that are developed in this thesis, will be indispensable promising strategies. AAO and PS templates are feasible in the constructing of three-dimensional complex nanoarchitectures. ALD enables target material keeping its thin film morphology and / or uniform dispersed nanoparticle on a constructed three-dimensionally nanostructured and electrical conductive matrix. Thereby, ALD multifunctionalization of three-dimensional nanoarchitectures will not only improve the performance of energy conversion and storage devices present here. Ultimately, they will exhibit significant performance enhancement to others energy conversion and storage devices over current diverse technologies. The results obtained within this thesis on nanostructuring of three-dimensional nanoarchitectures,

mulitfuctionlization of those constructed nanoarchitectures and the relative device integration should provide promising basis processes to develop more advanced complex three-dimensional nanoarchitectures with different active materials and functions, widening the range of applications

Extended works

During the process of my Ph.D, I devoted myself to work on atomic layer deposition fabrication and/or surface modification of three-dimensional nanostructures for clean energy conversation and storage. I also paid attention to environmental depuration by solar light. In particular the BiOX related nanostructure photocatalysts used for the photodegradation of environmental pollutants. Meanwhile, I also cooperated with some of my group members and scientists from other groups. Here, in this chapter, the introduction and experiment results are presented to highlight the achieved photocatalytic performances of the synthesized BiOX photocatalysts beyond the scope of this thesis.

E. 1 High efficient visible-light driven photocatalyst: Two-dimensional square-like bismuth oxyiodine nanosheets

Since the discovery of photocatalytic splitting of water on TiO_2 electrodes in 1972 by Honda and Fujishma [1] efficient utilization of solar energy for photocatalysis towards environmental purification and solar energy conversion have been attracting massive research interests [2] Various photocatalysts have been prepared and used in photocatalytic water splitting and photodegradation of organic pollutants [3–6]. However, the photocatalysis of many photocatalysts are limited only under ultraviolet irradiation ($\lambda < 380$ nm). Therefore, it is still of great significance to develop visible-light driven photocatalysts for highly efficient solar utilization.

Recently, as a series of novel layered ternary oxide semiconductors, bismuth oxyhalides (BiOX, X = Cl, Br, and I) have received much attention because of their excellent photocatalytic performances [7–10]. Bismuth oxyhalides possess a layered structure, which is consisting of $[Bi_2O_2]^{2+}$ slabs separated by double slabs of halogen atoms. The space of layered structures is large enough to increase for polarizing the related atoms and orbitals. The induced dipole could then improve the separation efficiency of hole-electron pairs. With the benefits from their open and layered crystalline structures, the bismuth oxyhalides show outstanding photocatalytic performances. BiOCl shows better photocatalytic activity than

TiO_2 under ultraviolet irradiation. Furthermore, bismuth oxyhalides can extend light absorption to visible light range. It is highly important for the direct use of sunlight.

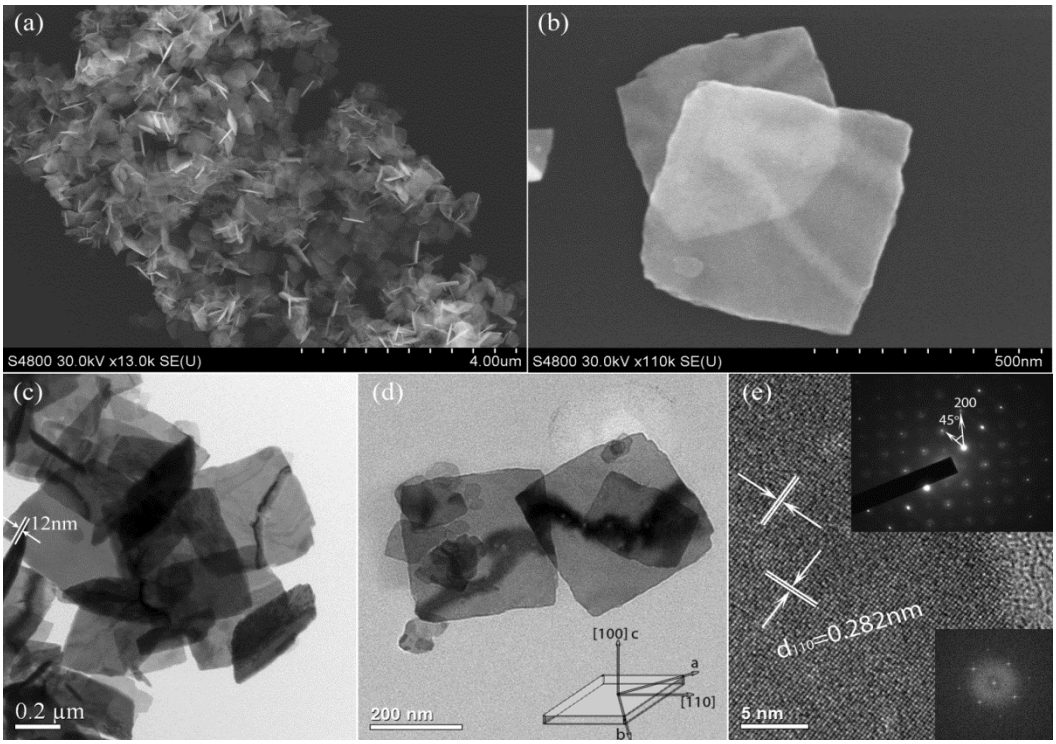

Figure E-1| (a) SEM image of large area of 2D square-like BiOI nanosheets; (b) the SEM image of two pieces 2D square-like BiOI nanosheets; (c) TEM image of bunches of 2D square-like BiOI nanosheets; (d) the TEM image of two pieces 2D square-like BiOI nanosheets and the schematic illustration of the crystal orientation of the BiOI nanosheet (inset bottom right); (e) the HRTEM image, SAED pattern (inset top right) and FFT pattern (inset bottom right) of 2D square-like BiOI nanosheet.

As known, properties of materials are determined by their crystalline structures. Meanwhile, the morphology structures are also play important roles. Profiting from high specific surface areas and large fraction of uncoordinated surface atoms, quasi-two-dimensional (quasi-2D) materials have attracted high research interests [8,9,11,12]. For photocatalytic applications, the exposed surface atoms of quasi-2D materials could easily escape from a lattice to form vacancies that could have strong advantageous effect to photocatalytic performance [8]. Especially quasi-2D structures of bismuth oxyhalide shall have largely improved photocatalytic performance, which has been partially approved recently by the excellent visible light photoactivity of BiOCl nanosheets [7–10]. For even

better visible light absorption comparing with BiOCl, various morphologies of BiOI (Eg = 1.77 ~ 1.92 eV) photocatalysts have also been fabricated [13,14]. However, so far quasi-2D nanostructure of BiOI has rarely been realized and reported. Therefore, nowadays, how to achieve quasi-2D nanostructure of BiOI presents a timely research topic within the field of photocatalytic application of BiOX. In this work, using a cost-effective and environmental friendly hydrothermal process, 2D square-like BiOI nanosheets with a high percentage of exposed {001} facet were achieved (Figure 8-1). Different from most of conventional hydrothermal processes using surfactants or special solvent that cause high experimental cost, our non-surfactant process and aqueous system is highly desirable for reducing cost. More importantly, these quasi-2D nanosheets show superior visible-light photocatalytic performance, which shall originates from the highly exposed active facets and several-nanometer thickness of the quasi-2D nanosheets. It is found that after only 15 min visible light irradiation, the decolouration ratio of RhB and MO reaches 90 % and 94 %, respectively.

E. 2 Building of Anti-Restack 3D BiOCl hierarchitecture by ultrathin nanosheets towards enhanced photocatalytic activity

Morphology engineering is an effective strategy to enable semiconductor photocatalysts with an excellent solar light photocatalytic performance [15–17]. Therefore, over years, photocatalysts with various morphologies have been substantially developed and applied for environmental remediation [18,19]. Particularly, ultrathin nanosheet semiconductor photocatalysts have triggered a high research enthusiasm in recent years, because of their superior photoactivity that originates from the advantage of promoting separation / transport of charge carriers and large surface area of ultrathin nanosheet [8,20]. However, an encountered challenge when using ultrathin nanosheets is the tendency to restack during processing, which persecutes and restricts their storage and long-term applications. From this point of view, it is promising to design three-dimensional (3D) hierarchical architecture constructed by these ultrathin nanosheets to minimize the corresponding possibility of agglomeration.

Benefiting from the typical layered structure featured as $[Bi_2O_2]^{2+}$ layers being sandwiched between two slabs of chloride ions, bismuth oxychloride (BiOCl) exhibits a comparable or even better photocatalytic performance than that of anatase TiO_2 [21]. The polarized

valence band resulted from the hybridization of Bi 6s and O 2p orbits generates a self-induced internal electric field perpendicular to the (001) plane, facilitating separation of photo-generated electron-hole pairs along the [001] direction [7,22,23]. Moreover, it is easy to attain activated oxygen molecule through one-electron transfer on (001) surface and the resultant oxygen radicals are of great advantages to mineralize the dyes in the solution [9]. In addition, the strong intra-layer bonding and the weak interlayer Van der Waals interactions are conducive to the exfoliation of bulk BiOCl to form ultra-thin sheets, which could reduce the recombination rate of the photogenerated charges by shortening the diffusion length [9,10,22,23]. Micro-assembly of BiOCl nanosheets has been proven to be a feasible strategy to improve the photocatalytic activity and recycling character [24,25]. However, the thickness of the previous reported BiOCl nanosheets is almost limited to several tens of nanometers. Chen's group reported the ultrathin nanosheets assembled porous micriflowers BiOCl with superior photosensitized degradation [25]. But the photodegradation efficiency has obviously decreased during the cycling experiment. Thus, it is indispensable to assemble the ultrathin nanosheets BiOCl into specially designed 3D micro/nanostructures achieving high-activity and high-stability for practical application

For this purpose, herein, the unique 3D BiOCl (UBOC) hierarchitecture, in which ultrathin nanosheets assembled nano-velvet substructures are formed on the surface of micro-scaffold, is synthesized (Figure 8-2). The ultrathin nanosheet with active (001) plane as the main surface is about five atomic-layers in thickness, allowing the facilitative separation and transport of photogenerated charge carries. Such 3D microstructure presents an excellent photocatalytic performance: 99 % decolouration and 74 % removal of total organic carbon (TOC) for rhodamine B (RhB) were achieved within 10 min under AM1.5 solar light irradiation. According to the merit of anti-restack and easy recyclability of the hierarchitecture, we believe that this work broadens the possibility of designing efficient photocatalyst using ultrathin nanosheets. The pronounced photocurrent of the photoelectrode also qualifies the structure as a potential candidate in water splitting.

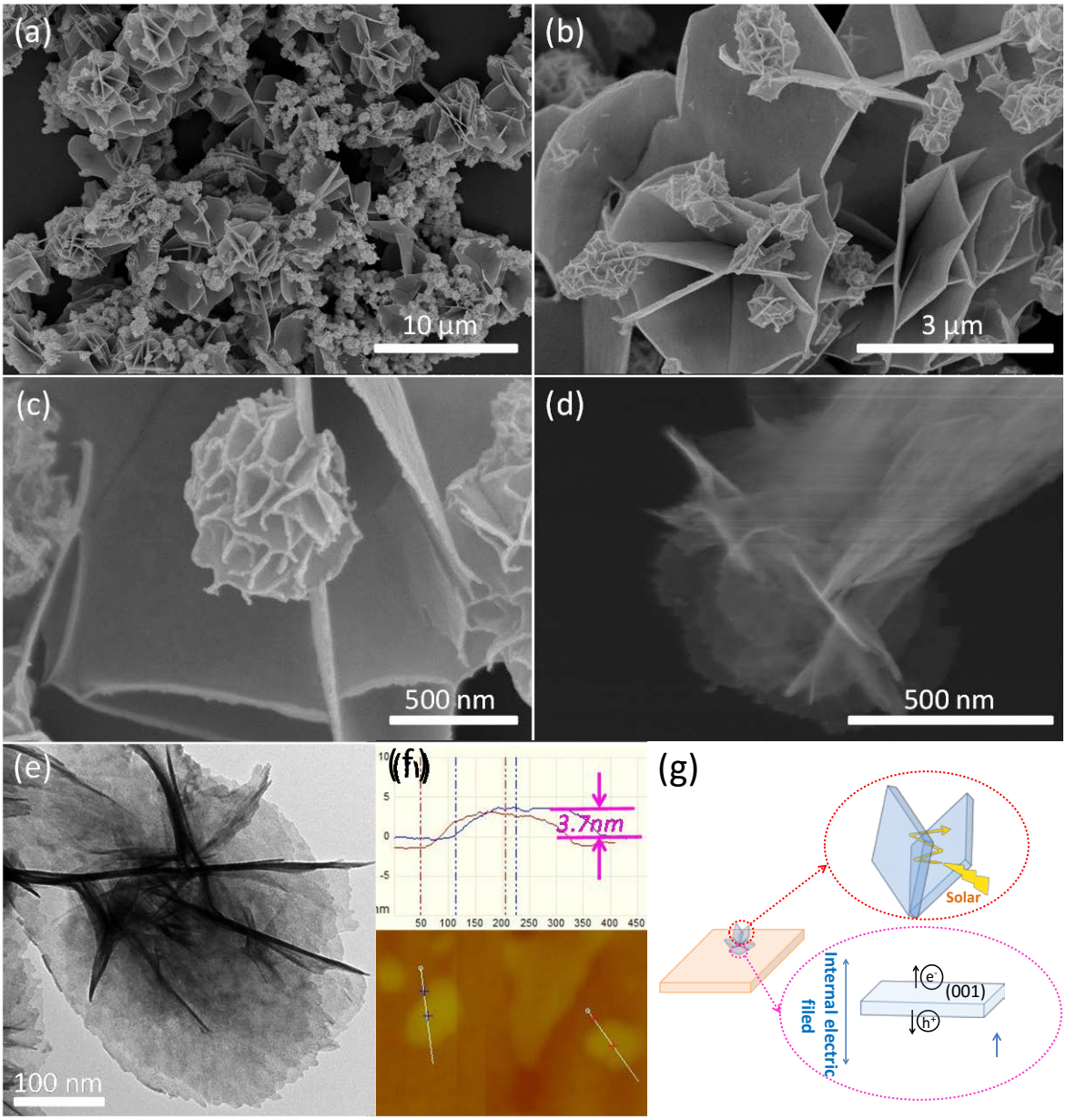

Figure E-2 | (a-d) SEM images; (e) TEM image; (f) AFM image and the corresponding height profile of UBOC and (g) The schematic of multi-light absorption and photogenerated electron-hole pairs separation / transfer with the help of appropriate internal electric field of BiOCl.

E. 3 Two-dimensional Fe:BiOCl ultrathin nanosheet: Surface doping of Fenton reagent for high efficient photocatalysis

The continuing deterioration of environment results in intensive researches for exploring new and efficient pollutant treatment strategies in the last three decades. As one of the promising alternative, the economic and environment-friendly photocatalysis technology

has received tremendous interests [26,27], in which the super oxidation potential ($E_{(\bullet OH/H2O)}$ = 2.80 V) of non-harmful hydroxyl radicals (•OH) that are produced by the photogenerated electron (e^-) / hole (h^+) pairs, could non-selectively and efficiently decompose most organics during the photocatalysis process [28–30]. Thus, many efforts have been devoted to enhance the generation of •OH radicals. Although the integrating of conventional Fenton reaction into photocatalysis process has been proved to be one of the efficient ways, the harsh acidic condition (pH = 2.5 - 3.5), the accumulation of iron-containing sludge, and the requirement of additional H_2O_2 consumption limits the photocatalytic activity [31]. Compared to other strategies, the doping of Fenton-regents into photocatalyst with non-extra H_2O_2 consumption has been demonstrated to be a probable resolution [32,33]. However, the other two disadvantages are still unfavourable for practical application. Therefore, it is high desirable to design and synthesize novel Fenton-reagent doped photocatalysts, which can effectively and high durably generate •OH in a wide range of conditions.

As a promising photocatalyst, the ternary bismuth oxychloride (BiOCl) captures growing attentions [7–10]. Though the unique layered structure of the BiOCl could facilitate the separation and transport of charge carries, the poor solar light utilization, which originated from the wide band gap of BiOCl, resulted in a weak photocatalytic activity. Very recently, a new Fenton-like reagent iron oxychloride (FeOCl) has been reported with good durability in a wide pH range [34]. Since the FeOCl has a similar ‘van der Waals layer’ crystallographic structure as that of the BiOCl, it is high probability to realize doping of Fe acting as FeOCl Fenton-reaction unit to promote the production of •OH radicals. Meanwhile, The Fe-doping may also narrow the band gap of BiOCl, extending the light utilization from the UV light to visible light range [35,36]. It is generally known that the surface exposure of Fe is beneficial for the Fenton reaction. As one of the highest surface atom exposure morphologies, the two-dimensional graphene-like ultrathin nanosheet shall be favourable to explore the full potential of Fenton reaction [8,37]. As a result, Fe-doping BiOCl ultrathin nanosheet (Fe:BOC NS) could be an ideal model to take the advantages of Fenton reaction, band gap narrowing and morphology engineering for maximizing the generating of •OH radicals.

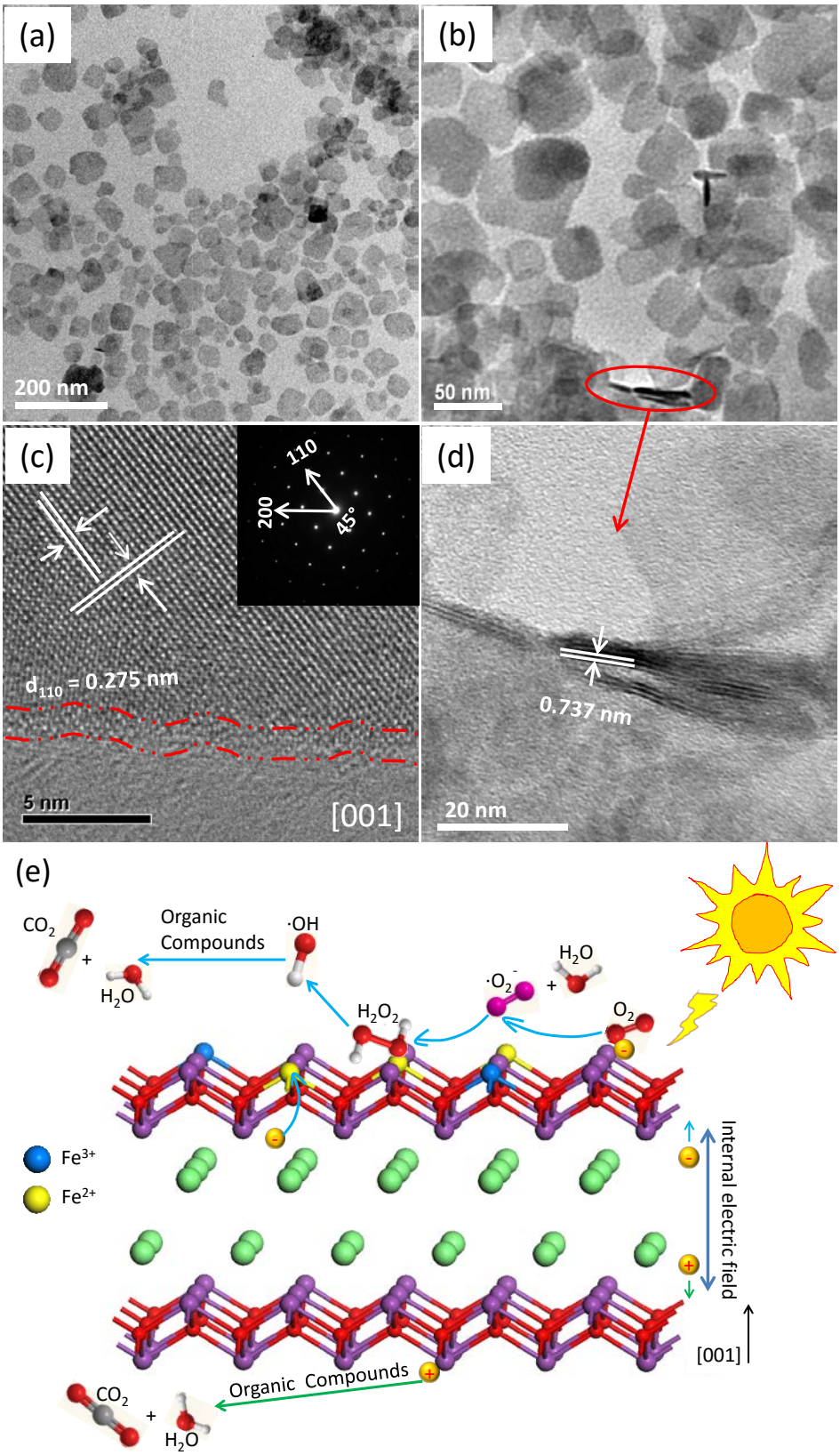

Figure E-3| (a-b) TEM images, (c) HRTEM image, SAED pattern (inset in (Figure c)) and (d) profile HRTEM image of the Fe-doping BiOCl ultrathin nanosheets (Fe:BOC NS), (e) The tentative photocatalytic degradation process for RhB over Fe:BOC NS under solar light irradiation.

Herein, utilizing a facile and scalable hydrothermal process, we demonstrated the first successful synthesis of Fe:BOC NS (Figure 8-3). The contribution of the introduced Fenton reaction is confirmed by electron spin resonance (ESR) experiment, which shows about two-fold increase of the •OH radicals yield. Meanwhile, the Fe-doping created trap levels extended the light utilization from UV (3,23 eV) to visible light (2,65 eV) range. In addition, less than 5 nm ultrathin nanosheets and [001] facets exposure fulfil the advantages of Fenton reaction, and facilitate the separation and transfer of charge carries. The systematic experiments and analyses revealed that all the benefits accelerate the degradation of organic contaminates. A more than two times mineralization degree of colored RhB and colorless phenol with Fe:BOC NS photocatalyst than that with the pristine BiOCl ultrathin nanosheets (BOC NS) is presented. Furthermore, considering the good durability from the cycling experiment, the prepared Fe:BOC NS is an excellent photocatalyst for efficient water treatment. Therefore, our work indicated that the surface Fenton-reagent doped two-dimensional graphene-like ultrathin nanosheet is a promising photocatalyst system to acquire excellent photocatalytic activity.

E. 4 Bibliography

[1] M.G. Walter, E.L. Warren, J.R. McKone, S.W. Boettcher, Q. Mi, E.A. Santori, et al., Solar Water Splitting Cells, Chem. Rev. 110 (2010) 6446–6473. doi:10.1021/cr1002326.

[2] A. FUJISHIMA, K. HONDA, Electrochemical Photolysis of Water at a Semiconductor Electrode, Nature. 238 (1972) 37–38. http://dx.doi.org/10.1038/238037a0.

[3] X. Chen, S. Shen, L. Guo, S.S. Mao, Semiconductor-based Photocatalytic Hydrogen Generation, Chem. Rev. 110 (2010) 6503–6570. doi:10.1021/cr1001645.

[4] A. Bergmann, I. Zaharieva, H. Dau, P. Strasser, Electrochemical Water Splitting by Layered and 3D Cross-linked Manganese Oxides: Correlating Structural Motifs and Catalytic Activity, Energy Environ. Sci. 6 (2013) 2745–2755. doi:10.1039/C3EE41194J.

[5] A. Kudo, Y. Miseki, Heterogeneous Photocatalyst Materials for Water Splitting, Chem. Soc. Rev. 38 (2009) 253–278. doi:10.1039/B800489G.

[6] M.T. Mayer, C. Du, D. Wang, Hematite/Si Nanowire Dual-Absorber System for Photoelectrochemical Water Splitting at Low Applied Potentials, J. Am. Chem. Soc. 134 (2012) 12406–12409. doi:10.1021/ja3051734.

[7] J. Jiang, K. Zhao, X. Xiao, L. Zhang, Synthesis and Facet-Dependent Photoreactivity of BiOCl Single-Crystalline Nanosheets, J. Am. Chem. Soc. 134 (2012) 4473–4476. doi:10.1021/ja210484t.

[8] M. Guan, C. Xiao, J. Zhang, S. Fan, R. An, Q. Cheng, et al., Vacancy Associates Promoting Solar-Driven Photocatalytic Activity of Ultrathin Bismuth Oxychloride Nanosheets, J. Am. Chem. Soc. 135 (2013) 10411–10417. doi:10.1021/ja402956f.

[9] K. Zhao, L. Zhang, J. Wang, Q. Li, W. He, J.J. Yin, Surface Structure-Dependent Molecular Oxygen Activation of BiOCl Single-Crystalline Nanosheets, J. Am. Chem. Soc. 135 (2013) 15750–15753. doi:10.1021/ja4092903.

[10] Y. Wu, B. Yuan, M. Li, W.-H. Zhang, Y. Liu, C. Li, Well-defined BiOCl Colloidal Ultrathin Nanosheets: Synthesis, Characterization, and Application in Photocatalytic Aerobic Oxidation of Secondary Amines, Chem. Sci. 6 (2015) 1873–1878. doi:10.1039/C4SC03229B.

[11] Y. Mi, Z. Huang, F. Hu, Y. Li, J. Jiang, Room-Temperature Synthesis and Luminescent Properties of Single-Crystalline $SrMoO_4$ Nanoplates, J. Phys. Chem. C. 113 (2009) 20795–20799. doi:10.1021/jp907328v.

[12] J. Feng, X. Sun, C. Wu, L. Peng, C. Lin, S. Hu, et al., Metallic Few-Layered VS_2 Ultrathin Nanosheets: High Two-Dimensional Conductivity for In-Plane Supercapacitors, J. Am. Chem. Soc. 133 (2011) 17832–17838. doi:10.1021/ja207176c.

[13] N.T. Hahn, S. Hoang, J.L. Self, C.B. Mullins, Spray Pyrolysis Deposition and Photoelectrochemical Properties of n-Type BiOI Nanoplatelet Thin Films, ACS Nano. 6 (2012) 7712–7722. doi:10.1021/nn3031063.

[14] Y. Wang, K. Deng, L. Zhang, Visible Light Photocatalysis of BiOI and Its Photocatalytic Activity Enhancement by in Situ Ionic Liquid Modification, J. Phys. Chem. C. 115 (2011) 14300–14308. doi:10.1021/jp2042069.

[15] F.E. Osterloh, Inorganic Nanostructures for Photoelectrochemical and Photocatalytic Water Splitting, Chem. Soc. Rev. 42 (2013) 2294–2320. doi:10.1039/C2CS35266D.

[16] M. Wang, J. Ioccozia, L. Sun, C. Lin, Z. Lin, Inorganic-modified Semiconductor TiO_2 Nanotube Arrays for Photocatalysis, Energy Environ. Sci. 7 (2014) 2182–2202. doi:10.1039/C4EE00147H.

[17] T.R. Gordon, M. Cargnello, T. Paik, F. Mangolini, R.T. Weber, P. Fornasiero, et al., Nonaqueous Synthesis of TiO_2 Nanocrystals Using TiF_4 to Engineer Morphology,

Oxygen Vacancy Concentration, and Photocatalytic Activity, J. Am. Chem. Soc. 134 (2012) 6751–6761. doi:10.1021/ja300823a.

[18] M. Zhang, J. Xu, R. Zong, Y. Zhu, Enhancement of Visible Light Photocatalytic Activities via Porous Structure of g-C_3N_4, Appl. Catal. B Environ. 147 (2014) 229–235. doi:http://dx.doi.org/10.1016/j.apcatb.2013.09.002.

[19] Z. Xiong, X.S. Zhao, Nitrogen-Doped Titanate-Anatase Core–Shell Nanobelts with Exposed {101} Anatase Facets and Enhanced Visible Light Photocatalytic Activity, J. Am. Chem. Soc. 134 (2012) 5754–5757. doi:10.1021/ja300730c.

[20] F. Lei, Y. Sun, K. Liu, S. Gao, L. Liang, B. Pan, et al., Oxygen Vacancies Confined in Ultrathin Indium Oxide Porous Sheets for Promoted Visible-Light Water Splitting, J. Am. Chem. Soc. 136 (2014) 6826–6829. doi:10.1021/ja501866r.

[21] K.-L. Zhang, C.-M. Liu, F.-Q. Huang, C. Zheng, W.-D. Wang, Study of the Electronic Structure and Photocatalytic Activity of the BiOCl Photocatalyst, Appl. Catal. B Environ. 68 (2006) 125–129. doi:http://dx.doi.org/10.1016/j.apcatb.2006.08.002.

[22] L. Zhang, W. Wang, S. Sun, D. Jiang, E. Gao, Selective Transport of Electron and Hole Among {001} and {110} Facets of BiOCl for Pure Water Splitting, Appl. Catal. B Environ. 162 (2015) 470–474. doi:http://dx.doi.org/10.1016/j.apcatb.2014.07.024.

[23] J. Li, L. Zhang, Y. Li, Y. Yu, Synthesis and Internal Electric Field Dependent Photoreactivity of Bi_3O_4Cl Single-crystalline Nanosheets with High {001} Facet Exposure Percentages, Nanoscale. 6 (2014) 167–171. doi:10.1039/c3nr05246j.

[24] X. Zhang, Z. Ai, F. Jia, L. Zhang, Generalized One-Pot Synthesis, Characterization, and Photocatalytic Activity of Hierarchical BiOX (X = Cl, Br, I) Nanoplate Microspheres, J. Phys. Chem. C. 112 (2008) 747–753. doi:10.1021/jp077471t.

[25] D.-H. Wang, G.-Q. Gao, Y.-W. Zhang, L.-S. Zhou, A.-W. Xu, W. Chen, Nanosheet-constructed Porous BiOCl with Dominant {001} Facets for Superior Photosensitized Degradation, Nanoscale. 4 (2012) 7780–7785. doi:10.1039/C2NR32533K.

[26] Y. Bi, S. Ouyang, N. Umezawa, J. Cao, J. Ye, Facet Effect of Single-Crystalline Ag_3PO_4 Sub-microcrystals on Photocatalytic Properties, J. Am. Chem. Soc. 133 (2011) 6490–6492. doi:10.1021/ja2002132.

[27] R.F. Fakhrullin, A.I. Zamaleeva, R.T. Minullina, S.A. Konnova, V.N. Paunov, Cyborg Cells: Functionalisation of Living Cells with Polymers and Nanomaterials, Chem. Soc. Rev. 41 (2012) 4189–4206. doi:10.1039/C2CS15264A.

[28] W. Kubo, T. Tatsuma, Mechanisms of Photocatalytic Remote Oxidation, J. Am. Chem. Soc. 128 (2006) 16034–16035. doi:10.1021/ja066041y.

[29] J. Schneider, M. Matsuoka, M. Takeuchi, J. Zhang, Y. Horiuchi, M. Anpo, et al., Understanding TiO_2 Photocatalysis: Mechanisms and Materials, Chem. Rev. 114 (2014) 9919–9986. doi:10.1021/cr5001892.

[30] M. Panizza, G. Cerisola, Direct And Mediated Anodic Oxidation of Organic Pollutants, Chem. Rev. 109 (2009) 6541–6569. doi:10.1021/cr9001319.

[31] E. Brillas, I. Sirés, M.A. Oturan, Electro-Fenton Process and Related Electrochemical Technologies Based on Fenton's Reaction Chemistry, Chem. Rev. 109 (2009) 6570–6631. doi:10.1021/cr900136g.

[32] S. George, S. Pokhrel, Z. Ji, B.L. Henderson, T. Xia, L. Li, et al., Role of Fe Doping in Tuning the Band Gap of TiO_2 for the Photo-Oxidation-Induced Cytotoxicity Paradigm, J. Am. Chem. Soc. 133 (2011) 11270–11278. doi:10.1021/ja202836s.

[33] T.R. Gordon, M. Cargnello, T. Paik, F. Mangolini, R.T. Weber, P. Fornasiero, et al., Nonaqueous Synthesis of TiO_2 Nanocrystals Using TiF_4 to Engineer Morphology, Oxygen Vacancy Concentration, and Photocatalytic Activity., J. Am. Chem. Soc. 134 (2012) 6751–6761. doi:10.1021/ja300823a.

[34] X. Yang, X. Xu, J. Xu, Y. Han, Iron Oxychloride (FeOCl): An Efficient Fenton-Like Catalyst for Producing Hydroxyl Radicals in Degradation of Organic Contaminants, J. Am. Chem. Soc. 135 (2013) 16058–16061. doi:10.1021/ja409130c.

[35] Q. Zhao, X. Liu, M. Sun, C. Du, Z. Liu, Natural Kaolin Derived Stable SBA-15 as a Support for Fe/BiOCl: A Novel and Efficient Fenton-like Catalyst for the Degradation of 2-nitrophenol, RSC Adv. 5 (2015) 36948–36956. doi:10.1039/C5RA01804H.

[36] J. Xia, L. Xu, J. Zhang, S. Yin, H. Li, H. Xu, et al., Improved Visible Light Photocatalytic Properties of Fe/BiOCl Microspheres Synthesized via Self-doped Reactable Ionic Liquids, CrystEngComm. 15 (2013) 10132–10141. doi:10.1039/C3CE41555D.

[37] K. Xu, P. Chen, X. Li, C. Wu, Y. Guo, J. Zhao, et al., Ultrathin Nanosheets of Vanadium Diselenide: A Metallic Two-Dimensional Material with Ferromagnetic Charge-Density-Wave Behavior, Angew. Chemie Int. Ed. 52 (2013) 10477–10481. doi:10.1002/anie.201304337.

Award and Scientific contributions

Award

Chinese Government Award for Outstanding Self-financed Students Abroad of the Year 2014 http://gb.cri.cn/42071/2015/05/11/3245s4957579_2.htm

I was selected as the representative of all the Chinese students in Germany to make a speech on the award ceremony of "Chinese Government Award for Outstanding Self-financed Students Abroad of the Year 2014" in Berlin.

Scientific Contributions

During the work period of my PhD, I have published 14 papers in SCI-indexed international scientific journals, including 6 papers with impact factor higher than 10 (*Advanced Energy Materials*, *Angewandte Chemie International Edition*, *Energy Environmental Science, ACS Nano, and Nature communication*) and 8 papers with impact factor between 3 to 10 (*Small, Applied Catalysis B: Environmental, Chemistry of Materials*, *Nanoscale, Catalysis Today, Dalton Transactions, and Journal of Materials Chemistry C*). Currently two additional papers are under review (*Applied Catalysis B: Environmental and Nature Nanotechnology*).

I also gave contributions at international conferences and meetings. They are 2 international conference proceedings, 6 talks and 1 poster.

Covers

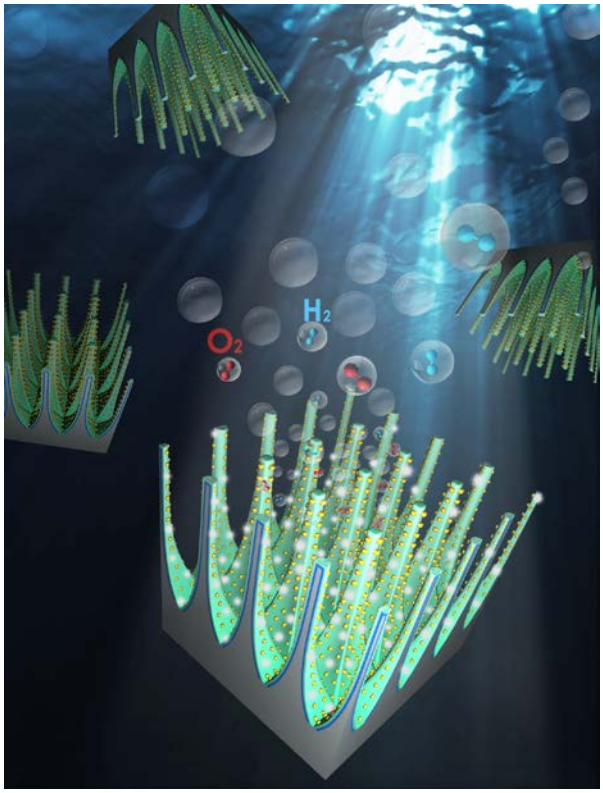

The paper "Constructing AZO/TiO_2 core/shell nanocone array with uniformly dispersed Au NPs for enhancing photoelectrochemical water splitting" was selected as the backside cover of *Advanced Energy Materials*; and was invited to highlight at *MaterialsViewsChina*.

The paper "Large-scale highly ordered Sb nanorod arrays anode with high capacity and rate capability for sodium-ion batteries" was selected as the inside backside cover of *Energy & Environmental Science.*

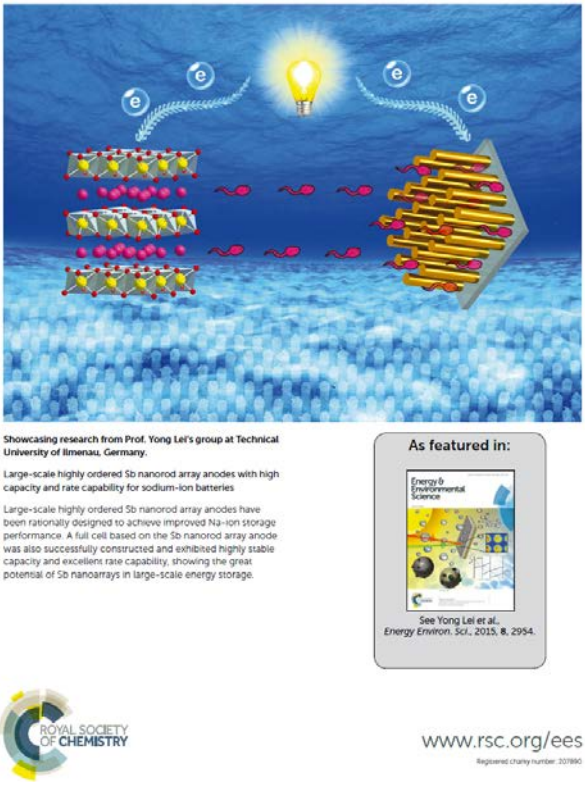

Publications in SCI-indexed Scientific Journals

1. **Mi Y.**[+], Wen L.Y.[+], Xu R., Wang Z.J., Cao D.W., Fang Y.G., Lei Y.*, Constructing AZO/TiO_2 core/shell nanocone array with uniformly dispersed Au NPs for enhancing photoelectrochemical water splitting, ***Advanced Energy Materials***, 2015, in press, (DOI: 10.1002/aenm.201501496) (backside cover paper) (Impact factor 16.146)
2. **Mi Y.**, Wen L.Y., Wang Z.J., Cao D.W., Fang Y.G., Lei Y.*, Building of anti-restack 3D BiOCl hierarchitecture by ultrathin nanosheets towards enhanced photocatalytic Activity, ***Applied Catalysis B: Environmental,*** 2015, 176, 331–337 (impact factor 7.435)
3. **Mi Y.**, Wen L.Y., Cao D. W., Wang Z. J., Zhao H.P., Zhou Y.L., Grote F., Lei Y.*, Ultra-low mass loading of platinum nanoparticles on bacterial cellulose derived carbon nanofibers for efficient hydrogen evolution, ***Catalysis Today***, 2015, (Impact factor 3.893)
4. Wen L.Y[+]., **Mi Y**[+].,([+]Contributed equally) Wang C.L., Fang Y.G., Grote F., Zhao H.P., Zhou M., Lei Y.*, Cost-effective atomic layer deposition synthesis of Pt nanotube arrays: application for high performance supercapacitor, ***Small*** 2014, 10, 3162–3168 (impact factor 8.368)

   (This work has been highlighted at MaterialsViewsChina)

   http://www.materialsviewschina.com/2014/08/yuan-zi-ceng-chen-ji-ji-shu-zhi-bei-gui-jin-shu-fu-za-na-mi-jie-gou-qu-de-jin-zhan-di-jia-gao-xiao-pt-na-mi-guan-he-cheng-ji-qi-ying-yong/
5. **Mi Y.**, Zhou M., Wen L.Y., Zhao H.P., Lei Y.*, High efficient visible-light driven photocatalyst: two dimensional square-like bismuth oxyiodine nanosheets, ***Dalton Transactions***, 2014, 43, 9549–9556, (impact factor 4.197)
6. Zhan Z.B., Xu R., **Mi Y.**, Zhao H.P., Lei Y.*, Highly controllable surface plasmon resonance property by heights of ordered nanoparticle arrays fabricated via a nonlithographic route, ***ACS Nano***, 2015, 9, 4583–4590 (impact factor 12.881)
7. Wen L.Y., Wang Z.J., **Mi Y.**, Xu R., Yu S.H.*, Lei Y.*, Designing heterogeneous 1D nanostructure arrays based on AAO template for energy applications, ***Small***, 2015, 11, 3408-3428, was selected as the frontispiece (frontispiece paper) (impact factor 8.368)
8. Wang C.L., Wen L.Y., Kups T., **Mi Y.**, Vellacheri R., Fang Y.G., Schaaf P., Zhao H.P., Lei Y.*, Growth control of AgTCNQ nanowire arrays by using a template-assisted electro-

deposition method, ***Journal of Materials Chemistry C***, 2013, 1, 8003-8006 (backside cover paper) (Impact factor 4.696)

9. Wang Z.J., Cao D.W., Wen L.Y., Xu R., Obergfell M., **Mi Y.**, Zhan Z.B., Nasori, Demsar. J, Lei Y., Manipulation of charge transfer and transport in nano-Au/PZT hybrids for photoelectrochemical applications, ***Nature communication***, 2015, accepted (Impact factor 11.470)
10. Cao D.W., Wang Z.J. , Nasori, Wen L.Y., **Mi Y**., Lei Y.*, Switchable charge-transfer in the photoelectrochemical energy-conversion process of ferroelectric $BiFeO_3$ photoelectrodes, ***Angewandte Chemie International Edition***, 2014, 126, 11207-11211 (impact factor 11.261)
11. Liang L.Y., Xu Y., Wang C.L., Wen L.Y., Fang Y.G., **Mi Y**., Zhou M., Zhao H.P., Lei Y.*, Large-scale highly ordered Sb nanorod arrays anode with high capacity and rate capability for sodium-ion batteries, ***Energy & Environmental Science***, 2015, DOI: 10.1039/C5EE00878F (inside back cover paper) (Impact factor 20.523)
12. Xu Y., Zhou M., Wen L.Y., Wang C.L., Zhao H.P., **Mi Y**., Liang L.Y., Fu Q., Wu M.H., Lei Y.*, Highly ordered three-dimensional Ni-TiO_2 nanoarrays as sodium ion battery anodes, ***Chemistry of Materials***, 2015, 27(12), 4274–4280 (impact factor 8.354)
13. Chi D., Lu S.D., Xu R., Liu K., Cao D.W., Wen L.Y., **Mi Y**., Wang Z.J.*, Lei Y.*, Qu S.C.*, Wang Z.G., Fully understanding the positive roles of plasmonic nanoparticles in ameliorating the efficiency of organic solar cells, ***Nanoscale***, 2015, DOI: 10.1039/C5NR04069H (Impact factor 7.394)
14. Xu Y., Zhou M., Wang X., Wang C.L., Liang L.Y., Grote F., Wu M.H., **Mi Y**., Lei Y.*, Oxygen vacancies enabled enhancement of sodium ion battery performance, ***Angewandte Chemie International Edition***, 2015, 54, DOI: 10.1002/anie.201503477 (impact factor 11.261)

Submitted and under revision

1. **Mi Y.**,† Wen L.Y.,† Wang Z.J., Cao D.W., Xu Y., Zhou Y.L., Lei Y.*, Two-dimensional Fe:BiOCl ultrathin nanosheet: Surface doping of Fenton reagent for high efficient photocatalysis, Applied Catalysis B: Environmental, submitted.

2. **Mi Y.**, Wen L.Y., Wang Z.J., Cao D.W., Zhou Y.L., Lei Y.*, Three-dimensional nanovalley for monomolecule SERS detection, preparing.
3. Wen L.Y., Xu R., **Mi Y.**, Lei Y.*, Building arbitrary binary nanostructure arrays with anodic aluminum oxide template, Nature Nanotechnology, submitted.

Talks

1. **Mi Y**., Lei Y.,* Constructing AZO/TiO_2 core/shell nanocone array with uniformly dispersed Au NPs for enhancing photoelectrochemical water splitting, Colloquium of physics and chemistry – Doktorandenseminar, November 17, 2015, Ilmenau, Germany.
2. **Mi Y**., Zhou M., Wen L.Y., Lei Y.,* Tow dimensional square-like bismuth oxyiodine nanosheets with high efficient visible-light driven photocatalytic activity, 78th Annual Conference of the DPG, March/April 31-04, 2014, Dresden, Germany.
3. **Mi Y**., Wen L.Y., Wang C.L, Zhao H.P., Lei Y.,* Realization of platinum 3D nanostructures using an improved atomic layer deposition process, 77th Annual Conference of the DPG, March 10-15, 2013, Regensburg, Germany
4. **Mi Y**., Lei Y.,* Three-dimensional nano-structuring for high performance devices, Highly Integrated 3D electronic systems for the intelligent production, May 5, 2013, Erfurt, Germany
5. Wen L., **Mi Y**., Grote F., Al-Haddad A., Zhan Z., Zhao H., Lei Y.*, Nano-engineered three-dimensional Pt/MnO_2 thin films for flexible, high performance supercapacitors, 77th Annual Conference of the DPG, March 10-15, 2013, Regensburg, Germany
6. **Mi Y**., Zhan Z.B., Sun H., Grote F., Zhao H., Lei Y.,* Highly sensitive gas sensors based on three-dimensional surface nano-patterns realized by UTAM nano-structuring technique, 76th Annual Conference of the DPG, March 25-30, 2012, Berlin, Germany.

Poster

1. **Mi Y.,** Surface patterning using for sensor device, 1st International Conference on Challenges and Perspectives of Functional Nanostructures, July 29-31, 2014, Ilmenau, Germany.

Declaration

I hereby declare that this Ph.D. dissertation entitled “Atomic Layer Deposition Functionalization and Modification of Three Dimensional Nanostructures for Energy Storage and Conversion” was carried out by me for the degree of Doctor of Philosophy under the supervision of Prof. Dr. Yong Lei. All dates or information in this dissertation that have been directly or indirectly consulted or used from other sources are clearly stated. This dissertation has not been submitted, in part or in whole, for any other degree or examination in any other University. I have acknowledged all main sources of help, and I have made clear exactly what was done by others and what I have contributed when the work was done jointly with others. Some of the results may have been published in scientific journals or elsewhere. I am aware that the falsity of this declaration will be regarded as an attempt of deception and will cause the derogation of the doctoral procedure.

Ilmenau, 18. Mai 20165
Yan Mi